ULTRASOUND PROPAGATION AND BINDING IN SOLIDS

A thesis submitted to the University of Durham

for the Degree of Doctor of Philosophy

by

N.G. Pace, B.Sc. (Dunelm)

Department of Applied Physics and Electronics,

Science Laboratories, South Road, Durham, England.

NOVEMBER 1970

ABSTRACT

Measurement of sound wave velocity and attenuation by the ultrasonic pulse-echo technique are used to obtain insight into the nature of weak interatomic binding forces which are present or develop in certain materials. In particular, anomalies are found in both the elastic and anelastic properties in the vicinity of the martensitic phase transformations which occur in TiNi and indium-thallium alloys. Considerable differences found between the elastic moduli of the two phases of TiNi are shown to arise mainly from a variation in the free carrier density. Previously reported elastic constant data of some fcc indium-thallium alloys are complemented by the present results and an overall picture of the compositional dependence of the elastic properties of these alloys in both the tetragonal and cubic phases is provided.

Zirconia can be forced into a cubic structure by the addition of more than 7 mole % yttria: elastic constant data of two zirconia-yttria solid solutions, technologically important materials, provides a basis for the discussion of the stability of the cubic phase.

Finally, on the basis of an evaluation of the elastic moduli of arsenic, a pronounced layer-type crystal, the ultrasonic wave propagation characteristics in this material are extensively

compared and contrasted with those of the other two rhombohedral elemental semimetals antimony and bismuth, neither of which are themselves layer-like. The elastic wave propagation in antimony and bismuth is shown to differ not only in degree but also in kind from that in arsenic which exhibits the characteristics expected for a layer-like crystal.

The weak binding forces in each of the materials studied are shown to play a dominant role in their elastic behaviour.

ACKNOWLEDGEMENTS

First and foremost I would like to express my sincere thanks to Dr. G.A. Saunders for his continual guidance, interest, support and encouragement during the period of this research.

My thanks also go to Professor D.A. Wright for providing many facilities; to Mrs. Henderson and particularly Mrs. McGauley for carefully typing this thesis; to the technical staff headed by Mr. F. Spence; in particular I wish to mention Mr. R. Waite for his cheerfully given and helpful service.

I am grateful to the Science Research Council for financial support.

CONTENTS

CHAPTER 1

Introduction

Introduction

Study of ultrasonic stress wave propagation provides basic information on both the elastic and anelastic behaviour of a solid. Because elastic moduli are directly related to the second derivative of the total energy of a solid with respect to strain, they lead to an insight into the nature of the binding forces.

The main theme of this thesis is an investigation of the elastic and anelastic properties of materials in which, for some reason certain interatomic binding forces are weak or develop a weakness. When the strength of the interatomic binding forces becomes very small, phase changes to a different crystal structure can ensue. Transitions of the martensitic type are of great theoretical and practical interest; effects on the ultrasonic wave propagation characteristics in the vicinity of such transitions in TiNi and indium-thallium alloys form a major part of this work. In addition an incipient phase change in the technologically important ionic zirconia-yttria solid solutions is investigated.

Another aspect of weak binding forces is manifested in layer-type crystals: arsenic is a case in point having tightly bound double layers held together by weak forces. In such crystals, highly anisotropic effects are expected not least in the elastic behaviour which is investigated here.

1.1 Elastic constants and binding in solids

There are two main theoretical approaches to the relationships between the binding forces and elastic moduli. One is the force constant method in which radial and angular forces are postulated to exist between an atom and its neighbours; the other attempts to explain the elastic properties by use of microscopic models. The classic force constant calculation is that by Born and von Karman (1912) for the simple cubic case: two nearest neighbour force constants and several second neighbour constants are employed. The force on an atom is calculated in terms of the force constants and atomic displacements. The equations of motion of the atom in the long wavelength limit in terms of the components of the strain gradients are then compared with the macroscopic equations of motion and the relations between the force constants and elastic moduli thereby obtained.

The quantum approach first requires a theory of the forces responsible for the cohesion of the solid and second an estimate of the strain dependence of these forces. The accuracy of any atomic model is severely tried in this process of differentiation and theories which can predict the cohesive energy satisfactorily may not give the correct elastic constants. Ionic solids are the simplest to consider. Born's (1923) theory of the lattice energy of

ionic crystals is based on the assumption that they are built up of positive and negative ions. If these ions have a spherically symmetrical charge distribution, then the attractive coulomb force between two such ions depends only on their separation. To prevent the lattice from collapsing, repulsive forces, in addition to the coulombic repulsion of like ions, are required. These arise from the overlap of electron shells of neighbouring ions and are quantum mechanical in origin. The lattice summations required to obtain the total coulombic potential energy are the same for all ionic crystals of the same structure and are given by the Madelung constant; only nearest neighbour interactions need be considered for the short range repulsive force contribution to the potential energy and may be expressed in terms of two adjustable parameters. This approach to the cohesion in ionic solids has been followed in the analysis of the elastic moduli of the zirconia-yttria solid solutions in chapter 6.

Metallic cohesion differs from that in ionic solids in that the closing of the outer electron shell takes place by a sharing of the valence electrons of all the atoms. Thus the interactions responsible for metallic bonds arise from forces between the positive metal ion cores and the collectively shared electrons. The contributing terms to the total energy W of a metal may be

written

$$W = W_o + W_F + W_R$$

where W_o is the energy of the valence electron lowest state, corresponding to wave vector $\underline{k} = 0$ or to zero momentum. W_F is the Fermi energy (kinetic energy) of the valence electrons measured with respect to W_o. W_R is the interaction energy between the closed shell ion cores. These contributions will now be discussed in turn. W_o may be split up into $W_o(I)$ and $W_o(II)$; the former is the electrostatic potential energy of a uniform distribution of valence charge in the field of the periodic structure of the positive ion cores and is termed the electrostatic energy W_E. The other portion $W_o(II)$ represents the kinetic energy and part of the potential energy of the lowest electron state. If those elastic distortions are considered which change the shape of the unit cell but leave the volume unaltered, then $W_o(I)$ and $W_o(II)$ and in the case of monovalent metals W_F, have no effect on these shear moduli. For example, Fuchs (1936) showed that the shear constants C_{44} and $(C_{11}-C_{12})/2$ for monovalent cubic metals can be obtained from a consideration of only the electrostatic energy W_E and the exchange energy W_R. For metals of higher valency an additional term derives from the change in Fermi energy caused by movements of the Brillouin zone planes as the metal is sheared. Taking this into account,

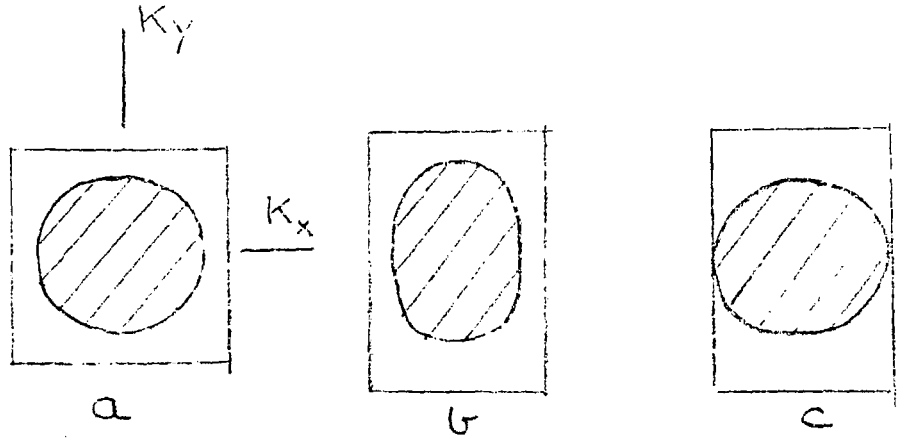

Figure (1.1) a,b,c. Schematic representation of a Brillouin zone with the electronic states half filled and having a spherical Fermi surface. (a) Zero shear; (b) shear strain present, electrons occupying same states as in (a); (c) shear strain as in (b) but electrons have relaxed to the same Fermi energy as in (a).

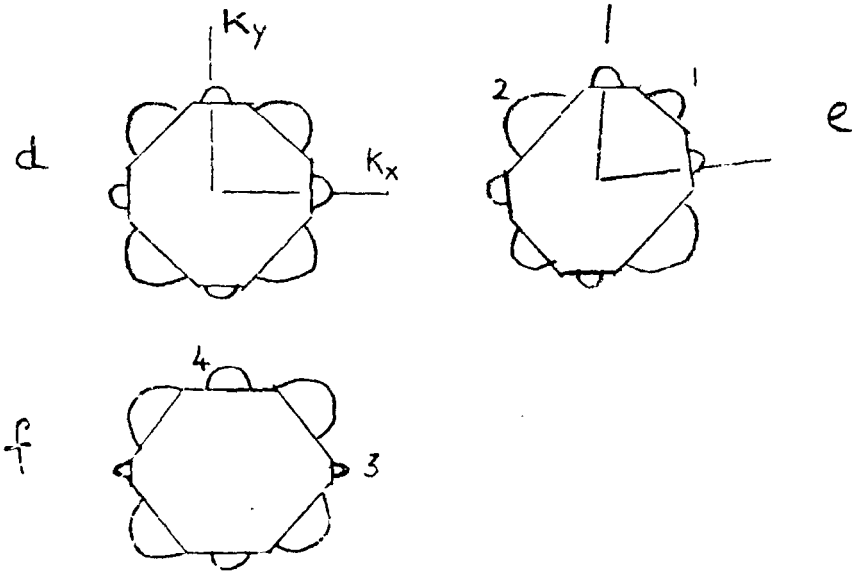

Figure (1.1) d,e,f. Schematic representation of the Brillouin zone and overlap electron populations of aluminium in various strain states (after Huntington 1958).

Leigh (1951) has shown that the observed near isotropy of the shear constants of trivalent aluminium results from the negligible effect of W_R coupled with the compensating effects of the individually anisotropic contributions from W_E and W_F. The origin of the effect the Fermi energy can have on the shear constants may be seen by initially considering the alkali metals: only half the states in the first Brillouin zone are filled as these metals are monovalent. On the assumption of a spherical Fermi surface any volume conserving distortion will not change the Fermi energy because of the availability of other states of the same energy: this is depicted schematically in Figure (1.1) a,b,c. But in the case of a strain which does not conserve volume the Fermi energy does contribute to the associated modulus. Jones (1949) has given an expression which provides that part of the bulk modulus attributable to the Fermi energy alone: use is made of this in analysing the elastic moduli of TiNi in chapter 4. In trivalent metals such as aluminium and indium there are enough electrons to fill more than one Brillouin zone and therefore the Fermi surface is cut by Brillouin zone planes. Figure (1.1) shows schematically the first Brillouin zone of a fcc material; Figure (1.1d) shows the unstrained condition while Figures (1.1e) and (1.1f) represent the strained Brillouin zone corresponding to elastic shear moduli C_{44} (= C) and $(C_{11}-C_{12})/2$ (= C') respectively.

The states just inside one pair of hexagonal faces (1) in Figure (1.1e) have receded from the origin and their energy (proportional to k^2 in the free electron theory) has increased: the situation is reversed for states just inside the other pair of hexagonal faces (2). The net result is an increase in the full zone energy and a positive addition to the shear modulus. An analogous situation occurs for the other type of shear in Figure (1.1f). Leigh (1951) found for aluminium that the full zone term alone could not account for the observed elastic isotropy. In a state of strain corresponding to C the energy of the overlap electrons on one pair (1) of hexagonal faces will have increased whereas the energy of the electrons on the other pair (2) of hexagonal faces will have decreased. Electrons then transfer from high energy overlap positions to low energy overlap positions until the maximum energy of the occupied states in the two sites attains the Fermi energy. There is then a large low energy population and a small high energy population and in fact the total overlap energy in this case for aluminium is decreased. When this negative overlap contribution to the shear moduli is added to those from the full zone and electrostatic terms, the observed elastic isotropy of aluminium is essentially explained.

Finally it should be mentioned that although van der Waals forces are present in all solids they are frequently negligible:

their origin is found in the fluctuations of the electrostatic field of an ion, the resultant dipole then interacting with neighbouring dipoles. However van der Waals forces can be important in highly anisotropic crystals; such a situation may exist in arsenic and in chapter 7 is critically discussed in the light of elastic constant data.

1.2 Plan of the work

The general characteristics of elastic wave propagation in solids and the way in which the velocity and attenuation of the ultrasound are measured is introduced in chapters 2 and 3 respectively. Subsequent chapters are concerned with the ultrasonic study of the transformations in TiNi (chapter 4), the indium-thallium system (chapter 5) and the zirconia-yttria system (chapter 6). Finally chapter 7 reports the elastic properties of arsenic and contrasts them with those of antimony and bismuth.

CHAPTER 2

Propagation of elastic waves in anisotropic solids

2.1 Introduction

All bodies are deformed under the action of external forces. If, after removal of the external forces, the body returns to its original form, it is said to be elastic. The physical property of elasticity may be understood as describing the relation between the stress field developed and the strain field caused. The functional relation between stress and strain must reflect the property of complete recovery from strain on removal of stress. The strain is thus a unique homogeneous function of stress.

This chapter will be concerned with the equation of motion of anisotropic elastic solids under the action of applied periodic stresses. The propagation velocity of the resultant high frequency stress wave is obtained as a solution to the equation of motion.

It is thus indicated how measurements of the propagation velocity of ultrasonic waves in specific directions in crystals of various symmetries may be related to the elastic moduli.

The subject of elastic wave propagation in anisotropic media has been dealt with in depth by many research workers: comprehensive and detailed discussions have been presented by Musgrave (1954 a,b, 1957), Waterman (1959), Brugger (1965) and Neighbours and Schacher (1967).

2.2 Stress-Strain relationships for a crystalline body.

2.2.1 Definition of strain

If a one dimensional solid of original length x is stretched to have a length x + R, then a portion of the solid of original length Δx will now have a length $\Delta x + \Delta R$. The strain in the section of original length Δx is defined as $\Delta R/\Delta x$. The strain e at a point in the one dimensional solid is thus the limiting value of $\Delta R/\Delta x$, that is

$$e = \lim_{\Delta x \to o} \frac{\Delta R}{\Delta x} = \frac{dR}{dx} \qquad (2.1)$$

In a three dimensional solid the strain is a second rank tensor which defines the deformation for small deformation, in the neighbourhood of a point specified in the undeformed solid by the position vector $x(x_1, x_2, x_3.)$ Analagous to the one dimensional case, the variation of the displacement R_i with position x_i in the body may be written in terms of the displacement gradients,

$$e_{ij} = \frac{\partial R_i}{\partial x_j}, \quad (i, j = 1, 2, 3) \qquad (2.2)$$

The tensor e_{ij} is composed of an antisymmetrical part which represents body rotations and a symmetrical part which represents the change in shape and size of the body. The symmetrical part of e_{ij} is ϵ_{ij} where,

$$\epsilon_{ij} = \tfrac{1}{2}(e_{ij} + e_{ji}) \tag{2.3}$$

and

$$\epsilon_{ij} = \tfrac{1}{2}\left(\frac{\partial R_i}{\partial x_j} + \frac{\partial R_j}{\partial x_i}\right) \tag{2.4}$$

The ϵ_{ij} defined by (2.3) and (2.4) have a simple geometrical meaning; $\epsilon_{ij}(i = j)$ is the change in length per unit length of a straight line segment originally parallel to the x_j axis; $\epsilon_{ij}(i \neq j)$ is twice the change in an angle whose defining sides were originally parallel to the x_j and x_i axes.

2.2.2 Definitition of Stress

The stress σ_{ij} in a three dimensional solid is a second rank tensor and represents the components of force acting on an element of area; the first subscript represents the normal to the plane on which the stress component acts and the second subscript the direction of the stress component. The stress tensor is symmetric ($\sigma_{ij} = \sigma_{ji}$).

2.2.3 Hookes Law

Hookes Law states that the stress acting on an elastic body is proportional to the strain. The stress components are thus linear functions of the strain components. The constants of proportionality C_{ijkl}, are fourth rank tensors and are called the elastic constants of the material. Thus Hookes Law may be written as,

$$\sigma_{ik} = C_{ijkl}\ \epsilon_{jl} \tag{2.5}$$

81 elastic stiffness constants are defined by this equation which is the most general linear stress-strain relation yielding zero strain for zero stress. In practice, the elastic constants in the tensor notation C_{ijkl} are written in a condensed or matrix notation; the following correspondence of indices is used.

Tensor notation	11	22	33	23,32	13,31	12,21
Matrix notation	1	2	3	4	5	6

For example C_{1231} in tensor notation would be written C_{65} in the matrix notation.

2.2.4 Physical Significance of the elastic constants

The quantity C_{ji} expresses the stress-strain ratio σ_j/ϵ_i under the condition that all the strains other than ϵ_j are zero. The physical significance of this can be seen by reference to a cubic crystal as follows.

If a normal stress σ_n (see Figure (2,1)) is applied to two (110) faces of a cubic crystal and such stresses are applied to other faces to ensure that only the normal strain ϵ_n parallel to the [110] direction occurs,

then $\sigma_n/\epsilon_n = C_n$ and is expressed

by $C_n = (C_{11} + C_{12} + 2C_{44})/2$ (2.6)

If the same sample is under a shear strain such that the angle between the [001] and the [110] directions decreases, then this

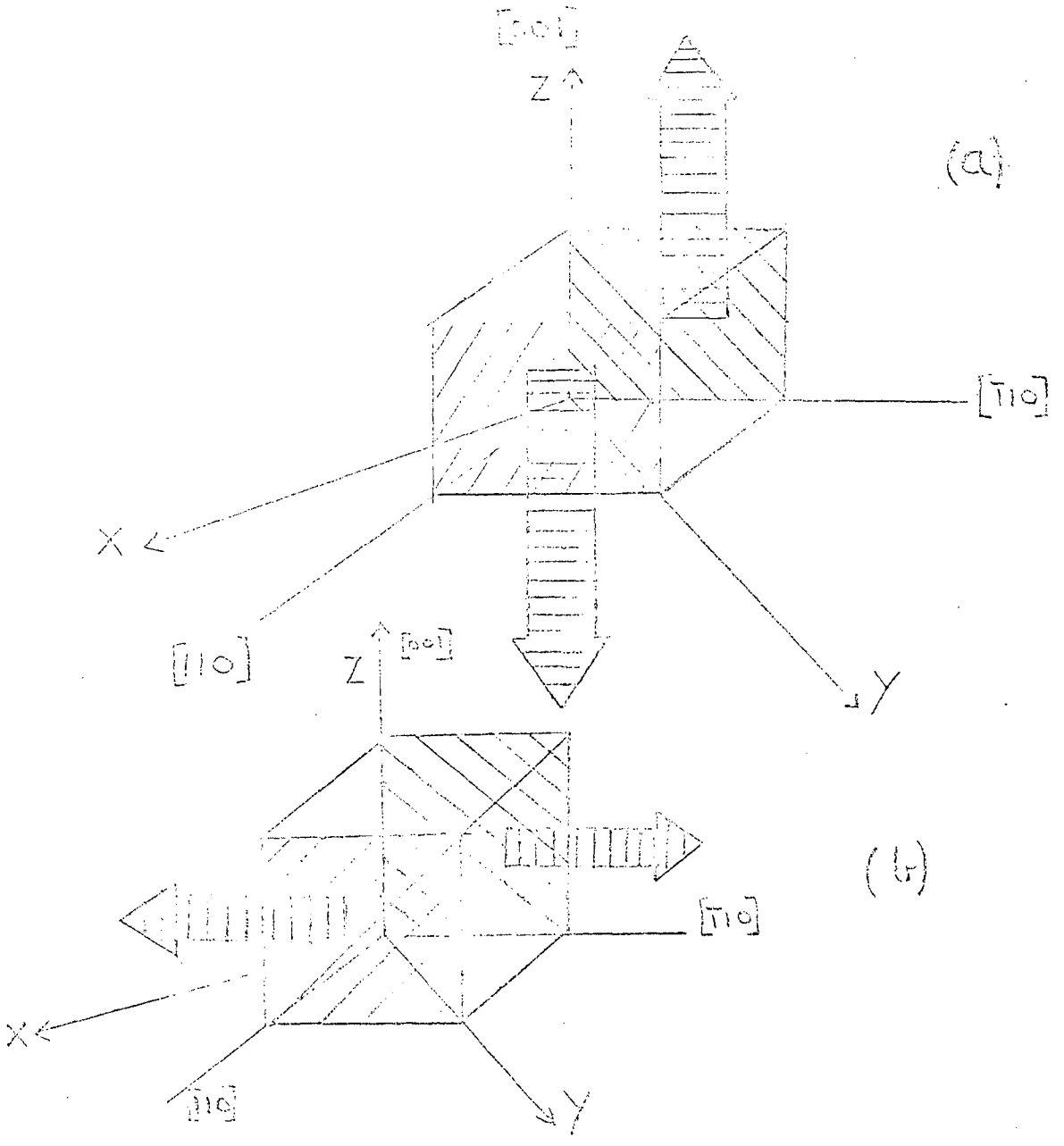

Figure (2.1) Illustration of the physical interpretation of the elastic moduli C_{44} (a) and $(C_{11} - C_{12})/2$ (b) of a cubic crystal (see text).

may be achieved by a shear stress applied to the (110) faces in the [001] direction (see Figure (2.1)); this is the only stress necessary. For this example, the ratio of shear stress to shear strain referred to cubic axes is $C(=C_{44})$.

In a similar way, a shear stiffness may be defined if the shear stresses are applied in the $[\bar{1}10]$ direction on the (110) faces to produce a shear strain measured by the decrease in angle between the [110] and $[\bar{1}10]$ directions. The stress strain ratio in this case is

$$C' = (C_{11} - C_{12})/2 \tag{2.7}$$

Thus, the three independent stiffnesses of a cubic crystal can be expressed as two shear stiffnesses and one normal stiffness.

2.3 Relations between the elastic stiffness constants and the elastic compliance constants

The set of linear homogeneous independent equations represented by (2.5) can be solved for the strains in terms of the stresses.

$$\epsilon_{ik} = S_{ikjl}\ \sigma_{jl} \tag{2.8}$$

where the S_{ikjl} are the elastic compliance constants.

The relation between the S_{ijkl} and the C_{ijkl} is given in matrix notation by

$$S_{ij} = (-1)^{i+j} \Delta^c_{ij} / \Delta^c \qquad (2.9)$$

where Δ^c is the determinant of the C_{ij} terms and Δ^c_{ij} is the minor of the element C_{ij}.

2.3.1 Adiabatic and isothermal elastic moduli

The total energy of an elastic body is, from the first law of thermodynamics, the sum of the mechanical and thermal energies. In measurements of elastic moduli by the ultrasonic pulse echo method the entropy is effectively constant and the adiabatic moduli are obtained. The difference between the adiabatic and isothermal moduli may be found by taking the elastic energy to be a function of the stresses and temperature.

$$(S_{ij})_{\text{Adiabatic}} = \left(\frac{\partial \epsilon_i (\sigma_i, T)}{\partial \sigma_i} \right)_S \qquad (2.10)$$

This may be written as

$$(S_{ij})_S = \left(\frac{\partial \epsilon_i}{\partial \sigma_j} \right)_T + \left(\frac{\partial \epsilon_i}{\partial T} \right)_{\sigma_i} \left(\frac{\partial T}{\partial \sigma_j} \right)_S$$

$$= (S_{ij})_T - \alpha_i \left(\frac{\partial T}{\partial S} \right)_{\sigma_j} \left(\frac{\partial S}{\partial \sigma_j} \right)_T \qquad (2.11)$$

where α_i is the change of strain ϵ_i with temperature and S is the entropy. For compressive strains α_i is a component of the linear thermal expansion tensor. From standard thermodynamic relationships,

$$\left(\frac{\partial T}{\partial S}\right)_{\sigma_j} = \frac{T}{C_p} \tag{2.12}$$

where C_p is the heat capacity at constant stress. Also,

$$\left(\frac{\partial S}{\partial \sigma_j}\right)_T = \frac{-\partial^2 F}{\partial \sigma_j \partial T} = \frac{-\partial^2 F}{\partial T \partial \sigma_j} = \frac{V \partial \epsilon_j}{\partial T} \tag{2.13}$$

where F is the Helmholtz free energy. Thus, by substituting (2.12) and (2.13) into (2.11) the difference between the adiabatic and isothermal elastic compliances is obtained as

$$\left(S_{ij}\right)_S - \left(S_{ij}\right)_T = -\frac{\alpha_i \alpha_j T V}{C_p} \tag{2.14}$$

This difference is usually small and of the order of 1% of the S_{ij}.

2.4 The effect of symmetry on the number of independent elastic moduli

Because both the stress and strain tensors are symmetrical, it follows that

$$C_{ikjl} = C_{kijl} = C_{iklj} \tag{2.15}$$

These conditions reduce the number of independent elastic constants from 81 to 36. A further condition is that the strain energy is a function of state of the body and is independent of the path by which the state is reached; this imposes the condition

$$C_{ijkl} = C_{klij} \tag{2.16}$$

thus further reducing the number of independent moduli to 21. Any further reduction in the number of independent moduli is determined by the symmetry of the crystal of interest.

For a lattice to be stable, the strain energy must be a positive definite quadratic function of the strain components (Born and Huang 1954). This is satisfied if the discriminants of the C_{ij} matrix are positive. For a cubic crystal this leads to the conditions

$$C_{12} > o; \quad C_{11} - C_{12} > o:$$

and for a trigonal ($\bar{3}_m$) crystal

$$C_{13}^{\,2} < C_{33}\left(\frac{C_{11} + C_{12}}{2}\right);$$

$$C_{11} > o; \quad C_{33} > o; \quad C_{44} > o;$$

$$2C_{14}^{\,2} < C_{44}\left(C_{11} - C_{12}\right):$$

whilst for tetragonal (4/mmm) crystals the condition requires,

$$C_{11}>o; \quad C_{33}>o; \quad C_{44}>o; \quad C_{66}>o;$$

$$C_{11}C_{33}>C_{13}^2; \quad C_{11}-C_{12}>o; \quad C_{33}(C_{11}+C_{12})>2C_{13}^2.$$

2.5 The equation of motion of an elastic body and its solutions

The equation of motion for an elastic medium is obtained by considering the forces acting on an element of volume in the medium. In particular if one considers the forces on opposite pairs of faces of a small rectangular parallelpiped, then by taking the differences between these pairs of forces the components of the resulting force on the volume considered are obtained. On equating the force components to the acceleration components for a medium of density ρ, the equations of motion are

$$\frac{\partial \sigma_{ij}}{\partial x_j} = \rho \frac{\partial^2 R}{\partial t^2} \quad (i = 1, 2, 3) \tag{2.17}$$

or $$\sigma_{ij,j} = \rho \ddot{R}_i$$

where $\underline{R}$ (R_1, R_2, R_3) is the displacement vector and $\underline{x}$ (x_1, x_2, x_3) the position vector. On substituting (2.5) into

(2.17) the equations of motion become

$$C_{ijkl} \epsilon_{kl,j} = \rho \ddot{R}_i \tag{2.18}$$

where from (2.4)

$$\epsilon_{kl,j} = \tfrac{1}{2} (R_{l,kj} + R_{k,lj})$$

and the comma notation is used to indicate differentiation with respect to $\underline{x}$.

Plane wave solutions to (2.18) will be looked for. Consider a plane wave travelling in a direction given by the propagation vector $\underline{k}$ (k_1, k_2, k_3) which is normal to planes of constant phase. The unit vector $\underline{n}$ (n_1, n_2, n_3) is also normal to the wave front and $\underline{k} = \left(\frac{\omega}{v}\right) \underline{n} = \left(\frac{2\pi}{\lambda}\right) \underline{n}$ where ω is the angular frequency, v is the phase velocity and λ the wavelength of the wave. The particle displacement vector $\underline{R}$ is in general not parallel to $\underline{k}$. The expression for the components of any one of the plane wave solutions is written as

$$R_1 = R_{o1} e^{i(\omega t - \underline{k}.\underline{x})}, \quad (1 = 1, 2, 3) \tag{2.19}$$

On differentiation (2.19) becomes,

$$R_{l,kj} = -n_k n_j R_{ol} \left(\frac{\omega^2}{v^2}\right) e^{i(\omega t - \underline{k}.\underline{x})} \tag{2.20}$$

and

$$\ddot{R}_l = -R_{ol} \omega^2 e^{i(\omega t - \underline{k}.\underline{x})} \tag{2.21}$$

Thus on substituting (2.20) and (2.21) into (2.18) the equations of motion of the elastic medium are finally obtained as,

$$C_{ijkl} R_{ol} n_k n_j = \rho v^2 R_{oi}, \quad (i = 1, 2, 3) \qquad (2.22)$$

The condition for (2.22) to have solutions is that the determinant of the coefficients of the displacement components R_{o1}, R_{o2}, R_{o3} be zero, and is written as

$$\begin{vmatrix} L_{11} - \rho V^2 & L_{12} & L_{13} \\ L_{12} & L_{22} - \rho V^2 & L_{23} \\ L_{13} & L_{23} & L_{33} - \rho V^2 \end{vmatrix} = 0 \qquad (2.23)$$

where

$$\begin{aligned}
L_{11} &= n_1^2 C_{11} + n_2^2 C_{66} + n_3^2 C_{55} + 2n_2 n_3 C_{56} + 2n_3 n_1 C_{15} + 2n_1 n_2 C_{16} \\
L_{12} &= n_1^2 C_{16} + n_2^2 C_{26} + n_3^2 C_{45} + n_2 n_3 (C_{46}+C_{25}) + n_3 n_1 (C_{14}+C_{56}) + \\
&\quad n_1 n_2 (C_{12}+C_{66}) \\
L_{13} &= n_1^2 C_{15} + n_2^2 C_{46} + n_3^2 C_{35} + n_2 n_3 (C_{45}+C_{36}) + n_3 n_1 (C_{13}+C_{55}) + \\
&\quad n_1 n_2 (C_{14}+C_{56}) \qquad (2.24) \\
L_{22} &= n_1^2 C_{66} + n_2^2 C_{22} + n_3^2 C_{44} + 2n_2 n_3 C_{24} + 2n_3 n_1 C_{46} + 2n_1 n_2 C_{26} \\
L_{23} &= n_1^2 C_{56} + n_2^2 C_{24} + n_3^2 C_{34} + n_2 n_3 (C_{44}+C_{23}) + n_3 n_1 (C_{36}+C_{45}) + \\
&\quad n_1 n_2 (C_{25}+C_{46}) \\
L_{33} &= n_1^2 C_{55} + n_2^2 C_{44} + n_3^2 C_{33} + 2n_2 n_3 C_{34} + 2n_3 n_1 C_{35} + 2n_1 n_2 C_{45}
\end{aligned}$$

and the n's are the direction cosines.

Equation (2.23) is a cubic equation in ρV^2. For a given propagation direction the roots of (2.23) yield in general three possible velocities and hence three elastic waves may be propagated. The values of R_{o1}, R_{o2} and R_{o3} corresponding to a given root are usually such that the wave is neither purely longitudinal (for which $\underline{R} \wedge \underline{n} = o$) nor purely transverse (for which $\underline{R} \cdot \underline{n} = o$). Directions of propagation may be chosen such that one pure longitudinal and two pure transverse waves result.

2.5.1 Solutions of the equations of motion for isotropic materials

In an isotropic material the elastic constants must be independent of the particular set of rectangular coordinate axes chosen. This requires that the elastic constants are unaltered by any rotation of axes and leads to the conditions,

$$C_{12} = C_{13} = C_{23}, \quad C_{44} = C_{55} = C_{66}, \quad C_{11} = C_{22} = C_{33}$$

and $C_{44} = (C_{11} - C_{12})/2$ (2.25)

with all the other elastic constants zero.

The solutions of (2.23) are the same whatever propagation direction is chosen; on taking $n_1 = 1$, $n_2 = 0$, $n_3 = 0$, equation (2.23) becomes

$$\begin{vmatrix} C_{11} - \rho V^2 & 0 & 0 \\ 0 & C_{44} - \rho V^2 & 0 \\ 0 & 0 & C_{44} - \rho V^2 \end{vmatrix} = 0 \qquad (2.26)$$

yielding three solutions namely

$$\text{(a)} \quad \rho V^2 = C_{11}, \quad \text{(b)} \quad \rho V^2 = C_{44}, \quad \text{(c)} \quad \rho V^2 = C_{44} \qquad (2.27)$$

To discover the particle displacement vector and thus which solutions correspond to longitudinal waves and which to transverse waves, the solutions (2.27) are substituted in turn into (2.22). For solution (a) the only component of the particle displacement vector is parallel to the propagation vector and thus (a) gives the velocity of a longitudinal wave. In the case of both (b) and (c), the solutions correspond to degenerate transverse waves. Thus

$$v_{long} = \left(\frac{C_{11}}{\rho}\right)^{\frac{1}{2}}; \qquad v_{shear} = \left(\frac{C_{44}}{\rho}\right)^{\frac{1}{2}} \qquad (2.28)$$

The elastic properties of isotropic materials are often expressed in terms of the Lame constants λ and μ which are defined by

$$C_{11} = \lambda + 2\mu \; ; \quad C_{44} = \mu \; ; \quad C_{12} = \lambda \qquad (2.29)$$

2.5.2 Solutions of the equations of motion for materials possessing cubic symmetry

In studying the elastic properties of crystals one is directly concerned with only the eleven Laue groups (Henry, Lipson and Wooster 1951) and not with the thirty two point groups. This results from the fact that elastic properties are always centrosymmetrical. As a result the speed of an elastic wave mode depends on the direction of propagation but not on the sense of this direction. All point groups belonging to the same Laue group have common arrays of elastic coefficients.

In the particular case of cubic symmetry the five point groups, each of which is contained in one or other of the two cubic Lane groups, have the same C_{ij} matrix. Cubic symmetry reduces the number of independent moduli from 21 to 3, namely C_{11}, C_{12}, C_{44}, as detailed in the matrix.

$$\begin{matrix} C_{11} & C_{12} & C_{12} & 0 & 0 & 0 \\ \cdot & C_{12} & C_{12} & 0 & 0 & 0 \\ \cdot & \cdot & C_{11} & 0 & 0 & 0 \\ \cdot & \cdot & \cdot & C_{44} & 0 & 0 \\ \cdot & \cdot & \cdot & \cdot & C_{44} & 0 \\ \cdot & \cdot & \cdot & \cdot & \cdot & C_{44} \end{matrix}$$

TABLE (2.1)

Propagation Direction	Particle Displacement sector	ρV^2
[100]	[100]	C_{11}
[100]	in (100) plane	C_{44}
[110]	[110]	$\frac{1}{2}(C_{11} + C_{12} + 2C_{44})$
[110]	[001]	C_{44}
[110]	$[1\bar{1}0]$	$\frac{1}{2}(C_{11} - C_{12})$
[111]	[111]	$\frac{1}{3}(C_{11} + 2C_{12} + 4C_{44})$
[111]	in (111) plane	$\frac{1}{3}(C_{11} + C_{44} - C_{12})$

Propagation and polarisation vectors for pure mode propagation in cubic crystals. The relation between the measured velocity of propagation V and the elastic moduli C_{ij} is given.

For a general propagation direction $\underline{n}(n_1, n_2, n_3)$ the determinant (2.23) becomes

$$\begin{vmatrix} (C_{11}-C_{44})n_1^2+C_{44}-\rho V^2 & n_1n_2(C_{12}+C_{44}) & n_1n_3(C_{12}+C_{44}) \\ n_1n_2(C_{12}+C_{44}) & n_2^2(C_{11}-C_{44})+C_{44}-\rho V^2 & n_2n_3(C_{12}+C_{44}) \\ n_1n_3(C_{12}+C_{44}) & n_2n_3(C_{12}+C_{44}) & n_3^2(C_{11}-C_{44})+C_{44}-\rho V^2 \end{vmatrix} = 0 \qquad (2.30)$$

Pure mode solutions of (2.30) are obtained for the crystallographic directions, [100], [111] and [110]. The relations between the various velocities and elastic constants for pure mode propagation are given in Table (2.1). It may be noticed that all three elastic moduli characterising a cubic solid are obtainable from measurement of the three possible wave velocities in the [110] direction.

2.6 Discussion of pure, quasi-pure and impure propagation directions and the associated energy flux vectors

Unless the propagation direction for the elastic wave is carefully chosen the direction of energy flow is not along the normal to the planes of constant phase nor is the particle displacement vector normal or parallel to these wave fronts.

A pure direction is defined such that the three possible elastic waves propagate with the particle displacement vector either parallel to (longitudinal mode) or perpendicular (transverse modes) to the propagation direction.

A quasi-pure direction allows propagation of one pure mode whilst the other two modes are neither pure transverse nor pure longitudinal modes. But usually these two quasi-pure modes have particle displacement vectors such that the modes closely resemble pure modes.

An impure direction is one in which none of the three elastic waves is a pure mode.

It may be noted that whatever the propagation direction, the three particle displacement vectors associated with the three elastic waves are always orthogonal.

In practice when measurements are made of wave velocities using the ultrasonic pulse-echo technique difficulties sometimes arise due to the deviation of the energy flux vector from the propagation direction. In particular when the specimen cross section is not appreciably larger than the cross section of the excited region or when for some reason it becomes necessary to excite the specimen near an edge, deviation of energy from the propagation direction may cause the wave to impinge on side walls, giving rise to mode conversion and deterioration of the echo train. (See Figure (2.2)).

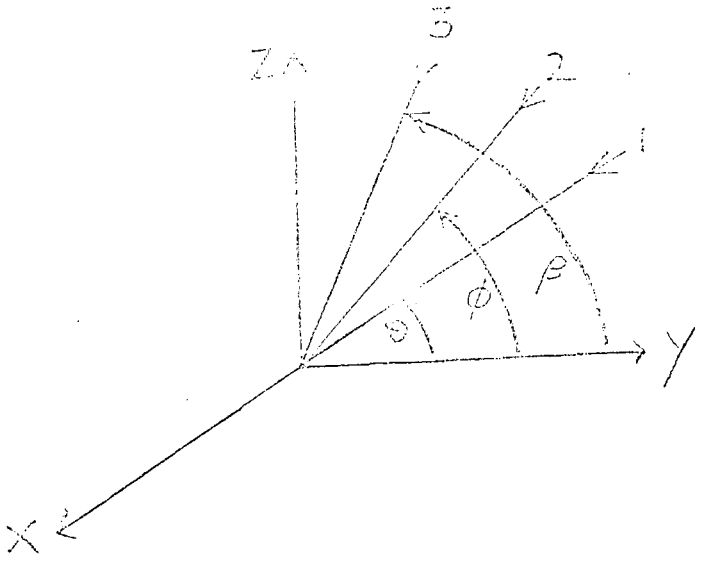

(a)

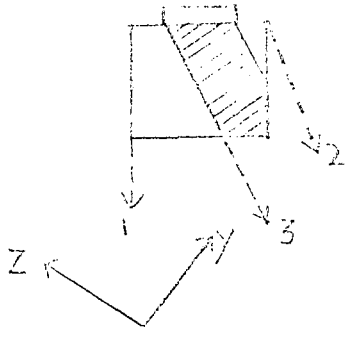

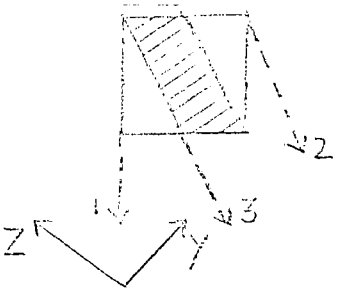

(b)

Figure (2.2) This illustrates the practical difficulties associated with energy flux, deviation from the propagation direction in the ultrasonic pulse echo technique. In (a) 1, 2, 3 represent the directions of propagation, particle displacement and energy flux respectively for Y - Z plane propagation in for example a tetragonal crystal. In (b) the siting of an X - cut transducer on the sample face is shown for two positions, one leading to sidewall reflections and the other avoiding the problem. If $\theta = \phi$ then $\beta = \theta$ because the mode is pure (see (a)).

Brugger (1965) has discussed the effect of the symmetry of the propagation direction on the energy flux vector and showed that for a pure longitudinal mode the energy flux vector can never deviate from the propagation direction. The same result holds for a pure transverse mode provided the propagation direction is a twofold, fourfold or sixfold rotational axis or normal to a plane of reflection symmetry. If the propagation direction is not included in these four categories, then in general a deviation of the energy flux from the propagation direction may be expected. Specifically for propagation along an axis of threefold symmetry, this deviation manifests itself in the form of internal conical refraction. A propagation axis of threefold symmetry is encountered in the [111] direction of a cubic crystal and along the Z direction of a trigonal crystal. (A threefold symmetry axis allows degenerate pure shear modes of arbitary polarisation to propagate). As the plane of particle vibration is rotated about the threefold axis through an angle π, the energy flux vector rotates about the threefold axis in the opposite sense through an angle 2π, thus generating a cone of possible directions for energy flow (Waterman 1959). Knowledge of the behaviour of the energy flux vector is especially important in the case of quasi-pure and impure propagation directions. In particular, the complete tensor set of elastic constants for both tetragonal and trigonal

symmetries, to name but the two which are of interest here, require wave propagation in quasi-pure directions. Thus, detailed below are the expressions for the energy flux components.

The ith Cartesian component of the energy flux P_i is given by Love (1944) as the negative of the scalor product of the component of the stress tensor on the surface normal to the ith direction with a particle displacement velocity $\dot{\underline{R}}$, as

$$P_i = -\sigma_{ij} \dot{R}_j \tag{2.31}$$

Equation (2.19), the plane wave solution to the equation of motion, may be written as

$$\underline{R} = p \underline{R_o} \; e^{i(\omega t - \underline{k} \cdot \underline{x})} \tag{2.32}$$

where p is the scalar amplitude of the displacement. After performing the necessary differentiations and substitutions P_i is obtained as

$$P_i = -\left(\frac{p\omega}{2v}\right)^2 C_{ijkl} R_{oj} R_{ok} n_l \tag{2.33}$$

where v and n_l are respectively the wave propagation velocity and the cosine of the angle between the propagation direction and the lth coordinate axis.

CHAPTER 3

Ultrasound velocity and attenuation measurements

3.1 Principle of the single ended pulse echo technique

The attenuation and velocity of ultrasound can be measured by introducing a single short duration pulse of high frequency stress waves into a solid normal to two parallel faces. The decrease in amplitude of successive echoes is a measure of the ultrasound absorption with time of travel; the distance in time between the echoes is the transit time and thus provides the ultrasound velocity. The pulse of sound is introduced by electrically exciting a quartz transducer which is bonded to one of the two parallel faces of the sample (see Figure (3.1)). A signal from a pulsed transmitter is applied between the transducer faces and as a consequence of the converse piezoelectric effect (see 3.4), a stress wave is produced which propagates into the sample. The transducer is both the source of the initial pulse and the receiver of the resultant echoes. The initial pulse is almost perfectly reflected from the opposite face of the sample and is returned to the transducer-sample interface where all but a small fraction of the energy is again reflected. By the time the first echo arrives at the transducer, the transmitter has been turned off. As the stress wave passes through the sample it loses energy and thus successive echoes produce smaller signals. The locus of the echo heights on an oscilloscope screen is exponential with time of travel of the sound in the sample (see Figure (3.2)). The measurement of ultrasonic attenuation and velocity by the pulse echo technique

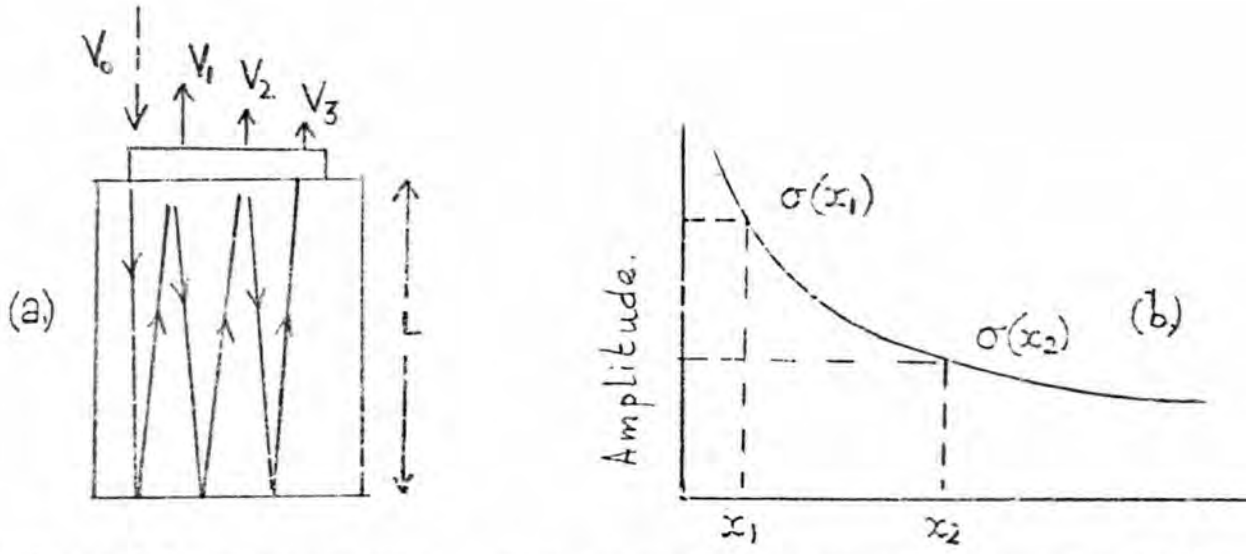

Figure (3.1) In (a) the transducer is shown schematically attached to the sample. V_0 is the amplitude of electrical oscillation exciting the transducer : $\sigma(x_1)$ and $\sigma(x_2)$ are amplitudes of sound waves at the transducer - specimen interface ; V_1 and V_2 are proportional to $\sigma(x_1)$ and $\sigma(x_2)$. Thus from equation (3.8) it is seen that a measurement of V_1 and V_2 an L can give the sound wave attenuation.

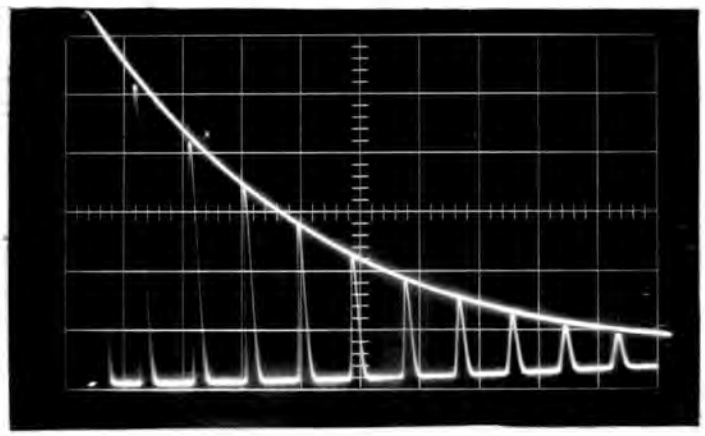

Figure (3.2) A typical oscilloscope display of the echoes in the ultrasonic single ended pulse echo technique

imposes a number of conditions and requirements that must be met in connection with sample preparation, with the bonding of the transducer to the specimen and with the interpretation of any special peculiarities of the resulting echo train. A pre-requisite is that opposite faces of the sample should be flat and parallel and that the sample face area should be somewhat larger than the transducer diameter (tolerances for these and other requirements are discussed in (3.6)).

3.2 Description of the measuring system

A Matec Inc attenuation comparator model 9000 was used for all the ultrasonic measurements. This equipment is a complete electronic system for the generation, detection and display of ultrasonic echoes and is shown in block diagram form in Figure (3.3). The unit generates pulsed oscillations which are continuously variable in frequency between 10 MHz and 310 MHz and are applied to the quartz transducer. The width of the pulses is variable between 0·5 and 5 μsec; the pulse amplitude is continuously variable and has a maximum of 3 kv peak-to-peak at 10 MHz which decreases a little at higher frequencies. The pulse repetition rate can be varied between 10 and 1000 pulses per sec. When each echo is reflected at the sample-transducer interface, the small amount of energy lost from the sound beam is converted by the

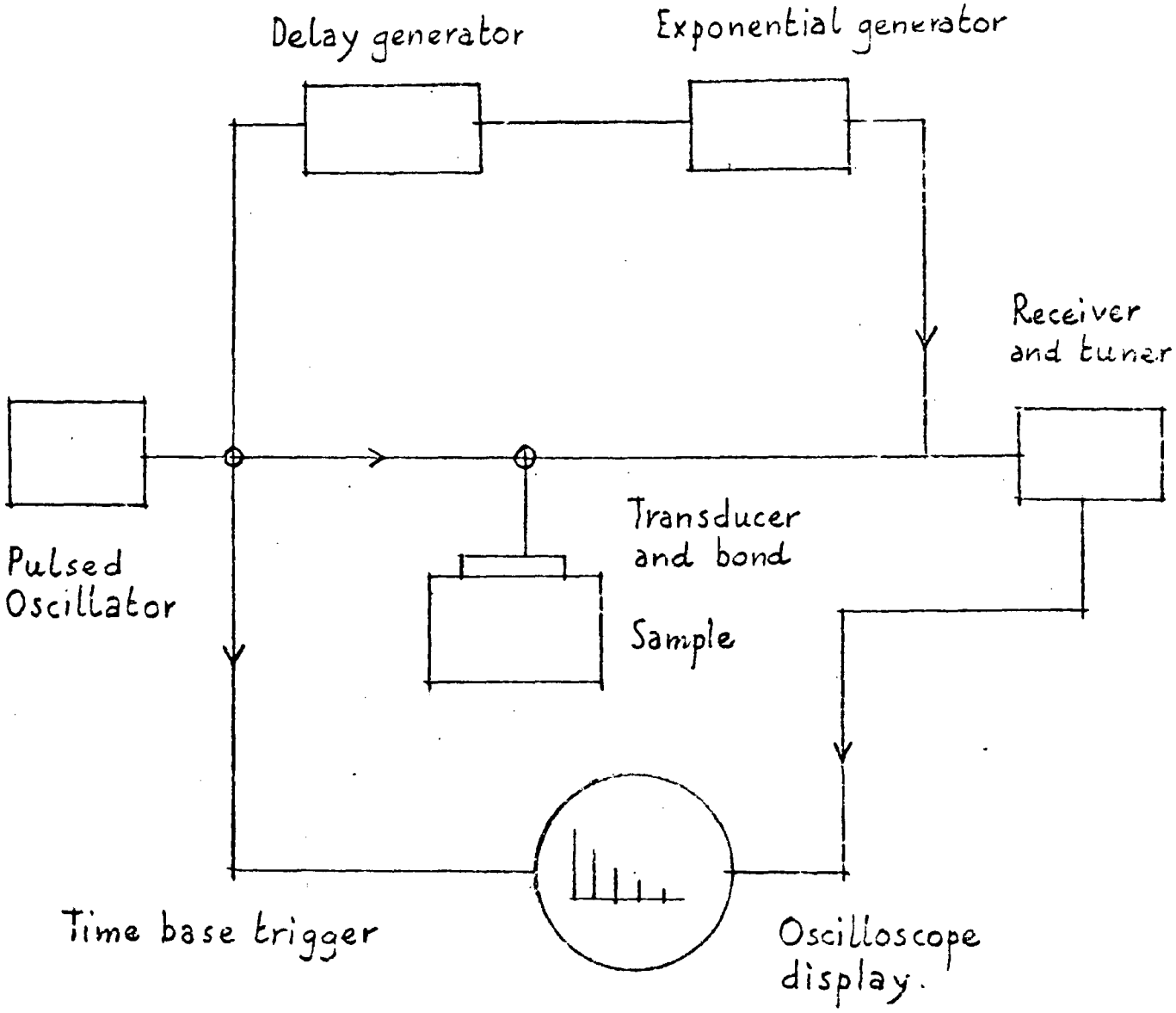

Figure (3.3) Block diagram of the measuring system.

direct piezoelectric effect (see 3.4) into an electrical signal which is then fed to a high gain (80 db), 4MHz bandwidth amplifier. Each high frequency wave group is rectified and its envelope displayed as an echo on a built in 5" oscilloscope screen. Figure (3.2) shows a photograph of a typical series of echoes. A calibrated exponential wave form is projected on the screen and by matching this to the echo peaks the attenuation suffered by the ultrasound in the sample is obtained in db per μsec from calibration curves. A calibrated delay generator allows measurement of the time separation of the echoes to an accuracy of ± 0·01 μsecs.

3.3 Units of attenuation

For the purpose of definition of the units of attenuation of the ultrasound in a material, it is assumed that the transducer produces a plane stress wave.

$$\sigma(x, t) = \sigma_o e^{i(\omega t - kx)} \tag{3.1}$$

where ω is the angular frequency and k is the propagation constant such that $k^2v^2 = \omega^2$ where v is the propagation velocity. This wave will be attenuated if either the propagation constant and velocity or the frequency is complex. On taking the former case v and k are written as

$$v = v_1 + iv_2 \tag{3.2}$$

$$k = k_1 - i\alpha \tag{3.3}$$

On substituting equation (3.3) into equation (3.1) the equation of a plane attenuated wave is obtained as

$$\sigma(x,t) = \sigma_o e^{-\alpha x} e^{i(\omega t - k_1 x)} \tag{3.4}$$

where α has the units of reciprocal distance. If, on the other hand, the frequency is taken to be complex then

$$\omega = \omega_1 - i\alpha_1 \tag{3.5}$$

and the resulting plane attenuated wave is

$$\sigma(x,t) = \sigma_o e^{-\alpha_1 t} e^{i(\omega_1 t - kx)} \tag{3.6}$$

where α_1 has the units of reciprocal time.

Since the attenuation is determined by the envelope of the high frequency wave, one can use

$$\sigma(x) = \sigma_o e^{-\alpha x} \tag{3.7}$$

to specify the attenuation α. If it is assumed that α is not a function of x, then

$$\alpha = \frac{1}{x_2 - x_1} \log_e \frac{\sigma(x_1)}{\sigma(x_2)}, \quad x_2 > x_1 \tag{3.8}$$

Because any ratio of two amplitudes such as $\sigma(x_1)$ and $\sigma(x_2)$ must, in order to be expressed in decibels or in nepers, be written respectively as,

$$20 \log_{10} \frac{\sigma(x_1)}{\sigma(x_2)} \quad \text{db} \tag{3.9}$$

or

$$\log_e \frac{\sigma(x_1)}{\sigma(x_2)} \quad \text{nepers} \tag{3.10}$$

then

$$\alpha = \frac{1}{x_2 - x_1} \; 20 \log_{10} \frac{\sigma(x_1)}{\sigma(x_2)} \quad \text{db/unitlength} \tag{3.11}$$

and

$$\alpha = \frac{1}{x_2 - x_1} \log_e \frac{\sigma(x_1)}{\sigma(x_2)} \quad \text{nepers/unitlength} \tag{3.12}$$

Thus $\alpha(\text{db/unitlength}) = 8{\cdot}686 \; \alpha(\text{nepers/unitlength})$

Energy loss can also be expressed in terms of the logarithmic decrement Δ which is defined for a harmonically oscillating system in free decay as $\Delta = W/2E$, where W is the energy loss per cycle in the specimen and E is the total vibrational energy stored in the specimen per cycle. It turns out that

$$\Delta(\text{nepers}) = \alpha(\text{nepers/cm}) \; \lambda(\text{cm}) \tag{3.13}$$

A dissipation factor "Q^{-1}" is sometimes used and is defined as,

$$Q^{-1} = 2\pi \frac{E}{W} \tag{3.14}$$

and is thus related to the decrement by

$$Q^{-1} \cdot \Delta = \pi \qquad (3.15)$$

The attenuation measurements made here using the pulse echo equipment are taken in db/μsec. These are then converted to db/cm in order to include any velocity changes.

Finally, listed below are the unit conversions.

$$\alpha(\text{db}/\mu\text{s}) = 8{\cdot}686 \times 10^{-6} \; v(\text{cm/s}) \; \alpha(\text{nepers/cm}) \qquad (3.16)$$

$$\alpha(\text{db}/\mu\text{s}) = \alpha(\text{db/cm}) \times 10^{-6} \times v(\text{cm/s}) \qquad (3.17)$$

$$\alpha(\text{db}/\mu\text{s}) = 8{\cdot}686 \times 10^{-6} \times f(\text{sec}^{-1}) \times \Delta(\text{nepers}) \qquad (3.18)$$

3.4 Quartz transducers as ultrasound generators and detectors

Appropriate stress waves can be produced from electrical ascillations by using the piezoelectric effect. If a stress is applied to a piezoelectric crystal, an electric moment is developed, whose magnitude is proportional to the applied stress. This is termed the direct piezoelectric effect: in the converse piezoelectric effect a strain results from an applied electric field. The polarisation component P_i is related to the stress σ_{jk} through

$$P_i = d_{ijk} \sigma_{jk} \qquad (3.19)$$

where the coefficients d_{ijk} are the piezoelectric moduli and form a third rank tensor. A similar relation holds between the applied field and strain in the converse effect; the coefficients are the same as for the direct case. Only non-centrosymmetric materials can be piezoelectric. Quartz (S_iO_2), having a point group 32, is a suitable material and has been employed here for both longitudinal and shear wave transducers. When the symmetry properties of quartz are taken into account all but 5 of the 18 piezoelectric moduli are zero. Using the matrix notation (see 2.2.4) equation (3.19) is written as

$$\begin{array}{cccccccc} & \sigma_1 & \sigma_2 & \sigma_3 & \sigma_4 & \sigma_5 & \sigma_6 \\ P_1 & d_{11} & -d_{11} & 0 & d_{14} & 0 & 0 \\ P_2 & 0 & 0 & 0 & 0 & -d_{14} & -2d_{11} \\ P_3 & 0 & 0 & 0 & 0 & 0 & 0 \end{array} \qquad (3.20)$$

Detailed consideration of equation (3.20) shows that no possible condition of stressing can produce a polarisation along the x_3 (z) axis, that a disc cut perpendicular to the x_1 (x) axis will produce a polarisation along the x_1 direction on being subjected to a tensile or compressive stress in this direction and that a disc cut perpendicular to the x_2 (y) axis, on being subjected to a shear stress in the x_1 - x_3 plane in the x_3 direction, will produce a polarisation in the x_2 direction.

Thus to generate longitudinal stress waves the transducer is cut from the quartz crystal so that the normal to the disc face is the x_1 direction : this is termed an "X-cut" transducer (see Figure 3.4). Similarly a transducer for generation of shear stress waves is cut with the disc face normal along the x_2 direction and is termed a "Y-cut" transducer.

Because the piezoelectric moduli are tensor components, the application of a field in one direction will produce, for example in an X-cut transducer, strains in addition to that produced parallel to the field. But in operation the transducer is excited at a frequency equal to the thickness mechanical resonant frequency and thus the response of the additional strains is small. When the transducer is excited to its nth harmonic, its thickness is divided into n equal parts with compressions and expansions taking place in adjoining sections; if n is even, no net strain results, and so in operation only the odd harmonics are used.

X-cut and Y-cut quartz transducers were obtained from Quartz Crystal Co. Ltd. to have fundamental frequencies between 8 and 25 MHz. The faces were gold plated to act as electrodes (see Figure 3.4)

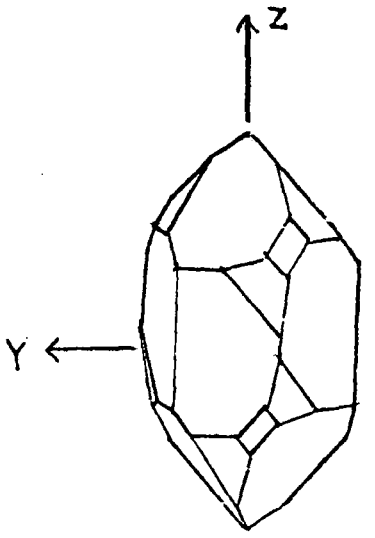

(a) Quartz crystal

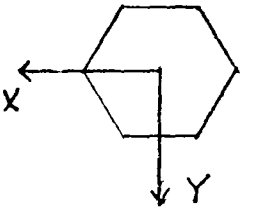

(b) cross section

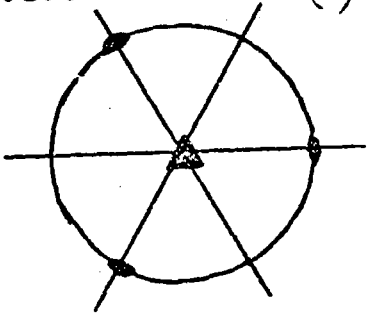

(c) symmetry of Class 32 crystals

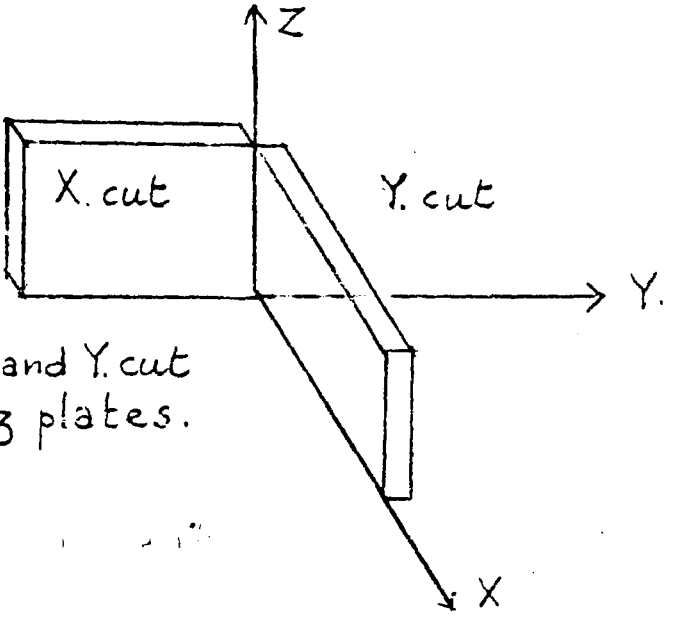

(d.) X. cut and Y. cut quartz plates.

Figure (3.4) The quartz crystal and quartz transducer cuts.

3.5 Preparation of samples for ultrasonic measurements

Single crystal samples for ultrasonic measurements require two flat and parallel faces cut perpendicular to the desired crystallographic direction with the minimum of mechanical damage.

Crystal orientations were determined by the back reflection Laue x-ray technique; the maximum misorientation of 0·5 degrees from the desired direction was sufficiently small to introduce negligible errors into the ultrasonic measurements (see (3.7.4) and (2.6)).

Either a spark machine or a diamond wheel was used to cut the samples, the choice of method being determined by the electrical conductivity of the material to be cut.

The spark machine

A Metals Research spark machine type SMD was used. The cutting action is produced by a rapid series of spark-discharges between the tool and the work, both of which are immersed in a kerosene bath. The sparks erode the work at a rate dependent on the energy and frequency of the discharge. A sensitive servo system is provided to eliminate the chance of mechanical damage due to contact between the tool and the work.

The tool employed was either a rigid brass plate or a continuously moving thin, tin coated copper wire. It was found that the brass plate was adequate as a tool for cutting both TiNi (Chapter 4) and arsenic (Chapter 7) but when used to

cut the indium-thallium alloys (Chapter 5), which are relatively soft materials, the tool began hunting when the cut was about half completed. Sometimes the tool actually made mechanical contact with the sample, which caused such deformation as to render the sample useless for purposes of ultrasonic measurements. Therefore a wire cutter was used for preparation of the indium-thallium samples with good results. After two cuts had been made, the sample faces were spark planed to achieve an accurate parallelism between them. The planing disc of the spark machine was first used to plane a brass reference surface onto which one flat face of the specimen was then fixed. After planing one face, the sample was turned over and the other face planed. In this way sample faces were prepared parallel to within 0·0002 cm at a separation of 1 cm. Lightly etched spark planed surfaces needed no further preparation: they were parallel to within the required tolerance (see (3.7.2)) and the Laue spots on back reflection x-ray photographs demonstrated the absence of significant mechanical damage.

The diamond wheel

Zirconia-yttria solid solutions (Chapter 6) were unsuitable for spark machining and were therefore cut with a diamond wheel. After being cut, sample faces were polished with diamond pastes until they were sufficiently parallel.

3.6 Transducer-specimen coupling

The character of the transducer-sample seal is of great importance in the successful use of the pulse echo technique; the following requirements are desirable:

(a) the thickness of the seal should be uniform and a small fraction of the ultrasound wavelength,

(b) any extraneous material or air bubbles must be excluded,

(c) the seal characteristics must not change over the temperature range of the measurements.

A bonding agent which forms a good seal between the transducer and one material may be ineffective in bonding the transducer to another material. In the present work several bonding agents were used and are detail below together with a description of the method of making the bonds. The quality of the resulting bond was evidenced by the exponential nature of the echo train (assuming wedge and sidewall effects were absent (see (3.7))).

3.6.1 Silicone Fluids (250000 and 1000000 cs)

These were found to be suitable mainly below room temperature and were used for bonding transducers to the zirconia-yttria solid solutions (Chapter 6).

Before making a bond (with any agent) both the sample and the transducer were carefully cleaned with acetone. A small drop of the silicone fluid was placed on both the sample and the transducer and spread out over the surfaces with a clean razor blade to form a thin, even layer. The transducer was pressed onto the sample and wrung down with a twisting motion to give a homogeneous, thin seal.

3.6.2 Mannitol, Resorcinol, Benzophenone and phenyl salicylate

For the measurements above room temperature on TiNi (Chapter 4) and the indium-thallium alloys (Chapter 5), the bonds which retained their characteristics most successfully over the required temperature range were found to be various organic materials: mannitol (m.pt. 169 °C), resorcinol (m.pt. 110 °C), benzophenone (m.pt. 48 °C), phenyl salicylate (m.pt. 44 °C). Transducer bonds using these materials were all made in a similar way. A small amount of the particular bonding agent was placed on the surface of the sample which was then warmed on a hot plate until the bonding material melted. A transducer at the same temperature was floated on this liquid and gradually pressed down onto the sample surface; a small weight was then placed on the transducer and the sample allowed to cool so that a solidified bond was formed.

3.6.3 Tensol Cement

Extreme difficulty was found in bonding transducers to arsenic (Chapter 7). Many materials were tried including those mentioned above. Tensol cement was eventually found to give reasonable results but only at room temperature. To form the bond, a thin layer of cement was spread over the sample and transducer faces with a razor blade. The transducer was then pressed onto the sample with a slight twist motion and held there with finger tight pressure until the cement became hard.

3.7 Sources of error in the measurement of ultrasonic attenuation

When ultrasonic attenuation is measured by the pulse echo method, there are, in addition to intrinsic material absorption mechanisms, contributions due to diffraction of the sound beam, non-parallelism of the sample faces, slight misorientation of the sample in the case of single crystals and transducer coupling to the sample. These will now be discussed in turn.

3.7.1 Diffraction loss

A vibrating transducer produces a radiation pattern of mechanical waves travelling into the specimen. Energy is lost from the cylindrical region defined by the area of the source and the propagation direction because the transducer is finite in extent and thus has an associated diffraction field. In the extreme case of a small diameter transducer on a not much larger diameter sample the beam divergence is such that parts of the beam reach the sidewalls after a number of passages through the sample. Reflections then occur in such a way that a part of this energy returns to the main beam and interference effects results. These appear similar to the effects of non-parallelism (discussed in (3.7.2)) of the sample faces shown in Figure (3.5). If sidewall effects are absent, the apparent attenuation caused by diffraction is only important at frequences of 10 MHz or lower in materials with low intrinsic attenuation. The attenuation due to diffraction has been estimated as 1 db per a^2/λ where a is the transducer radious and λ the wavelength of the ultrasound (Granato and Truell, 1956). This relation serves as a useful estimate of the diffraction loss.

3.7.2 Losses due to non-parallelism of the sample

Because the transducer is a phase sensitive device and the measured voltage is an integrated response of the transducer over its area, phase variations that occur over its area lead to interference effects. Thus effects which cause phase variations to occur at the transducer are a source of error in the measurement of attenuation.

In the pulse echo method a plane wave, after reflection from a surface not quite parallel to the first will meet the transducer in such a way that the planes of constant phase will not be parallel to the plane of the transducer; consequently the different surface area elements of the transducer will detect different phases of the wave. From an analysis of this source of error Truell and Oates (1963) found that the locus of the amplitude of the echo pattern is modulated by an envelope factor to give the appearance shown in Figure (3.5). When the wedge effect is small, as is the case for the parallelisms achieved here (see 3.5) the apparent attenuation β due to this effect is

$$\beta = 8.686\ \pi^2\ f^2\ a^2 \theta^2\ n\ /\ L\ v^2\ \text{db cm}^{-1} \qquad (3.21)$$

where f is the sound frequency, a is the transducer radius, n is the echo number, v is the sound velocity, L is the sample thickness and θ is the wedge angle. The equation (3.21) may also

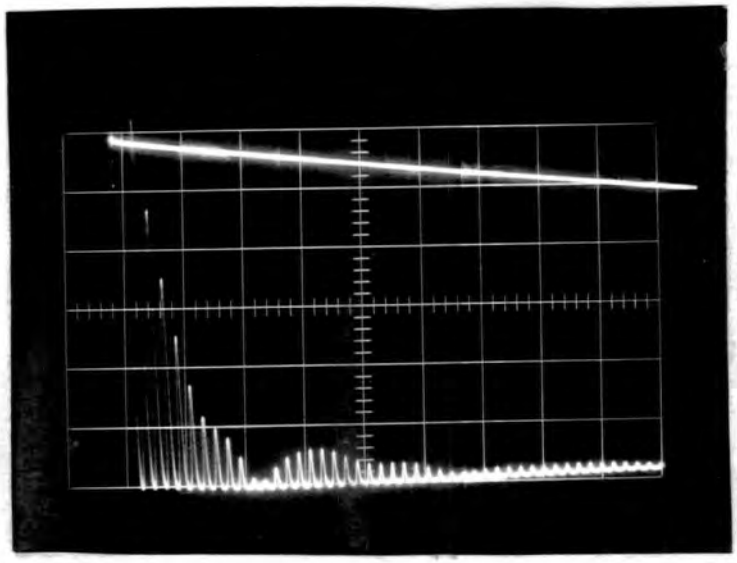

Figure (3.5) An example of the appearance of ultrasonic echoes in a non-parallel sample.

be used to estimate the degree of parallelism in order to measure the attenuation to some prescribed accuracy. For example, in TiNi (see Figure (4.8)) for accuracy of 5% in an attenuation of 6 db/cm it is found on putting the relevant numerical values into equation (3.21) that the wedge angle θ must be less than 9×10^{-4} radians for a frequency of 25 MHz. Tolerances of better than 10^{-4} radians can be achieved by the spark planing technique used: this loss can be made negligible by careful sample preparation.

An apparent loss process can result from mode conversion which is the partial conversion of say a longitudinal mode to a shear mode. For example, if the wave vector of a longitudinal wave is incident at some angle α ($\neq 90^{\circ}$) to the boundary of the medium this wave on reflection gives rise to a longitudinal wave with wave vector at an angle α and a transverse wave with wave vector at an angle β to the boundary. For normal incidence there is no mode conversion. Thus lack of parallelism of the sample faces in ultrasonic measurements causes apparent attenuation which could be confused with intrinsic material absorption mechanisms. Again, careful sample preparation renders this loss negligible.

3.7.3 Transducer coupling losses

Measurement of the losses arising from the transducer and the transducer-specimen coupling were made by the method described below.

On each of several samples of different lengths L_i, identical transducers are bonded. Then under the same conditions the attenuation (K_i db/μs) is measured in each sample. The measured attenuation ($K_i t_i$ db) is then equal to the real attenuation (αt_i db) plus any losses (α_i db) to the bond and transducer. (t_i is the time for the sound to make two transits of the sample). Then using the equations

$$K_i\ t_i = (\alpha t_i + \alpha_i)\ \text{db} \tag{3.22}$$

the intrinsic material attenuation is

$$\alpha = (K_i\ t_i - \alpha_i)/t_i \quad \text{db}/\mu\text{s} \tag{3.23}$$

and i = 1, n where n is the number of samples of different lengths available. At least three samples are required to test whether $\alpha_1 = \alpha_2 = \alpha_3$, as required. It is best to use as high a frequency as possible in these measurements to avoid any diffraction effects contributing different amounts due to dissimilarities in sample geometries.

The above procedure was followed in the analysis of the attenuation measurements on TiNi (Chapter 4). The room temperature attenuation was measured in three samples of different lengths but having the same right circular cylindrical shape at an ultrasonic frequency of 15 MHz. Values of α_i were : $\alpha_1 = 3.9$; $\alpha_2 = 4.3$; $\alpha_3 = 4.5$ db.

3.7.4 Errors in the velocity measurements

There are three main sources of error associated with values of velocities measured by the pulse-echo technique used here. Firstly, measurement of the time separation of echoes using the calibrated delay can only be done to about 1% accuracy. Secondly, the transit distance, measured with a micrometer is accurate to about 0·1%. In single crystals any misorientation from the desired propagation direction will not of its own accord result in an error in velocity measurement but the velocity measured does not correspond to that in the desired direction. For an error in the orientation of $0{\cdot}5^{\circ}$ the misorientation velocity error is typically about 0·03%. Waterman (1959) has discussed this point extensively.

When the velocities are converted to elastic moduli, the velocity errors are doubled and density errors are introduced.

3.8 Sample holder used in ultrasonic measurements

The sample holder, shown in Figure (3.6), is designed so that electrical contact can be made with a transducer bonded to the sample over the range of experimental conditions without disturbing the bond character. The sample (A) is located on a brass platform (B) which may be moved vertically by tightening or slackening three springs (C); only two are shown in the

diagram. These springs are mounted concentric with three brass columns (D) which pass freely through the sample platform (B). A sensitive screw arrangement (E) allows a second platform to move vertically and control the tightness of the springs and hence the position of the sample platform (B). The sample is thus gently raised until the transducer and the spring loaded plunger (F), which terminates a coaxial line, make contact. The dimensions of this plunger (F) are such that it covers the gold plated centre region of the transducer (see Figure (3.4)); the reverse side of the transducer is earthed by contact between the outer gold plated ring on the transducer and the sample holder (see Figure (3.6)); a conducting path through the sample to the gold plated reverse side of the transducer is thus completed. (In the case of non-conducting samples a highly conducting silver paint can be used to provide this conducting path). In practice sample holders of this design were satisfactory for the temperature range (-196°C to 150°C) of the ultrasonic measurements. The sample holder illustrated in Figure (3.6) is the one which was used for measurements above room temperature in the oil bath (see 3.8). For measurements between room temperature and liquid nitrogen temperatures a sample holder built to the same design but with smaller dimensions was used; the size was dictated by the cryostat bore (see 3.9.2).

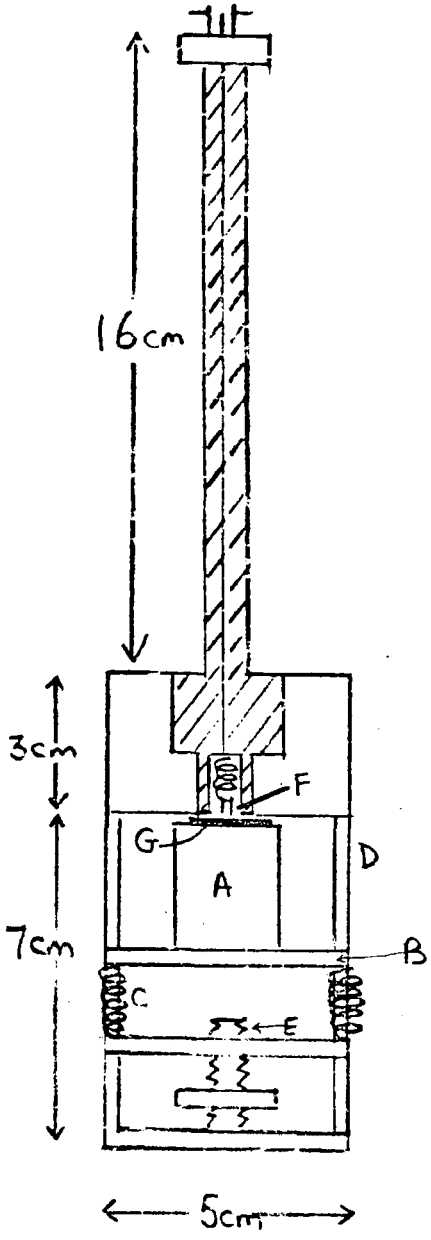

Figure (3.6) Sample holder used for the ultrasonic measurements.

3.9.1 Oil bath for high temperature ultrasonic measurements

For ultrasonic measurements above room temperature samples were immersed in a modified Grant Instrument oil bath type SB 1 (Figure (3.7)). A main heater (maximum power 1·5 kw), supplied from the mains through a voltage stabiliser and a variac, allowed the bath temperature to be set roughly. A subsidiary heater (60 watt electric light bulb) was switched in and out in response to a signal from a Jumbo-Shandon adjustable contact thermometer located in the oil bath. When well stirred this oil bath could be maintained to within $\pm$ 0·1°C of the desired temperature over long periods.

3.9.2 Cryostat for measurements below room temperature

The cryostat design allowed stabilisation of the sample temperature at any temperature between 300°K and 77°K. This cryostat is the one designed and built by Dr. O. Oktu and used by him for galvanomagnetic measurements and is detailed in his Ph.D. thesis (Durham University 1967). The essentials of the method of temperature control are as follows: the space between an inner and outer vessel is evacuated; the outer vessel is surrounded by a dewar of liquid nitrogen; the sample in the sample holder (as in Figure (3.6) but of smaller dimensions) is placed inside the inner vessel which contains a refrigerant liquid; the temperature of the sample is stabilised by controlling the air pressure between the two vessels and if necessary using aheater which is wound on the outside of the inner vessel.

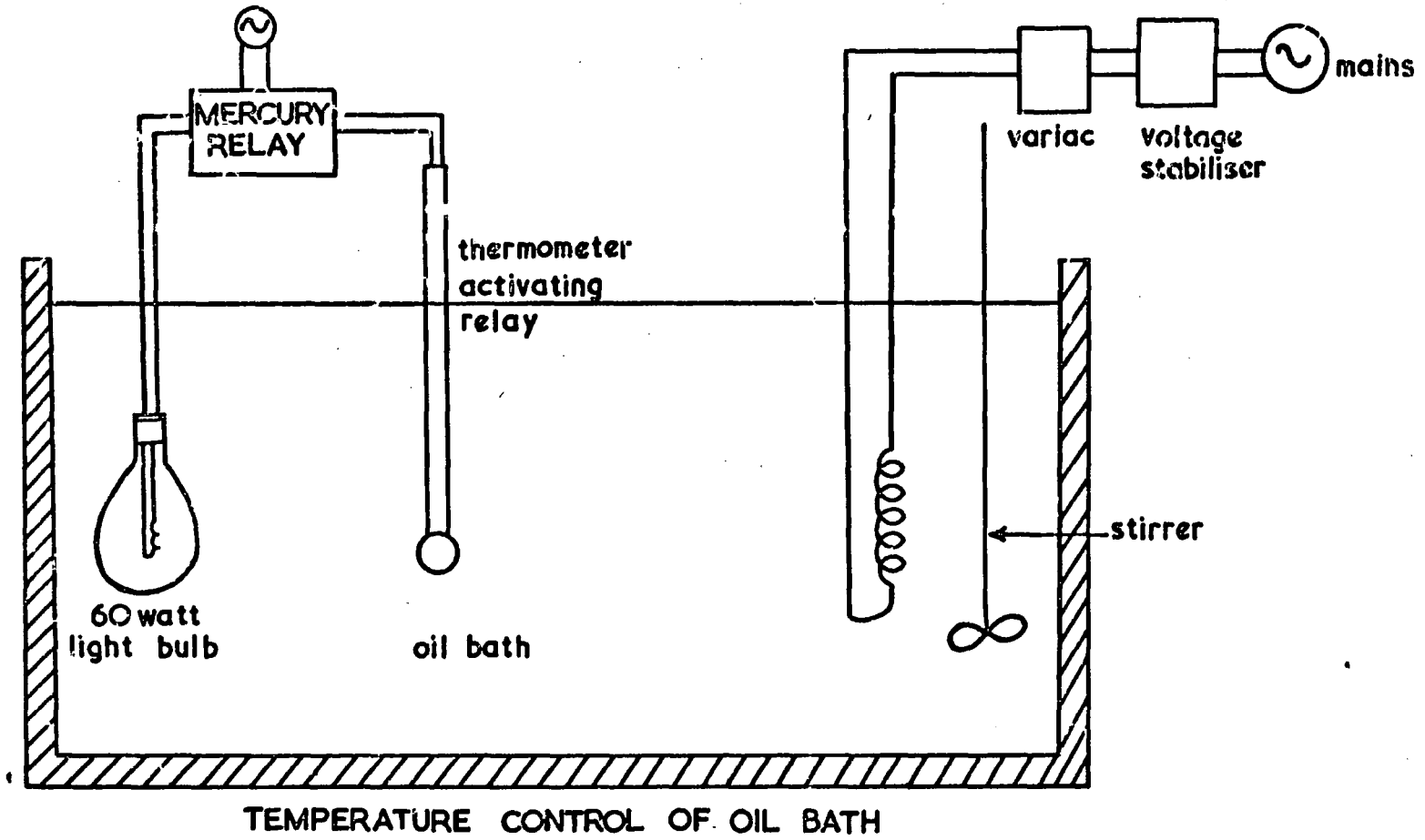

Figure (3.7) Oil bath used for measurements above room temperature.

CHAPTER 4

An ultrasonic study of the martensitic transition in TiNi

4.1 Introduction

The direct connection which exists between the velocity of elastic waves and the binding energy of a solid is of great value in the study of solid state phase transformations. The instabilities which are responsible for the onset of phase changes manifest themselves as anomalous variations in both the velocity and the attenuation of ultrasonic waves; insight into the transformation mechanisms is provided by ultrasonic measurements.

The main objective of the work presented in this chapter has been to measure the ultrasonic wave propagation characteristics in the vicinity of the martensitic phase transition in nitinol (TiNi). This transition, which occurs in the vicinity of $60^{\circ}C$ is now recognised as the archetype of the shape memory effect (de Lange and Zijderveld, 1968) and is thus of special interest. Because of the intimate relation between transition mechanisms and crystal lattice behaviour, data complementing the ultrasonic results was provided by measurements of the thermal expansion and thermal conductivity in the transition region.

Before the present work is dealt with, a brief description of martensitic transitions in general is presented and is followed by an account of the pertinent work on TiNi previously reported. Section (4.2) deals with the present experimental work and

section (4.3) deals with the differences between the elastic properties of the two phases away from the transition region while section (4.4) discusses the anelastic effects in preparation for the discussion of the transition region in section (4.5).

4.1.1 Martensitic transitions

The name martensite was originally used to describe the plate-like appearance of the product of certain phase changes in steels. Now the term martensite refers to the product of phase transitions which exhibit certain characteristics and are termed martensitic transitions. The following features are often observed in martensitic transitions (see Barrett (1966) and Pretty (1970) for further discussions).

(a) The transformation only proceeds whilst the temperature is falling and is thus termed athermal. It takes place over a characteristic range of temperature beginning at M_s and continuing until at M_f the parent phase is entirely converted or the reaction becomes self stopping. In general the martensite is surrounded by untransformed material and the constraints imposed on it produces various shapes of platelets.

(b) The individual atoms execute well defined and correlated movements which are similar to those which occur during mechanical

twinning, the movements being somewhat less than one interatomic distance. In a martensitic transformation a different crystal structure results from these atomic movements. Each martensite plate is a single crystal whose lattice orientation is strictly determined by the lattice orientation of the parent phase.

(c) No diffusion of atoms is required in a martensitic transition as evidenced by the impossibility of retaining the parent phase by quenching. An important consequence of such a diffusionless transition is that the martensite has exactly the same composition as the parent phase.

(d) The metallographic appearance of the martensite is as upheavals or tiltings of the surface which manifests the macroscopic strains accompanying the transition.

4.1.2 The TiNi martensitic transition

At elevated temperatures the structure of the intermetallic compound TiNi is B2 (CsCl) with a lattice spacing of 3·00Å. On cooling, the material undergoes a diffusionless transition to two slightly different but distinct base centred monoclinic martensites (a_o^m = 5·19Å, b_o^m = 4·96Å, c_o^m = 4·25Å, γ^m = 99°; $a_o^{m'}$ = 5·19Å, $b_o^{m'}$ = 5·52Å, $c_o^{m'}$ = 4·25Å, $\gamma^{m'}$ = 116°; where m and m' refer to two martensites) (Marcinkowski, Sastri and Koskimaki 1968).

If atom types are not considered, the martensite lattices have distorted hexagonal structures. The transition is accomplished by a simple shear on the $(1\bar{1}2)$ planes of the original B2 structure. When equal amounts of the two martensites are present there is no net shear strain. It is athermal, the transformation taking place over a temperature range which is extremely composition sensitive, and is not usually complete at room temperature. Further transformation can be induced by plastic deformation. If, after such plastic deformation, the sample temperature is raised above the transition point, the original shape is regained because the reverse transformation annihilates the deformation (deLange and Zijderveld 1968). This phenomenon has been termed the shape memory effect and has engineering potential in stored energy devices. Because of the interesting nature of the shape memory effect the hypothesis put forward by deLange and Zijderveld will be described briefly. Since a definite crystallographic relationship exists between the parent phase and the martensite, the number of possible variants of the martensite is determined both by this orientation relationship and the symmetries of the two phases. Martensite formed by thermal transformation is formed throughout the sample randomly distributed over the possible directions dictated by the above considerations. A limitation on the possibilities is introduced, if the transformation occurs by

mechanical deformation; only those orientations will be formed that contribute to a release of applied stress by change of lattice parameter. The texture induced by tensile stress should be different from that induced by compressive stress; this was observed by deLange and Zijderveld, who then proposed that: the oriented crystals of martensite formed by deformation transform on heating to the original crystal structure and the latter transformation causes a deformation which annihilates the former mechanical deformation.

Associated with the transition are many anomalous property changes. An extensive investigation of such changes in the electrical resistance, Hall effect, magnetic susceptibility and differential thermal analysis has been made (Wang, deSavage and Buehler 1968). The elastic and anelastic properties of TiNi have been looked at in the kilocycle frequency range (Wasilewski 1965, Spinner and Rozner 1966) and demonstrate a large damping capacity below the transition. But the sound velocity at room temperature calculated by Spinner and Rozner from measurements of Young's modulus and Poisson's ratio (3.8×10^5 cm.sec^{-1}) is in complete disagreement with the then only direct measurement of sound velocity (5.25×10^5 cm.sec^{-1}) reported by Bradley (1965); prior to the present measurements, those of Bradley of the longitudinal sound velocity at 5MHz were the only ultrasonic data available on TiNi.

Two kinds of information have resulted from this ultrasonic wave propagation study; first comparison between the elastic behaviour on either side of the transition has lead to an understanding of the basic energy difference between the two phases; second, the data in the near vicinity of the transition has been found to be consistent with the hypothesis that phonon mode softening takes place.

4.2 Experimental

Samples of an arc cast TiNi alloy with a composition close to 50 at. % Ni were kindly supplied by Dr. B.F. deSavage (U.S. Naval Ordnance Laboratories); since the majority of the reported work on TiNi has been carried out at these laboratories, correllation of the results obtained here with other studies is readily made. The transition temperature is extremely composition sensitive (Figure (4.1)) near 50 at. % Ni, and that of the samples used here is 59°C which indicates a nickel content of 50.8±0.1 at. %. (The "transition temperature" in TiNi referred to throughout this work is identified with the temperature of the maximum in the ultrasonic attenuation in Figure (4.8)).

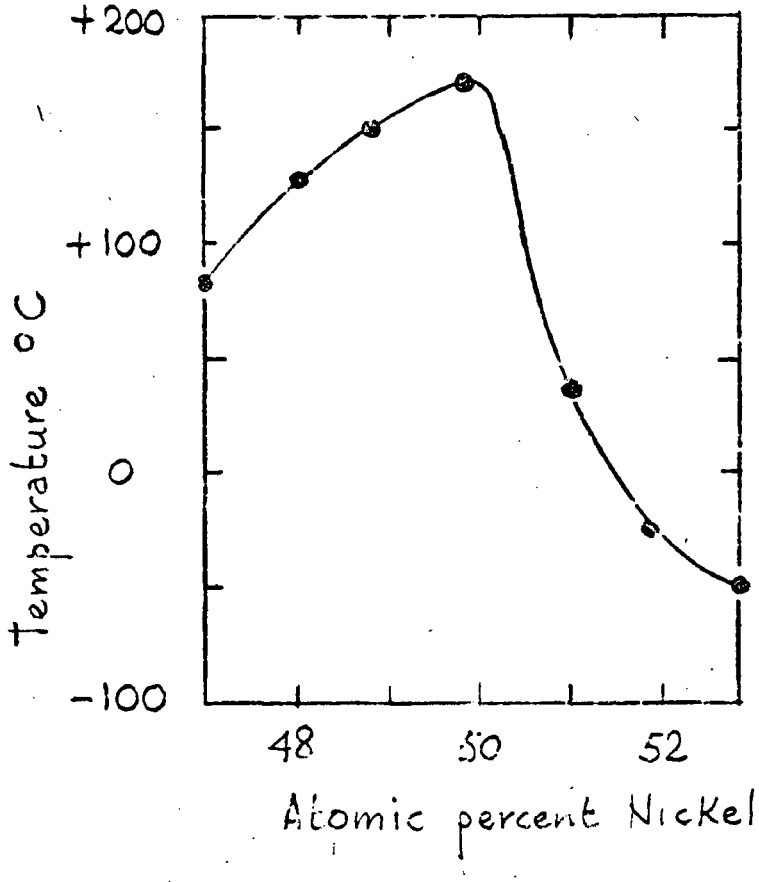

Figure (4.1) The damping curve of the TiNi near stoichiometric alloys is plotted versus the atomic percent nickel. Above the curve the alloy is low damping: below the curve the alloy is high damping. (Wang et al 1965).

4.2.1 Grain size determination

The size and shape of grains in polycrystalline materials are important factors in ultrasonic scattering. Therefore these parameters were evaluated in the TiNi samples actually used in the ultrasonic experiments. Usually etches are used to reveal these grains. An etch (HF, HNO_3 and H_2O) given by Buehler and Wiley (1962) for TiNi was tried on carefully polished surfaces but without success. But microscopic examination of spark planed but otherwise untreated surfaces showed up the grain clearly, plausibly because of preferential erosion by the spark planer at the grain boundaries. Photographs of grains revealed in this way are shown in Figure (4.2) and are seen to be on the whole equiaxed. This latter point is important because an analysis of the ultrasonic attenuation due to Rayleigh scattering (see (4.4)) is based on equiaxed grains. Papadakis (1968) has shown how an average grain size may be obtained from photographs such as Figure (4.2). A grain volume T, which is the effective scattering volume of importance in ultrasonic work is

$$T = 1{\cdot}0\, d_{95}^3 \qquad (4.1)$$

where d_{95} is the diameter of an image on the photograph (Figure (4.2)) in the 95th percentile. The largest 5% of images cover about 25% of the area of the photograph, so it is sufficient to block off the largest images until 25% of the area is covered and to

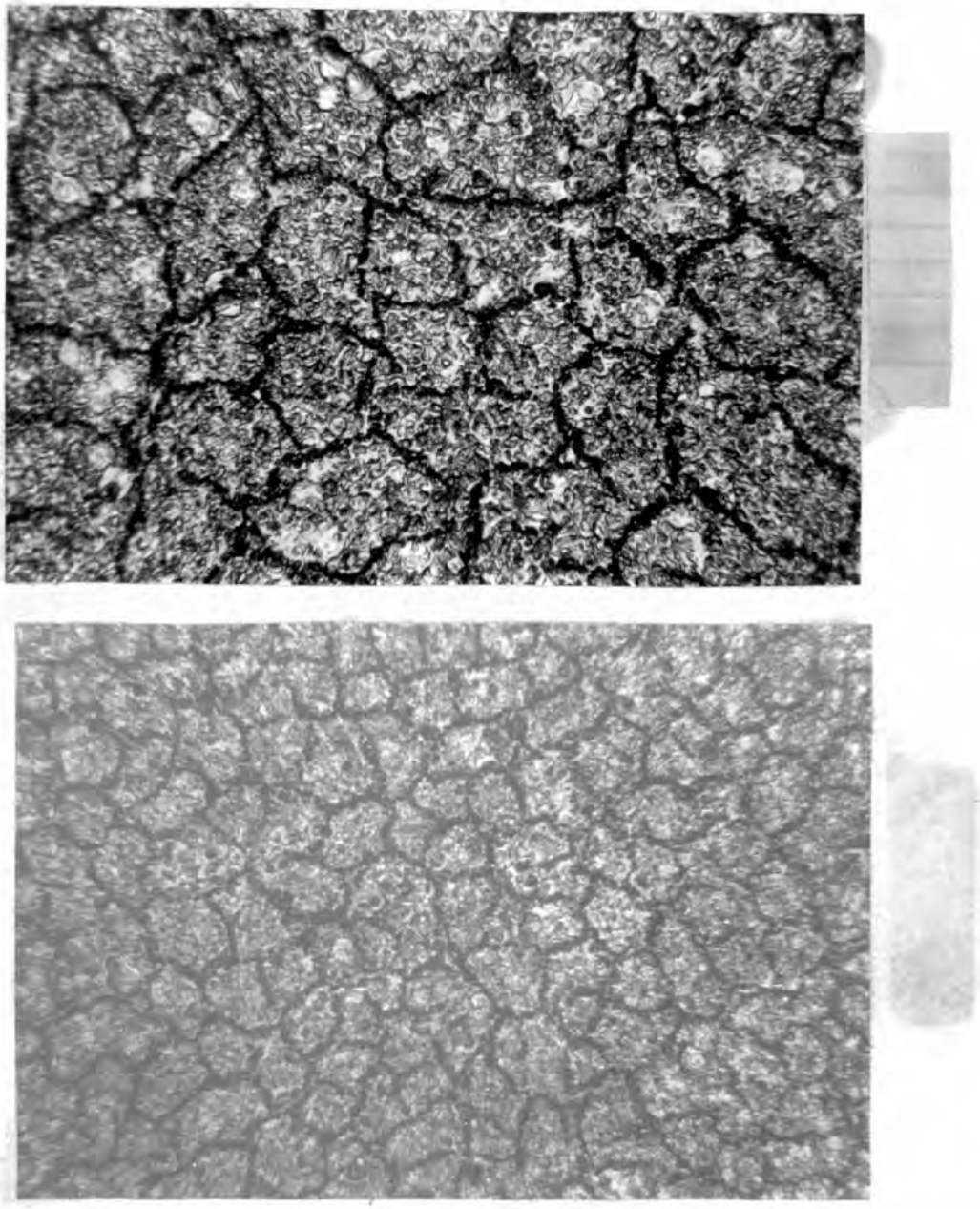

Figure (4.2) Grains in TiNi. The smallest scale division is 10 microns.

take the diameter of the next largest image as d_{95}. The value of d_{95} obtained in this way from several photographs of various parts of the surface of the TiNi samples was 26 ± 4 microns.

4.2.2 Ultrasonic velocity and attenuation measurements in TiNi

Ultrasonic samples were cut between 0.4 cm and 1 cm in length with opposite faces spark planed flat and parallel to within 0.0001 inches. The X-cut quartz transducers were successfully bonded to the sample at all temperatures in the range 100°C to -196°C with mannitol (see (3.6.2)). Bond quality for Y-cut transducers deteriorated in the vicinity of the transition temperature. This difficulty was compounded by the high shear wave attenuation (see Figure (4.8)), thus subjecting measurements of shear wave velocities near the transition to considerably larger errors ($\pm 3\%$) than those for the longitudinal wave velocities ($\pm 1\%$; see (3.7.5)). Improved bond quality for shear wave injection was achieved by using benzophenone (see (3.6.2)) below the transition.

The importance of the thermal history on the physical properties of TiNi has been stressed (Wang et al. 1968). Preliminary experiments were carried out which showed that thermal cycling within the limits of 50°C either side of the transition greatly affects the ultrasonic propagation characteristics of the sample: successive sets of results differed by amounts greater

than the errors associated with the measurement. A twenty hour 650°C anneal followed by a furnace cool was used to remove effects of prior work (deSavage, private communication). Then to ensure an identical thermal history for each set of measurements, samples were always cycled completely between 200°C and -196°C. Once heating or cooling commenced the sense of the temperature changes was not altered. This procedure gave reproducible results. Because the transition is athermal, the measurements were always made during either continuous slow heating or cooling in the oil bath (see (3.9.1)). Most of the measurements were made during slow cooling (0·05°C per minute). The temperature (measured with precalibrated copper/constantan thermocouples) was effectively constant (±0·02°C) for the time taken over a reading.

In the absence of preferred orientation, polycrystalline samples are elastically isotropic. That this was so for the TiNi samples used here was substantiated by the lack of dependence of the sound velocities on the wave direction and polarisation; longitudinal velocities parallel to and perpendicular to the axis of the rod shaped samples were the same within the experimental error at room temperature; shear wave velocities were independent of both the plane of the particle displacement and propagation direction. However, if an isotropic material is subjected to

uniaxial compression, elastic isotropy is removed. Throughout the temperature range studied the longitudinal wave velocity showed no dispersion between 10MHz and 25MHz to within the experimental accuracy of the transit time measurement. Measurements of wave velocities under conditions of uniaxial compression can lead to knowledge of the three third order elastic constants which describe the non-linear elasticity of an isotropic body. In TiNi, a stress of 10^8 dynes $cm.^{-2}$ was applied perpendicular to the velocity propagation direction; no resultant change in velocity could be observed.

The elastic moduli characteristic of an elastically isotropic solid (see (2.5.1)) are related to the sound velocities (V_L and V_S) by the equations

$$K = (3\rho V_L^2 - 4\rho V_S^2)/3 \qquad (4.2)$$

$$\mu = \rho V_S^2 \qquad (4.3)$$

$$E = \rho V_S^2(3\rho V_L^2 - 4\rho V_S^2)/(\rho V_L^2 - \rho V_S^2) \qquad (4.4)$$

$$\sigma = 0.5(\rho V_L^2 - 2\rho V_S^2)/(\rho V_L^2 - \rho V_S^2) \qquad (4.5)$$

where K is the bulk modulus, μ is the shear modulus, E is Young's modulus, σ is Poisson's ratio (defined as the ratio between the lateral contraction and the longitudinal extension of the specimen, the lateral surfaces being free). ρ is the density which was obtained as 6.39 gms. $cm.^{-3}$ by Archimedes method. The measured

velocities in TiNi, converted to the elastic moduli using equations (4.2) to (4.5) are shown in Figures (4.3) to (4.7) as a function of temperature. At -196°C the longitudinal and shear elastic stiffnesses are 1·90 x 10^{12} and 0·39 x 10^{12} dynes $cm.^{2}$ respectively. Although the linerea thermal expansion coefficient passes through a large maximum at the transition (see (4.2.3) and Figure (4.11)), the maximum apparent change in the velocity which results from neglecting the change in length of the sample is less than 0·5%, well within the uncertainty in the transit time measurements: no corrections need be made.

The ultrasonic attenuation in TiNi is shown in Figure (4.8) as a function of temperature in the frequency range 10MHz to 25MHz. The main errors in these attenuation measurements arise from diffraction effects (see (3.7.1)) and transducer coupling losses (see (3.7.3)) and constitute an apparent background damping upon which intrinsic material effects are superimposed. The diffraction loss has been shown theoretically to be 1 db per a^{2}/λ (see (3.7.1)) and experimentally verified for the system used here (Alper 1969) and is readily substracted; coupling losses, estimated by the method described in (3.7.3) were found to be about 4·2 db (knowledge of sample length and sound velocity allow the coupling losses to be substracted from the measured attenuation).

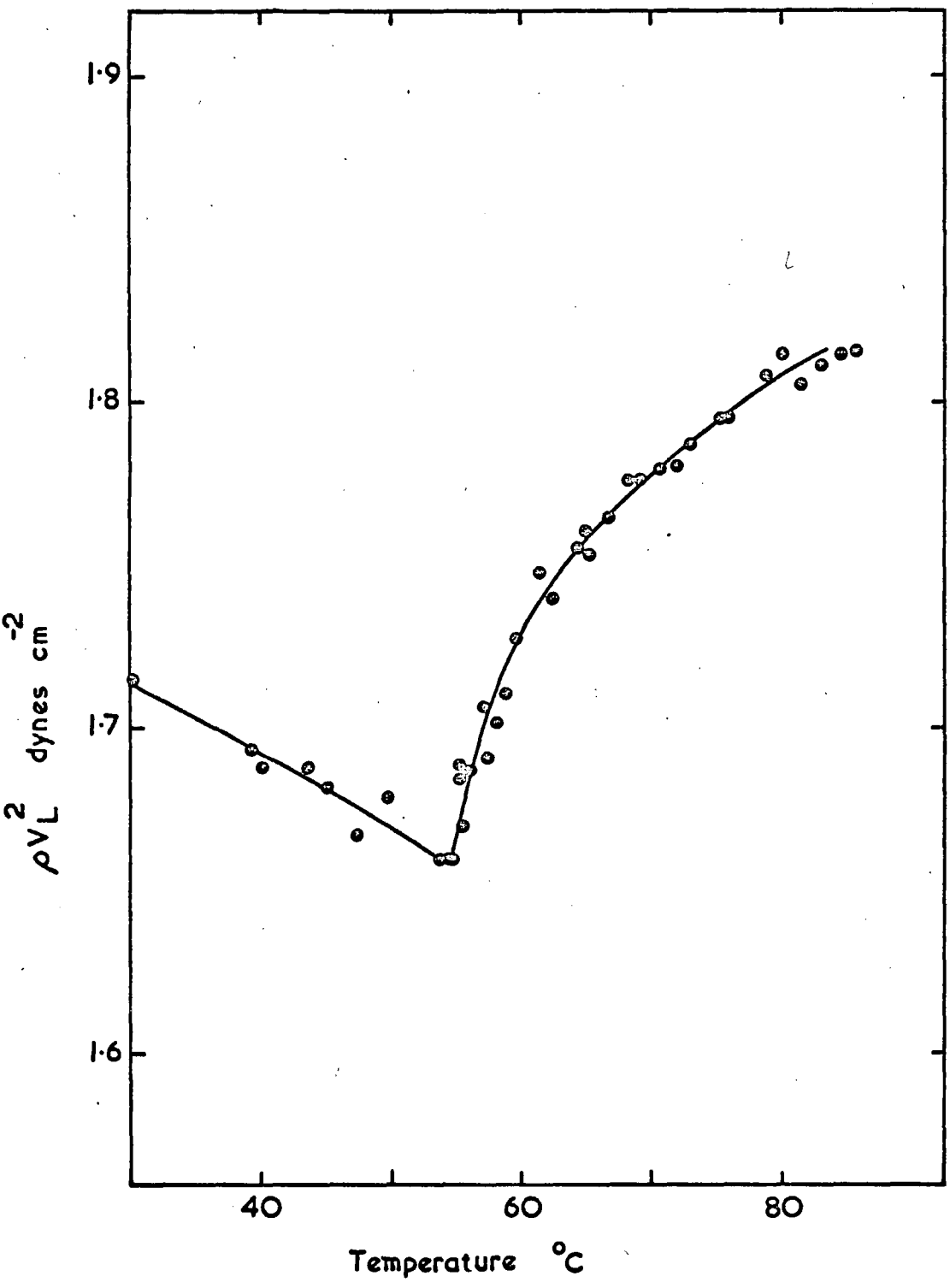

Figure (4.3) Longitudinal modulus near the transition in TiNi.

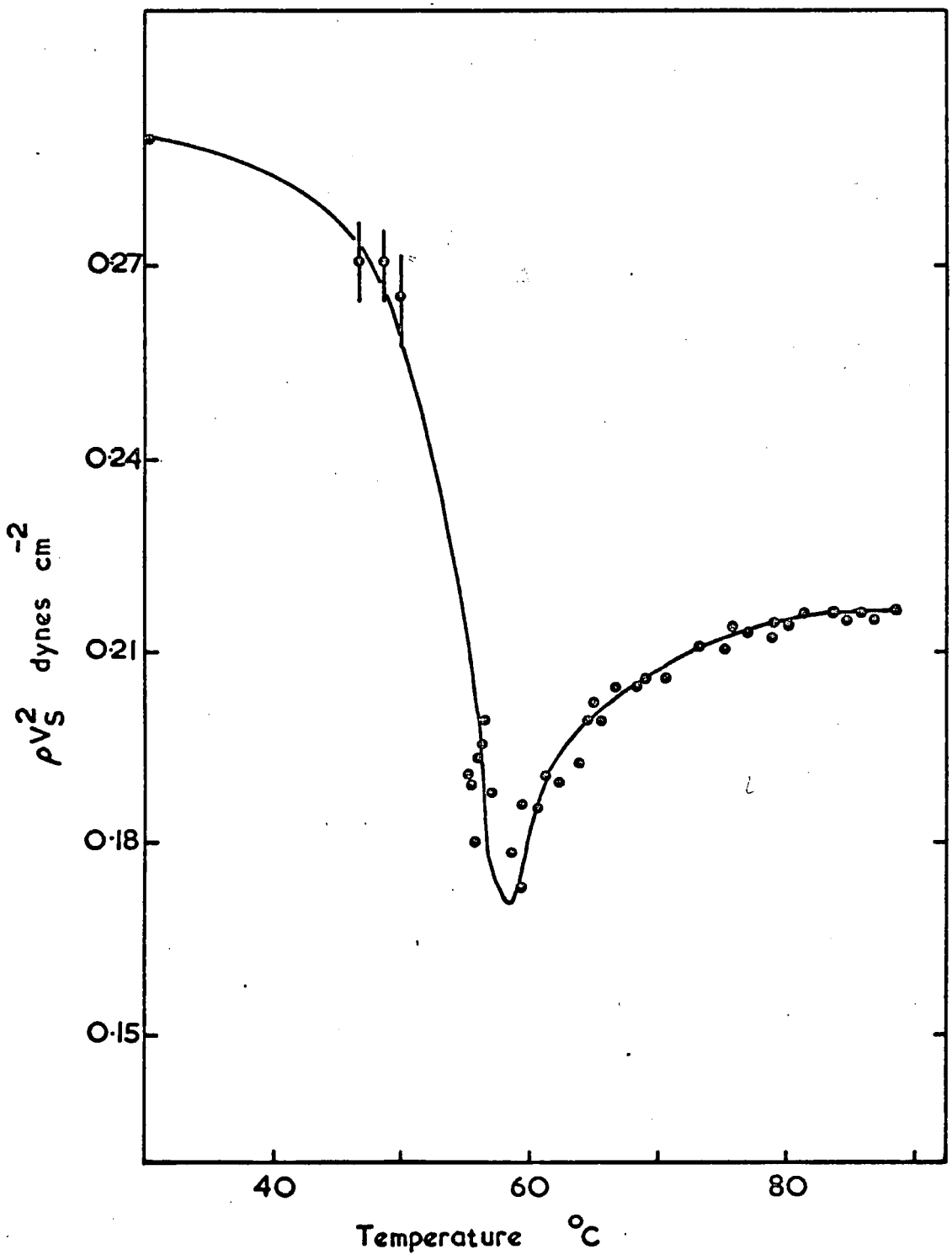

Figure (4.4) Shear modulus near the transition in TiNi.

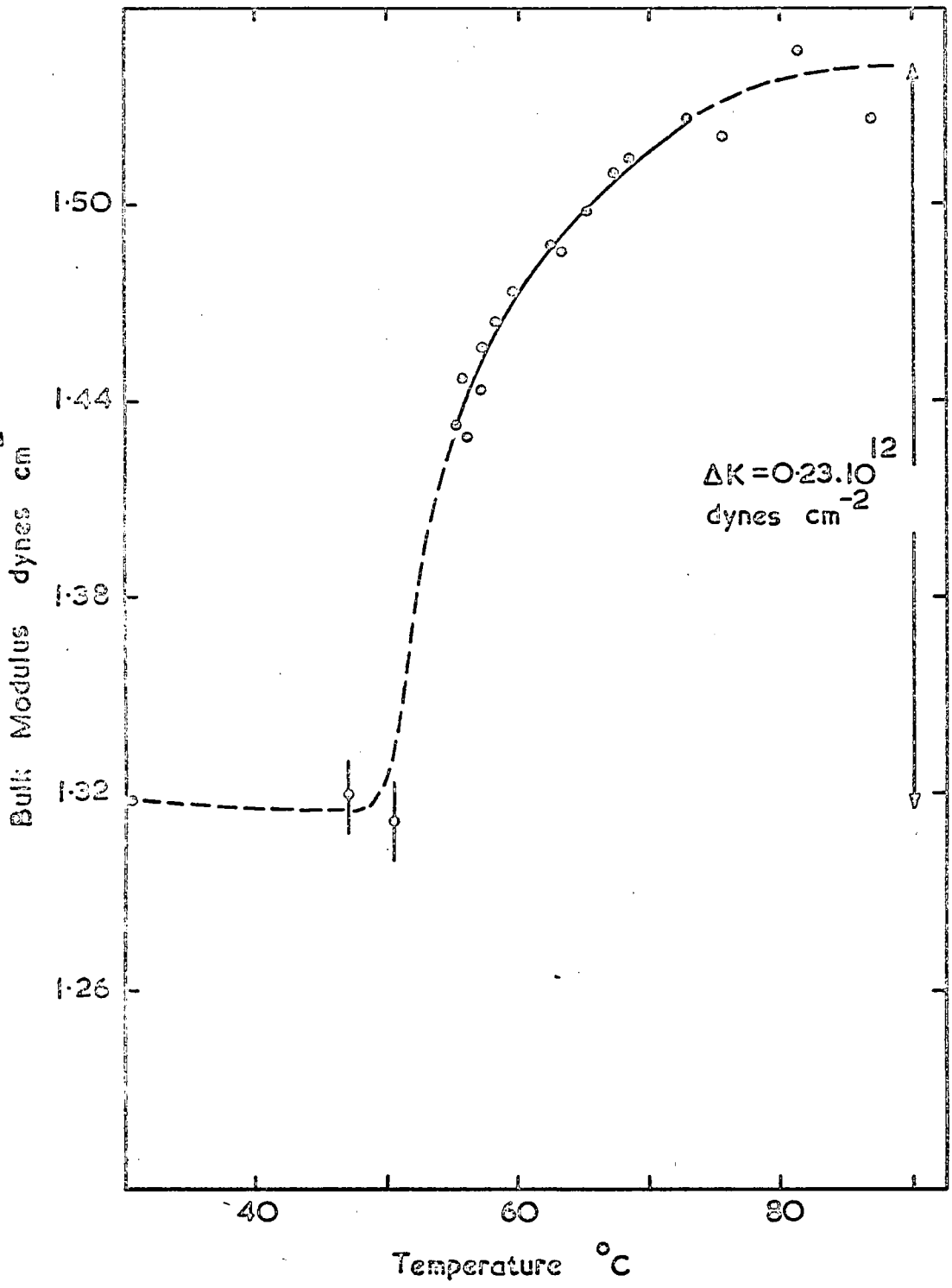

Figure (4.5) Bulk modulus near the transition in TiNi.

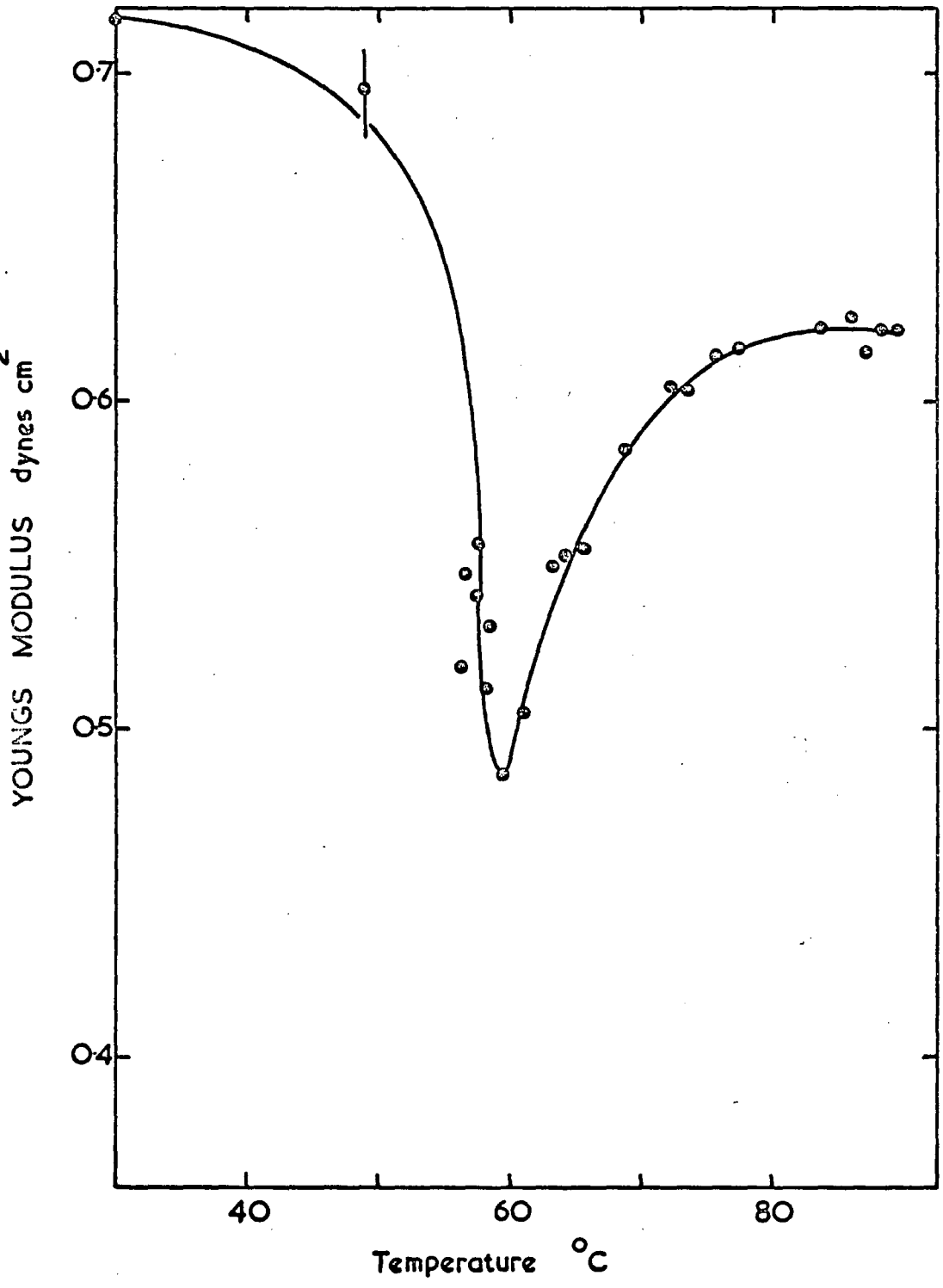

Figure (4.6) Young's modulus near the transition in TiNi.

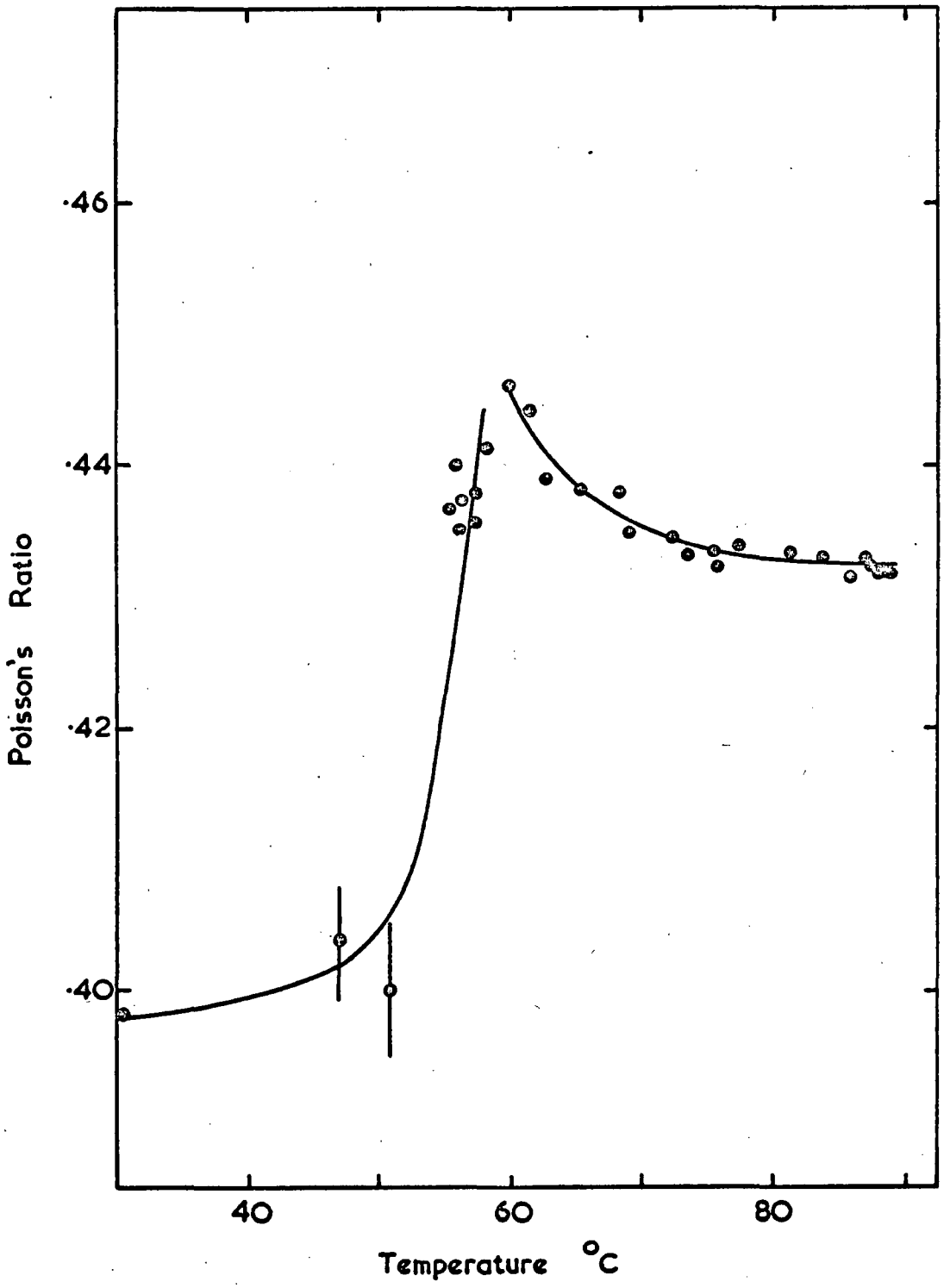

Figure (4.7) Poisson's ratio near the transition in TiNi.

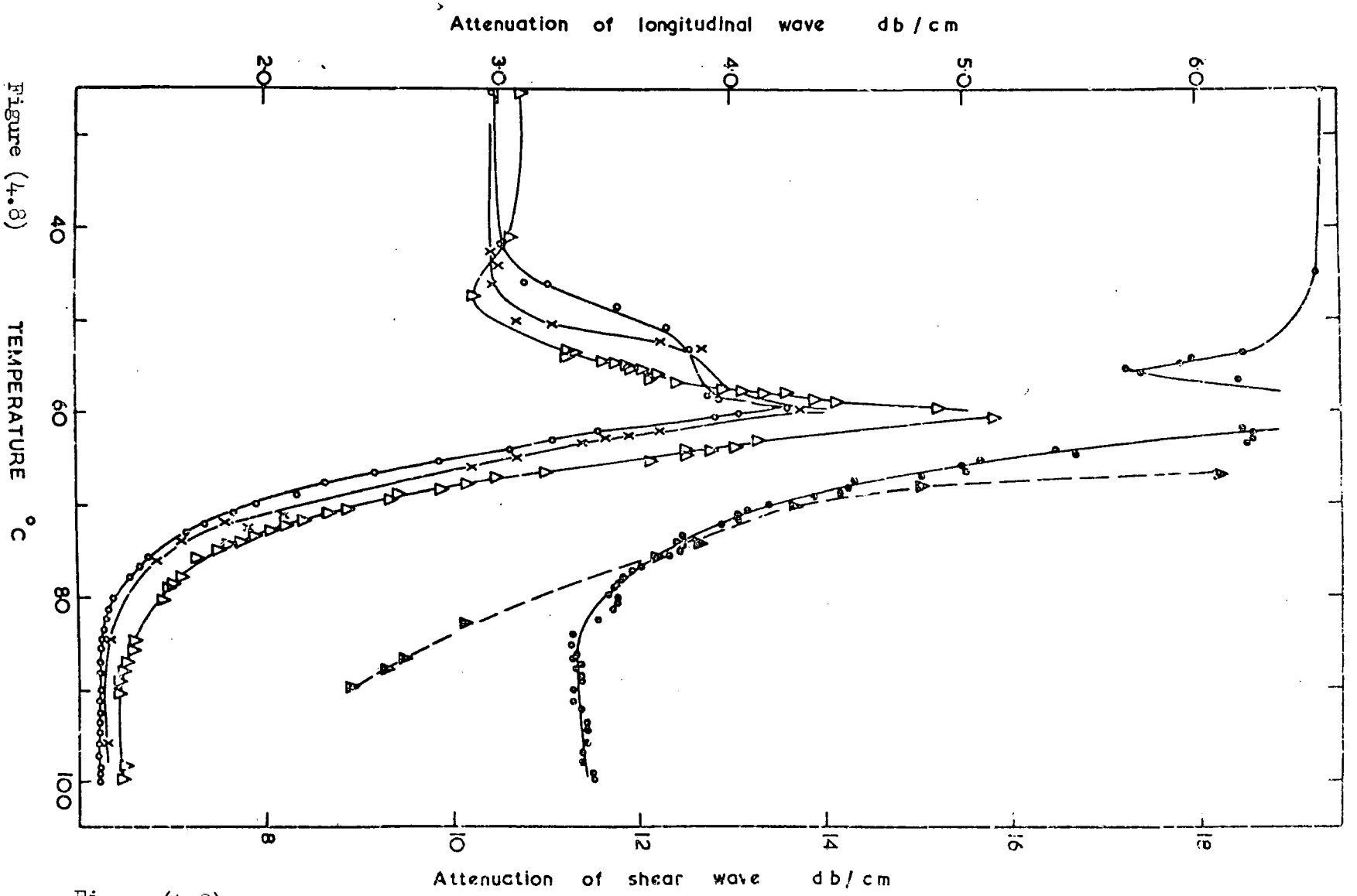

Figure (4.8) Measured ultrasonic attenuation in TiNi of longitudinal (o) 10 MHz , (x) 12 MHz , (Δ) 15 MHz , (●) 25 MHz and shear (▲) 12 MHz waves.

4.2.3 Thermal expansion of TiNi

The thermal expansion of TiNi was measured as a function of temperature using a dilatometer technique (Figure (4.9)) with a dial gauge reading to 2 x 10^{-5} inches. The arrangement shown in Figure (4.9) compensates for any expansion in the quartz rod (A) by an equal movement of the dial gauge due to expansion of the quartz tube (B). Measurements were taken during either slow heating or cooling in the oil bath (see (3.9.1)). The same thermal cycling procedure, described in (4.2.2), was followed. The thermal expansion is shown in Figure (4.10); the usual displacement of the transition to a higher temperature during heating from that occurring during cooling is well demonstrated. It is also evident that the initial room temperature length is not the same when the sample is cooled to room temperature from temperatures above the transition: the transition has not gone to completion at room temperature but requires further cooling. The reference length used for calculating the linear thermal expansion coefficient was taken to be that measured by a micrometer at room temperature: errors introduced into the thermal expansion coefficient by the changing value of the reference lengths were negligible in comparison with other errors: measurement of length changes were accurate to $\pm 2 \times 10^{-5}$ inches and the actual length was measured to a $\pm 0.1\%$ accuracy.

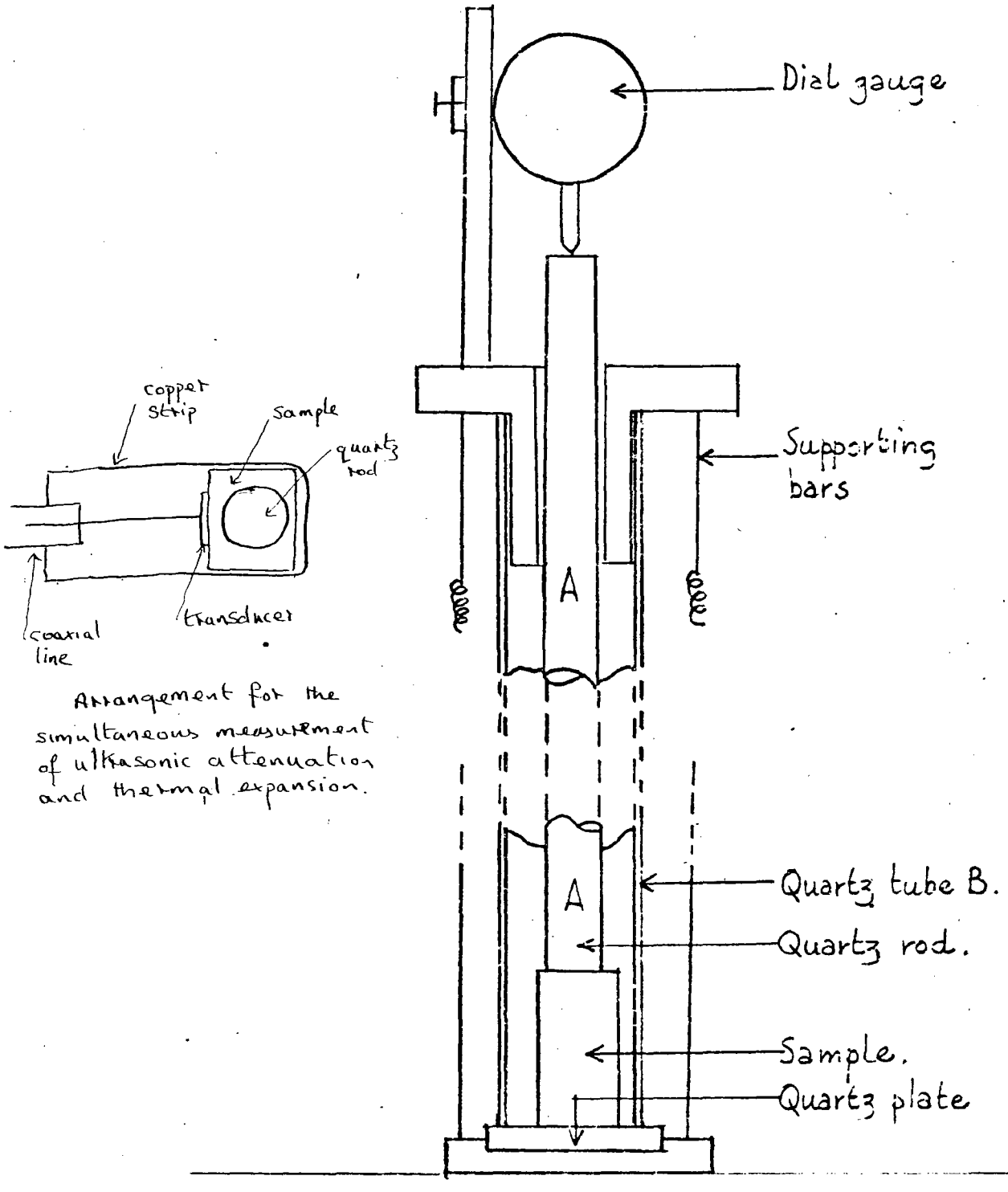

Figure (4.9) The dilatometer used for thermal expansion measurements.

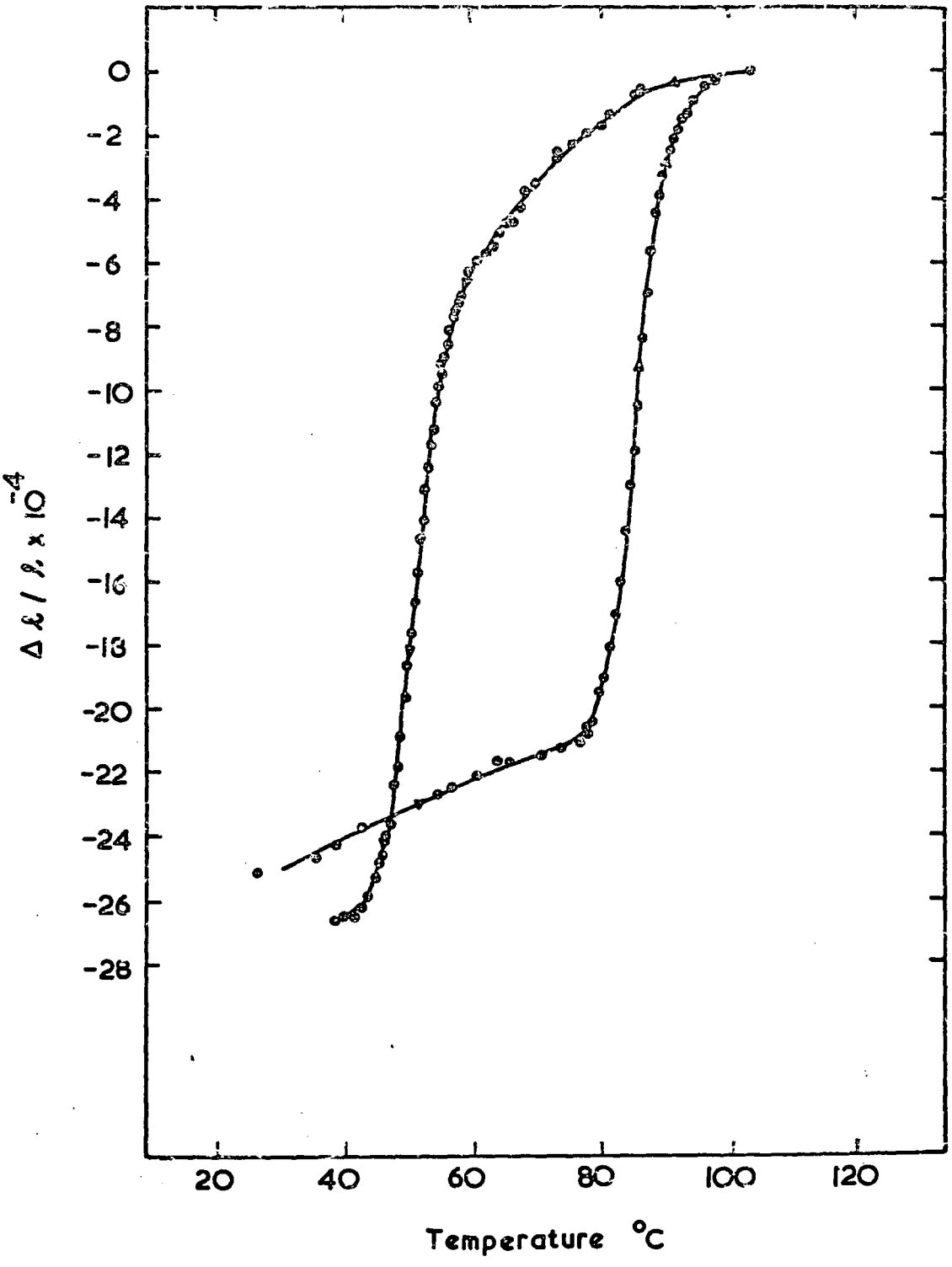

Figure (4.10) Thermal expansion of TiNi.

An arrangement was provided (see Figure (4.9)) for the simultaneous measurement of thermal expansion and ultrasonic attenuation to confirm that the attenuation and thermal expansion coefficient maxima occur at the same temperature.

4.2.3.1 Discussion of the thermal expansion results

The thermal expansion coefficient (Figure (4.11)) exhibits a pronounced maximum at the transition temperature in TiNi which indicates that the lattice vibrations undergo drastic changes. Because the major contribution to the thermal expansion of solids arises from the anharmonicity of the lattice vibrations, the large change in the thermal expansion in the vicinity of the transition is a manifestation of the presence of a lattice instability.

The Gruneisen parameter γ (see (7.5.1) for a definition) is important in the analysis of ultrasonic attenutation data and is available from the thermal expansion coefficient (a) and bulk modulus (K):

$$\gamma = \frac{3aK}{C_p} \qquad (4.6)$$

where C_p* is the total lattice constant pressure specific heat if

---

* The specific heat of TiNi has been found (Berman et al. 1967) to exhibit a sharp peak at the transition temperature which has been (Wang et al. 1968) attributed entirely to the changes in the free carrier density. The background specific heat upon which the peak is superimposed has a value of 2.9×10^7 ergs deg.$^{-1}$ cm.$^{-3}$ which is close to the Dulong and Petit value of 2.8×10^7 ergs deg.$^{-1}$ cm.$^{-3}$. All values of the Gruneisen parameter quoted here and in (4.5) are calculated on the basis of a constant value of lattice specific heat equal to 2.9×10^7 ergs deg.$^{-1}$ cm.$^{-3}$.

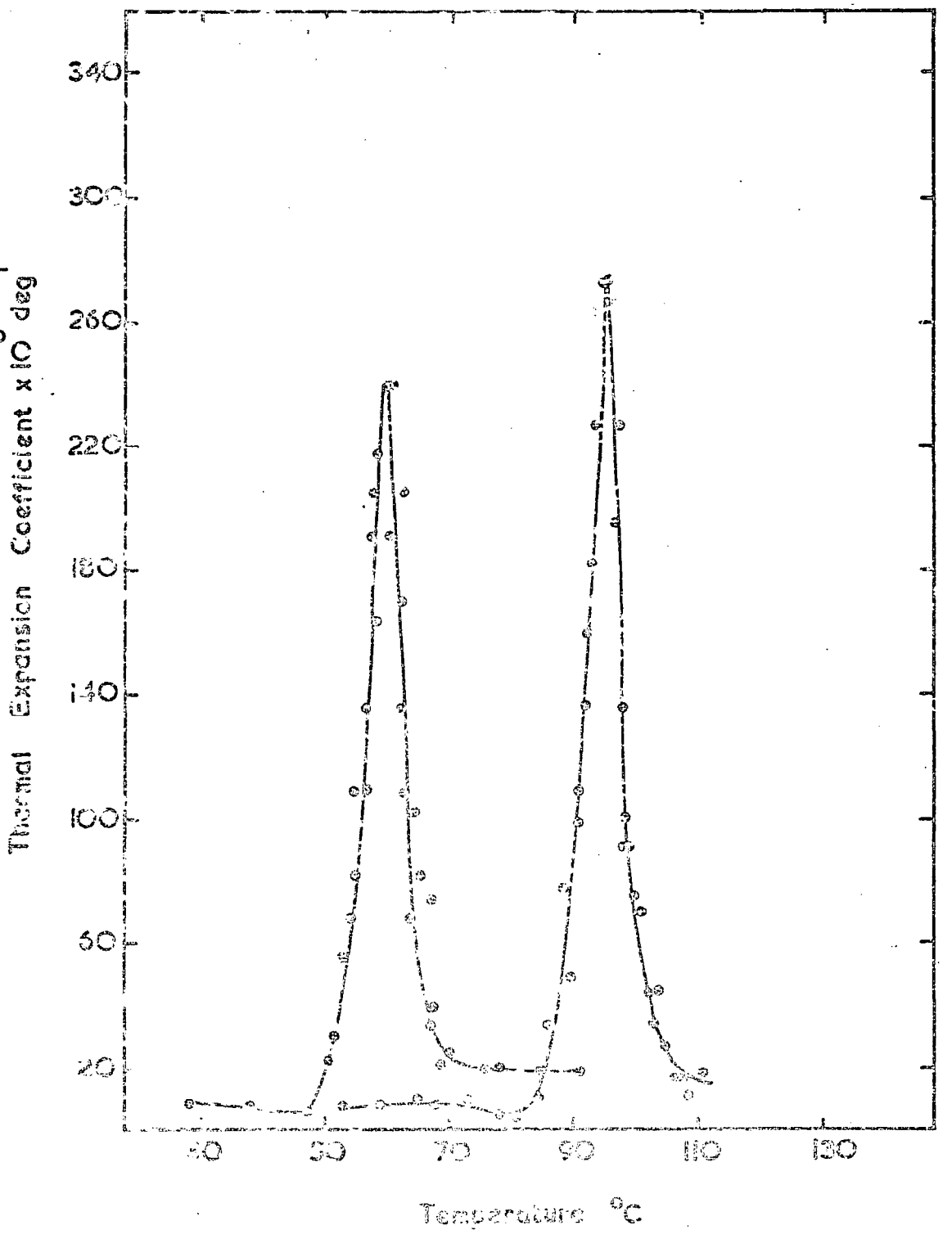

Figure (4.11) Thermal Expansion coefficient of TiNi : the maximum moves to lower temperatures during cooling.

the adiabatic bulk modulus is used (see (2.3.1)).

The anomalous behaviour of the thermal expansion (Figure (4.11)) and bulk modulus (Figure (4.5)) is reflected in the Gruneisen parameter shown in Figure (4.12). The relevance of the rapid changes in the Gruneisen parameter to those in the ultrasonic attenuation (Figure (4.8)) and velocity (Figure (4.3)) is discussed later (see (4.5)).

For body centred cubic metals and alloys it has been found (Sirdeshmukh 1967) that the product aV where V is the molar volume is inversely proportional to the bulk modulus. TiNi has such a cubic structure above the transition and fits well into this scheme as shown in Figure (4.13).

4.2.4 Thermal conductivity measurements in TiNi

The method adopted for thermal conductivity measurements was that of measuring the temperature gradient developed by a known quantity of heat passing along a bar of the material.

The sample holder used for the thermal conductivity measurements is shown in Figure (4.14). The TiNi sample (see Figure (4.14) for details of size) was cemented into slots in the heater block and heat sink using a silver dispersion (Silverdag, Acheson Colloids Ltd.) in order to obtain good thermal contacts. The two copper/constantan thermocouples for measuring the temperature gradient along the sample were held tightly in place against the

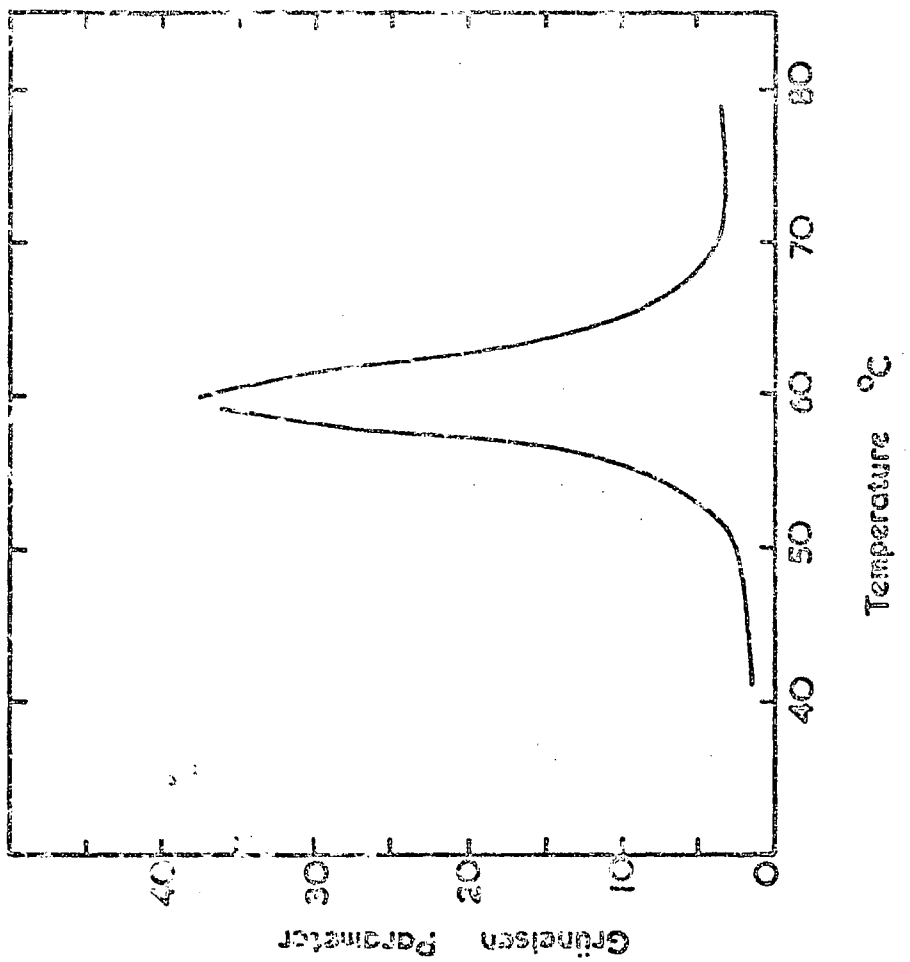

Figure (4.12) The Grüneison parameter of TiNi in the transition region.

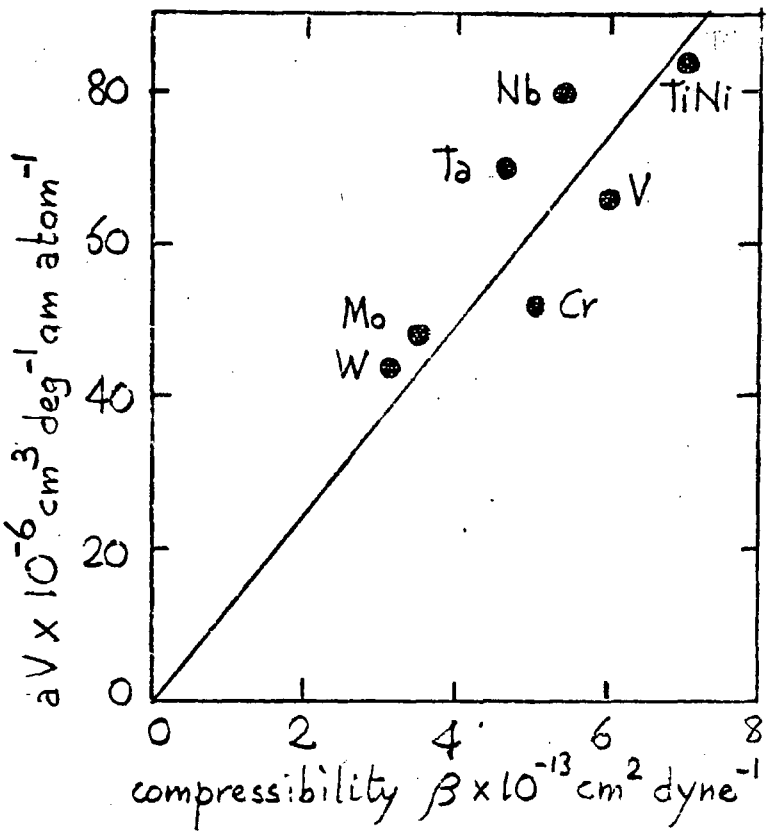

Figure (4.13) Plot of β versus αV for b.c.c metals and alloys.

sample by attaching them to lengths of small diameter enamelled copper wire wound once round the sample. Sample dimensions and the distance between the two thermocouple junctions were measured with a travelling microscope. The arrangement of the thermocouples allowed both the actual isotherms at the points of contact with the sample and also the temperature difference between these isotherms to be measured (see Figure (4.14)). The heater ($\sim$ 2 ohms) used to develop the temperature gradient was made by coiling a length of refrasil covered Kanthal wire and cementing into the cavity provided in the heater block. The potential and current leads to the heater were thermally anchored to the heat sink. An accummulator supplied the heater current through a variable series resistance; both the heater current and the voltage across the heater were measured potentiometrically as were all thermocouple voltages.

Measurements were taken with the sample holder in an evacuated enclosure (about 10^{-5} torr). All leads in and out of the vacuum chamber were continuous; they were passed through a neoprene seal (see Figure (4.14)).

4.2.4.1 Errors in the measurement of thermal conductivity

The errors in the measurement of the temperature gradients developed along the sample and the uncertainty in the knowledge of

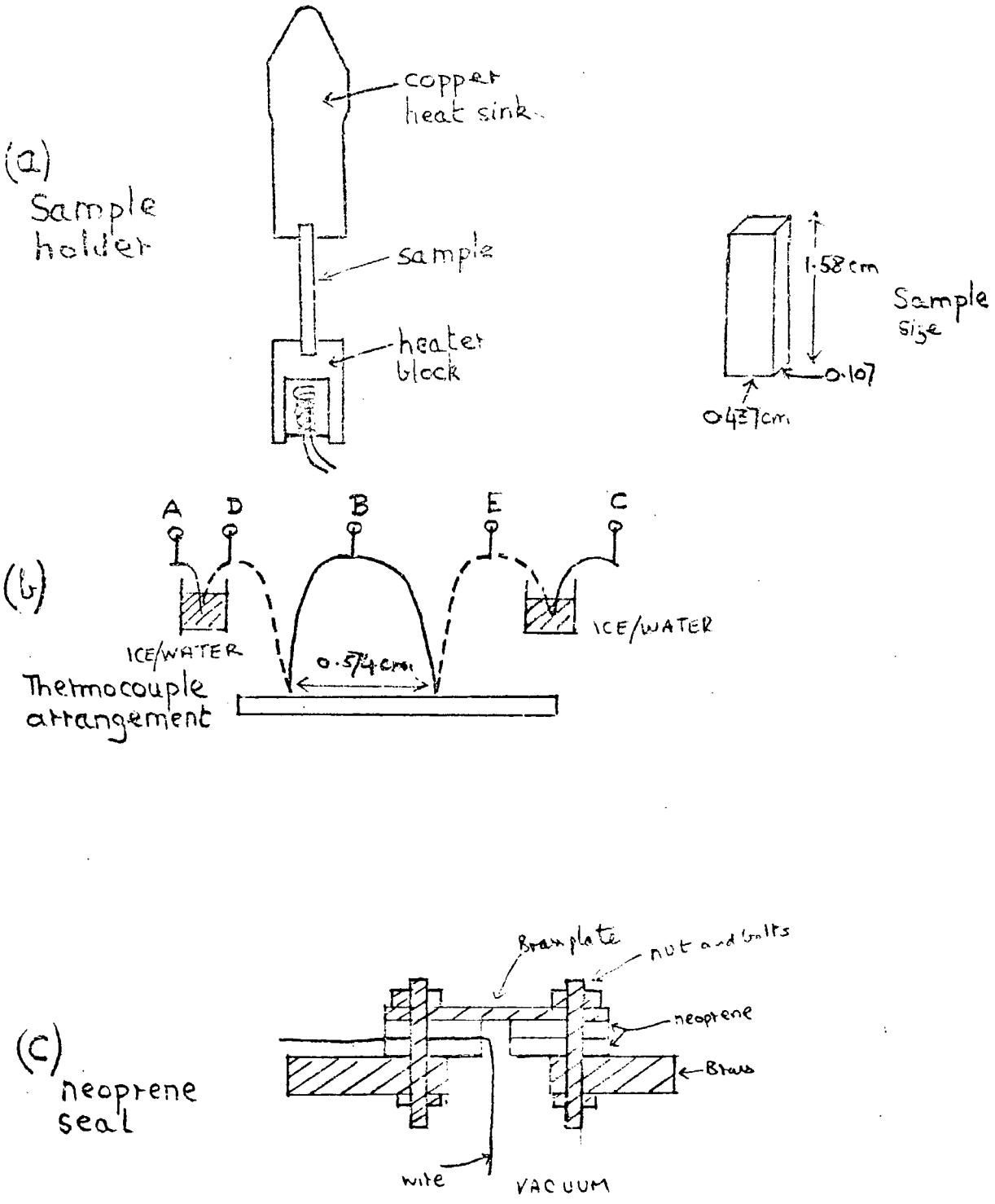

Figure (4.14) Sample holder for thermal conductivity measurements.

the heat flow and their effect on the measurement of the thermal conductivity will now be discussed in turn.

In the temperature range of the measurements a temperature gradient of $1^{\circ}C$ along the sample produces a difference in the output of the thermocouples AB and BC (see Figure (4.14)) of $39\mu v$. Stray voltages of the order of a few microvolts are easily generated, for example by a temperature variation along a strained thermocouple wire. But with the arrangement of thermocouples used here, the temperature gradient may also be read directly using terminals D and E (Figure (4.14)). Throughout the experiment the disagreement between the two different measurements of temperature gradient was never greater than 3%. When the errors associated with the room temperature measurement and temperature variation of the sample dimensions are included, then only changes greater than 4% in the thermal conductivity may be detected with confidence.

Not all the power supplied to the heater is responsible for the observed temperature gradient: heat losses from the heater block in addition to that lost to the sample, arise in the following ways:

(a) The residual pressure in the evacuated enclosure was about 5×10^{-4} torr; heat losses due to gaseous conduction are always to be expected and can be estimated from the expression (White 1959)

$$\dot{Q} = BP(T_2 - T_1)A \qquad (4.7)$$

where B is a constant for the residual gas and for air is 0·016, P is the residual pressure, T_2 is the temperature of the heater block and T_1 is that of the enclosure walls and A (= 1·6 cm^2) is the surface area of the heater block. For a temperature difference $T_2-T_1 = 65^{\circ}K$ the heat loss is only 8×10^{-4} watts: gaseous conduction losses were thus negligible.

(b) Thermal conduction along the current and potential leads is another source of heat loss and is easily calculated when the heater block and heat sink temperatures are known. Losses occurring in this way are shown in Figure (4.15).

(c) By far the greatest source of heat loss is by radiation; this may be estimated roughly from (White 1959)

$$\dot{Q} = \sigma A(T_2^4 - T_1^4)\epsilon \qquad (4.8)$$

where σ is Stefan's constant, ϵ is the emissivity of the heater block surface and is expected to be about 0·9 (ϵ for tarnished brass is approximately unity). But because of the importance of these radiation losses, they were experimentally determined as follows. When the sample holder without the sample in place is in thermal equilibrium, the heat supplied to the heater block to maintain equilibrium is equal to the total heat losses from the heater block. After the calculated loss by thermal conduction along the leads, which

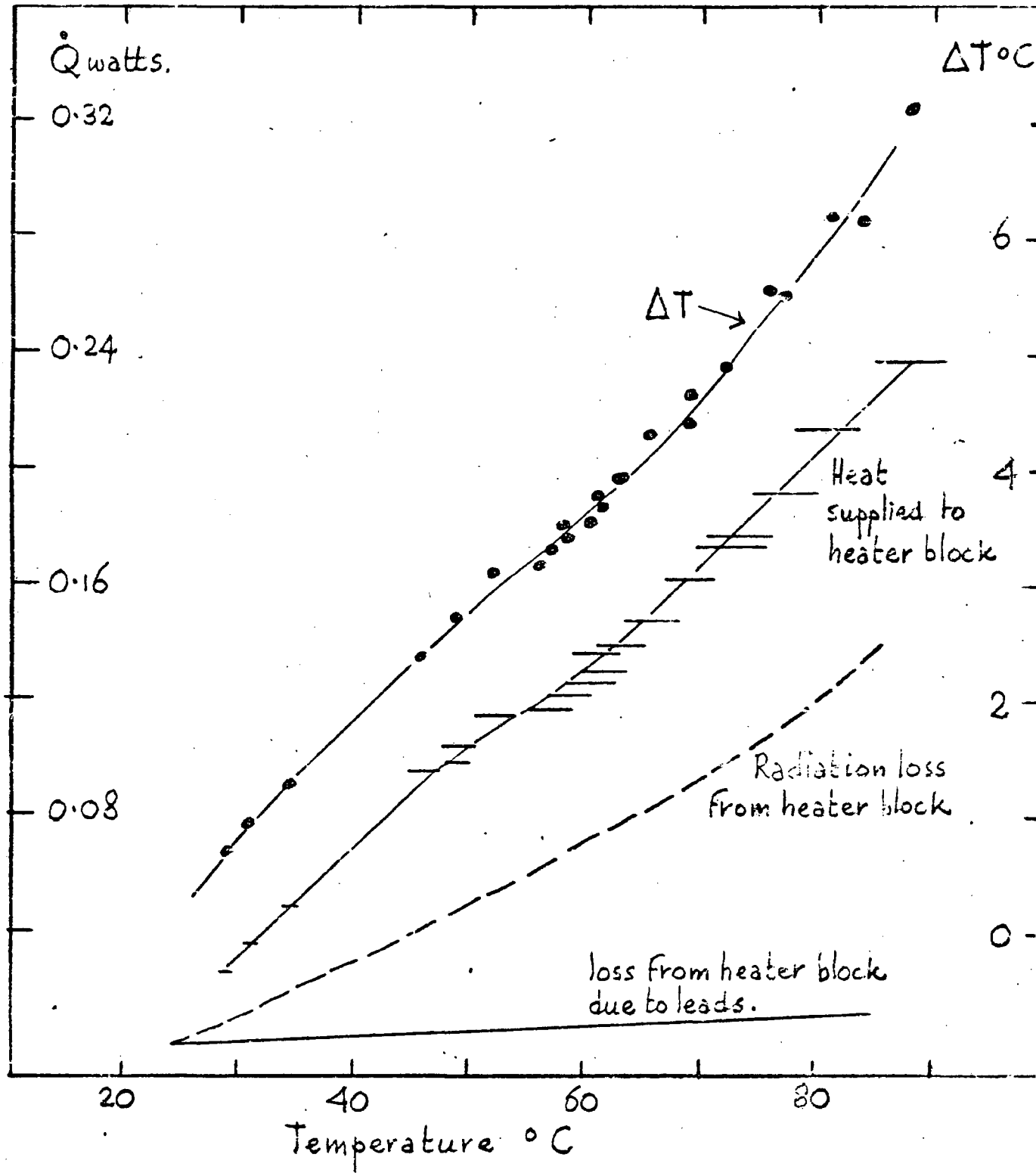

Figure (4.15) Analysis of the heat losses during thermal conductivity measurements. (see text).

is greater than when the sample is in place, have been subtracted, the remainder is that lost by radiation from the heater block. Details are available in Figure (4.15).

4.2.4.2 Results and discussion of thermal conductivity of TiNi

The temperature dependence of the thermal conductivity of TiNi, calculated from the data in Figure (4.15) is shown in Figure (4.16). A distinct change is evident at the transition. The only other thermal conductivity data available is that reported by Goff (1964) which extends from about $4^{\circ}K$ to room temperature and thus does not include the transition region, the main concern here. The room temperature value obtained by Goff, included in Figure (4.16), is in reasonable agreement with the present results.

In general, the thermal conductivity k is the sum of lattice k_L and electronic k_e components. The latter is related to the electrical resistivity ρ by the Lorentz number L ($= k_e\rho/T$) which has the Sommerfeld value of 2.44×10^{-8} watts. In the vicinity of a structural change the thermal conductivity might be expected to show changes due to either the lattice or electronic component. A case in point where the lattice contribution is affected is an anomalous dip in the thermal conductivity of ferro electric crystals (Suemune 1967; Inone 1968) at their Curie temperatures. In the present case, a calculation of the Lorentz number (see

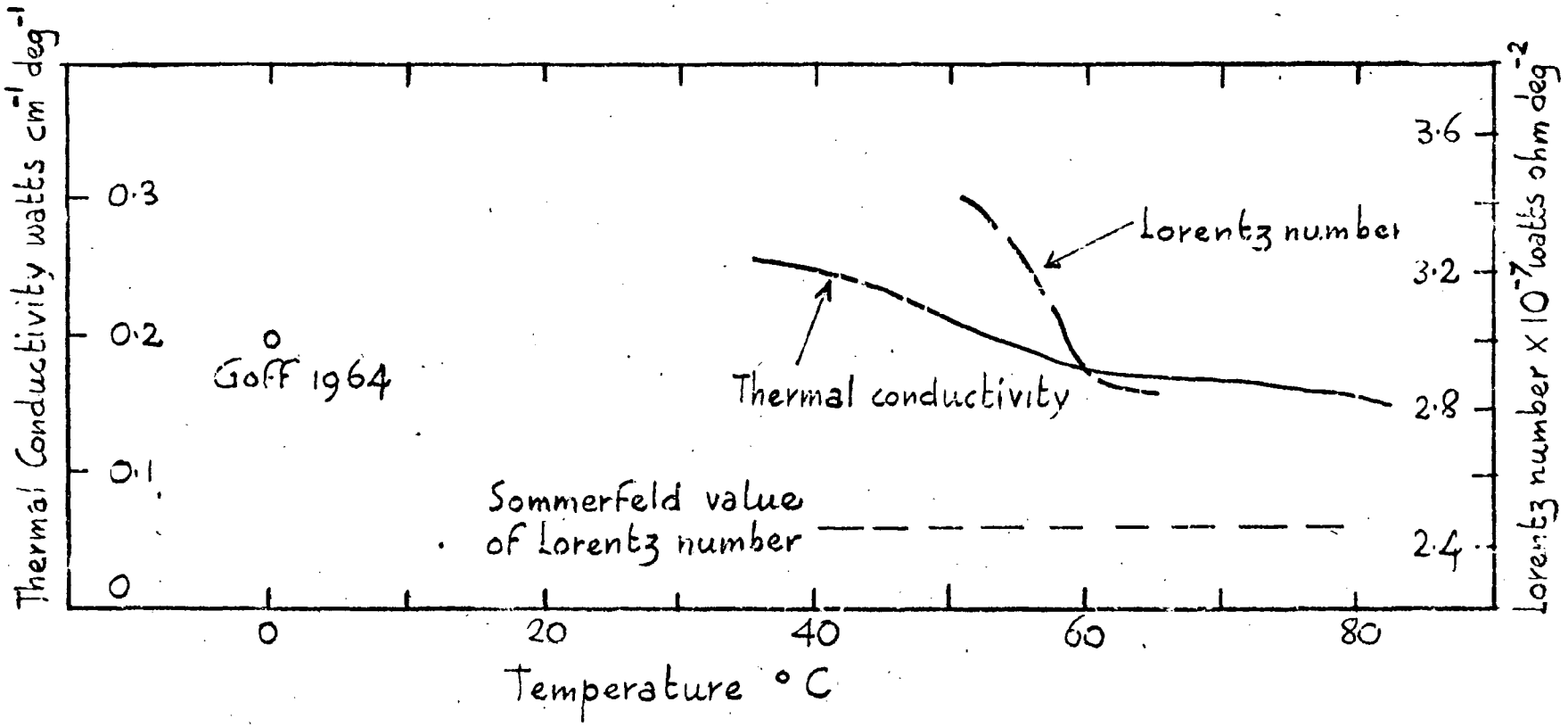

Figure (4.16) The thermal conductivity and Lorentz number for TiNi. in the vicinity of the transition.

Figure (4.16)) using the electrical resistivity data of Wang et al. (1968) and the measured total thermal conductivity, shows that the lattice component is not negligible in comparison with the electronic component. In fact by assuming the Sommerfeld value for L, most (65%) of the change in the thermal conductivity in the vicinity of the transition is attributable to that in the lattice component.

4.3 Discussion of the ultrasonic velocity results in the two phases away from the transition region

It has been suggested (Wang et al. 1968) that the instabilities associated with the transition are largely electronic in origin, and that the anomalous specific heat (see 4.2.3.1) can be accounted for by carrier density changes. A two-band model has been put forward for the high temperature CsCl phase (Allgaier 1967); in a reduced zone scheme the Fermi surface is essentially a hole octahedron (the s band) located near the zone corners and an electron jack at the zone centre. In the high temperature phase both the number of holes and the electrical resistance are larger than in the low temperature phase (Wang, deSavage and Buehler 1968), results considered by Wang, deSavage and Buehler on the basis of a 'conduction' to 'covalent' electronic transformation. However, the electrical behaviour on either side of the transition can be

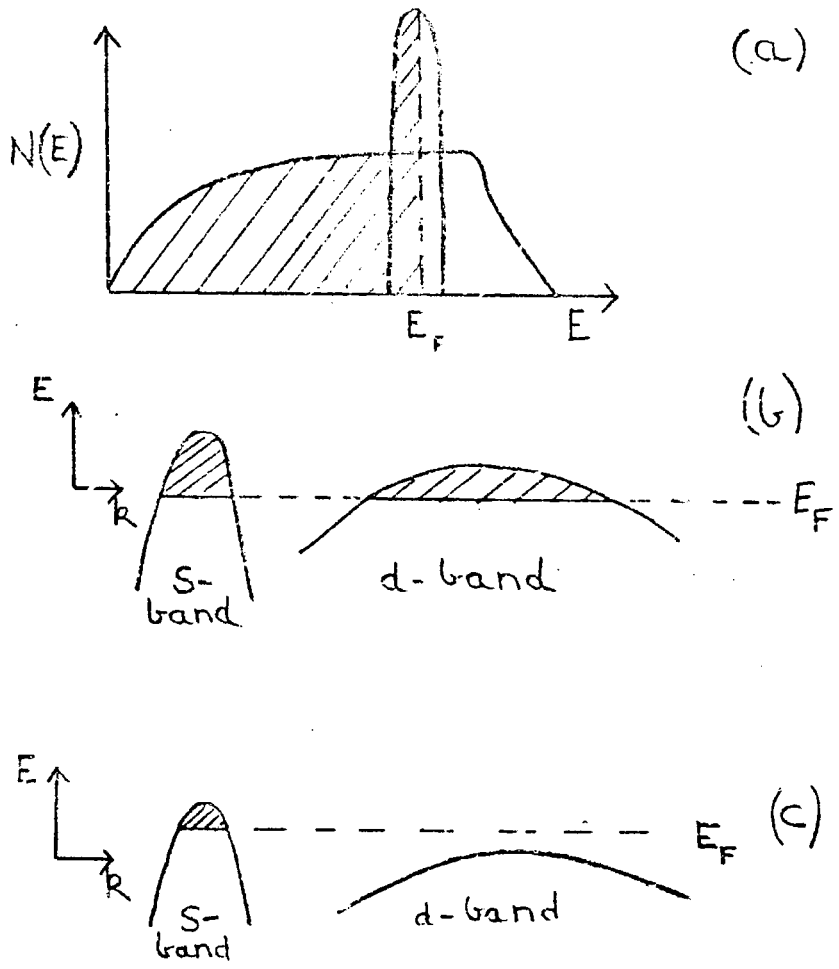

Figure (4.17) In (a) a typical density of states function N(E) is shown schematically for transition metals. The Fermi level is shown as a dotted line such that states are occupied almost to the d-band edge. This is also the situation shown in (b). The d-band is a trap with a high density of states into which carriers in the s-band may be scattered. As the phase transformation in TiNi proceeds it is suggested that the Fermi level moves up in energy so that below the transition it has as shown in (c) risen above the d-band edge; s-d scattering cannot now take place.

interpreted as follows by recourse to the usual features exhibited by transition metals and their alloys (see Figure (4.17)). Above the transition the Fermi level location is such that the octahedral pockets of the Fermi surface contain a large number of holes and the overlapping d band a smaller number of heavy holes. Holes in the broad s band carry the current and vacant sites in the narrow, low mobility d band result in high s-d scattering probability, which reduces the relaxation time for carriers in the s band: the carrier Hall mobility is only 0.6 cm^2 $volt^{-1}$ sec^{-1}, so the resistance in this phase is high. Below the transition the Fermi level is above the d band edge, so that the d band is full, and the reduced number of carriers in the s band are more mobile (μ_H = 3.7 cm^2 $volt^{-1}$ sec^{-1}) with longer lifetimes thus enhancing the conductivity, although the free carrier density (0.35 x 10^{23} cm^{-3}) is lower in this phase than in the other (1.56 x 10^{23} cm^{-3}).

The large changes in the number of free carriers will be reflected in the binding forces and thus in the elastic properties (see 1.1). The temperature variations of the elastic moduli (see Figures (4.3) and (4.4)) exhibit both pronounced changes at the transition point and the considerable differences between the elastic properties of the two phases of TiNi. The total energy of a system, the second derivative of which with respect to strains

gives the elastic constants, may be expressed as the sum of terms which can be calculated separately. These include the Fermi energy, the energy of the lowest electron state and exchange and correlation terms (see 1.1). A reasonable hypothesis is that the difference between the total energy of the two phases in TiNi can be attributed largely to the change in the Fermi energy. The elastic constant data attest to this. The contributions to the bulk modulus due to the Fermi energy alone is given by (Jones 1949):

$$K_F = \frac{1}{9}\frac{r^2}{\Omega}\frac{d^2E_F}{dr^2} \qquad (4.9)$$

where r is the radius of the atomic sphere defined so that $(4/3)\pi r^3$ equals Ω. Assuming a free-electron model, that is that the s-band hole octahedra are spheres, the Fermi energy E_F is given by,

$$E_F = \frac{3}{5}\left(\frac{3}{\pi}\right)^{2/3}\left(\frac{\pi^2\hbar^2}{2m}\right)\left(\frac{n}{\Omega}\right)^{2/3} \qquad (4.10)$$

where n is the number of free carriers per atom. The radius of the atomic sphere is found from the unit cell dimensions to be effectively the same above and below (1.4774Å) the transition.

Differentiation of the Fermi energy twice with respect to r gives the bulk modulus from (4.9). Therefore, the change in the bulk modulus between the two phases due to the change in the volume

of the Fermi sphere is:

$$\Delta K_F = \frac{3\pi\hbar^2}{20m}\left(\frac{9}{4\pi^2}\right)^{2/3}\left(\frac{n_1^{2/3} - n_2^{2/3}}{r^5}\right) \qquad (4.11)$$

where 1 and 2 refer to the high and low temperature phases respectively. From Hall effect measurements (Wang et al. 1968) the number of free carriers per atom in the high and low temperature phases is found to be $n_1 = 2{\cdot}11$ and $n_2 = 0{\cdot}47$ respectively. These give a value of ΔK_F equal to $3{\cdot}16 \times 10^{11}$ dynes cm.$^{-2}$ which compares with the experimental value of $2{\cdot}3 \times 10^{11}$ dynes cm.$^{-2}$ (see Figure (4.5)). Thus a most important contribution to the change in those binding forces responsible for resistance to bulk deformation comes directly from the change in the free carrier concentration. Further, this suggests that the magnitudes of the binding energy contributions arising from the energy of the lowest electron state and the exchange and correlation energies are not very different on either side of the transition. The calculated contributions K_F from the Fermi energy to the total bulk modulus K are about 30% of the experimental value above the transition and only 14% below the transition (see Table (4.1)). Thus while the total bulk modulus accrues from the large contributions other than that due to the Fermi energy, the difference in the bulk modulus between the two phases can be largely accounted for by the free carrier component.

TABLE (4.1)

	$T > T_c$	$T < T_c$
Radius of atomic sphere	1•4772 Å	1•4774 Å
Atomic volume	13•50 $Å^3$	13•51 $Å^3$
Number of free carriers per cm^3	$1•56.10^{23}$	$0•348.10^{23}$
Number of free carriers per atom	2•11	0•47
Number of atoms per cm^3	$0•74.10^{23}$	$0•74.10^{23}$

(a) Parameters for TiNi above and below the transition temperature T_c.

K, $T > T_c$ measured	15•6
K_F, $T > T_c$ calculated	4•99
K, $T < T_c$ measured	13•4
K_F, $T < T_c$ calculated	1•83
ΔK measured	2•3
ΔK_F calculated	3•16

(b) Values of the measured and calculated bulk moduli K for the two phases of TiNi. K_F is the Fermi energy contribution. (Units are 10^{11} dynes cm^{-2})

The main feature exhibited by the shear modulus shown in Figure (4.4) is that the low temperature phase is the more resilient against shears. This is demonstrated strikingly by the difference between the Poisson ratios of the two phases away from the transition region (see Figure (4.7)). The larger Poisson's ratio is (the maximum possible value is 0·5), the less stable the material is to shears. No contribution is made by the Fermi energy to the shear modulus unless the Fermi surface is in contact with, or intersects as it does in TiNi, the Brillouin zone boundaries (see 1.1). For example, the stability of β-brass with respect to shears across the (110) plane in the $[1\bar{1}0]$ direction arises mainly from the change in the Fermi energy as a result of shearing the Brillouin zone (Jones 1952). Similarly in TiNi, since the number of holes is less in the low temperature phase, the area of the Brillouin zone boundary which the hole octahedron cuts is smaller than that in the high temperature phase, thus giving an increase in the shear stability below the transition, as demonstrated by the shear modulus and the Poisson ratio.

The difference in elastic properties of TiNi between the two phases away from the transition point thus arises mainly from changes in the free carrier concentration.

4.4 Discussion of the background ultrasonic attenuation

The anomalous ultrasonic attenuation effects in the vicinity of the transition (see Figure (4.8)) are superimposed upon a background attenuation composed of the apparent attenuations due to diffraction and transducer coupling losses (see (4.2.2) and (3.7)) and the attenuation due to scattering in the polycrystalline material. In such a material each grain is elastically anisotropic and has it crystallographic axes misoriented with respect to those of its neighbours, thus giving rise to elastic gradients which cause an ultrasonic energy loss. In general the frequency dependence of the attenuation due to this scattering varies between the fourth and second power, depending upon whether the wavelength of the ultrasound is greater or less than $2\pi D$, where D is an average grain diameter (Papadakis 1968). In the samples used here the grains were equiaxed and had an average diameter of 26 ± 4 microns (see (4.2.1)). Thus Rayleigh ($\lambda > 2\pi D$) scattering is expected. The attenuation separates at $90^{\circ}C$ into a constant term and one varying as the fourth power of the frequency as shown in Figure (4.18). For longitudinal waves propagating in an elastically isotropic, polycrystalline material with single phase, equiaxed grains, the attenuation α due to Rayleigh scattering is given by (Papadakis 1968):

$$\alpha_L = TSf^4 \text{dB per cm.} \qquad (4.12)$$

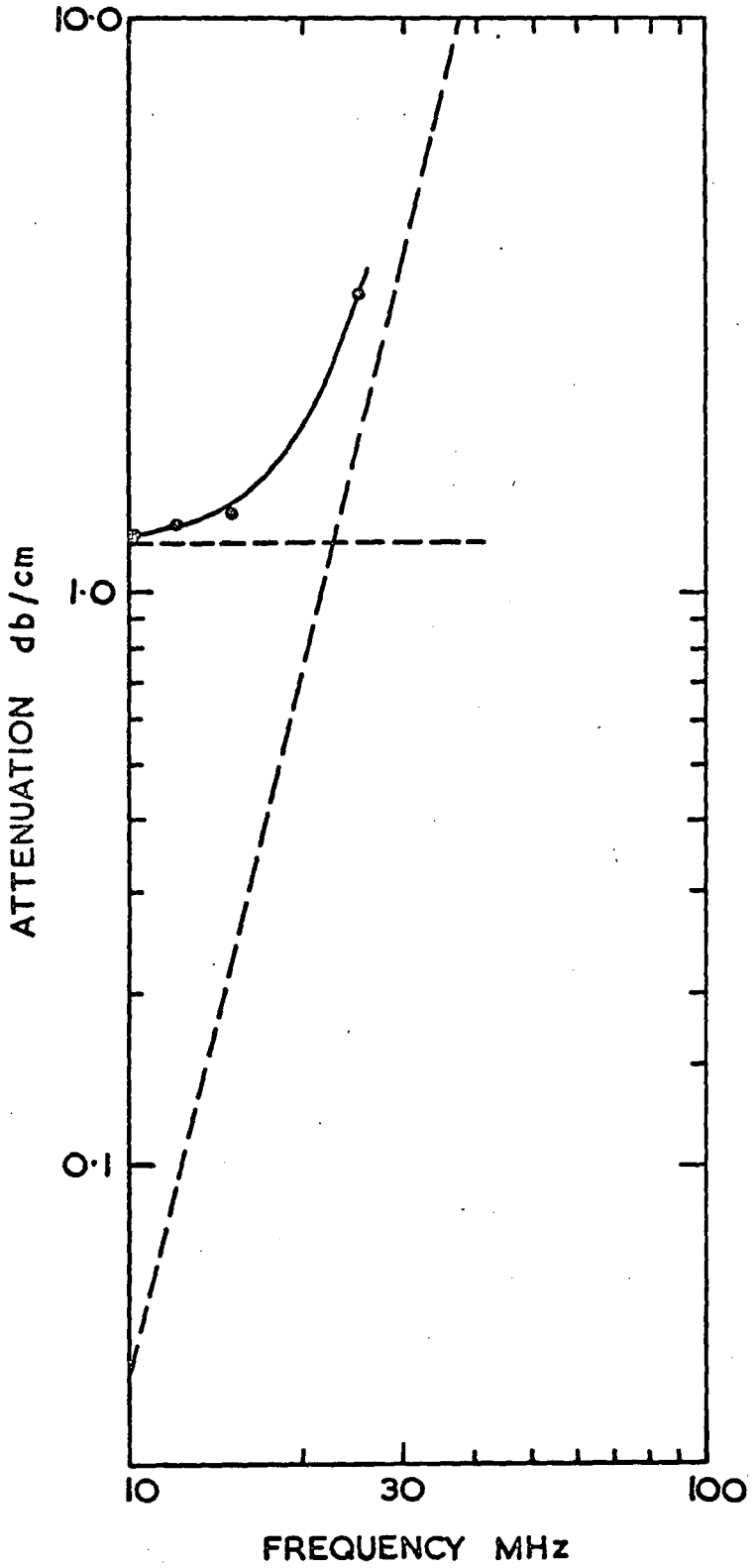

Figure (4.18) Separation of measured longitudinal attenuation in TiNi at 90 °C into a frequency independent portion and one varying as frequency to the fourth power.

Here f is the frequence and T is the effective grain volume (see (4.2.1)). The scattering coefficient is:

$$S = \gamma^2(8.686.\ 8\pi^3/375\rho^2 V_L^{\ 3})\ (2/V_L^{\ 5} + 3/V_S^{\ 5}) \qquad (4.13)$$

γ is the anisotropy factor $(C_{11}-C_{12}-2C_{44})$ and is estimated for TiNi as $(-2.3\pm0.5) \times 10^{11}$ dynes cm.$^{-2}$ and S as 830 ± 350 db cm.$^{-4}$ MHz^{-4}. These may be compared with those for nickel ($\gamma = -14.7 \times 10^{11}$ dynes cm.$^{-2}$ and S = 896 db cm.$^{-4}$ MHz^{-4}; Papadakis 1968).

In this material shear wave velocity is sufficiently small to carry the scattering losses out of the Rayleigh into the frequency squared region. Above the transition (which was the only temperature range in which the shear wave attenuation could be measured) the ratio of the attenuation of the longitudinal wave due to scattering to the measured attenuation of the shear wave corrected for diffraction and coupling losses was found to be 7.5×10^{-3} at 12MHz. This ratio may be calculated from (Papadakis 1968):

$$\frac{\alpha_L}{\alpha_S} = \frac{1.12\ T\ f^2\ V_S^6}{D\ V_L^3}\left(\frac{2}{V_L^5} + \frac{3}{V_S^5}\right) \qquad (4.14)$$

where D is the average grain diameter. This equation does not contain the anisotropy factor which is the only unknown quantity and the ratio turns out to be 7.8×10^{-3} in agreement with the experimental value.

Each grain continues to act as a scattering centre as the transition proceeds. Depending on whether the grains become more or less anisotropic below the transition, so the attenuation due to Rayleigh scattering will either increase or decrease. Below the transition each grain will contain both untransformed material and monoclinic martensite, the amount of the latter increasing the more the sample is cooled. Papadakis (1968) suggests that if the ratio of the anisotropy factor of the martensite to that of the high temperature phase is greater than $\sqrt{2}$ then the scattering will increase. Unfortunately, knowledge of single crystal elastic constants are required to calculate this ratio. But even so the attenuation below the transition results from a more complicated scattering procedure: the grains are no linger single phase but contain both untransformed material and martensite, the latter being formed in a number of different orientations within each original grain.

Away from the transition region the ultrasonic attenuation can thus be accounted for by scattering by the grains. But in addition there are other mechanisms of absorption present which could become more important as the transition is approached. These include the thermoelastic loss, Zener loss and losses due to interaction with free carriers. These will now be discussed in turn.

The thermoelastic loss results from temperature changes which take place in the strained regions due to passage of a longitudinal stress wave; heat flows from the hotter compressed regions to the cooler extended regions. The thermoelastic loss α_{th} is given by (Lucke 1956):

$$\alpha_{th} = \frac{1}{2\tau}\frac{\Delta M}{M}\frac{\omega^2\tau^2}{1+\omega^2\tau^2} \qquad (4.15)$$

where $$\frac{\Delta M}{M} = \frac{1+\sigma}{(1-2\sigma)(1-\sigma)} \cdot \frac{a^2 TE}{C_p}$$

and $$\tau = k_L/C_p V_D$$

V_D is the Debye velocity, σ is Poisson's ratio, E is Youngs modulus and k_L the lattice component of the thermal conductivity. The maximum thermoelastic loss occurs at the transition where both σ and a have their maximum values. At this point the thermoelastic attenuation is 0·30 db $cm.^{-1}$ at an ultrasonic frequency of 15MHz; while this is a relatively large value for thermoelastic loss (see Table (5.8)) it still makes a negligible contribution to the total attenuation. Furthermore, the shear wave attenuation also undergoes a sharp rise as the transition is approached and shear waves cannot suffer thermoelastic loss. Thus although the thermoelastic loss is present, it is small in comparison with the measured loss.

Zener (1937) loss is due to heat flow between neighbouring grains resulting from their different states of strain when the material is deformed elastically. Zener has given a relation for the frequency at which the resultant loss is a maximum,

$$f_{max} = 3\pi k/C_p \overline{D}^2 \qquad (4.16)$$

where k is the thermal conductivity and $\overline{D}$ an average grain diameter: for TiNi this frequency is about 0·1MHz. The Zener loss is typically smaller than the thermoelastic loss and thus may be neglected in TiNi. Even though the transition in TiNi involves a large change in the free carrier density, the resultant changes in the ultrasonic attenuation due to this are superimposed on a background free carrier attenuation of the order of 10^{-6} db $cm.^{-1}$ (estimated from expression given by Mason (1955)) and may also be neglected.

Finally, phonon viscosity losses will be present both away from the transition where they are small in comparison with that due to Rayleigh scattering and also in the vicinity of the transition where they achieve dominance; this is the subject of the next section.

4.5 Discussion of the ultrasonic attenuation and velocity in the vicinity of the transition

While the considerable differences found between the elastic moduli of the high temperature structure and the low temperature phase were shown in (4.3) to accrue essentially from changes in the free carrier density, this concept can provide no information on the mechanism by which the transformation proceeds. From consideration of the ultrasonic propagation characteristics it seemed likely that marked changes in the lattice behaviour in TiNi onset in the vicinity of the transition. This has been substantiated by the thermal expansion behaviour (Figure (4.11)) further consideration of which in conjunction with the ultrasonic data now leads to some insight into the microscopic nature of the transition. The peak observed in the thermal expansion is reflected in the Gruneisen parameter $\bar{\gamma}$ (= $3a\beta/C_p$) plotted in Figure (4.12). The marked peak in the Gruneisen parameter strongly evidences a direct connection between the transition mechanism and the lattice vibration spectrum. Somewhat similar behaviour of the Gruneisen parameter has been observed in the perovskites $SrTiO_3$ (Rewald 1970) and $KTaO_3$ (Barrett 1969). The ferroelectric transition in crystals of this type is known to be associated with the lowering of the frequency of transverse optic

(TO) phonon modes and a consequent incipient lattice instability as the temperature approaches T_c (Cochran (1961); Cowley (1965)). In these circumstances the Gruneisen parameter rises since it becomes approximately inversely proportional to the square of the soft optic mode frequency (Barrett (1969)).

As the transition is approached in both TiNi and in the displacive type ferroelectrics there is a large increase in ultrasound absorption accompanied by pronounced decreases in the ultrasonic wave velocities (Rehwald (1970); Cochran (1960, 1961); Cowley (1965)).

The large attenuation peak at T_c in TiNi has been shown to be superimposed upon a background attenuation due to Rayleigh scattering by the grains (see (4.4)) and an apparent attenuation due to diffraction and transducer coupling losses (see (3.7)). Cowley has explained the temperature dependence of the ultrasonic attenuation and the elastic constants in $SrTiO_3$ in terms of an accidental degeneracy in the TO and LA dispersion curves. The large peak in the ultrasound attenuation and the step in the sound velocity found in $SrTiO_3$ as a function of temperatures can then be explained quantitatively in terms of an Akhieser-type process with a strongly temperature dependent Gruneisen parameter (Rehwald (1970)).

Here the hypothesis is put forward that the ultrasound wave propagation behaviour in the vicinity of the martensitic phase transformation in TiNi can also be explained by increased damping due to Akhieser-type interactions with soft lattice modes near T_c. In the Akhieser process strains produced by the propagating ultrasonic wave modulate the thermal lattice mode frequencies and thus the equilibrium phonon populations; a finite relaxation time τ is required to regain the equlibrium configuration; the actual populations lag in phase behind the driving strain wave and there is a net energy dissipation during each cycle. The detailed treatment of the Akhieser effect by Woodruff and Ehrenreich (1961) was modified by Barrett (1969) to obtain expressions for the attenuation and velocity of ultrasound resulting from modulation of soft phonon modes.

In Barrett's treatment all the low frequency phonon modes are lumped together into a single "mode" characterised by a specific heat C_a, and a Gruneisen constant γ_a, a frequency ω_a and a relaxation time τ_a. Similarly, a single "mode" denoted by subscript b, is used to describe all the acoustic phonon modes. Near T_c the soft phonon mode contributes little to the total specific heat (C_a+C_b). The ultrasound attenuation due to Akhieser-type interaction with the soft mode is (Barrett (1969)):

$$\alpha = \frac{C_a T\gamma^2\omega^2\tau}{2\rho V_o^3(1+\omega^2\tau^2)} \qquad (4.17)$$

where $\gamma = \gamma_a = \gamma_b$, T is the absolute temperature, τ is an effective relaxation time, ρ is the density and V_o is the sound velocity when γ_a equals γ_b, that is in the absence of soft mode damping. The change in velocity $\Delta V (= V - V_o)$ resulting from the anharmonic contribution of the soft mode to the velocity is

$$\Delta V = \frac{-C_a T\gamma^2}{2\rho V_o} \frac{1}{1+\omega^2\tau} \qquad (4.18)$$

and thus, the effective relaxation time τ is found from

$$\tau = \frac{\alpha V_o^2}{\Delta V \omega^2} \qquad (4.19)$$

Thus the experimental results for the attenuation and velocity of sound may be used to calculate the soft mode specific heat and the effective relaxation time. The effect of the transition in TiNi on the ultrasonic attenuation is found by subtracting off the effect of the various background attenuation mechanisms from the measured attenuation (see (4.4)); the contribution of the soft mode to the velocity is more uncertain: the approach used has been to estimate the deviation of the ultrasound velocity from the straight line extrapolation of the velocity measured from -196°C to

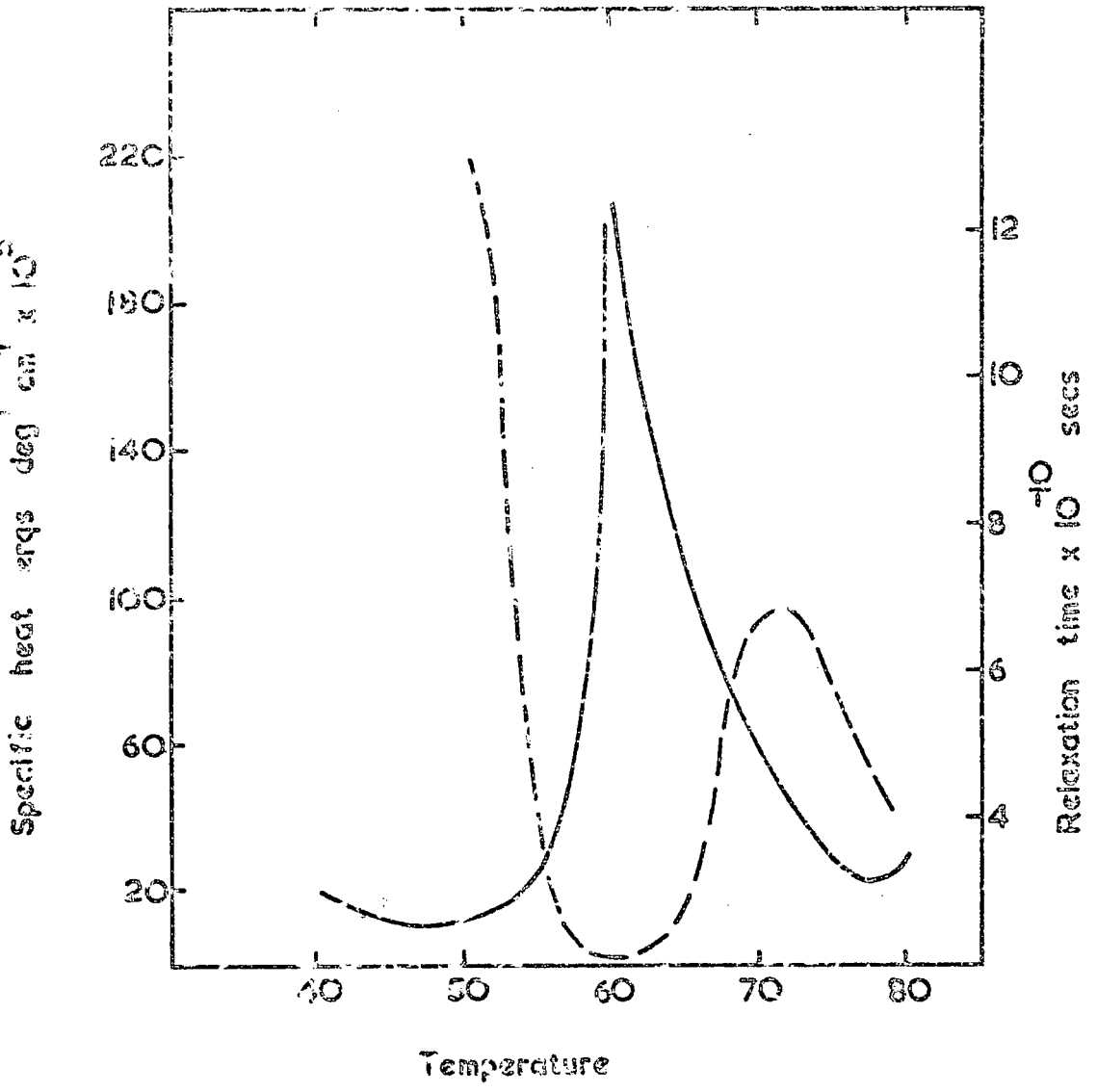

Figure (4.19) The soft mode specific heat C_a (— — —) and relaxation time τ (———) calculated from equations (4.17) and (4.18) using the experimental ultrasonic attenuation and velocity data as described in the text.

$0^{o}C$ up towards T_c. Although the calculated values of C_a and τ shown in Figure (4.19) cannot be considered as exact due to this uncertainty in ΔV, their order of magnitude and general behaviour are certainly consistent with a phonon mode softening in the vicinity of the transition. For the model used, τ can be written as $(\tau_a+(C_a/C_b)\tau_b)$; close to the transition C_a is much less than C_b and τ is dominated by the relaxation time τ_a due to ultrasound interaction with the soft modes.

4.6 Conclusion

The martensitic transition in TiNi has been the subject of a primarily ultrasonic investigation. It has been shown that the difference in elastic properties between the two phases away from the transition region arises mainly from changes in the free carrier concentration. Further, the measured lattice properties of TiNi - the ultrasonic wave attenuation and velocity, the thermal expansion and Gruneisen parameter - attest to a marked alteration in lattice behaviour in the vicinity of the martensitic phase transition. Increased Akhieser-type damping by thermal vibrations can account for the ultrasonic effects. The large value achieved by the Gruneisen parameter is a characteristic expected in a material in which a low lying soft phonon mode develops. However, the hypothesis that this transition proceeds through a soft phonon mode

mechanism is contentious. Ultrasonic, thermal and lattice transport measurements cannot establish the model conclusively; a neutron diffraction analysis of the phonon dispersion curves would provide a further test.

CHAPTER 5

Elastic properties in relation to the binding and structure of indium-thallium alloys

5.1 Introduction

During the progress of the work on TiNi it was decided to extend the study of martensitic phase transitions to include that which occurs in the indium-thallium system, alloys of which may be prepared in single crystal form. These alloys transform in a certain composition range (see Figure (5.1)) from a high temperature face centred cubic (fcc) to a low temperature face centred tetragonal (fct) structure. The present work in which the characteristics of ultrasonic wave propagation in a number of tetragonal and cubic alloys are measured complements previous studies (Novotny and Smith 1965) of the elastic properties of some fcc indium-thallium alloys.

A complete breakdown of the elastic wave propagation in tetragonal (4/mmm) crystals is given in (5.2) which is then used in (5.4) to discuss extensively the elastic behaviour of a 10 at.% thallium alloy and to compare it with pure indium. However, tetragonal alloys which have suffered the phase change consist of fine parallel bands of twins; this precludes measurement of all the independent elastic moduli of samples of these compositions (see Figure (5.1)). Nonetheless, an overall picture is provided of the compositional dependence of some of the elastic moduli of alloys from well below (pure indium) to well above (39 at.% thallium)

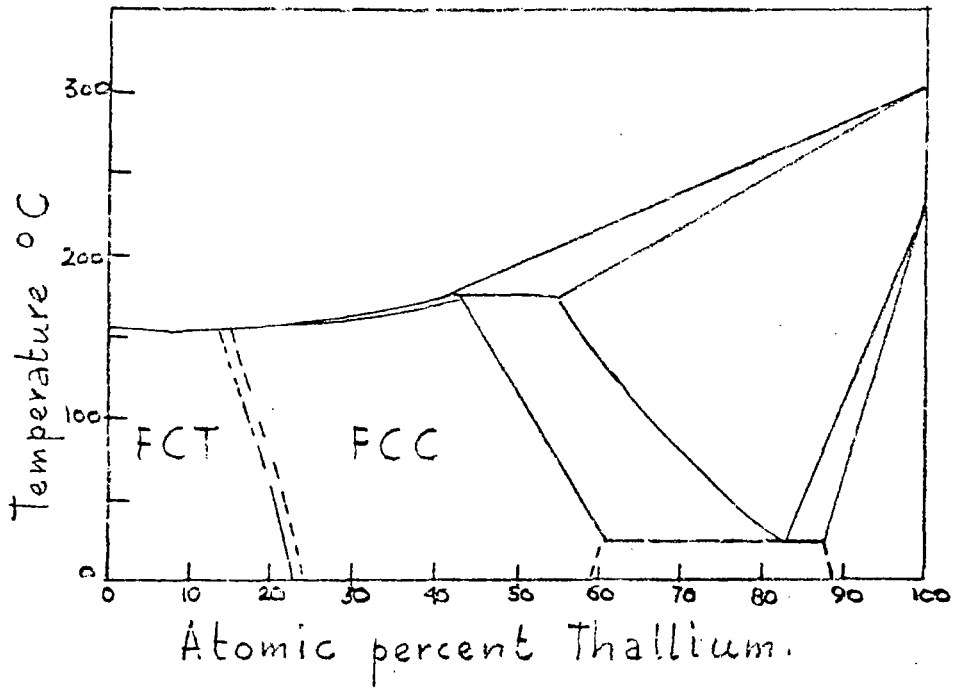

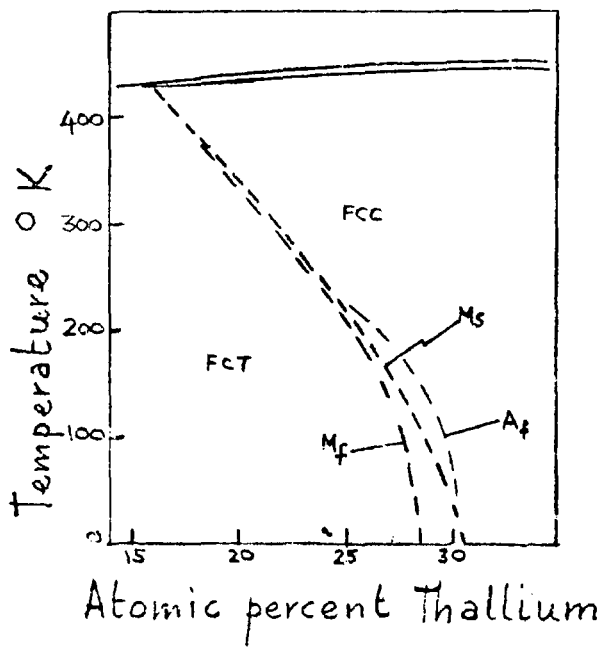

Figure (5.1) Phase diagram of the indium - thallium system after Novotny and Smith (1965) ; the enlarged fcc to fct region is after Pollock and King (1968)

the room temperature transition composition (22 at% thallium). In addition to the elastic data large anomalies are observed in the ultrasonic attenuation in the vicinity of the martensitic transition.

Before the present work is dealt with, previous pertinent studies of the indium-thallium system are reviewed.

5.1.1 Phase diagram of the indium-thallium system

The composition-temperature phase diagram at atmospheric pressure of the indium-thallium system (Figure (5.1)) is a composite of results reported by several workers (Valentiner 1940; Lipson and Stokes 1941; Guttman 1950; Meyerhoff and Smith 1963; Pollock and King 1968; Luo, Hagen and Merrian 1965; Stout and Guttman 1952). The region of interest here (the fcc to fct transformation) is shown enlarged (Pollock and King 1968) in Figure (5.1b). The apparent two phase region which is evident below about 200°K has been discussed at length by Pollock and King (1968); as the fcc to fct transformation proceeds by cooling some plastic deformation must occur in the as yet untransformed fcc matrix because of the stresses involved in maintaining the coherent interface between martensite (fct) and austentite (fcc). At transformation temperatures close to the melting point this plastic deformation should recover continuously; but the growth of existing

martensite in alloys with larger thallium content and thus lower transformation temperatures may be inhibited by the plastic deformation ahead of the interface: the temperature must be lowered to provide an additional driving force before the transformation can proceed by further growth. Thus it must be emphasised that the boundary lines between the fcc and fct structures are not to be regarded as equilibrium boundaries; the two phase region represents a metastable equilibrium between two phases of the same composition under conditions of varying temperature and pressure, that is the restraining effect of the untransformed region on the transformed region. The two phases have the same composition as a result of the diffusionless nature of the transition.

5.1.2 Crystallography of the cubic to tetragonal transformation

Visual observations of the cubic to tetragonal transition in indium-thallium alloys have been reported by several workers (Bowles, Barrett and Guttman 1950; Burkart and Read 1953; Pollock and King 1968). When a well annealed single crystal of the cubic phase transforms by slow cooling, the low temperature tetragonal phase consists of a banded twin aggregate formed by the passage of a single plane interface which traverses the specimen from one end to the other (Burkart and Read 1953). The plane of this interface

which is the habit plane, has been shown to be approximately a (110) plane of the cubic phase; anyone of the six different (110) planes could form the interface. Transformation by the passage of more than one interface can be observed if the specimen is bent, mishandled or subjected to violent transformation upon heating. The presence of twins in the tetragonal phase is a result of the structural difference between the two phases: it is not possible to have a coherent interface between two single crystals of these phases without severe strain over appreciable distances from the interface. However this misfit strain can be minimised if the tetragonal phase is twinned so that the sign of the strain changes from twin to twin. Bowles, Barrett and Guttman (1950) have analysed the transition in terms of a double shear mechanism: the observed (110) habit plane was taken as the plane of first shear; a second shear on another (110) plane at 60° to the plane of first shear was postulated; these two shears very nearly produce the observed tetragonal structure. More recently Wechsler, Lieberman and Read (1953) have shown, by using the concept of zero average interfacial strain between the two phases, that the shears actually occur on irrational planes 0.43° from the (110) planes.

Extrapolation of Novotny and Smith's (1965) elastic constant data of fcc alloys towards the indium rich region indicates the

TABLE (5.1)

Constant	Composition at % Tl.	A	B	Temperature Range °K
C_{44}	28·13	0·938±0·003	-0·35±0·18	277-300
	30·16	1·058±0·001	-0·69±0·04	273-330
	35·15	1·103±0·002	-0·78±0·05	204-300
	39·06	1·118±0·001	-0·83±0·03	193-301
$\frac{1}{2}(C_{11}-C_{12})$	28·13	0·0162±0·0002	+0·043±0·016	274-299
	30·16	0·0410±0·0001	-0·011±0·006	234-299
	35·15	0·0870±0·0003	-0·092±0·008	207-300
	39·06	0·1394±0·0003	-0·212±0·008	209-269
C_{11}	28·13	4·172±0·005	-0·55±0·12	206-298
	30·16	4·424±0·003	-1·17±0·07	203-361
	35·15	4·401±0·004	-1·10±0·09	203-297
	39·06	4·451±0·004	-1·25±0·10	198-347

Elastic moduli of fcc Indium-Thallium alloys (Novotny and Smith 1965): $C = A+10^{-3}BT$ with C in units of 10^{11} dynes cm^{-2} and T in °K.

At % thallium	0	10	16·5	18	21	25
Density gms/cm^3	7·28	7·66	7·87	7·87	7·97	8·40

Density of indium-thallium alloys determined by Archimedes method.

onset of instability of the fcc structure near the fcc-fct transformation. The elastic constant $(C_{11}-C_{12})/2$ reflects the instability strongly. Because these results will be frequently referred to in the present work, a summary of the values is presented in Table (5.1).

5.2 Relations between elastic wave velocities and elastic moduli in tetragonal crystals

Before the elastic wave velocities in tetragonal crystals can be used to determine the elastic moduli, it is essential to have a full understanding of the advantages and disadvantages of wave propagation in certain crystal directions as well as the usual elastic moduli - wave velocity relationships. Thus, in this section the most suitable procedure for the measurement of the elastic moduli of tetragonal crystals is developed.

Indium and its fct alloys with thallium exhibit 4/mmm symmetry which place them in the T I Laue group. The six independent elastic stiffness moduli required to describe their elastic behaviour are:

$$\begin{matrix} C_{11} & C_{12} & C_{13} & 0 & 0 & 0 \\ C_{12} & C_{11} & C_{13} & 0 & 0 & 0 \\ C_{13} & C_{13} & C_{33} & 0 & 0 & 0 \\ 0 & 0 & 0 & C_{44} & 0 & 0 \\ 0 & 0 & 0 & 0 & C_{44} & 0 \\ 0 & 0 & 0 & 0 & 0 & C_{66} \end{matrix} \qquad (5.1)$$

TABLE (5.2)

Propagation direction	Polarisation direction	Elastic constant equation = ρV^2
100	100	$C_{11} = \rho V_1^2$
100	010	$C_{66} = \rho V_2^2$
100	001	$C_{44} = \rho V_3^2$
001	001	$C_{33} = \rho V_4^2$
001	in x-y plane	$C_{44} = \rho V_5^2$
110	110	$(C_{11}+C_{12}+2C_{66})/2 = \rho V_6^2$
110	$1\bar{1}0$	$(C_{11}-C_{12})/2 = \rho V_7^2$
110	001	$C_{44} = \rho V_8^2$
On_2n_3	100	$n_2^2(C_{66}-C_{44})+C_{44} = \rho V_9^2$
On_2n_3	ϕ	$\frac{1}{2}[L_{22}+L_{33}+\{(L_{22}+L_{33})^2-4(L_{22}L_{33}-L_{23}^2)\}^{\frac{1}{2}}] = \rho V_{10}^2$
On_2n_3	$\phi+\pi/2$	$\frac{1}{2}[L_{22}+L_{33}-\{(L_{22}+L_{33})^2-4(L_{22}L_{33}-L_{23}^2)\}^{\frac{1}{2}}] = \rho V_{11}^2$

Relations between the elastic wave velocities and elastic stiffness constants for tetragonal (4/mmm) structures. (The angle ϕ is explained in the text as are the n's and L's).

The propagation and polarisation vectors of the sound waves are available from solutions of equation (2.23):

$$\begin{aligned}
(L_{11} - V^2)R_{01} + L_{12}R_{02} + L_{13}R_{03} &= 0 \\
L_{12}R_{01} + (L_{22} - V^2)R_{02} + L_{23}R_{03} &= 0 \qquad (5.2) \\
L_{13}R_{01} + L_{23}R_{03} + (L_{33} - V^2)R_{03} &= 0
\end{aligned}$$

where for the crystal symmetry of interest here

$$\begin{aligned}
L_{11} &= n_1^2 C_{11} + n_2^2 C_{66} + n_3^2 C_{44} \\
L_{12} &= n_1 n_2 (C_{12} + C_{66}) \\
L_{13} &= n_3 n_1 (C_{13} + C_{44}) \\
L_{22} &= n_1^2 C_{66} + n_2^2 C_{11} + n_3^2 C_{44} \\
L_{23} &= n_2 n_3 (C_{44} + C_{13}) \\
L_{33} &= n_1^2 C_{44} + n_2^2 C_{44} + n_3^2 C_{33}
\end{aligned}$$

For practical reasons it is convenient to perform sound velocity measurements in direction of high symmetry. Solutions of equation (5.2) for the [100], [001] and [110] directions are collected in Table (5.2). By substitution of these solutions in turn into equation (5.2), the particle displacement vectors associated with each mode can be determined; in each of these directions all three modes are pure modes (Table (5.2)). Further, as a result of

the symmetries exhibited along these directions, the energy flux associated with the transverse modes is parallel to the propagation direction (see (2.6)).

Examination of Table (5.2) shows that all the elastic moduli with the exception of C_{13} are available from velocity measurements in the pure directions [100], [001] and [110].

Inspection of equation (5.2) shows that C_{13} can be obtained from velocity measurements in any direction which does not require both n_1 and n_2 to be zero or n_3 to be zero. The most convenient directions which satisfy these requirements are those which lie in the $(1\bar{1}0)$ plane at any angle to the [110] direction except 0° and 90° and those which lie in the (100) plane at any angle to the [010] direction except 0° and 90°. All directions in the $(1\bar{1}0)$ plane which might be used for determination of C_{13} are impure except for one which is pure. Knowledge of all the elastic moduli is required to calculate the direction cosines of this pure mode: Brugger (1965) gives these as

$$n_1=n_2=\frac{(C_{33}-2C_{44}-C_{13})^{\frac{1}{2}}}{(2(C_{11}-2C_{44}-C_{13})-(C_{11}-2C_{66}-C_{12})+2(C_{33}-2C_{44}-C_{13})^{\frac{1}{2}})} \qquad (5.3)$$

$$\text{and} \quad n_3=\frac{(2(C_{11}-2C_{44}-C_{13})-(C_{11}-2C_{66}-C_{12}))^{\frac{1}{2}}}{(2(C_{11}-2C_{44}-C_{13})-(C_{11}-2C_{66}-C_{12})+2(C_{33}-2C_{44}-C_{13})^{\frac{1}{2}})} \qquad (5.4)$$

In a cubic crystal this pure direction is the [111]. A choice of the [111] direction for the tetragonal case could perhaps

be useful for a first approximate determination of C_{13}. To obtain the three wave velocities in an arbitary direction in the $(1\bar{1}0)$ plane, the solutions of a cubic equation in ρV^2 are required. For such a direction ($n_1=n_2=\frac{1}{\sqrt{2}}\cos\theta$, $n_3=\sin\theta$, where θ is the angle the propagation direction makes with the [110] direction) the determinental equation (2.23) becomes

$$\rho^3V^6-A\rho^2V^4 + B\rho V^2 + C = 0 \qquad (5.5)$$

where

$$A = 2L_{11} + L_{33}$$

$$B = L_{11}^2 + 2L_{11}L_{33}-2L_{13}^2-L_{12}^2$$

$$C = -[L_{11}(L_{11}L_{33}-2L_{13}^2)-L_{12}(L_{12}L_{33}-2L_{13}^2)]$$

But since directions in the $(1\bar{1}0)$ plane are impure, it is impossible to know in advance whether one predominately longitudinal and two predominately transverse waves can be excited. Another unknown factor is the behaviour of the energy flux vector.

However from an experimental viewpoint it is more profitable to consider wave propagation in the (100) plane. All directions from which C_{13} is available in this plane are quasi-pure except one which is pure. Again knowledge of the elastic moduli is required to determine this pure mode direction. The advantage of

(100) plane propagation is that an arbitary quasi-pure direction may be chosen for velocity measurements from which an initial determination of the elastic constant set may be completed. Use of this preliminary moduli set allows the pure mode direction to be closely estimated. The velocities of the three possible elastic waves in the $[0, n_2, n_3]$ direction are obtained from (5.2) as

$$\rho V^2 = n_2^2(C_{66}-C_{44}) + C_{44} \tag{5.6}$$

and

$$2\rho V^2 = L_{22}+L_{33} \pm ((L_{22}+L_{33})^2-4(L_{22}L_{33}-L_{23}^2))^{\frac{1}{2}} \tag{5.7}$$

Equation (5.6) gives the velocity of a pure transverse wave polarised along the [100] direction and equation (5.7) the velocities of the quasi-longitudinal (+ve sign) and quasi-transverse (-ve sign). The particle displacement vector for the quasi-longitudinal wave is obtained from substitution of equation (5.7) into equation (5.2) whence

$$\frac{R_{03}}{R_{02}} = -\frac{(L_{22}-\rho V^2)}{L_{23}} \tag{5.8}$$

Thus ϕ $(= \tan^{-1}(R_{03}/R_{02}))$ is the angle the particle motion direction makes with the [010] direction for the quasi-longitudinal wave; that for the quasi-transverse is $\phi+\pi/2$. The pure mode

occurs when

$$\phi = \cos^{-1}(n_2) \qquad (5.9)$$

5.3 Experimental Procedure

The choice of alloy composition was influenced by the existence of previous elastic constant measurements (Novotny and Smith 1965) of cubic alloys of the indium-thallium system. To allow the determination of all the elastic moduli of a tetragonal alloy, the composition 10 at.% thallium was chosen because it is almost as close to the phase boundary as the phase diagram allows without the restricting effect of banded twins: this alloy never suffers transformation with temperature. A direct comparison of its elastic properties with those of indium is possible. A 25 at.% thallium alloy was also grown and thus elastic moduli were obtained close to the phase boundary in the cubic phase. Samples of other compositions, namely 16·5, 18 and 21 at.% thallium alloys were also prepared. These particular alloys are twinned at room temperature and velocity measurements had to be treated with caution.

5.3.1 Crystal growth and sample preparation

The specimens were prepared from 99·999% purity indium and thallium by a modified Bridgman technique. The material, placed inside an evacuated quartz growth tube, was lowered through a

stationary temperature gradient produced in a vertical furnace. The indium was weighed first and put immediately into the pre-cleaned quartz growth tube (see Figure (5.3)) which was then evacuated. Special precautions were needed with thallium which oxidizes rapidly in air. The thallium was first weighed roughly and then etched to remove the oxidized layer by successive washings in dilute nitric acid and distilled water. Accurate weighing was completed while the thallium was immersed in distilled water and then the material put into the growth tube which was again immediately evacuated. After the tube had been sealed the indium and thallium were melted and thoroughly mixed. The furnace, shown in Figure (5.2), has three windings whose resistance may be varied to obtain the temperature gradient (Figure (5.3)) which experience showed gave satisfactory crystal growth. The current through the windings and thus the stability of the temperature gradient was controlled by a solid state potentiometric device. The growth tube was placed on top of a stainless steel rod and lowered through the temperature gradient at a slow constant rate (0.7 mm per hour) by an electric motor coupled to a gear system. The problem of removing the crystal from the tube without damage was overcome most satisfactorily by dissolving the growth tube completely in hydrofluoric acid; the boule was also attacked but only very slowly.

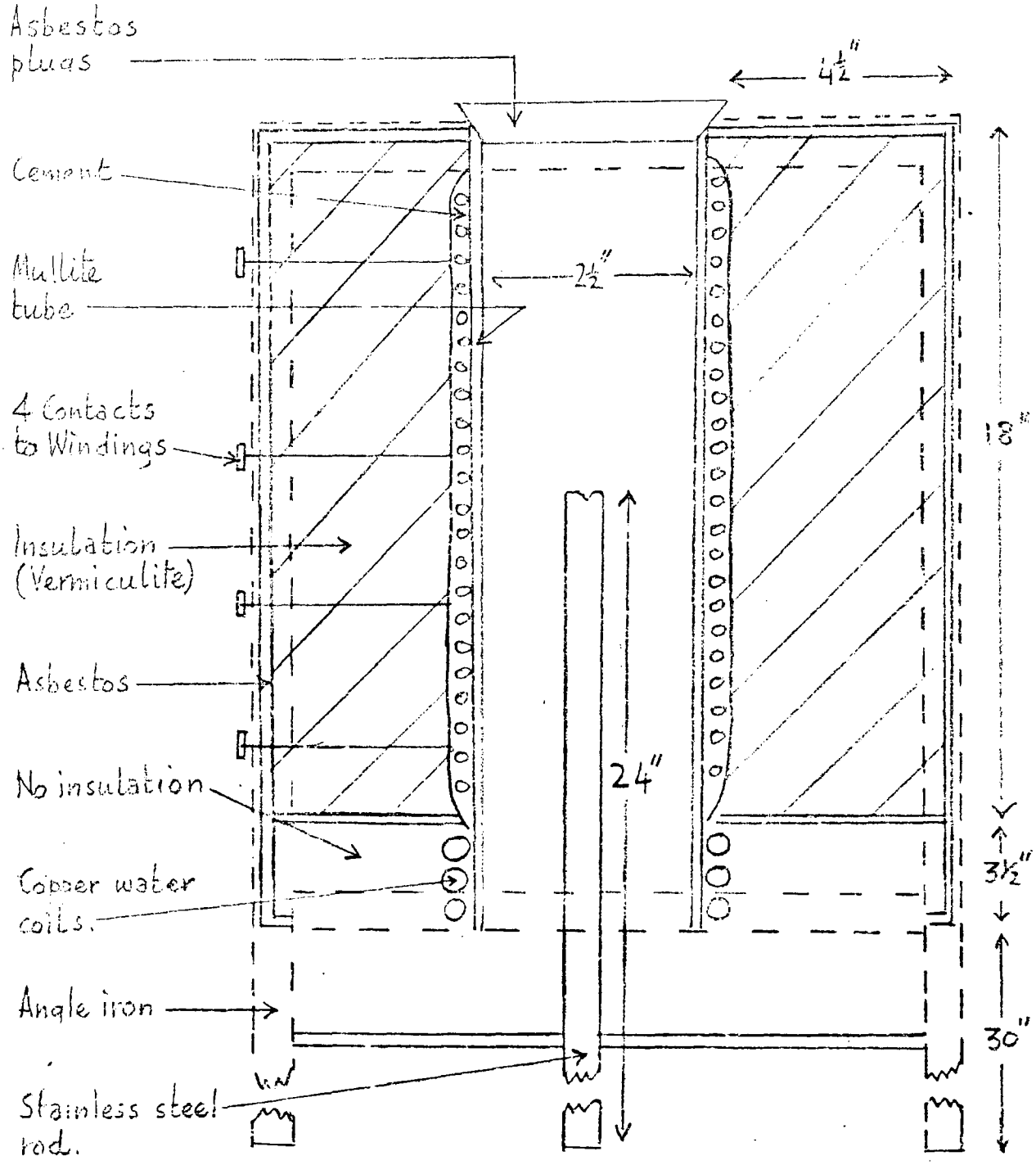

Figure (5.2) The furnace used for growth of indium - thallium alloys.

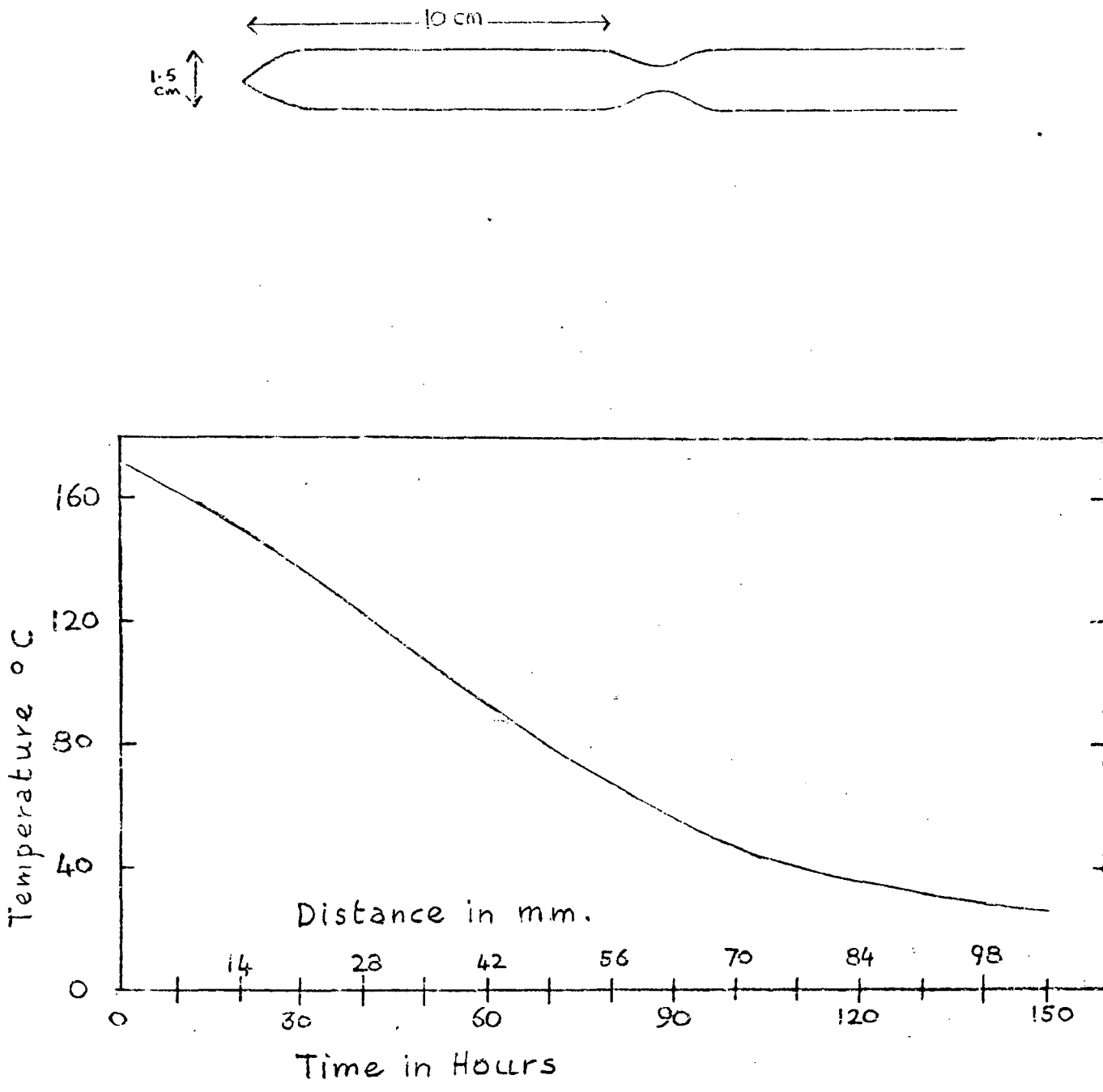

Figure (5.3) The growth tube and temperature gradient used in the growth of indium - thallium alloys.

The samples were then lightly etched in dilute nitric acid and washed in distilled water. There was no tendency for the crystals to oxidise in air.

X-ray back reflection Laue photography of the single crystal samples and the twinned samples differed in that while the former evidenced good crystal perfection the latter showed a break up of the Laue spots. Figure (5.4a) shows a Laue photograph taken down the fourfold axis, that is the [001] direction in the (tetragonal) 10 at.% thallium alloy which does not exhibit twinning. Although the Laue spots on photographs of twinned compositions (16.5, 18 and 21 at.% thallium) were split, the same Laue photographs were obtained at different points along the samples indicating that the transformation had ensued probably by passage of a single interface: Figure (5.4b) is a Laue photograph of a twinned alloy.

The 4/mmm symmetry (see Figure (5.5)) of the tetragonal alloys introduces the problem of distinguishing between the two twofold symmetry axes which occur along the <100> and along the <110> direction forms. This can be resolved by reference to the fact that these tetragonal alloys are close to being cubic: the c/a ratio for alloys from pure indium to the phase boundary (22 at.% thallium at room temperature) varies from the small value of 1.08 to unity. As cubic crystals exhibit threefold rotational symmetry

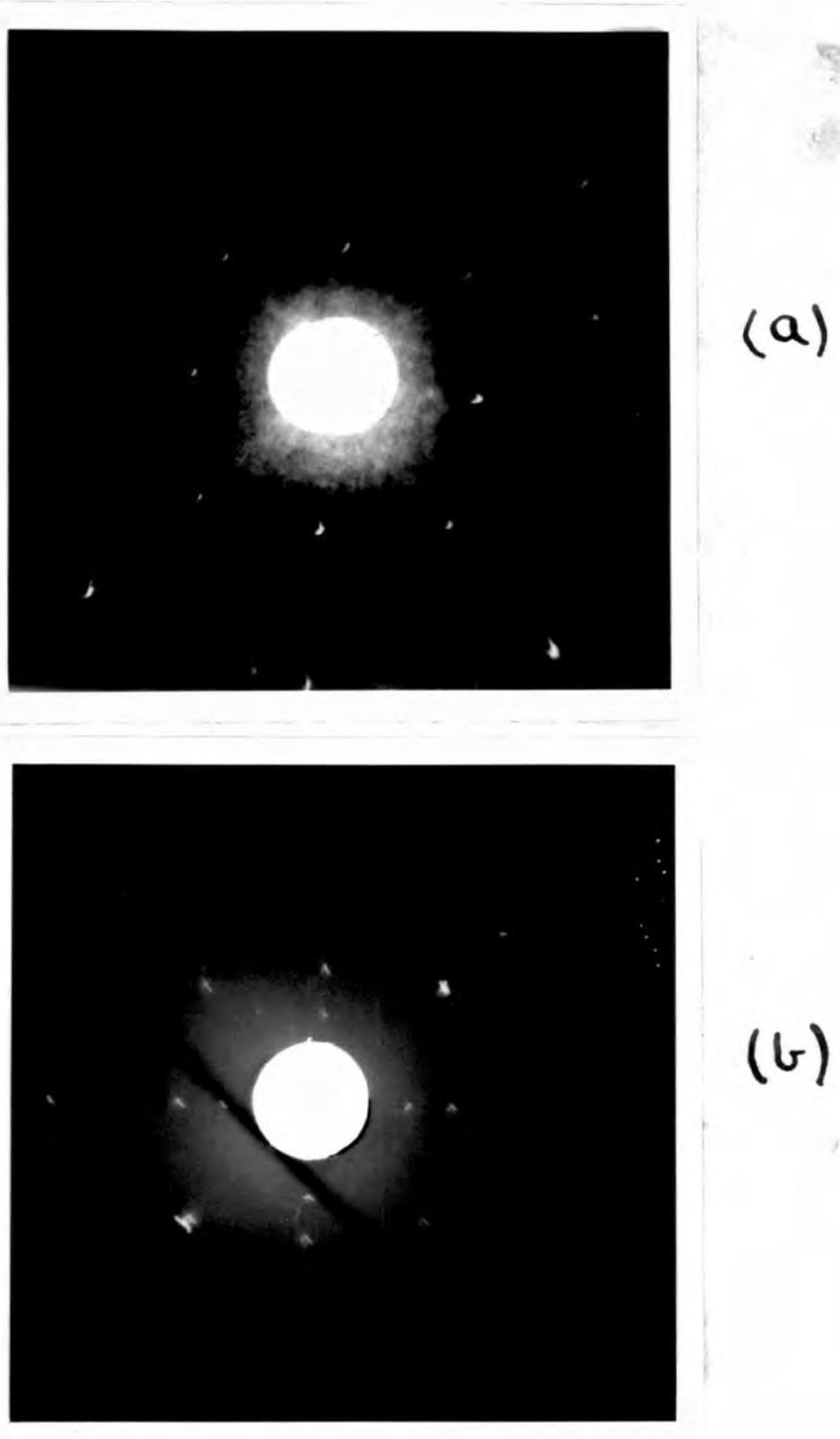

Figure (5.4) Laue back reflection X-ray photographs of tetragonal indium-thallium alloys : (a) single crystal ; (b) twinned sample.

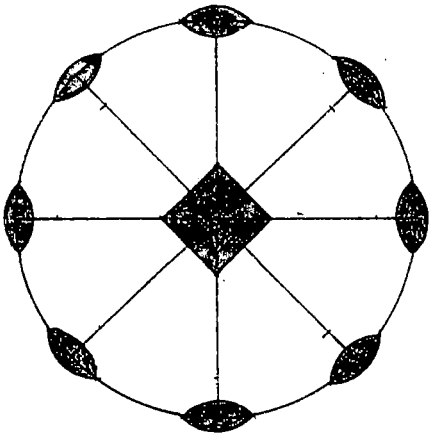

Figure (5.5) Symmetry of (4/mmm) tetragonal crystals.

in the <111> direction forms, then in these nearly cubic alloys a pseudo-threefold symmetry axis is readily distinguishable on X-ray Laue photographs in the <111> tetragonal direction forms. Thus the procedure adopted was first to locate the fourfold symmetry axis and the two different twofold symmetry axes: a rotation from a twofold towards a fourfold axis passes through a pseudo-threefold axis if that twofold axis was a [110] direction. The aligned samples were cut out by the spark cutter (see (3.5) for details).

5.3.2 Elastic wave velocity measurements

The details of transducer-specimen coupling have been described in (3.5) and the errors associated in general with ultrasonic velocity measurements by the pulse echo method in (3.7.5). Errors in velocity measurements peculiar to indium-thallium specimens are detailed below. The sample holder used here has been described in (3.8) as have the oil bath (3.9.1) for measurements above room temperature and the cryostat (3.9.2) for those below room temperature. Wave velocity measurements in each alloy composition will now be described in turn.

5.3.2.1 Velocity measurements in indium-10 at.% thallium

All the elastic stiffness moduli of this tetragonal crystal were measured. The equations relating the wave velocities to the

six independent moduli have been developed in (5.2): Table (5.2) gives the propagation and polarisation directions which were used. Velocity measurements in the (100) plane are the most favourable from a practical point of view for obtaining C_{13}. After all the velocities required, except those in the (100) plane, had been measured an experimental extrapolation procedure was employed for the accurate determination of the elastic moduli in general and C_{13} in particular: the three velocities in the direction $[0, \cos 14{\cdot}5^{\circ}, \sin 14{\cdot}5^{\circ}]$ were measured. Then using the six elastic moduli obtained, the direction in the (100) plane, which in addition to the [010] and [001], is a pure direction was calculated and found to be $[0, \cos 50^{\circ}, \sin 50^{\circ}]$. A further three wave velocities were measured in this direction with the advantage that the energy flux associated with the longitudinal wave would be almost parallel to the propagation direction (see (2.6) and (5.2)); even if this initial determination of the pure mode direction was exact the energy flux associated with the two pure transverse waves would not coincide with the propagation direction. Thirteen velocities (see Table (5.2)) were measured from room temperature to $-170^{\circ}C$. The transducers were bonded successfully to the sample over this range with silicone fluids (see (3.6.1)). The experimental velocities obtained are given at selected temperatures in Table (5.3).

TABLE (5.3)

		300°K	246°K	218°K	186°K	149°K	104°K
Experimental velocity x 10^5 cm sec^{-1}	V_1	2·40	2·43	2·45	2·48	2·49	2·59
	V_2	1·23	1·26	1·29	1·32	1·35	1·39
	V_3	0·957	0·966	0·973	0·984	0·996	1·01
	V_4	2·38	2·41	2·44	2·47	2·49	2·50
	V_5	0·953	0·956	0·962	0·970	0·981	1·00
	V_6	2·52	2·53	2·56	2·57	2·58	2·58
	V_7	0·453	0·493	0·533	0·588	0·650	0·735
	V_9	1·14	1·14	1·15	1·15	1·16	1·17
	V_{10}	2·38	2·41	2·44	2·48	2·51	2·53
	V_{11}	0·870	0·887	0·913	0·937	0·961	0·979
	V'_9	1·10	1·12	1·13	1·15	1·17	1·20
	V'_{10}	2·51	2·53	2·55	2·56	2·57	2·57
	V'_{11}	0·460	0·495	0·536	0·582	0·642	0·710
Experimental modulus x 10^{11} dynes cm^{-2}	ρV_1^2	4·40	4·51	4·60	4·72	4·73	4·84
	ρV_2^2	1·16	1·22	1·28	1·33	1·40	1·47
	ρV_3^2	0·705	0·715	0·725	0·745	0·760	0·780
	ρV_4^2	4·34	4·46	4·56	4·68	4·75	4·78
	ρV_5^2	0·70	0·703	0·710	0·721	0·737	0·767
	ρV_6^2	4·84	4·92	5·01	5·06	5·10	5·10
	ρV_7^2	0·157	0·186	0·218	0·264	0·324	0·414
	ρV_9^2	0·987	1·00	1·01	1·02	1·03	1·04
	ρV_{10}^2	4·35	4·45	4·58	4·70	4·82	4·92
	ρV_{11}^2	0·580	0·600	0·640	0·672	0·710	0·735
	$\rho (V'_9)^2$	0·925	0·958	0·985	1·02	1·06	1·10
	$\rho (V'_{10})^2$	4·83	4·91	4·99	5·01	5·05	5·05
	$\rho (V'_{11})^2$	0·162	0·188	0·222	0·260	0·317	0·386

The experimental velocities of elastic waves in indium-10 at.% thallium. The velocities V_9, V_{10}, V_{11} correspond to a propagation direction [0, cos 14·5°, cos 75·5°] and V'_9, V'_{10}, V'_{11} to a propagation direction [0, cos 50°, cos 40°]

Figure (5.6) Elastic moduli of indium - 10 at% thallium.

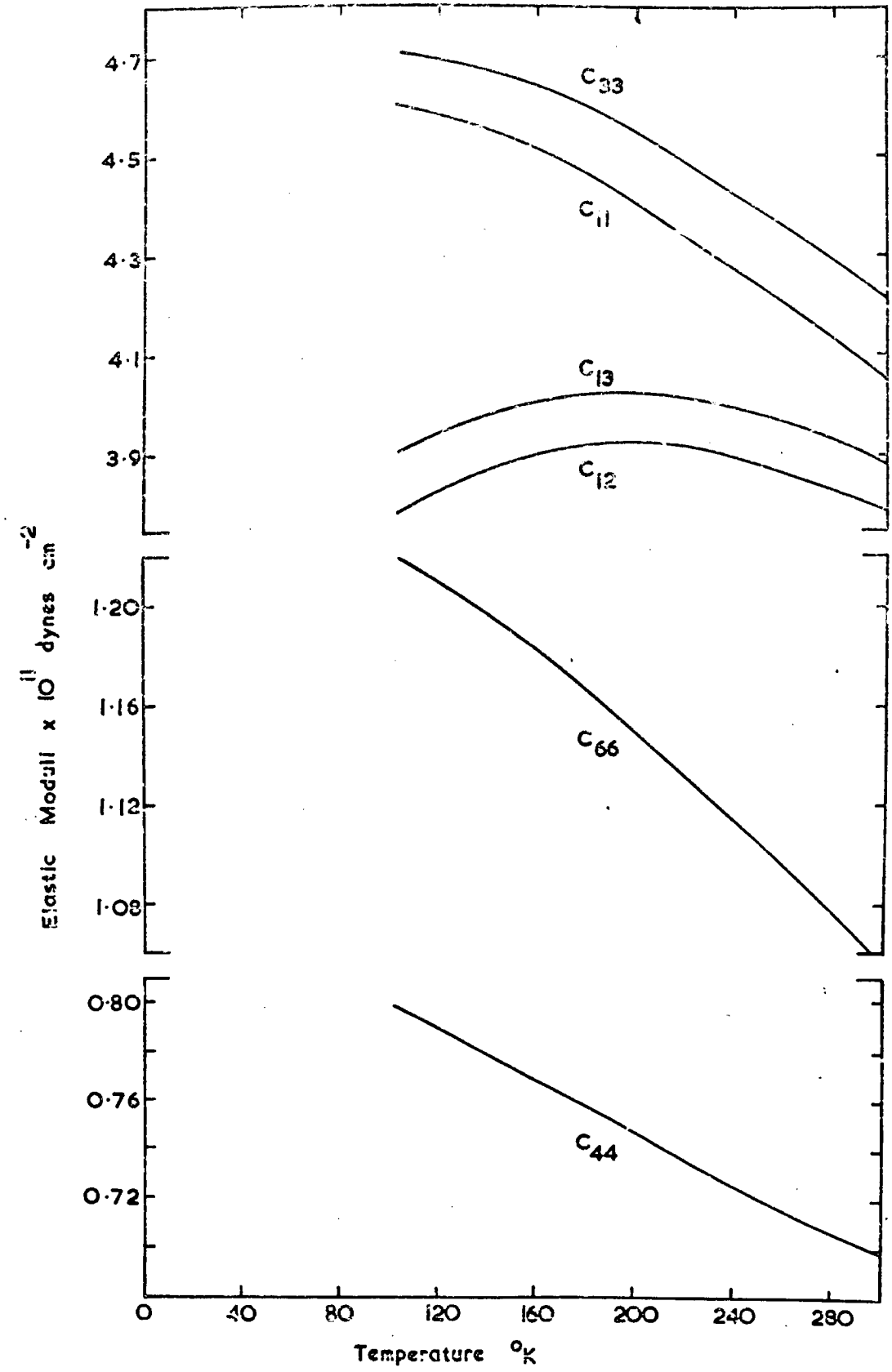

The six elastic moduli may be found from the thirteen equations but an exact solution will not exist because of experimental errors, which in the case of this alloy were no larger than the normally expected errors in pulse-echo measurements; see (3.8). A least-mean squares computer fit was obtained using a programme developed by Jeavons (1969). The basic idea may be seen by considering the overdetermined case of three equations in two unknowns:

$$A = f_1(x,y); \quad B = f_2(x,y); \quad C = f_3(x,y)$$

Define $$M = [(f_1-A)^2 + (f_2-B)^2 + (f_3-C)^2] \qquad (5.10)$$

If all three equations are exact, x and y exist such that

$$f_1-A = f_2-B = f_3-C = 0 \qquad (5.11)$$

and therefore M=0. If the equations are approximate, then the best values of x and y may be found by minimising M. This procedure is easily extended to thirteen equations in six unknowns. Further details of this programme are given by Jeavons (1969).

The six moduli obtained by the least-mean squares computer fit are given in Table (5.4) at 273°K and are plotted as a function of temperature in Figure (5.6). The errors in the velocity measurements (see (3.8)) will produce errors in the moduli which are greater for some moduli than for others. With the exception of C_{12} and C_{13} all the moduli are related directly to a velocity measurement:

TABLE (5.4)

	C_{11}	C_{12}	C_{13}	C_{33}	C_{44}	C_{66}	Error in moduli
Indium (a) (Room Temp.)	4.44	3.94	4.04	4.43	0.653	1.22	
Indium (b) (300° K)	4.535	4.006	4.151	4.515	0.651	1.207	
Indium (c) (300° K)	4.520	4.004	4.191	4.512	0.650	1.207	±1%
Indium-10 at.% thallium (d) (273°K)	4.160	3.847	3.941	4.299	0.709	1.078	±2%
Indium-25 at.% thallium (d) (273°K)	4.005	3.958	3.958	4.005	0.808	0.808	±2%

Units are 10^{11} dynes cm^{-2}

(a) Winder and Smith (1958)

(b) Chandrasekar and Rayne (1961)

(c) Re-calculated values of (b) - see text

(d) This work.

Single crystal elastic stiffness constants of indium, indium-10 at.% thallium and indium-25 at.% thallium.

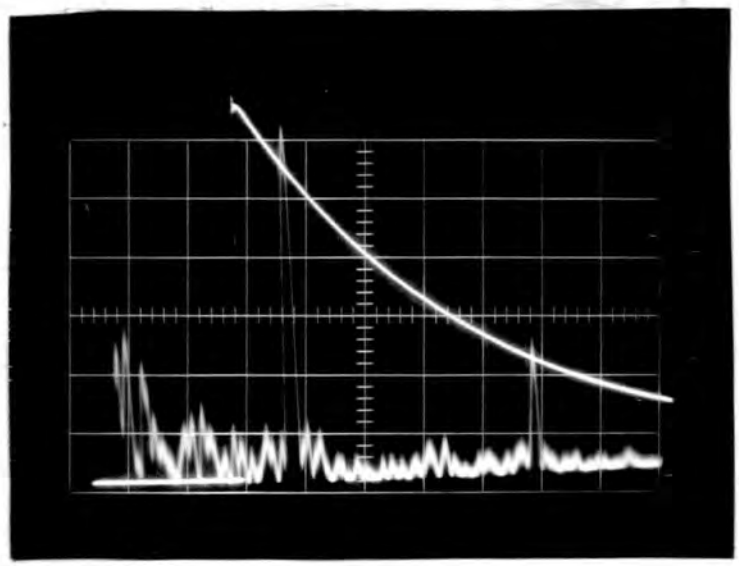

Figure (5.7) Typical echo display for $[1\bar{1}0]$ $(1\bar{1}0)$ sound waves in indium-thallium samples : the echo separation shown is approximately 75 microseconds.

errors for these moduli will be double that in the velocity. C_{12} and C_{13} are indirectly related to two and four measured velocities respectively; errors in these may be slightly greater than those in the other moduli.

5.3.2.2 Velocity measurements in indium-25 at.% thallium

The moduli C_{11}, C_{12} and C_{44} of this cubic alloy were obtained from measurement of the three pure wave velocities along the [110] direction (see (2.5.2)). Difficulty was found in obtaining echoes for the slow shear wave polarised along the $[1\bar{1}0]$ direction; this velocity is given by $\rho V^2 = \frac{1}{2}(C_{11}-C_{12})$. Because this composition at room temperature is close to the fcc to fct boundary $(C_{11}-C_{12})/2$ is small and thus this wave velocity is slow; in fact the time between echoes for a sample of length 0.628 cm was 75μs. at room temperature and only two echoes were visible on the oscilloscope. The Y-cut transducer polarisation needed to be accurately oriented along the $[1\bar{1}0]$ direction in order to excite and receive this mode. The room temperature velocities and elastic moduli are collected in Table (5.4).

5.3.2.3 Velocity measurements in alloys containing 16.5, 18 and 21 at.% thallium

All these alloys are twinned tetragonal at room temperature. If the split spots on Laue X-ray photographs were ignored, these

samples could be rotated from one symmetry axis to another as if they were single crystals. With this reservation, the twinned samples were prepared for sound propagation along "[110]" direction.

As in the 25 at.% thallium alloy the slow shear wave velocity was so small that only two echoes could be obtained. Any reduction in the normal 1% error in transit time measurements in this case due to the very large values of the transit time were overshadowed both by the small amplitude of the second echo as a result of the large decibel loss per double transit time and the received pulse spread (see Figure (5.7)). In both the 18 and 21 at. % thallium alloys the slow shear velocity could only be measured in a limited temperature range: as the temperature approached that of the transition the separation between the two echoes visibly altered, the decibel loss per double transit time also increased markedly until the second echo was not longer measurable.

An investigation of the thermal expansion of indium-thallium alloys along the [110] direction in the vicinity of the transition has been reported by Pahlman and Smith (1968); large increases in the coefficient of linear expansion were found. In the present case the thermal expansion of the 21 at.% thallium alloy was measured using the dilatometer technique described in (4.2.3). Figure (5.8) shows the results along the "[110]" direction. Although

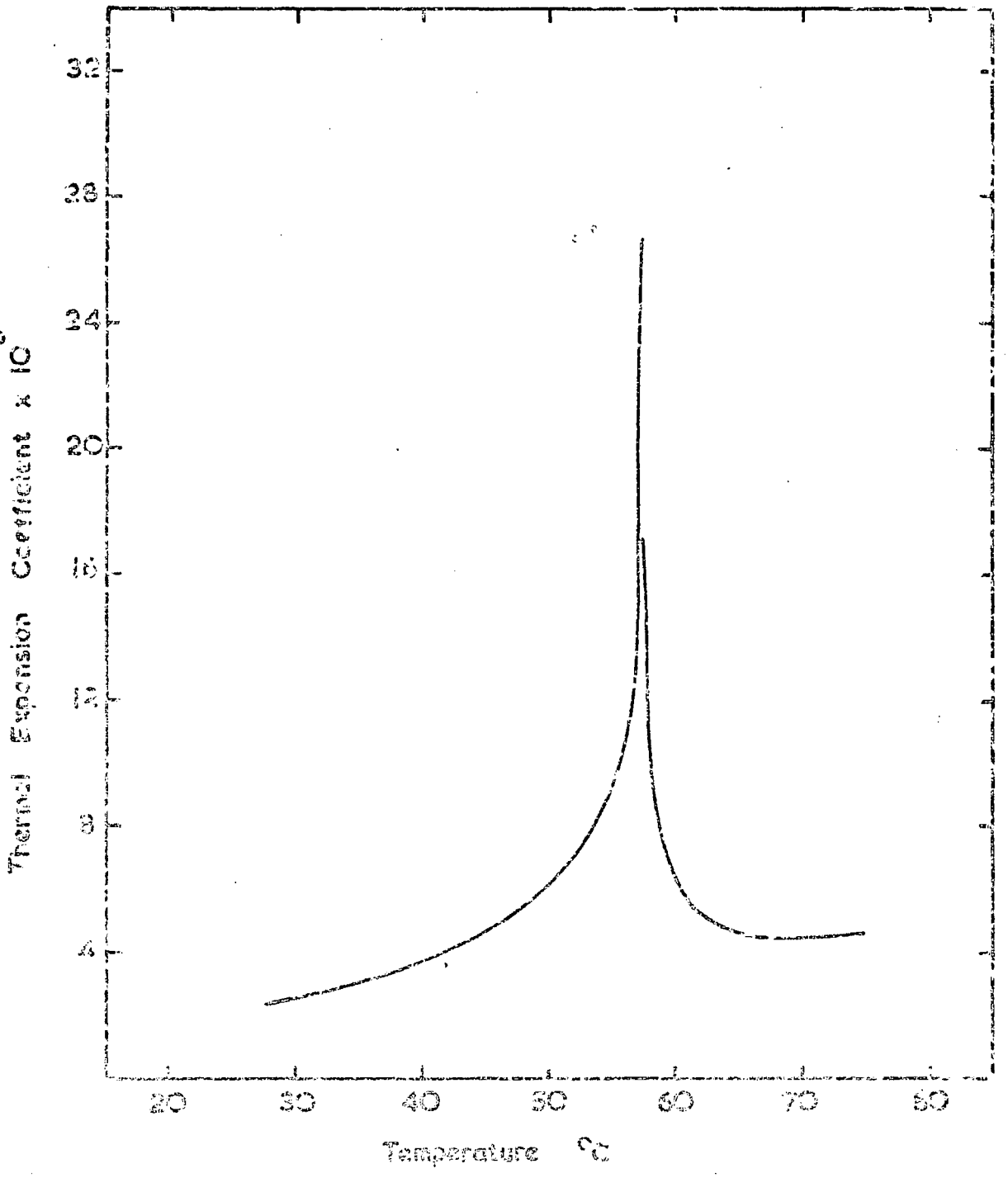

Figure (5.8) Thermal Expansion coefficient of indium-21 at.% thallium.

the coefficient passes through a large maximum at the transition, the maximum apparent change in the velocity which results from neglecting the change in length of the sample is less than 0•2% well within the uncertainty in the transit time measurements: no corrections need be made.

Thus although the error in the measured moduli of these particular alloys is about ±2%, that involved in identifying these moduli with those characteristic of the [110] direction of the tetragonal crystal is more uncertain. The velocity of a sound wave which is propagated normal to the twin plane is the same as it would be in a single crystal. In the present case the twin plane is a (110) plane of the cubic phase: the three sound velocities measured in the "[110]" twinned tetragonal direction will be closely related to the moduli $\frac{1}{2}(C_{11}+C_{12}+2C_{66})$, C_{44} and $(C_{11}-C_{12})/2$ respectively.

The moduli corresponding to the three wave velocities in the "[110]" direction of the 18 and 21 at.% thallium alloys are shown as a function of temperature in Figures (5.9) and (5.10). The most interesting fact is the complete lack of temperature dependence of the longitudinal modulus for both alloys. In contrast the moduli corresponding to the fast shear velocities in both alloys exhibit anomalies at temperatures close to the fct to fcc transition.

Figure (5.9) The three measured velocities, converted to moduli in the "[110] " direction of indium - 18 at.% thallium as a function of temperature.

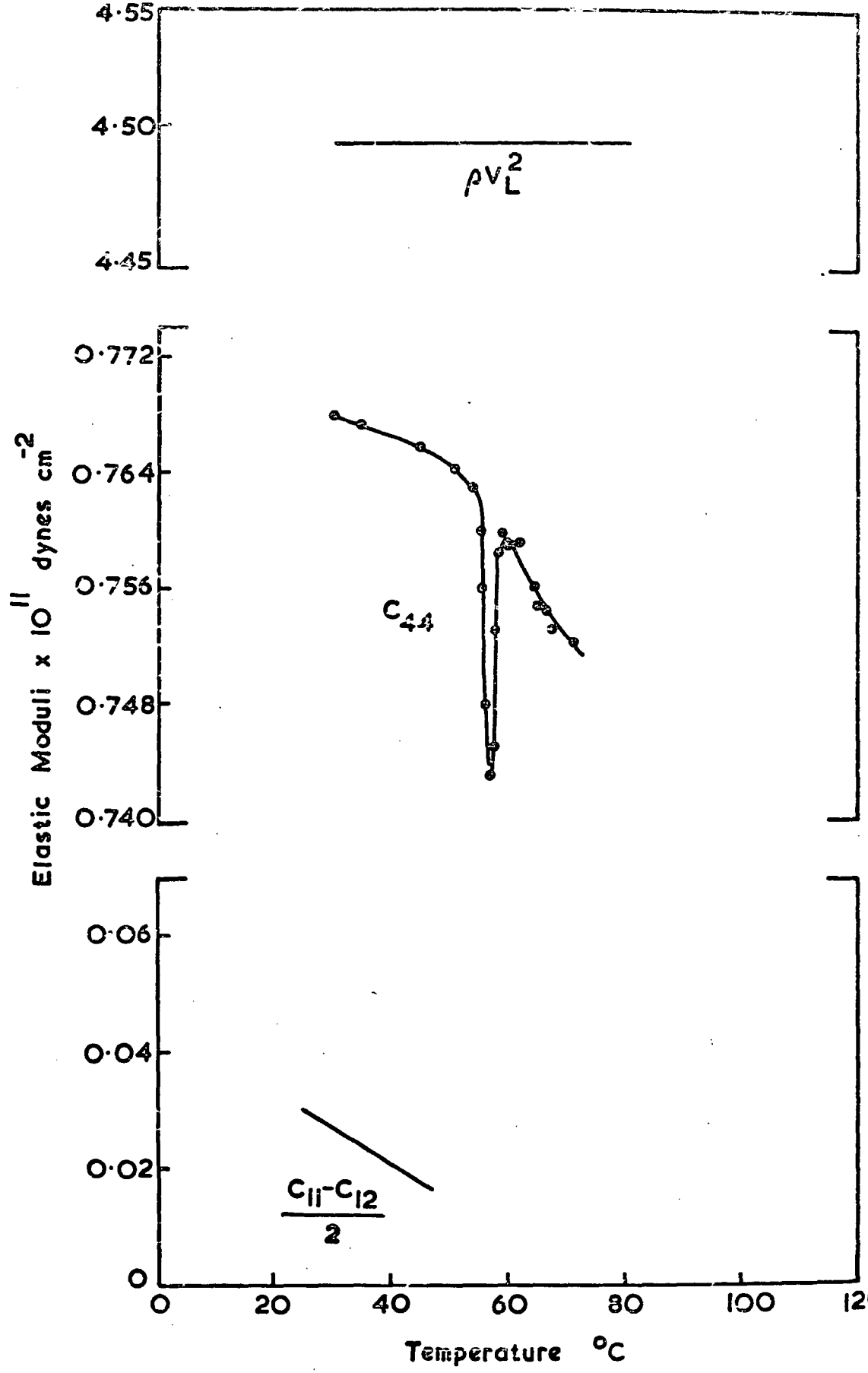

Figure (5.10) Temperature dependence of the three moduli in the "[110]" direction of a 21 at % thallium alloy.

The modulus corresponding to the slow shear velocity approaches very close to zero in both alloys as the temperature approaches that of the transition. This modulus is effectively equal to $(C_{11}-C_{12})/2$. In crystals of tetragonal symmetry (see (2.4)) $(C_{11}-C_{12})/2$ must be positive; a negative value results in a spontaneous collapse of the lattice. The transformation mechanism involves shears on approximately (110) planes in $[1\bar{1}0]$ directions and these are the shears specifically associated with the modulus $\frac{1}{2}(C_{11}-C_{12})$. A similar approach of this modulus to zero occurs in the fcc 28.13 at.% thallium alloy (Novotny and Smith 1965); the temperature coefficient in the cubic phase is positive near the phase boundary.

5.3.3 Ultrasonic attenuation measurements

The ultrasonic attenuation was measured primarily in the region of the fcc to fct phase change. Figures (5.11), (5.12) and (5.13) show the attenuation as a function of temperature and frequency of both longitudinal and fast shear waves in a 21 at.% thallium sample. The attenuation of the slow shear wave along the "[110]" direction in the vicinity of the transition could not be measured. This was not primarily because the decibel loss per unit time was too high but rather because the decibel loss per transit time was anomalously large (see (5.3.2.3)). The errors associated with attenuation

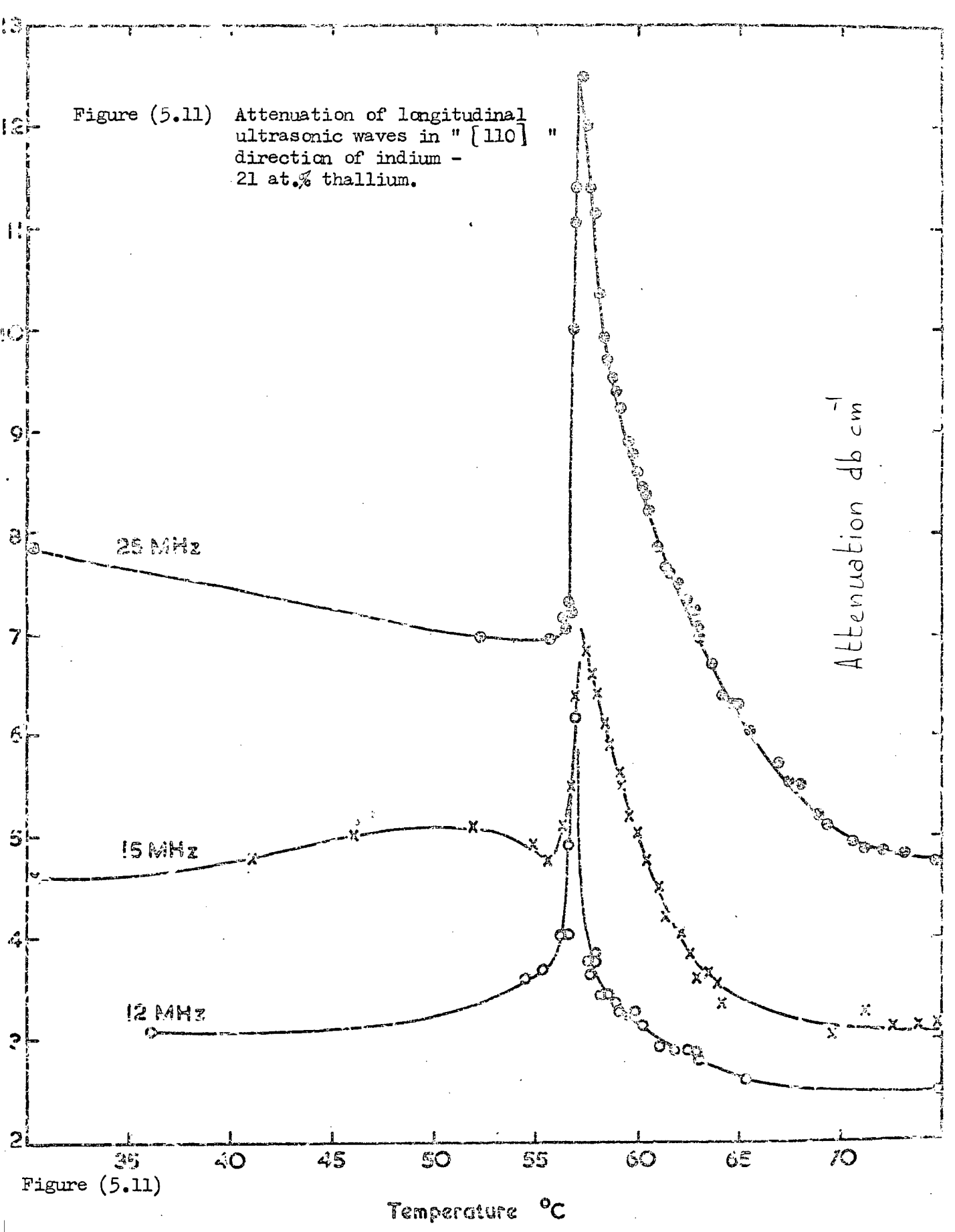

Figure (5.11) Attenuation of longitudinal ultrasonic waves in " [110] " direction of indium - 21 at.% thallium.

Figure (5.11)

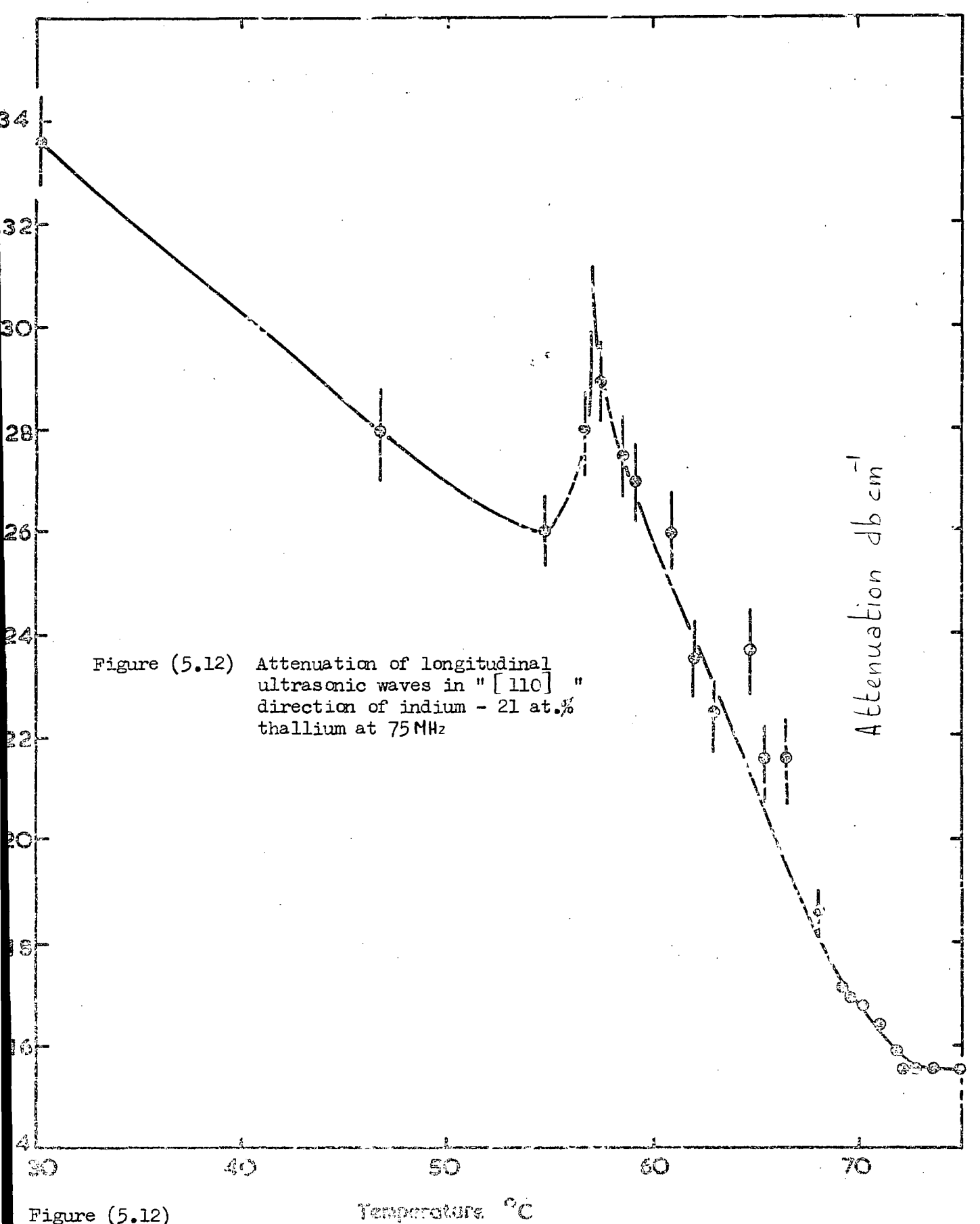

Figure (5.12) Attenuation of longitudinal ultrasonic waves in "[110]" direction of indium - 21 at.% thallium at 75 MHz

Figure (5.12)

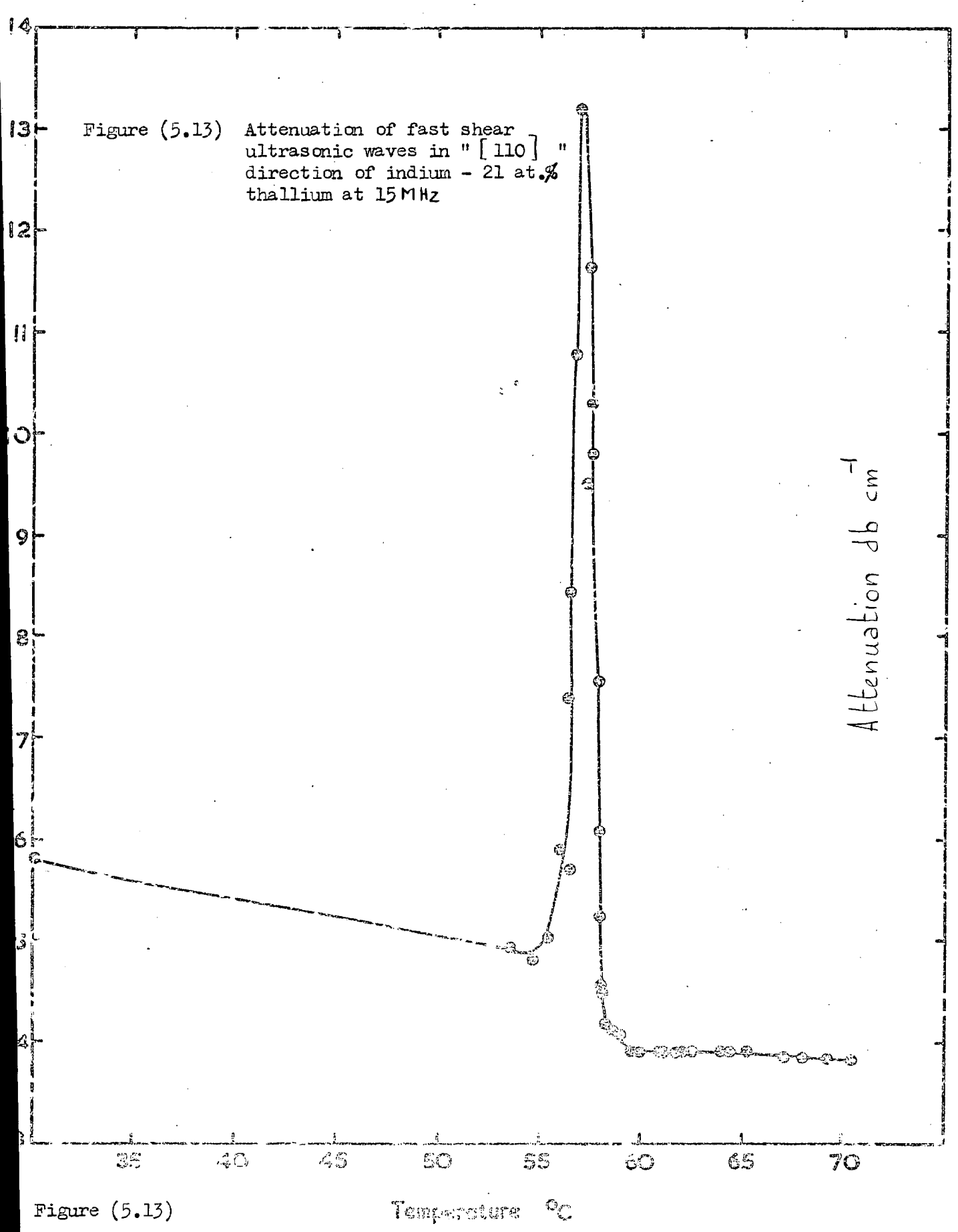
Figure (5.13) Attenuation of fast shear ultrasonic waves in " [110] " direction of indium - 21 at.% thallium at 15 MHz
Attenuation db cm⁻¹
Temperature °C
14
13
12
11
10
9
8
7
6
5
4
35
40
45
50
55
60
65
70

Figure (5.13)

measurements have been discussed elsewhere (see (3.7) and (4.4)). The diffraction loss is readily subtracted and knowledge of transducer coupling losses can be obtained from measurements on several samples of different lengths. As the sample was aligned and cut in the twinned tetragonal condition, a further loss of energy from the ultrasonic beam in the tetragonal phase results from mode conversion at the twin boundaries. In general six waves are generated by a single elastic wave incident on a solid-solid interface, one quasi-longitudinal and two quasi-transverse modes on either side of the boundary. At certain angles of incidence various surface waves may also be propagated along the interface itself (Musgrave 1959). The echoes picked up by the transducer correspond to waves of the same polarization as that initially generated by the transducer: energy is thus lost from the ultrasonic beam. The large anomalous attenuation near the transition which is the particular interest here will thus be superimposed upon a background attenuation arising from the several causes mentioned above, as well as from the background intrinsic material losses. Among these are frequency squared dependent terms which are due to the thermoelastic and phonon viscosity losses neither of which are negligible in metals. The thermoelastic loss (see (4.4)) is given by (Lucke 1956):

$$\alpha = \frac{1}{2}\frac{\Delta M}{M}\frac{\omega^2\tau}{1+\omega^2\tau^2} \qquad \text{Np./}\mu\text{s} \qquad (5.12)$$

where $\Delta M/M$ is the fractional change of the adiabatic and isothermal elastic moduli

$$\frac{\Delta M}{M} = \frac{M_{ad}-M_T}{M_T} \qquad (5.13)$$

and is for a cubic crystal given by

$$\frac{\Delta M}{M} = \frac{2(C_{11}+2C_{12})^2 a^2 T}{(C_{11}+C_{12}+2C_{44})\ C_p} \qquad (5.14)$$

in the [110] direction; a is the thermal expansion coefficient. In the megahertz frequency range the product of the frequency and relaxation time τ is much less than unity and the thermoelastic loss reduces to

$$\alpha = \frac{8.68}{2}\frac{\Delta M}{M}\omega^2\tau \quad \text{db/}\mu\text{s} \qquad (5.15)$$

The specific heat is estimated from the Dulong and Petit law to be 1.8×10^7 ergs deg^{-1} cm^{-3} and the relaxation time is given by $\tau = 3K/\ C_p V^2$ where K is the thermal conductivity and is estimated, by assuming the Wiedmann and Franz law to be 0.4 watts cm^{-1} deg^{-1} at 70°C. The relaxation time turns out to be 0.7×10^{-11} secs and

TABLE (5.5)

	τ x 10^{11} secs	$\left(\frac{\Delta M}{M}\right)_{110}$ x 10^{-2}	α/f^2 x 10^{-16}
Al	0•227	3•37	0•122
Cu	0•526	3•17	0•147
Ag	1•21	3•93	0•531
Pb	0•455	6•87	0•365
αFe	0•064	1•63	0•011
In-Tl * (21 at.% Tl)	0•73	1•22	1•6

Thermoelastic loss parameters for various materials. * this work; all other values are taken from Truell and Elbaum (1962).

the attenuation due to the thermoelastic loss at 70°C is 0·016 db/cm at 10 Mhz. Table (5.5) collects the thermoelastic loss parameters for the present case together with similar parameters for other materials for purposes of comparison. At temperatures closer to the transition the thermoelastic attenuation will increase as a result of the increase in the thermal expansion coefficient. At the transition temperature the maximum attenuation attributable to the thermoelastic loss is expected to be of the order of 0·5 db $cm.^{-1}$ at 10 Mhz. Although this is a very large thermoelastic attenuation, it is certainly not significant enough to account for the observed anomalies in the measured attenuation. This is further emphasised by the large, sharp peak in the attenuation of the fast shear wave (Figure (5.13)); shear waves cannot suffer thermoelastic loss because the adiabatic and isothermal shear moduli are always identical (see (2.3.1) and (4.4)).

The background phonon viscosity (see (4.5)) which is also termed the Akhieser loss is given by (Woodruff and Ehrenreich 1961)

$$\alpha = \frac{C_p T \gamma^2 \omega^2 \tau}{3\rho V^3} \qquad (5.16)$$

where γ is an average Gruneisen constant (see (4.5) and (7.5.1)) and τ is a relaxation time. The Gruneisen constant can be got from the bulk modulus and thermal expansion data but evaluation of τ

requires a knowledge of the lattice component of the thermal conductivity; this is not available for the indium-thallium alloy. Typically (Mason 1968) the background phonon viscosity losses are of the same order as the thermoelastic loss at high temperatures. Additional background losses which occur below the transition find their origin in the presence of the banded twins. The loss due to mode conversion at the twin interfaces has already been mentioned; losses due to stress induced movement of twin boundaries are expected. The anelasticity of twinned tetragonal copper-manganese (90% Mn) has been studied by Siefert and Worrel (1951) who concluded that high internal friction is due to stress relaxation across twin boundaries.

The large peak in the attenuation occurs at the same temperature as that in the thermal expansion (Figure (5.8)); a resistivity experiment showed a slight change at the transition in an 18 at.% thallium alloy (see Figure (5.14)) but not in the 21 at.% thallium sample. In the case of TiNi large changes in both the longitudinal and shear velocities accompanied the peak in attenuation. However the present case differed in that changes only occurred in the shear velocities at the transition, the longitudinal velocity remaining constant (see Figure (5.10)).

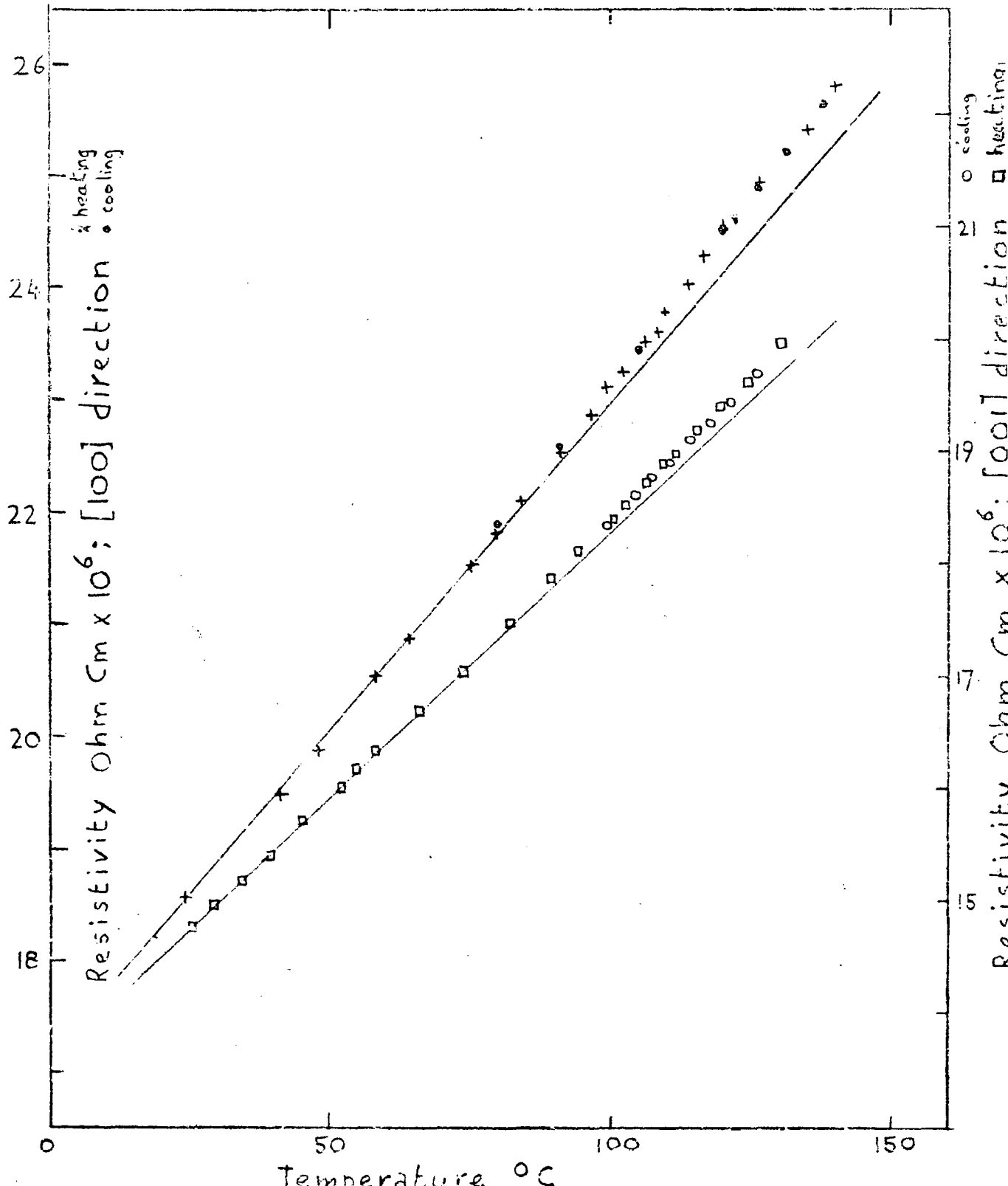

Figure (5.14) Resistivity of Indium - 15 atomic percent thallium.

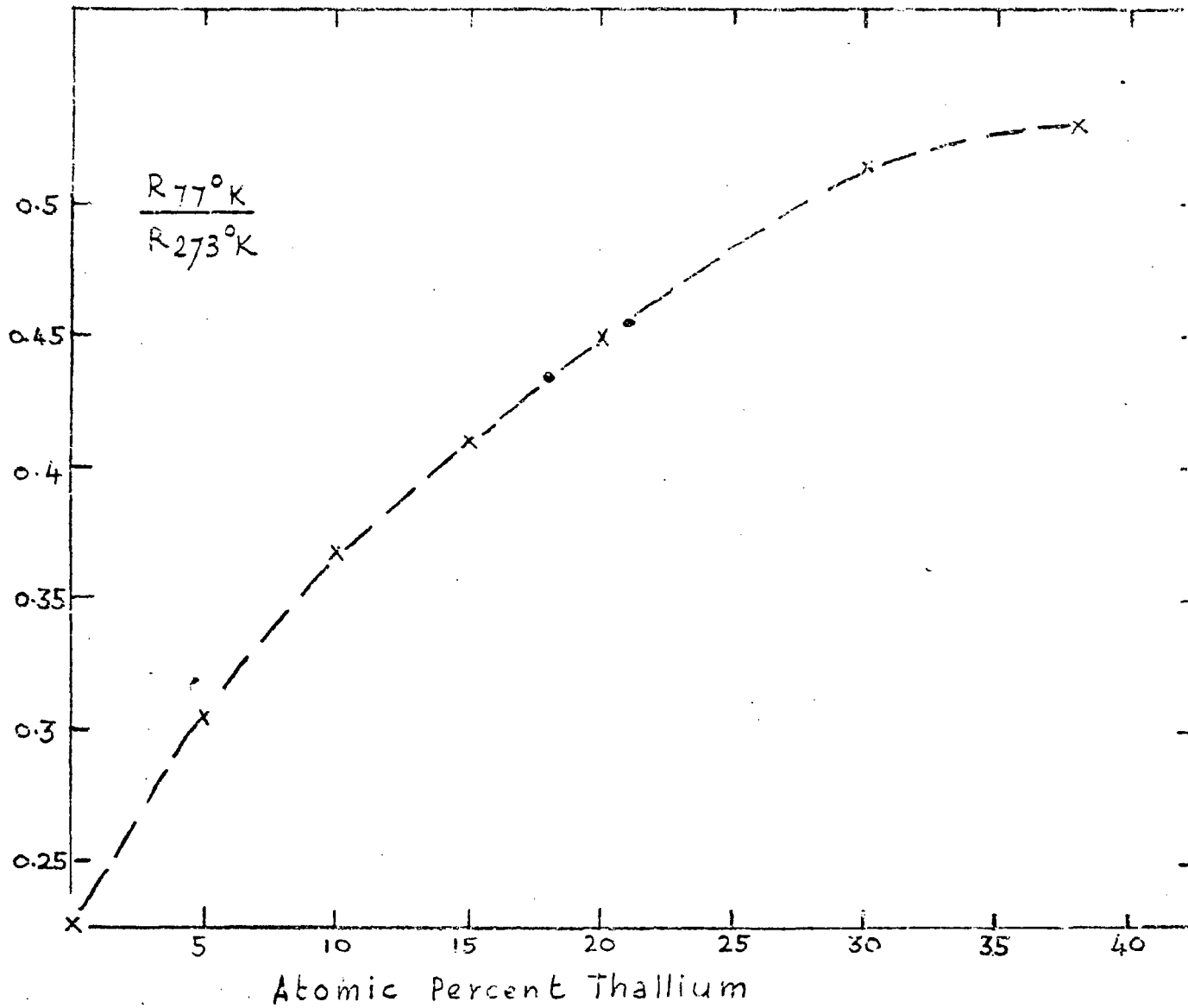

Figure (5.15) Resistivity ratios for indium thallium alloys :
(●) this work ; (X) Stout and Guttman (1952).

Interpretation of the large attenuation near the transition must await further measurements of thermal parameters such as lattice-thermal conductivity and specific heat.

5.4 Discussion of elastic moduli results

5.4.1 Elastic wave velocities in indium and indium-10 at.% thallium

Here the elastic wave propagation in the monocrystalline 10 at.% thallium alloy is compared and contrasted with that in pure indium. The elastic moduli of indium have been reported at room temperature (Winder and Smith 1958) and as a function of temperature between 1·4°K to 300°K by Chandrasekar and Rayne (1961) (hereinafter referred to as CR). To measure C_{13}, CR chose a direction in the (100) plane at 51·5° to the [001] direction but they knowingly used the equations relating the sound velocities to the elastic moduli which are applicable only at 45°. A recalculation of the elastic moduli of pure indium was undertaken here using the velocity data of CR and the relevant velocity-elastic moduli equations (see (5.2)). Results are presented in Table (5.4); where it is seen that C_{13} is the only modulus to be significantly changed from the CR value and that only by 1%.

The recalculated CR values for indium and those obtained for the 10 at.% thallium alloy were used to evaluate the orientation dependence of elastic wave velocities in the two materials in the (100) and (110) planes. Figures (5.16) and (5.17) show the three (100) plane velocity sections for indium and the 10 at.% thallium alloy obtained by solutions of equations (5.6) and (5.7) at one degree intervals. The two materials show little difference in behaviour; the fast shear wave velocity section for indium is slightly more prolate along the [010] direction than it is for the alloy, manifesting the effect of its slightly larger c/a ratio.

The (110) plane is much the most interesting; if indium and the 10 at.% thallium alloy were to undergo the fct to fcc transition*, the sound wave velocities in a plane near the (110) plane would be the ones most affected. The (110) velocity sections for the three waves for both indium and the 10 at.% thallium alloy are shown in Figures (5.18), (5.19) and (5.20). These sections were obtained by a computer solution (see appendix (1)) of the cubic equation (5.5) at degree intervals. All three velocity sections indicate a decrease in the stability of the 10 at.% thallium alloy over that for pure indium. This is most evident along [110] directions (Figure (5.20)) as might be expected: wave velocities in those directions are related to the modulus $(C_{11}-C_{12})/2$.

---

* In fact it has been suggested (Graham 1955) that if melting could be inhibited then indium would undergo a crystallographic transformation.

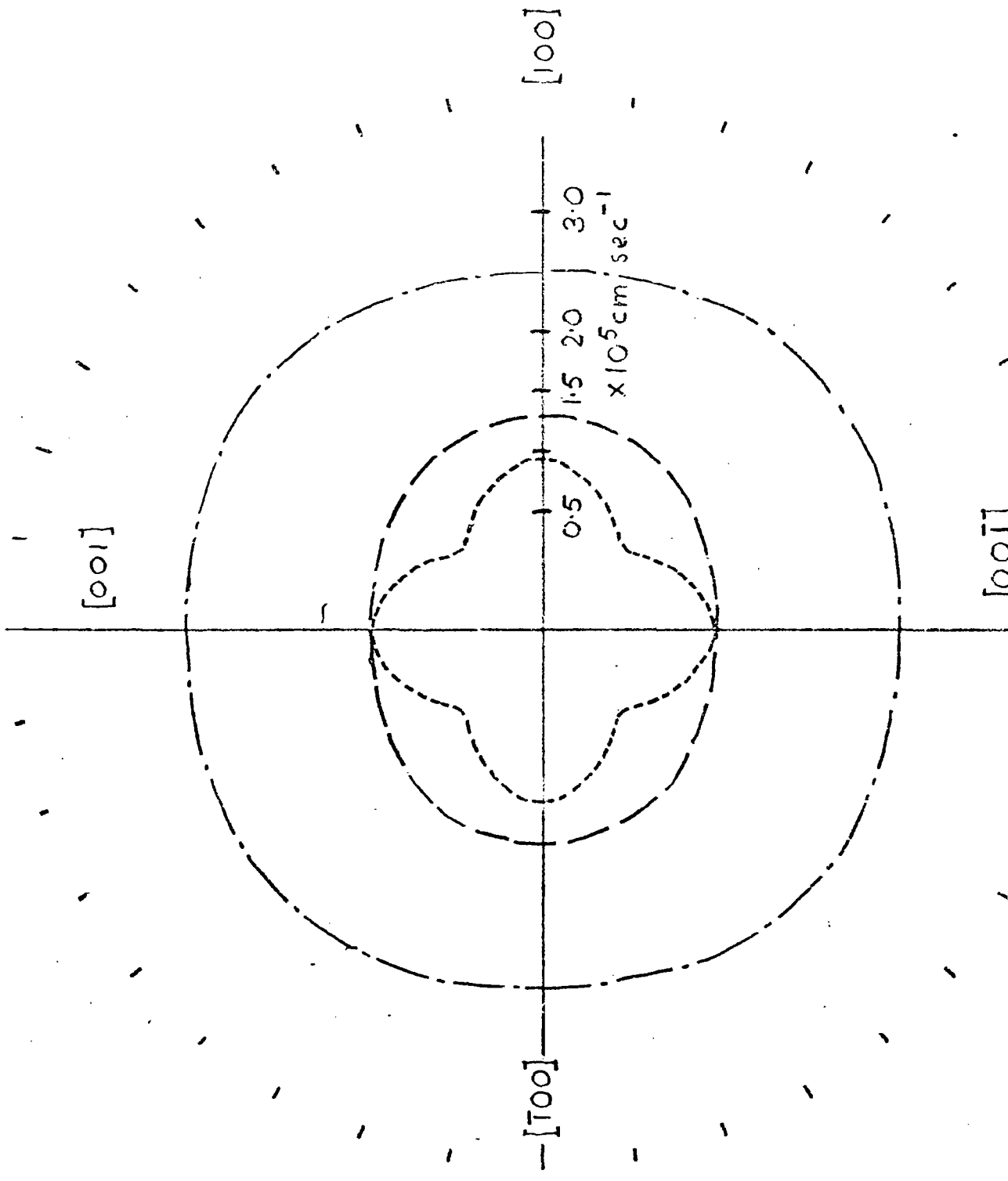

Figure (5.16) The (100) velocity section of pure indium : ---- slow shear; — — — fast shear ; —·—· longitudinal.

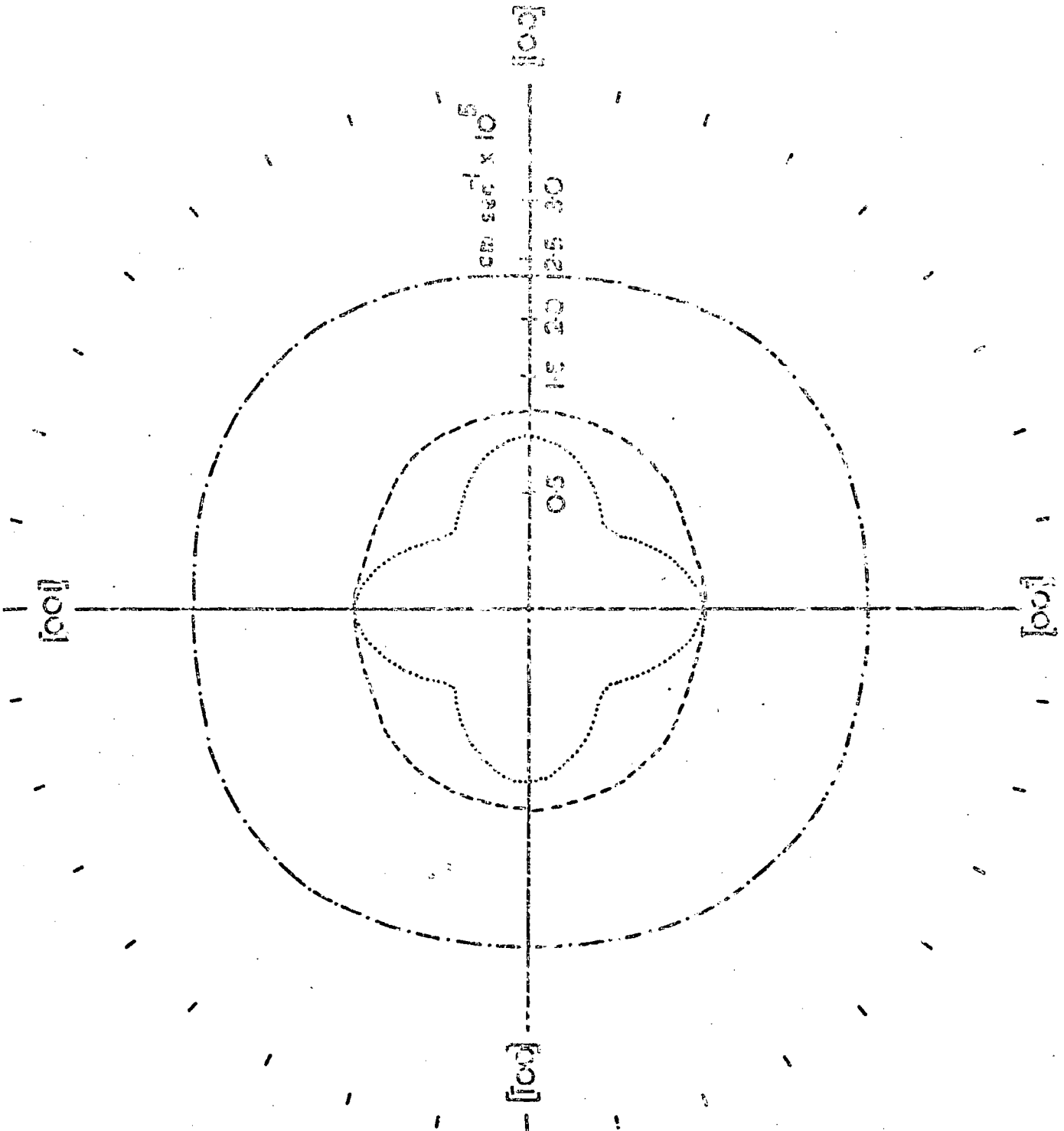

Figure (5.17) The three wave velocities in the (100) plane of indium - 10 at. % thallium : (—·—·—) quasi - longitudinal ; (— — —) pure shear ; (·····) quasi - shear.

Figure (5.18) "Longitudinal" wave velocity section in (110) plane for indium (– – –) and indium - 10 at.% thallium (·····).

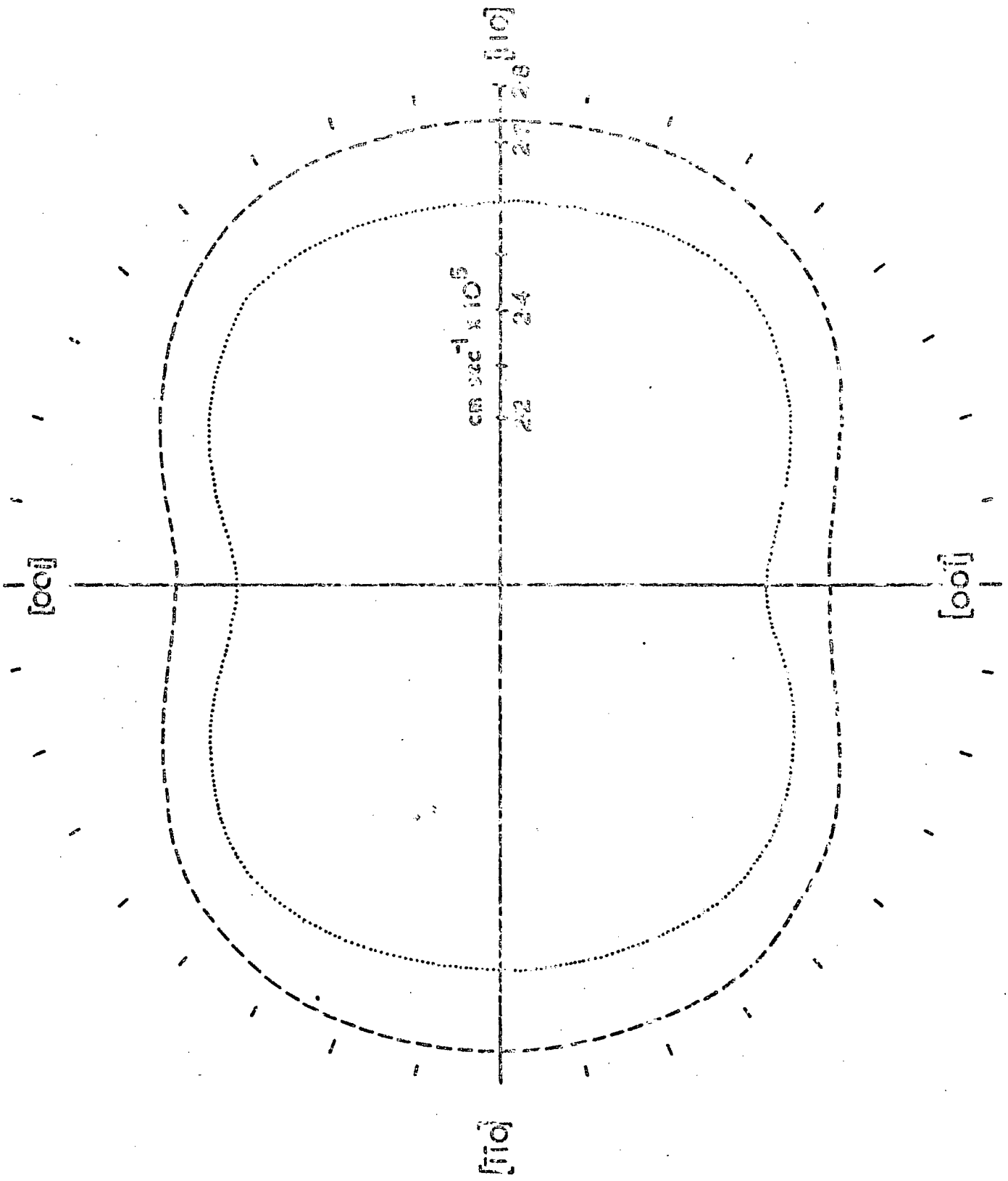

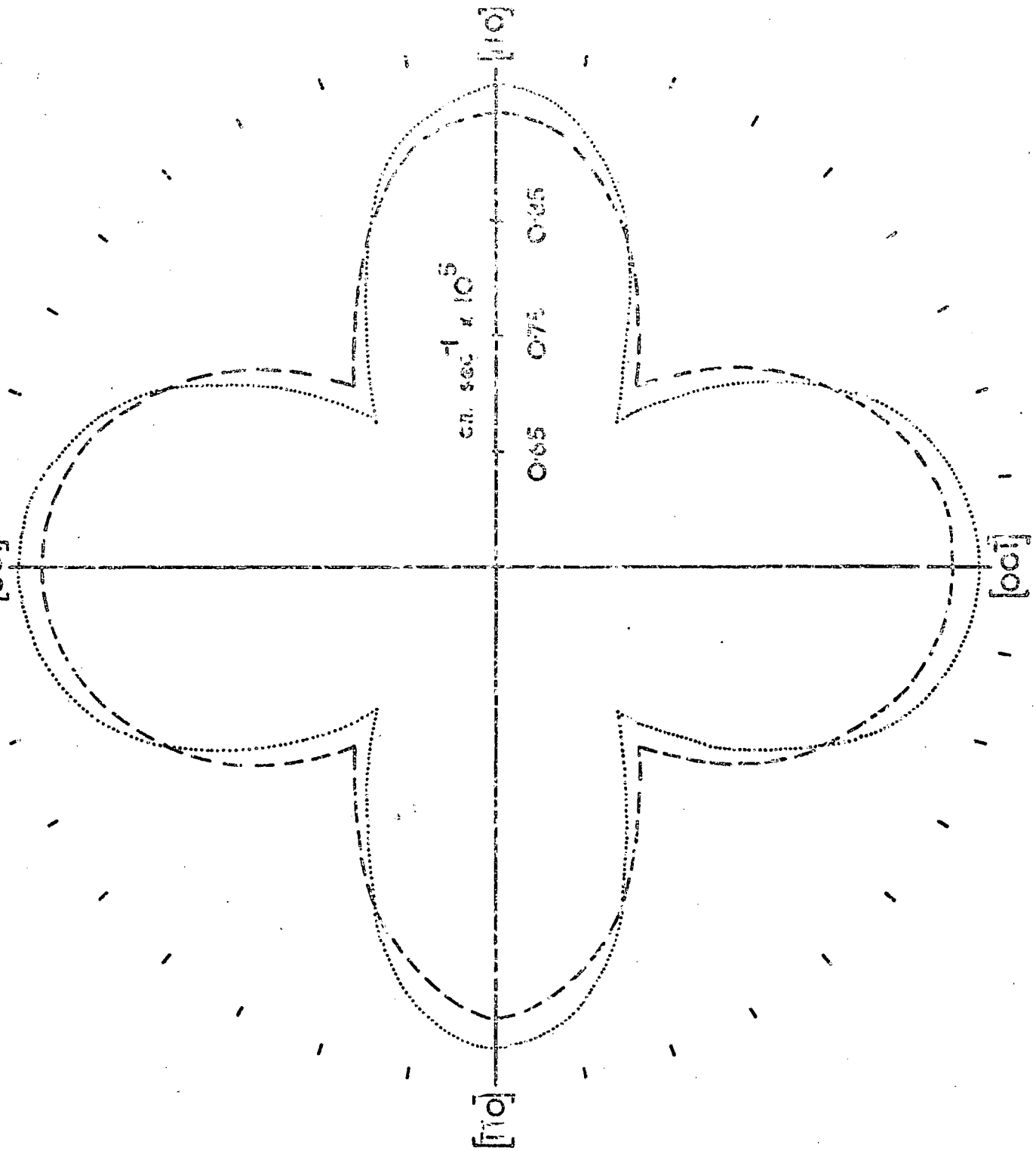

gure (5.19) Fast "shear" wave velocity section in (110) plane for indium (— — —) and indium - 10 at.% thallium (·····).

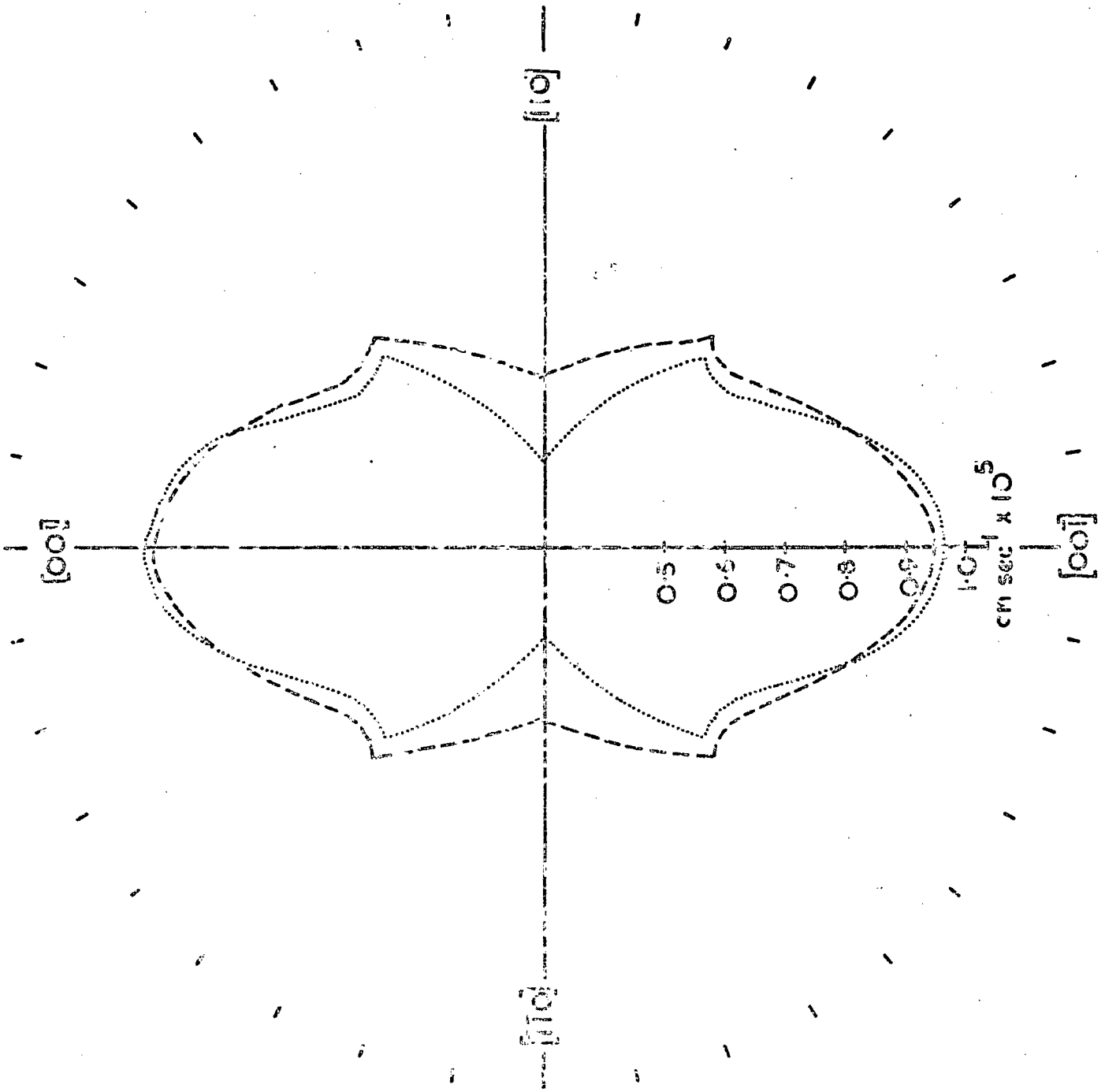

Figure (5.20) Slow "shear" wave velocity section in (110) plane for indium (— — —) and indium - 10 at.% thallium (·····).

Knowledge of the behaviour of the energy flux associated with particular modes can be of great importance in ultrasonic experiments on crystals. Accordingly, expressions are now derived for the energy flux for directions in the (100) plane. The ith component of the energy flux vector $\underline{P}$ is given by equation (2.33) as

$$P_i = -\frac{(P\omega)^2}{2V} C_{ijkl} R_{0l} R_{0k} n_l \qquad (5.17)$$

Because P_1 is zero for all directions in the (100) plane, the angle which the energy flux vector associated with any one of the three modes makes with the [010] direction is

$$\beta = \tan^{-1}(P_3/P_2) \qquad (5.18)$$

In particular for the pure transverse wave

$$\beta_{T_1} = \tan^{-1}(\tan\theta C_{44}/C_{66}) \qquad (5.19)$$

while for the quasi-longitudinal wave

$$\beta_L = \tan^{-1} \frac{C_{44}\sin\theta+(C_{44}+C_{13})\cos\theta\tan\phi+C_{33}\sin\theta\tan^2\phi}{C_{11}\cos\theta+(C_{13}+C_{44})\sin\theta\tan\phi+C_{44}\cos\theta\tan^2\phi} \qquad (5.20)$$

The energy flux vector for the quasi-transverse wave β_{T_2}, is obtained from equation (5.20) by replacing the angle the particle displacement vector makes with the [010] direction for the quasi-

longitudinal wave ϕ by $\phi \pm \frac{\pi}{2}$ as a result of orthogonality of particle displacements (see (7.2)). θ is the angle the propagation direction makes with the [010] direction. A computer programme (see appendix (1)) was written to calculate the energy flux and particle displacement directions for the three modes at one degree intervals. Results are plotted in Figures (5.21) and (5.22) as angular deviations from the propagation direction versus propagation direction.

The deviation of the energy flux associated with the quasi-shear mode is substantial in both indium and the alloy for most directions: it is zero along the [010] as a result of crystal symmetry and close to the [011] direction. The energy flux associated with the pure shear mode follows the propagation direction more closely: in the case of indium the deviation is always ~~positive~~ negative (i.e. the energy flux vector makes a ~~greater~~ smaller angle with the [010] direction than does the propagation vector) ~~while~~ and for the alloy it is also negative. The behaviour of the particle displacement and the energy flux associated with the quasi-longitudinal mode indicates that this mode and thus the quasi-shear mode is close to being pure for all directions in the (100) plane. In fact at one direction in addition to the [010] and [001] an accidental pure mode (see equation (5.9)) does occur: this is manifested in Figures (5.21) and (5.22) by the zero deviation of

Figure (5.21) The quasi - longitudinal particle displacement (——) vector and energy flux vectors associated with the quasi-longitudinal (- - - -), quasi-shear (— —) and pure shear (-·-·-) modes in the (100) plane of pure indium plotted as deviations from the propagation direction.

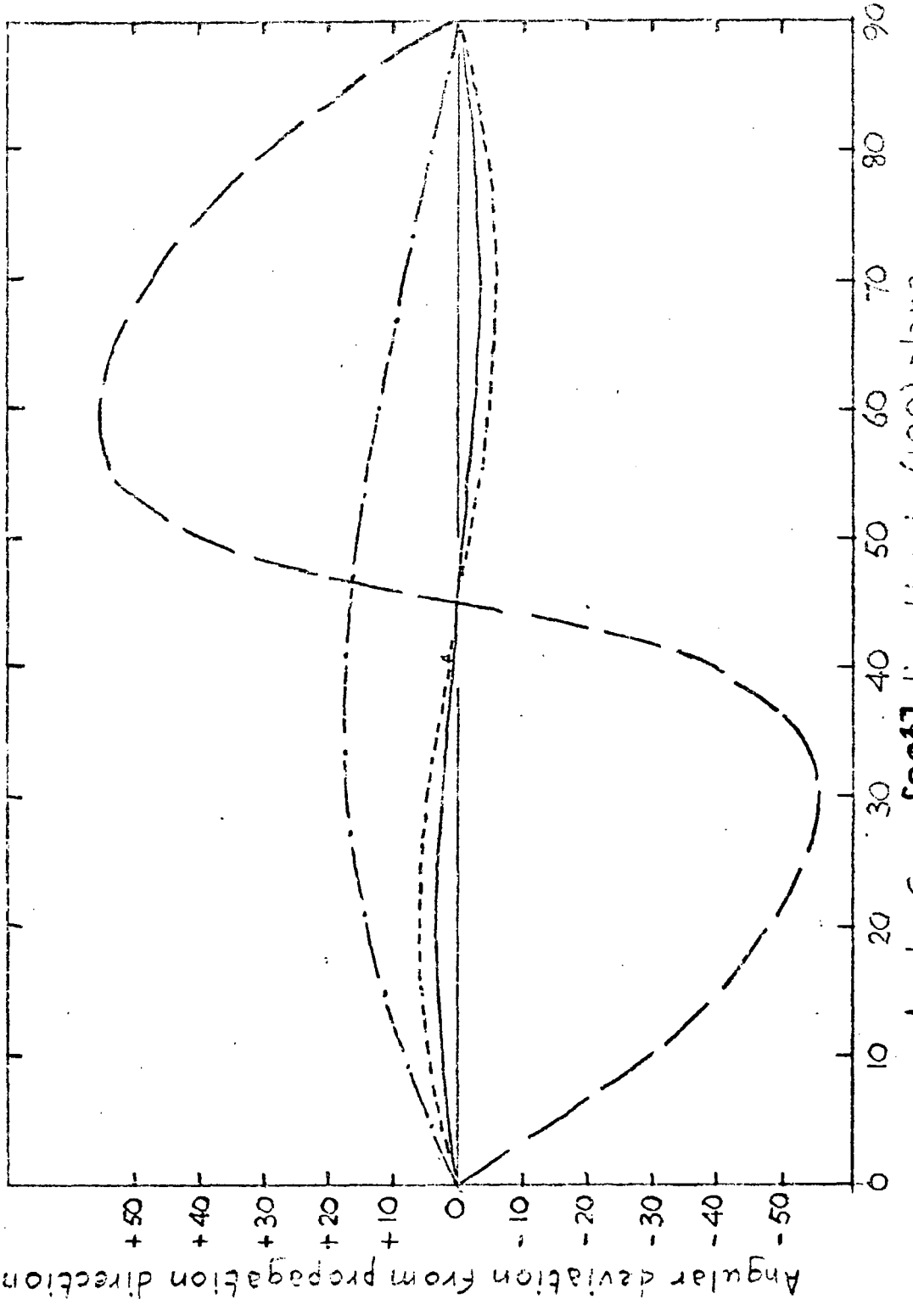

Figure (5.22) The quasi - longitudinal particle displacement (——) vector and energy flux vectors associated with the quasi-longitudinal (- - - -), quasi-shear (- · — -) and pure shear (— · —) modes in the (100) plane of indium-10 atomic percent thallium plotted as deviations from the propagation direction.

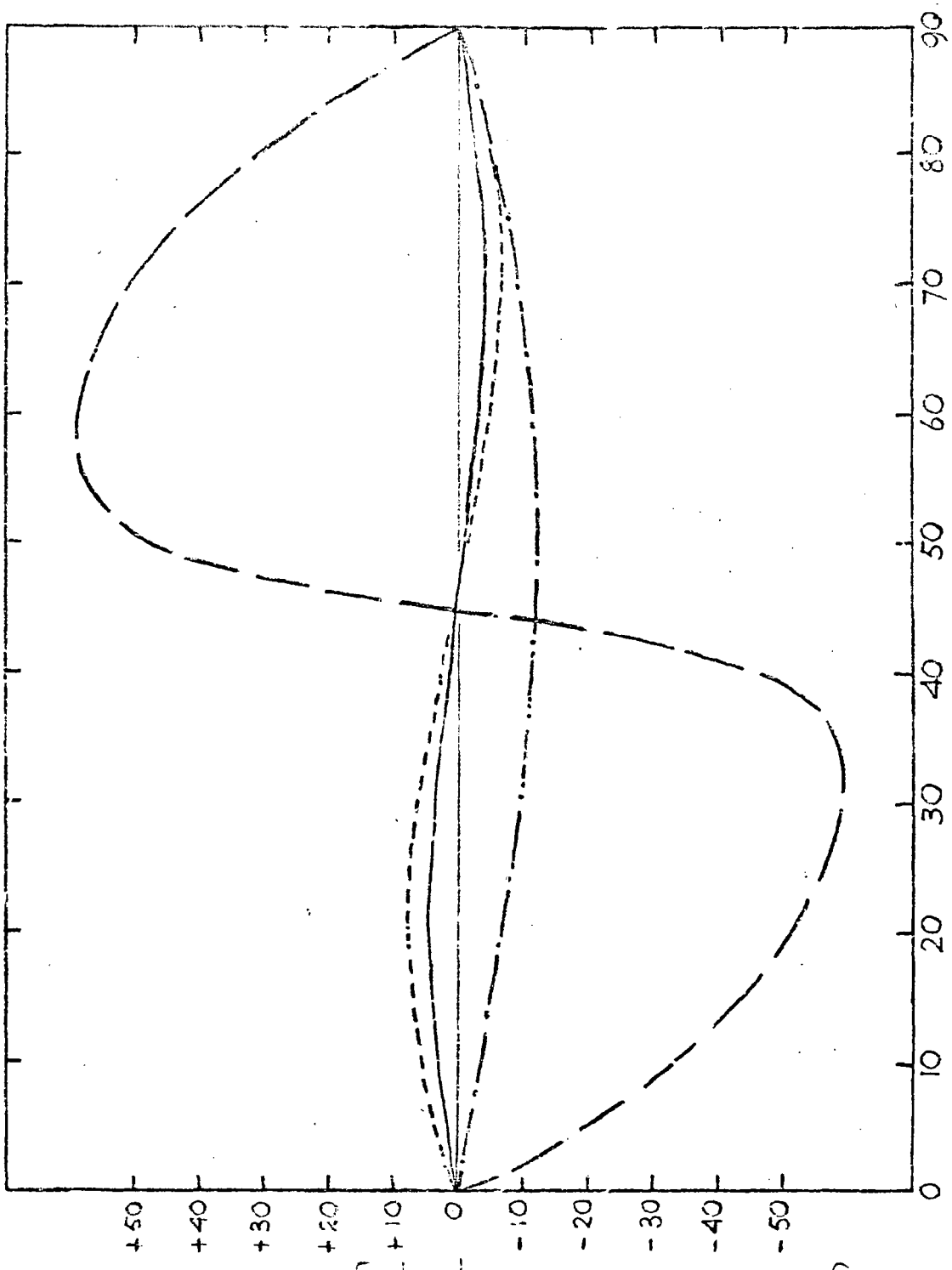

both the particle displacement and energy flux associated with the quasi-longitudinal mode from the propagation direction. It is termed an accidental pure mode direction because it does not occur in the same direction for all crystals belonging to the same Laue group irrespective of their individual elastic moduli values; the direction for indium is 44.90° and for the alloy 46.75° to the [010] direction. The fact that this accidental pure mode direction occurs so close to the [011] direction in these crystals is a consequence of their approximate cubic symmetry.

5.4.2 A force constant model for indium and indium-10 at.% thallium

Sharan and Bajpai (1969) have developed a force constant model for tetragonal crystals involving first, second and third nearest neighbour, central and non-central interactions. Six force constants are obtained in terms of the lattice parameters and elastic moduli;

$$C_{11} = \frac{2}{c}\left[\alpha^1 + \frac{\alpha-\alpha^1}{4n_1^2} + \beta\right] \tag{5.21}$$

$$C_{12} = \frac{2}{c}\left[\frac{\alpha-\alpha^1}{4n_1^2} - \alpha^1 - \beta^1\right] \tag{5.22}$$

$$C_{13} = \frac{2}{c}\left[\frac{\alpha-\alpha^1}{4n_1^2} n^2 - (\alpha^1 + \gamma^1)n^2\right] \tag{5.23}$$

$$C_{13} = \frac{2}{c}\left[\frac{\alpha-\alpha^1}{4n_1^2}\, n^2 - (\alpha^1 + \beta^1)\right] \tag{5.24}$$

$$C_{44} = \frac{2}{c}\left[(\alpha^1 + \frac{\alpha-\alpha^1}{4n_1^2})n^2 + \gamma^1 n^2\right] \tag{5.25}$$

$$C_{44} = \frac{2}{c}\left[\alpha^1 + \frac{\alpha-\alpha^1}{4n_1^2}\, n^2 + \beta^1\right] \tag{5.26}$$

$$C_{33} = \frac{2}{c}\left[(\alpha^1 + \frac{\alpha-\alpha^1}{4n_1^2}\, n^2)\, n^2 + \gamma n^2\right] \tag{5.27}$$

$$C_{66} = \frac{2}{c}\left[\alpha^1 + \frac{\alpha-\alpha^1}{4n_1^2} + \beta^1\right] \tag{5.28}$$

where α, β, γ are the central force constants and α^1, β^1, γ^1 are the angular force constants and

$$n_1 = (\tfrac{1}{2} + \frac{c^2}{4a^2})^{\frac{1}{2}} \; ; \quad n = \frac{c}{a} \tag{5.29}$$

where c and a are the lattice parameters.

Force constant models have been discussed in depth by Keating (1966) who points out a simple test of adequacy for any model: the expression for the bulk modulus which in the present case of tetragonal symmetry is $(S_{11}+S_{22}+S_{33}+2(S_{12}+S_{23}+S_{31}))^{-1}$, must be independent of angular force constants. Several widely

TABLE (5.6)

	central force constants			angular force constants		
	α	β	γ	α^1	β^1	γ^1
Indium	+5.58 ~~12.6~~	+12.0 ~~9.68~~	+3.08 ~~7.46~~	−2.78 ~~−3.66~~	+0.590 ~~−0.235~~	+1.51 ~~−0.109~~
Indium–10 at.% Thallium	+6.81 ~~13.0~~	+10.6 ~~8.16~~	+2.54 ~~6.71~~	−2.39 ~~−3.10~~	0.427 ~~−0.508~~	+1.11 ~~−0.501~~

Units: 10^3 dyne cm.

Force constants for indium and indium–10 at.% thallium in the Sharan-Bajpai (1969) model at room temperature.

	$\frac{C_{13}}{C_{12}}$	$\frac{C_{66}}{C_{44}}$	$\frac{C_{33}}{C_{11}}$
Indium	1.05	1.86	.995
Indium–10 at.% Thallium	1.03	1.54	1.03

Ratio of elastic constants which would be equal if the materials were cubic.

quoted (Born and von Karman 1912; Born 1914) force constant models do not obey this requirement. Neither does this one. In the case of the alloy the presence of two different atomic masses further invalidates the applicability of the model. However it is instructive to calculate the various force constants for pure indium and compare them with those for the 10 at.% thallium alloy. The results of a computer least-mean squares fit of the elastic constant data to equations (5.21) to (5.28) is presented in Table (5.6). The two angular force constants β^1 and γ^1 for the alloy are very close whilst for pure indium the separation is much larger: β^1 and γ^1 are equal if the crystal is cubic.

5.4.3 The compositional dependence of the elastic properties of indium-thallium alloys

The compressibilities of tetragonal crystals are given by

$$\beta = \frac{2(C_{33}-C_{13}) + C_{12} + C_{11}}{C_{33}(C_{11} + C_{12}) - 2C_{13}^2} \qquad (5.30)$$

$$\beta_{11} = \frac{C_{11} + C_{12} - 2C_{13}}{C_{33}(C_{11} + C_{12}) - 2C_{13}^2} \qquad (5.31)$$

$$\beta_1 = \frac{C_{33} - C_{13}}{C_{33}(C_{11} + C_{12}) - 2C_{13}^2} \qquad (5.32$$

where β is the bulk compressibility and $\beta_{\perp}$ and β_{11} are the linear compressibilities perpendicular and parallel to the c-axis respectively. The relations for cubic crystals are obtained by replacing C_{33} by C_{11} and C_{13} by C_{12}. Table (5.7) collects the results for indium, and the 10 at.% and 25 at.% thallium alloys. The compressibilities show that the 10 at.% thallium alloy is more resilient to volume changes under hydrostatic pressure than is indium and has the more anisotropic response: a much greater fraction of the volume change in both indium and the alloy results from length changes along the a-axis than from changes along the c-axis: this is more pronounced in the alloy than in indium. Thus under hydrostatic pressure both indium and the alloy show a tendency to adopt a cubic structure: in the alloy the effect is much the greatest. Figure (5.23) collects the available bulk modulus ($^{1}/\beta$) data for the indium-thallium alloys. Novotny and Smith (1965) found that the bulk modulus of some fcc alloys and that of indium reported by Winder and Smith (1958) all lay on a straight line when plotted as a function of composition. A more accurate elastic moduli set for indium (see Table (5.4)) and the results obtained here for the 10 at.% and 25 at.% thallium alloys indicate that the bulk modulus is not linear with composition but rather varies as shown in Figure (5.23).

TABLE (5.7)

	β	β_{11}	β_1
Indium	27.6±0.8	9.66±0.29	4.28±0.13
Indium-10 at.% Thallium	26.2±1.6	10.71±0.64	3.75±0.22
Indium-25 at.% Thallium	25.2±0.5	9.8 ±0.2	9.8 ±0.2

The bulk and linear compressibilities of indium, indium-10 at.% thallium and indium-25 at.% thallium at 273°K: units are 10^{-13} cm^2 $dyne^{-1}$.

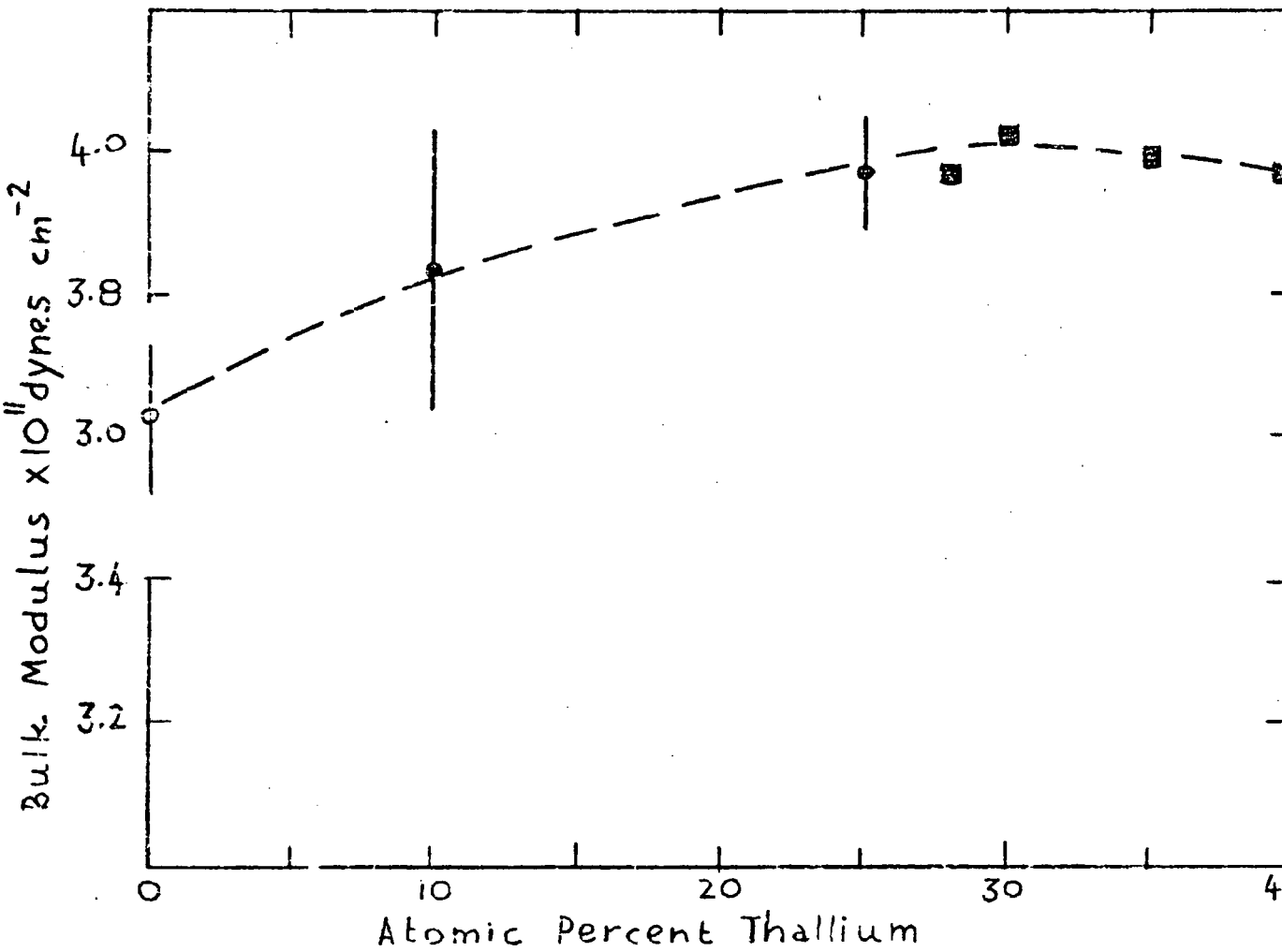

Figure (5.23) Bulk modulus of indium - thallium alloys : (●) this work, (○) Chandrasekar and Rayne (1961) ; (■) Novotny and Smith (1965).

The moduli corresponding to the three sound wave velocities measured along the [110] direction are shown in Figure (5.24) for several alloys. Changes in the composition dependence of these moduli are associated with the transition at 22 at.% thallium composition.

Table (5.8) collects values of the stability criteria (see (2.4)) for indium and the 10 at.%, 25 at.% and 39 at.% thallium alloys: the criteria are less well satisfied for the composition (25 at.% thallium) closest to the room temperature transition composition (22 at.% thallium).

5.5 Conclusion

The various contributions to the total energy for a solid have been discussed in (1.1) and in particular the effect of the Fermi energy term on the elastic shear constants was described with reference to Leigh's (1951) treatment of aluminium, a polyvalent fcc metal. Winder and Smith (1958) adapted Leigh's approach to interpret the elastic data of indium by treating indium as a pseudo-cubic fcc structure with a lattice constant equal to $(a^2c)^{1/3}$. The two pseudo-cubic shear constants of indium were taken as

$$(2C_{44} + C_{66})/3; \quad \text{and} \quad \frac{2(2C_{44} + C_{66})}{2(C_{11} + C_{33} - 2C_{13}) + (C_{11} - C_{12})/2}$$

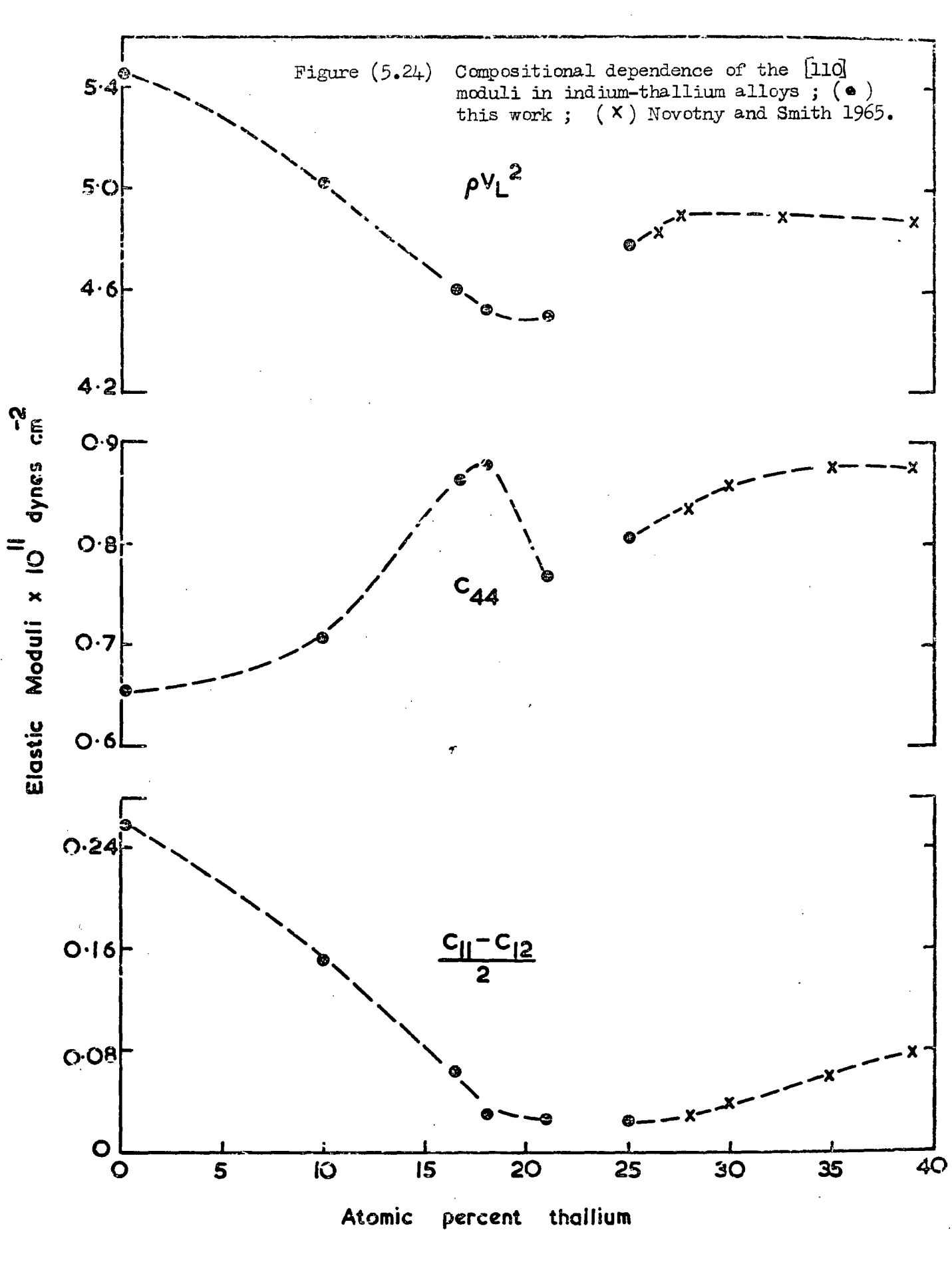
Figure (5.24) Compositional dependence of the [110] moduli in indium-thallium alloys ; (●) this work ; (X) Novotny and Smith 1965.
ρV_L^2
C_{44}
$\frac{C_{11}-C_{12}}{2}$
Elastic Moduli x 10^{11} dynes cm^{-2}
5·4
5·0
4·6
4·2
0·9
0·8
0·7
0·6
0·24
0·16
0·08
0
0
5
10
15
20
25
30
35
40
Atomic percent thallium

TABLE (5.8)

Material	Stability Criteria						
	$C_{11}C_{33}-C_{13}^2>0$	$C_{11}-C_{12}>0$	$C_{33}(C_{11}+C_{12})-2C_{13}^2>0$	$C_{11}>0$	$C_{33}>0$	$C_{44}>0$	$C_{66}>0$
Indium	2•8	0•516	5•1	4•52	4•51	0•650	1•21
Indium-10 at.% thallium	2•4	0•313	3•4	4•16	4•30	0•709	1•08
Indium-25 at.% thallium	0•4	0•047	0•4	4•01	4•01	0•808	0•808
Indium-39 at.% thallium	1•06	0•152	1•7	4•08	4•08	0•869	0•869

Stability criteria for tetragonal and cubic indium thallium alloys: units 10^{11} dynes cm^{-2}

In a cubic crystal these two constants are the familiar C_{44} and $(C_{11}-C_{12})/2$ respectively. The first Brillouin zone for a fcc structure bounded by six square faces normal to 100 and eight hexagonal faces normal to 111 direction forms was adopted. Since indium has three electrons per atom the first zone is completely filled, the remaining electron density overlapping into the second zone in a similar way to the schematic diagram in Figure (1.1). By following Leigh closely, Winder and Smith obtained the numerical values of the coulomb, first zone, hexagonal face overlap and square face overlap theoretical terms which contribute to the two pseudo-cubic shear constants of indium. These are given in Table (5.9).

The effect of the addition of thallium, which is also trivalent, to indium eventually results in the adoption of the cubic structure at a certain composition. It is thus instructive to visualise qualitatively the effect a tetragonal lattice would have on the pseudo-cubic Winder and Smith model of indium. The Brillouin zone plane in the tetragonal structure normal to the c-axis will move inwards with respect to the position of the same plane in the pseudo-cubic structure; square face overlap transfer terms should then be greater for c-a transfer than a-a transfer and so on see Figure (1.1)). On this simple basis $(C_{11}+C_{33}-2C_{13})/4$ is

TABLE (5.9)

	$\Omega(2C''+C')/3$	$\Omega(2C_{44}+C_{66})/3$
Coulomb	0.67	5.99
First zone electron	1.15	3.44
Hexagonal face overlap	3.91	-8.74
Square face overlap	-5.38	0.69
TOTAL	0.35	1.38
Observed (Winder and Smith)	0.35	1.38
Observed (see Table (5.4)	0.24	1.37

Numerical values of the terms contributing to the pseudo-cubic shear constants of indium. Energy units are ev. and Ω is the atomic volume. (Winder and Smith 1958): $C' = (C_{11}-C_{12})/2$; $C'' = (C_{11}+C_{33}-2C_{13})/4$.

expected to be greater than $(C_{11}-C_{12})/2$ as found experimentally (these two shear constants in a cubic structure are equal). The effect of thallium in indium has been discussed by Novotny and Smith (1965) in the case of fcc alloys. They conclude that the sharp rise in the anisotropy ratio $2C_{44}/(C_{11}-C_{12})$ as the composition approaches that of the transition (see Figure (5.25)) was not caused by core-core interactions. In fact the contribution of the coulomb term to the anisotropy ratio $(2(2C_{44}+C_{66})/(2(C_{11}+C_{33}-2C_{13})/4 + (C_{11}-C_{12})/2))$ in pure indium obtained from Winder and Smith's calculations, has the same value as have the fcc alloys. It may thus be expected that changes in the electronic energy distribution control the rapid increase in shear anisotropy and the associated decrease in lattice stability of both the tetragonal and cubic alloys. Further, it seems plausible that the full zone contributions to the shear anisotropy will not alter markedly with change in thallium content or with temperature at constant composition. Thus the origin of the instabilities in the indium-thallium alloys appears to arise from that part of the Fermi surface not in the first zone. In the case of TiNi (Chapter 4) the change of the Fermi level results in an appreciable change in the effective number of free carriers and their mobilities above and below the martensitic phase change in

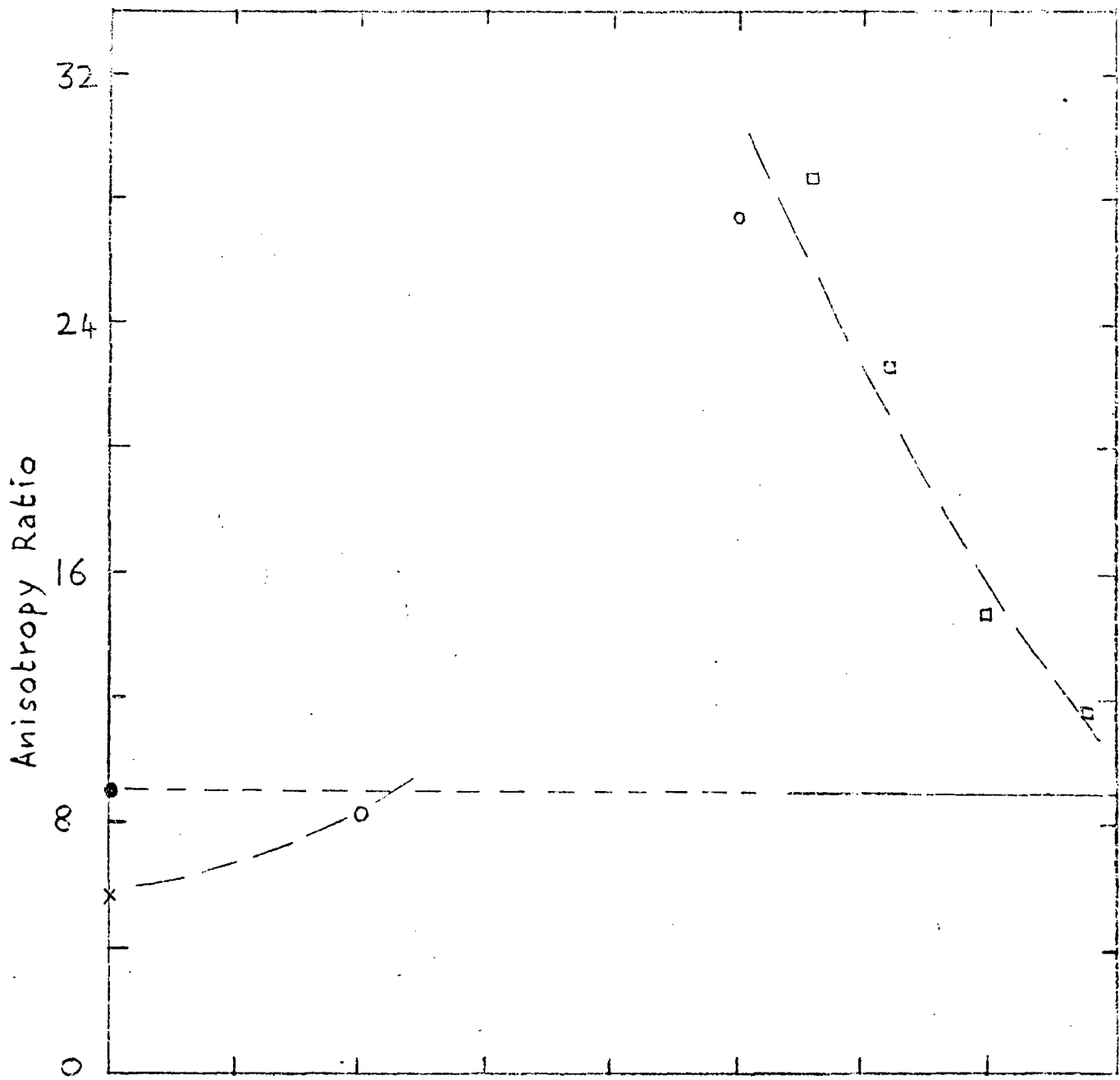

Figure (5.25). The anisotropy ratio (see text) for indium - thallium alloys : (O) this work ; (X) Chandrasekar and Rayne (1961); (□) Novotny and Smith (1965) (●) Winder and Smith (1953). The full line is the core-core contributio calculated by Novotny and Smith.

that material: this is manifested in large changes in resistivity and Hall coefficient. However in the present case, careful measurements of electrical resistivity (5.3.5) showed no drastic changes between the fct and fcc modifications of the indium-thallium alloys; this does not however preclude the conclusion reached above that the instabilities in the indium-thallium alloys are electronic in origin.

5.6 Resume

Alloys in the indium-thallium system have been the subject of an ultrasonic study. Large increases were found in the ultrasonic attenuation in the vicinity of the fcc to fct transformation: it seems plausible that these anomalies are connected with a softening of the lattice similar to the hypothesis put forward in the case of TiNi (chapter 4). A complete breakdown of the characteristics of elastic wave propagation in tetragonal (4/mmm) crystals and for the first time the elastic moduli of a tetragonal indium-thallium alloy has been given: a detailed comparison of the elastic properties of this alloy (10 at.% thallium) with those of pure indium showed that although the two materials are similar in many ways there are in fact significant differences particularly in their compressibilities. Correlation of the present measurements with those of other workers has provided a more complete picture of the elastic behaviour of the

indium-thallium alloys in the vicinity of their martensitic phase transformation.

CHAPTER 6

The elastic constants and interatomic binding in yttria-stabilised zirconia

6.1 Introduction to the zirconia-yttria system

The technical importance of zirconia (ZrO_2) as a high temperature refractory conductor is frustrated by the existence of a phase transformation at 1000°C which takes the usual monoclinic form to a tetragonal modification. Both phases are close to being cubic; the monoclinic (baddeleyite) lattice which may be considered as a distorted fluorite structure has parameters a = 5·174Å, b = 5·266Å, c = 5·308Å, γ = 80·8° while those of the tetragonal (rutile) lattice are a = 5·07Å and c = 5·16Å (Ruff and Ebert, 1929). The fluorite and rutile lattices are typical of ionic compounds that have the formula MX_2 where M is a metal and X is either fluorine or oxygen. The deciding factor in most cases between the adoption of one structure or the other is the ratio of the cation to anion radius. If $r_c:r_a < 0{\cdot}73$, then the rutile structure occurs; otherwise the fluorite lattice is the stable one. Zirconia has a value of 0·66 for this ratio (Zhdanov 1965) which is close to the bounding value. Only at high temperatures is the expected rutile lattice adopted. This transformation is accompanied by a 9% volume contraction which renders the production of coherent, strong pieces of sintered material impossible.

With a view to avoiding the problems associated with the phase transformation, solid solutions of zirconia with several materials have been studied (Ryshkewitch 1960). Because both the monoclinic

and tetragonal forms of zirconia are almost cubic, certain cubic oxides, when alloyed with zirconia result in a cubic structure. In particular, cubic solid solutions of yttria (Y_2O_3) in zirconia do not exhibit phase changes with temperature and are thus referred to as "stabilised." Magnesia (MgO) and Calcia (CaO) are also known to force the adoption of the fluorite type lattice when in solution with zirconia (Ryshkewitch 1960). But not all cubic oxides have this stabilising effect; strontium oxide and barium oxide are insoluble in zirconia as a result of the dissimilarity between their cation radius and that of zirconium. The latter ions has a radius of 0.9Å, that of calcium is 1.05Å and that of magnesium is 0.8Å. In contrast, the radius of the barium ion is 1.43Å : it cannot be accommodated in the zirconia lattice.

The latest phase diagram reported (Duwez, Brown and Odell 1951) shown in Figure (6.1) demonstrates that the lower limit for stabilisations is 6 mole% yttria : below this composition the solid solutions exist only in the monoclinic form; the cubic phase extends to 55 mole% yttria at room temperature. In the region of 56 to 76 mole% yttria two phases are present. A simple eutetic, composed of both end solid solutions, forms the miscibility gap. Above 76 mole% yttria there exists a single phase of cubic solutions of zirconia in yttria.

At low temperatures pure zirconia is an insulator, having a resistivity of 10^{13} to 10^{14} ohm cm (Schweitzer 1931). At 1000°C

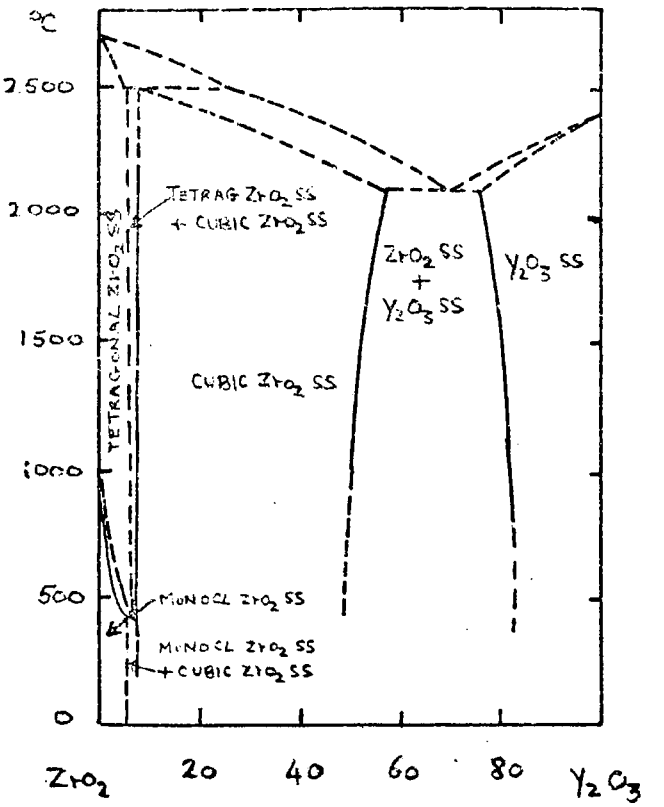

Figure (6.1) Phase diagram of the zirconia-yttria system after Duwez et al (1951).

the resistivity is still about 10^7 to 10^8 ohm cm. In contrast yttria stabilised zirconia is a comparatively good conductor, particularly at high temperatures : at 1000°C the resistivity is 200 ohm cm and at 2200°C it is 0·6 ohm cm. This enhanced conductivity results from the replacement of the tetravalent zirconium ion by the trivalent yttrium ions producing oxygen vacancies with which, for electroneutrality of the lattice, an electron is associated.

Zirconia-yttria solid solutions are of technical importance as refractory conductors, especially as high temperature electrodes in magnetohydrodynamic generators and as solid electrolytes for fuel cell applications. An unfortunate result of high temperature current passage through zirconia-yttria solid solutions is a marked tendency for fragmentation of both sintered, polycrystalline and single crystal electrodes. Much effort has been put into finding practical solutions to this problem but the reason for the effect is not yet known. One relevant aspect which has been neglected is the mechanical properties and their relation to crystal stability.

The concern here has been to look for variations in the mechanical properties of the cubic solid solutions near the stability edge composition of 6 mole% yttria in zirconia. In particular, the elastic constants, certain of which are very sensitive to changes in crystal stability, of two compositions (8 mole% and 12 mole% yttria) of yttria stabilised-zirconia close to the stability edge,

have been measured by the ultrasonic pulse echo technique.

In spite of the obvious importance of the yttria stabilised solutions, no previous studies have been reported of any lattice properties. And elastic constant data is able to give positive indications of the type of binding and the nature of the lattice stability.

6.2 Experimental details

Two different compositions of yttria-stabilised zirconia have been studied. One of 8 mole% yttria was chosen because it is near the stability edge (see Figure (6.1)) of the cubic to monoclinic transformation; the other contained 12 mole% yttria, being further away from the transition composition. The crystals were grown by electrofusion and supplied by Dr. J.S. Thorpe.

The physical appearance of the two compositions differed in that the 8 mole% yttria sample was a translucent amber while the 12 mole% sample was an opaque brown. Chemical purities were high. Optical spectrographic analysis showed that the only impurities present at trace level were silicon, hafnium, magnesium and tin. This result was substantiated by the absence of observable electron spin resonance spectra (sought at 9GHz and 4.2K) which also indicated freedom from other paramagnetic impurities (J.S. Thorpe 1969, Private Communication). Examination of the crystals by x-rays

showed on back reflection Laue photographs the pin point spots which gave evidence of high crystal perfection. These are shown in Figure (6.2) and exhibit the fourfold and twofold rotational symmetries characteristic of the [100] and [110] crystallographic directions. The calcium fluoride structure has the point group $m\bar{3}m$, the symmetry elements of which are shown in Figure (6.3); also shown is a unit cell of the calcium fluoride structure. The lattice parameters of the two compositions were obtained from Debye-Scherrer powder photographs. The Nelson-Riley extrapolation procedure (Nelson and Riley 1947) was performed in order to obtain most accurately the lattice parameters. Values for the 8 mole% yttria and 12 mole% yttria compositions were found to be $5{\cdot}1276 \pm 0{\cdot}0001$ Å and $5{\cdot}1401 \pm 0{\cdot}0001$ Å respectively. The densities of the crystals, found by Archimedes principle, were for the 8 mole% and 12 mole% yttria $6{\cdot}036 \pm 0{\cdot}001$ gms cm^{-3} and $5{\cdot}894 \pm 0{\cdot}001$ gms cm^{-3} respectively at room temperature. All the elastic constants of a cubic crystal may be obtained from measurement of the velocities of the three possible polarisations of pure mode, ultrasonic waves propagated in the [110] direction (see 2.5.2). Samples for ultrasonic measurements were aligned for this direction by the x-ray Laue back reflection technique to within $\pm 0{\cdot}5^{\circ}$. Because of this misorientation the equations shown in Table (2.1) relating the measured velocities to the elastic constants are not strictly accurate. Waterman (1959) gives

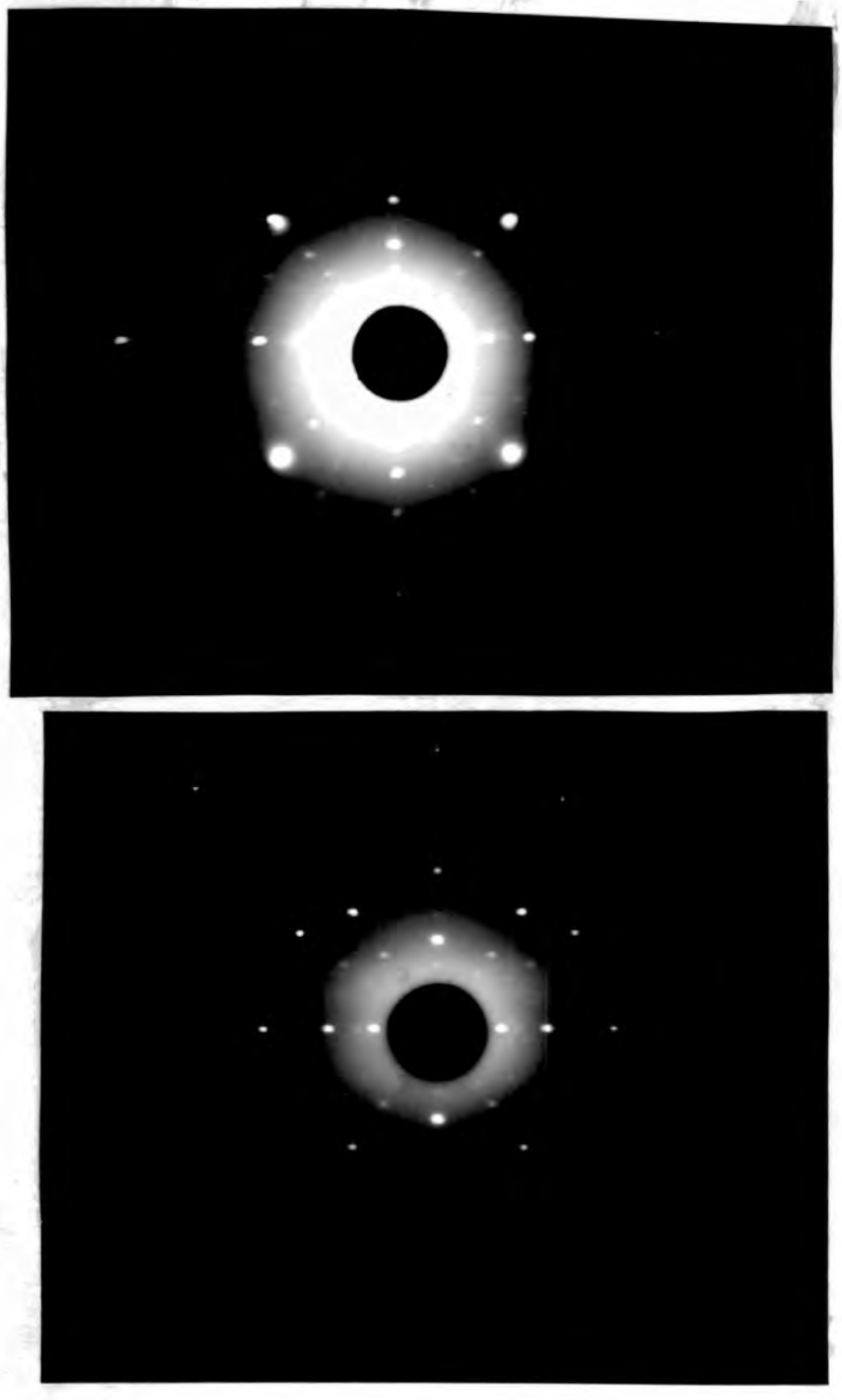

Figure (6.2) Laue X-ray back reflection photograpsh of zirconia-yttria solid solutions : (a) [100] direction; (b) [110] direction.

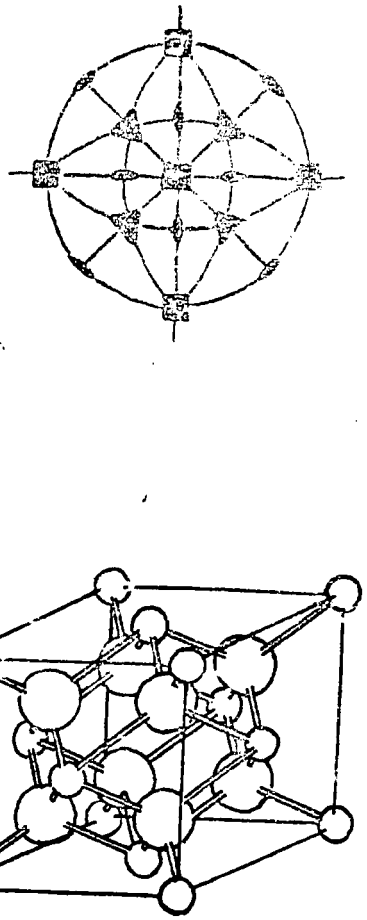

Figure (6.3) The symme try elements and unit cell of the calcium fluoride type structure.

expressions for the change in velocity for small deviations from pure mode propagation directions. For example, the longitudinal velocity in the 8 mole% yttria sample in the $\left\{ \frac{0.9911}{2}, \frac{0.9911}{2}, 0 \right\}$ direction differs by 0·4 cm/sec from the velocity (7.09×10^5 cm/sec) in the $\left\{ \frac{1}{2}, \frac{1}{2}, 0 \right\}$ direction. Thus a misorientation of $\pm 0.5^\circ$ contribution less than 0·01% to the total error in the elastic moduli determination which is estimated to be 2·6% (see Chapter 3). Two parallel [110] faces were cut, using a diamond wheel, and then polished with diamond pastes of successive fineness down to one micron. The final faces were parallel to within 0·0001" at a separation of about one cm. For both compositions the most successful fluid for bonding the quartz transducers to the crystal surface was found to be 10^6CS silicone fluid; the bonding procedure is discussed fully in Chapter 3. X-cut transducers, used for generation of longitudinal waves, were satisfactorily bonded with this fluid at all temperatures between 300°K and 77°K, but the bond quality for Y-cut transducers used for shear wave injection deteriorated at temperatures above about 200°K, thus limiting the range of measurements. However the temperature dependence of the velocities was slight.

The sample holder and cryostat system used in these measurements is described in Chapter 3.

6.3 Results and discussion

The linear combinations of the elastic constants derived from the velocity data using equations shown in Table (2.1) are given as a function of temperature for the two compositions in Figure (6.4). The sound velocities for the three wave polarisations propagated in the [110] direction are given at 77°K and 196°K for the two compositions in Table (6.1). Also included are the elastic compliances (see Chapter 2, Section 3 for definition), the bulk moduli, the anisotropy ratios and the Cauchy relations. That the mechanical properties of the two compositions are fairly close is evidenced by the similarity in their elastic properties. This is well demonstrated by the sections of the velocity surfaces in the (110)plane (Figure (6.5)) and the (100) plane (Figure (6.6)). These sections were obtained using the computer programme written for the tetragonal case (Chapter 4) suitably modified. Because the 8 mole% yttria sample is the closer to the phase boundary for the cubic to monoclinic transformation this should be reflected in any conditions which are demanded for crystal stability. The condition that the crystal energy density be positive definite (see Chapter 2, Section 4) leads to various relations between the elastic constants which must be satisfied. For cubic crystals in particular these are all satisfied if C_{12} and $(C_{11}-C_{12})$ are greater than zero. Table (6.2) presents values for these criteria for both compositions:

TABLE (6.1)

	$(ZrO_2)_{0.92}$ $(Y_2O_3)_{0.08}$		$(ZrO_2)_{0.88}$ $(Y_2O_3)_{0.12}$	
Elastic Constants dynes cm^{-2} x 10^{12}	77°K	196°K	77°K	196°K
$(C_{11} + C_{12} + 2C_{44})/2$	3·03	3·03	3·14	3·14
$(C_{11} - C_{12})/2$	0·585	0·585	0·627	0·617
C_{44}	1·58	1·58	1·54	1·54
C_{11}	2·04	2·04	2·23	2·22
C_{12}	0·870	0·870	0·973	0·983
$\frac{C_{11} + 2C_{12}}{3}$ Bulk Modulus	1·26	1·26	1·39	1·40
$\frac{2C_{44}}{C_{11}-C_{12}}$ Anisotropy ratio	2·70	2·70	2·46	2·50
Sound Velocities cm sec^{-1} x 10^5				
Propagation Direction / Polarisation Direction				
110 / 110	7·09	7·09	7·30	7·30
110 / 001	5·12	5·12	5·78	5·78
110 / $1\bar{1}0$	3·11	3·11	3·26	3·24
Elastic Compliance cm^2 $dynes^{-1}$ x 10^{-12}				
S_{11}	0·658	0·658	0·610	0·619
S_{12}	-0·197	-0·197	-0·185	-0·190
S_{44}	0·633	0·633	0·649	0·649

The elastic moduli of $(ZrO_2)_{0.92}$ $(Y_2O_3)_{0.08}$ and $(ZrO_2)_{.88}$ $(Y_2O_3)_{.12}$ at 77°K and 196°K. Also included are values for the three pure mode sound velocities in the [110] direction for both compositions.

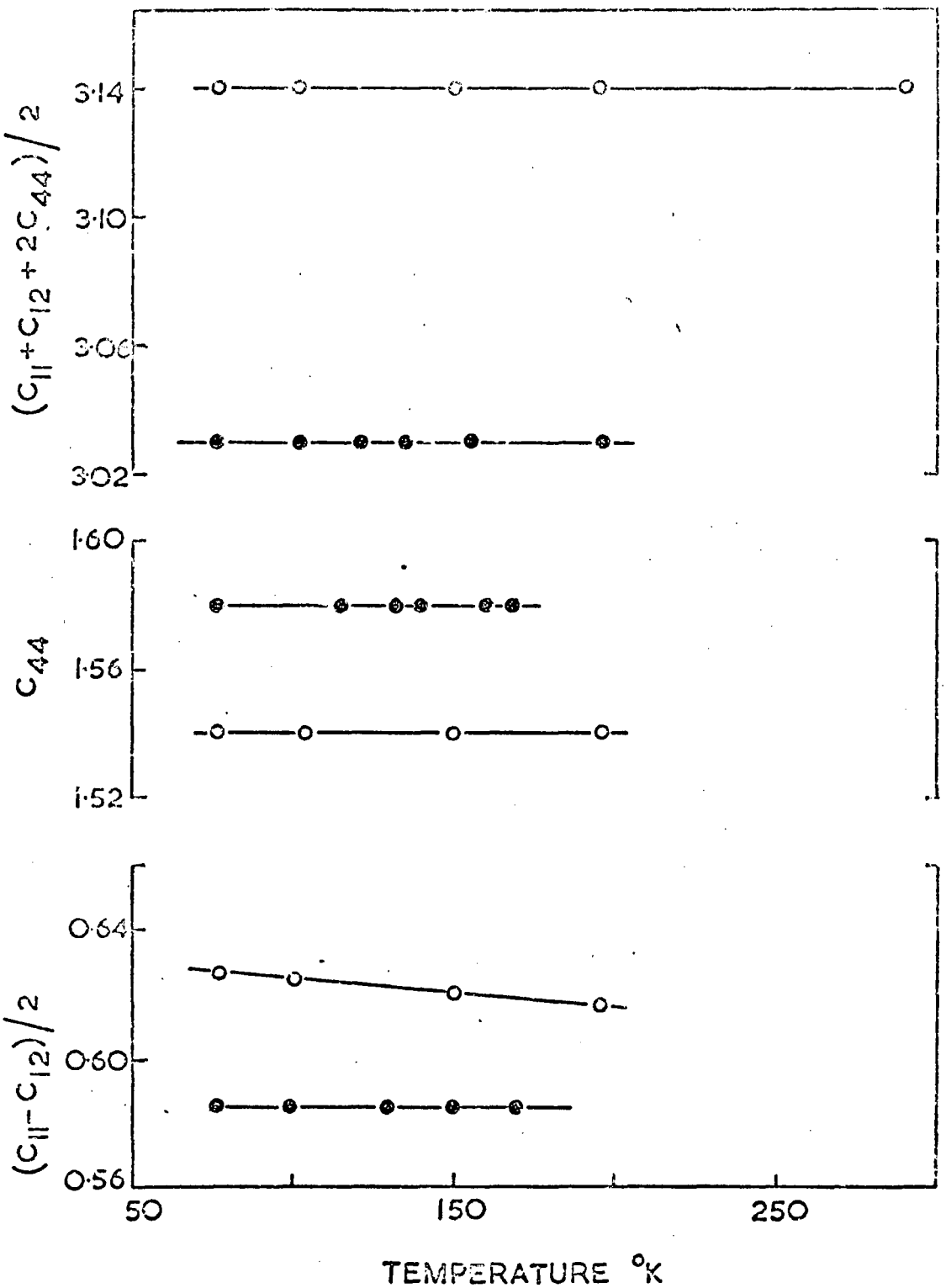

Figure (6.4) Temperature dependence of the measured linear combinations of elastic constants of zirconia containing 8% (⊛) and 12% (○) yttria. Units are 10^{12} dynes cm.$^{-2}$.

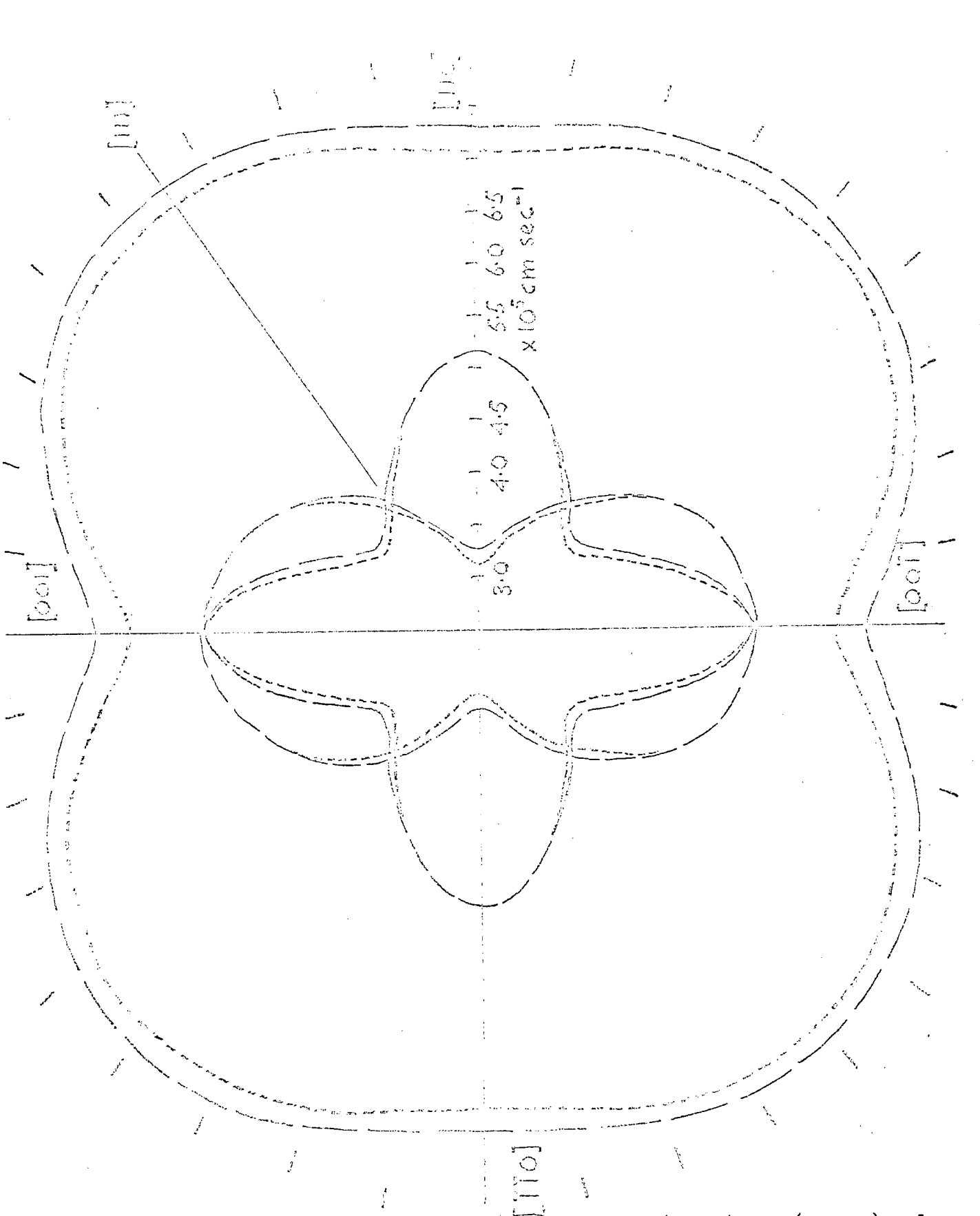

Figure (6.5) The (110) velocity sections for $(ZrO_2)_{0.88}$ $(Y_2O_3)_{0.12}$ (— — —) and $(ZrO_2)_{0.92}$ $(Y_2O_3)_{0.08}$ (--------)

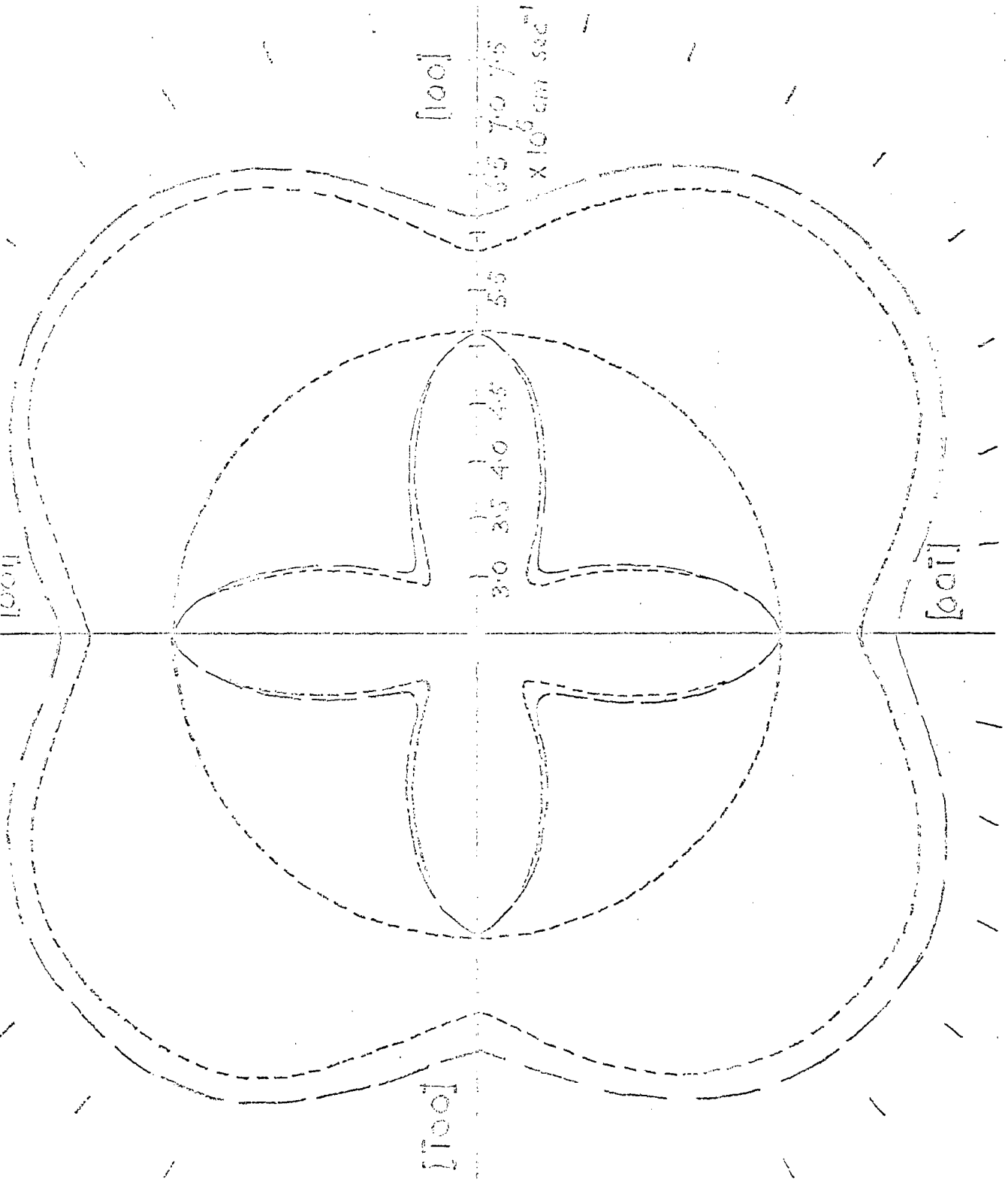

Figure (6.6) The (100) velocity sections for $(ZrO_2)_{0.88}(Y_2O_3)_{0.12}$ (– – –) and $(ZrO_2)_{0.92}(Y_2O_3)_{0.08}$ (------) : the fast shear velocity is effectively the same for both compositions.

TABLE (6.2)

Stability Criteria	$(ZrO_2)_{0.92}\ (Y_2O_3)_{0.08}$	$(ZrO_2)_{0.88}\ (Y_2O_3)_{0.12}$
$\frac{1}{2}(C_{11} - C_{12}) > 0$	0.585	0.627
$\frac{1}{3}(C_{11} + 2C_{12}) > 0$	1.26	1.39
$C_{11}^2 - C_{12}^2 > 0$	3.305	4.032

(Units of C_{ij}'s are 10^{12} dynes cm^{-2})

The elastic stability conditions for $(ZrO_2)_{0.92}\ (Y_2O_3)_{0.08}$ and $(ZrO_2)_{0.88}\ (Y_2O_3)_{0.12}$ at $77^{o}K$.

it is seen that all the conditions are well satisfied. Values for the 8 mole% yttria crystals are all significantly lower than those for the 12 mole% yttria which is consistent with the composition edge for stabilisation occuring near 6 mole% yttria in zirconia (see Figure (6.1)). C_{44} is the only elastic tensor coefficient which may be interpreted directly in terms of the crystal structure (see Chapter 2, Section 2.4). It is a measure of the resistance to deformation with respect to a shearing stress applied across the (100) plane in the [010] direction (see Figure (2.1)). It is desirable to find linear combinations of C_{11} and C_{12} which have simple interpretations. The bulk modulus, $(C_{11} + 2C_{12})/3$, is a measure of the resistance to deformation with respect to hydrostatic pressure and must be positive. The combination $(C_{11}-C_{12})/2$, the resistance to deformation by a shear stress applied across the (110) plane in the $[1\bar{1}0]$ direction, must also be positive, (see Figure (2.1)). That both $(C_{11} + 2C_{12})/2$ and $(C_{11} - C_{12})/2$ decrease between the 12 mole% and 8 mole% yttria samples is again consistent with the 6 mole% yttria lower limit to the fluorite phase. A negative value for either of these moduli would cause a spontaneous collapse of the lattice.

The absence of a substantial temperature dependence of $(C_{11} - C_{12})/2$ for these crystals is a reflection of the vertical phase boundary line between the cubic and monoclinic modifications (see Figure (6.1)). If the composition at which stabilisation of

the fluorite structure is achieved did vary substantially with temperature, then $(C_{11} - C_{12})/2$ near the limit would be temperature sensitive.

For an elastically isotropic cubic crystal $(C_{11} - C_{12})$ should equal $2C_{44}$. The extent to which this relation holds is a good indication of the isotropy of the crystal. Values of $2C_{44}/(C_{11} - C_{12})$, quoted in Table (6.2) for the two solid solutions are not close to unity: a shear on a (100) cube face is resisted rather more than one on a diagonal (110) face. Values for the anisotropy ratio for the 8 mole% yttria are about ten per cent greater than for the 12 mole% yttria sample, indicating a decrease in the resistance to shears on a (110) face as the composition tends to that of the phase boundary.

Knowledge of the bulk modulus and equilibrium lattice spacing can be used to develop an understanding of the type of binding between the atoms in the crystals. The approach used here is to assume that the binding is predominately ionic and then to see if this is justified by the results.

The potential energy function and its relation to the bulk modulus

The lattice energy of a crystal may be defined as the energy involved in the process of bringing the ions from infinity to the positions which they occupy in the crystal. The net result of the electrostatic attraction between unlike ions and the electrostatic

repulsion between like ions is that each ion is closer to ions of opposite charge. In the calcium fluoride lattice, each fluorine ion is surrounded tetrahedrally by four calcium ions and each calcium ion is at the centre of a cube of eight fluorine ions (see Figure (6.3)). In order to account for the observed stability of crystals composed of ions, it is necessary to introduce interionic non-coulombic forces of repulsion. This repulsive term may be chosen to contain just two empirical parameters. In the early treatments of ionic crystals the repulsive term was taken to vary as the inverse nth power of the ionic separation, so that the potential energy ϕ of a system consisting of two ions at a distance and apart is written as

$$\phi = \frac{-Z_1 Z_2 e^2}{r} + \frac{b}{r^n} \qquad (6.1)$$

where Z_1 and Z_2 are the valencies of the ions, e is the electronic charge and b is a positive constant. This is the potential initially used by Born (1921). But because the repulsive interaction is of a quantum mechanical nature essentially resulting from the Pauli exclusion principle, Born and Mayer modified the initial treatment (1932, 1933). They replaced the b/r^n type repulsion by one varying as $ae^{-r/p}$, where a and p are constants. This form was suggested by the exponential behaviour of electron wave functions

at large distances from the nucleus. In addition they included terms due to the van der Waal's interaction and dipole-quadrupole interaction. A constant term due to the zero point energy (ϵ_o) was also put in. The final equation for the potential energy between two unlike ions was

$$\phi = -\frac{A}{r} - \frac{B}{r^6} + ae^{-r/p} + \frac{D}{r^8} + \epsilon_o \qquad (6.2)$$

where B/r^6 is the van der Waal's attractive term and D/r^8 is the dipole-quadrupole term.

The most detailed quantum mechanical treatment of ionic crystals was performed by Löwdin on a series of alkali halides (1947). These calculations assumed that the wave functions of the ions could be taken as those determined self-consistently for the corresponding free ions. Good agreement with experiment was obtained. As mentioned later, this theory gave the first explanation of the observed departures for ionic crystals from the Cauchy relations.

A large amount of data has been collected on the elastic and thermochemical behaviour of ionic crystals. The vast majority have been analysed on the basis of the original Born equation (6,1). Theoretical values of crystal energies have been computed from knowledge of two quantities: the bulk modulus, the equilibrium lattice spacing. These crystal energies were then compared with those experimentally determined from the Born-Haber thermochemical

cycle (Born, 1919; Haber, 1919). The fair agreement which resulted in most cases is contained in the small variation in computed values of crystal energies which would result from a variation in the repulsive exponent by as much as unity (see Table (6.3)).

The data for the zirconia-yttria solid solutions may be analysed on the basis of the Born equation and the results, compared with the ionic crystals which have been dealt with in the same way.

The crystal energy per unit cell is obtained by summing equation (6.1) over all pairs of ions. Because the repulsive potential varies rapidly with distance, only nearest neighbours need be considered for this term. Following Sherman (1932), the energy per unit cell may be written as

$$\phi = \frac{-\alpha e^2 \mu A_{R_o}}{r} + \frac{B}{r^n} \qquad (6.4)$$

where α is the largest common factor in the valencies of all the ions (in this case 2), μ is the number of molecules in the unit cell and A_{R_o} is the Madelung constant which will be defined below. B and n are constants; B can be determined by setting the forces of attraction and repulsion equal and opposite at the equilibrium configuration of the lattice, and is expressed by putting $(d\phi/dr)_{r=R_o}$ equal to zero; R_o is some characteristic

TABLE (6.3)

Substance	Repulsive Exponent	Cauchy Relation C_{12}/C_{44}	U_o experimental	U_o calculated
AgCl	9·5	5·77	207·3	187·3
$C_a F_2$	8·0	1·45	618·0	617·7
K Br	9·5	1·15	156·2	157·8
K Cl	9·0	0·99	164·4	164·4
K I	10·5	1·02	151·5	149·0
Li F	6·0	0·67		240·1
Mg O	7·0	0·59		940·1
Na Cl	8·0	0·98	182·8	180·4
Pb S	10·5	1·20	731	705
Zn S	9·0	1·75	851	819
$Pb O_2$	9·5		2831	2620
$Al_2 O_3$	7·0		3617	3708
$(ZrO_2)_{.92} (Y_2O_3)_{.08}$	8·5	0·55		2597
$(ZrO_2)_{.88} (Y_2O_3)_{.12}$	9·1	0·63		2571

The analysis of various ionic crystals on the basis of the Born equation. The calculated crystal energy is compared with that obtained experimentally from the Born-Haber cycle. Also included is the repulsive exponent and the Cauchy relation.

equilibrium distance and is related to the lattice parameters in a way to be defined below.

From equation (6.4)

$$\left(\frac{d\phi}{dr}\right)_{r = R_o} = \frac{\alpha^2 e^2 \mu A_{R_o}}{R_o^2} \quad \frac{-nB}{R_o^{n+1}} = 0 \tag{6.5}$$

Hence,

$$B = \frac{\alpha^2 e^2 \mu A_{R_o} R_o^{n-1}}{n} \tag{6.6}$$

Substituting for B in equation (6.4)

$$\phi = \frac{-\alpha^2 e^2 \mu A_{R_o}}{r} + \frac{\alpha^2 e^2 \mu A_{R_o} R_o^{n-1}}{nr^n} \tag{6.7}$$

Thus, for a crystal in equilibrium,

$$\phi_o = \frac{-\alpha^2 e^2 \mu A_{R_o}}{R_o} \left(1 - \frac{1}{n}\right) \tag{6.8}$$

$$\phi_o = \phi_o^{(1)} + \phi_o^{(n)}$$

where $\phi_o^{(1)}$ is the potential energy due to the coulombic forces and $\phi_o^{(n)}$ that due to the intrinsic repulsive forces. The lattice energy per mole is

$$U_o = \frac{N}{\mu} \phi_o \tag{6.9}$$

where N is Avogadros number. By combining (6.8) and (6.9) and choosing R_o to be the cube root of the molecular volume δ_o

$$U_o = - \frac{\alpha^2 e^2 N A_{\delta_o}}{\delta_o} \left(1 - \frac{1}{n}\right) \tag{6.10}$$

This choice of R_o, to a first approximation takes into account the presence of oxygen vacancies.

The Madelung constant A_{δ_o} for a particular choice of equilibrium distance δ_o is defined as follows. The electrostatic energy per unit cell may be written as

$$\phi^{(1)} = \frac{-e^2}{2} \sum_{s=1}^{y}{}' \sum_{t=1}^{\infty}{}' \frac{Z_s Z_t}{r_{st}} \tag{6.11}$$

where Z_s and Z_t are the valencies of the Sth and tth ion respectively and r_{st} is the distance between them. The primes indicate that the terms for r equal to zero (s = t) are omitted. y is the number of ions per unit cell and the factor $\frac{1}{2}$ ensures that each ion pair is only counted once. If $\phi_o^{(1)}$ is written as

$$\phi^{(1)} = \frac{-e^2}{2} \sum_{s}^{y}{}' Z_s \eta_s \tag{6.12}$$

then η_s is given by

$$s = \sum_{t}{}' \frac{Z_t}{r_{st}} \tag{6.13}$$

From equation (6.8)

$$\frac{A_{\delta_o}}{\delta_o} = \frac{1}{2\alpha^2\mu} \sum_s{}' Z_s \eta_s \qquad (6.14)$$

The series for η_s was first calculated by Madelung for sodium chloride. The most commonly used method for computing Madelung constants is that given by Ewald (1921).

The final expression for the lattice energy per mole becomes

$$U_o = -329{\cdot}7\,\alpha^2\,(\rho/M)^{1/3}\,A_{\delta_o}\,(1 - \tfrac{1}{n}) \qquad (6.15)$$

Where M is the weight in grams of one molecule and ρ is the density; values of (ρ/M) are given in Table (6.4). A_{δ_o} for the fluorite lattice is 7·33058 (Sherman 1932; van Gool and Piken 1969). Calculated values of the Madelung energy $(329{\cdot}7\,\alpha^2\,(\rho/M)^{1/3}\,A_{\delta_o})$ are collected in Table (6.4). The attractive energies of the solid solutions are slightly greater than for pure zirconia. The difference between the Madelung energies for the two compositions of zirconia-yttria is small; in fact that for the 8 mole% yttria is larger than that for the 12 mole% yttria composition. At first sight this might seem surprising; but it must be remembered that the stability of a crystal is governed by the second derivative of the total cohesive

TABLE (6.4)

	ρ/M $\mathring{A}^{-3}$	Madelung attractive energy U_M	Repulsive energy U_N	Total binding energy $U_o=U_M+U_N$	Debye Temperature
ZrO_2		-2889	-	-	-
$(ZrO_2)_{0.88}$ $(Y_2O_3)_{0.12}$	0.0268	-2892	+321	-2571	604°K
$(ZrO_2)_{0.92}$ $(Y_2O_3)_{0.08}$	0.0283	-2945	+348	-2597	595°K

Energy units are kcals/mole

Results of the analysis of the bulk modulus and lattice parameter data for the zirconia-yttria solid solutions on the basis of the Born equation. The Debye temperature calculated from elastic constant data is also included.

energy with respect to ionic separation; thus it is the repulsive term which dominates the mechanical properties of ionic crystals.

The total cohesive energy of the solid solutions becomes available when the repulsive exponent is known. One way of calculating the repulsive exponent is via the bulk modulus as follows. Within the region where Hookes law is obeyed, the ratio of the applied hydrostatic pressure to the volume strain defines the bulk modulus K and is written as

$$K = -V. \frac{dP}{dV} \tag{6.16}$$

where P is the applied hydrostatic pressure and V is the volume of a mole. The pressure applied to the crystal is related to the total energy E of the crystal by the thermodynamic equation.

$$P = T\left(\frac{\partial P}{\partial T}\right)_V + \left(\frac{\partial E}{\partial V}\right)_T \tag{6.17}$$

At $0^{\circ}K$, E is equal to U if the zero point energy is negligible in comparison with the total potential energy. Assuming this to be so, then

$$P = \left(\frac{\partial E}{\partial V}\right)_T = \frac{dU}{dV} = \frac{dU}{dr} \quad \frac{dr}{dV} \tag{6.18}$$

On differentiating P with respect to V

$$\frac{dP}{dV} = \frac{d^2U}{dr^2} \left(\frac{dr}{dV}\right)^2 + \frac{d^2r}{dV^2} \cdot \frac{dU}{dr} \tag{6.19}$$

When the crystal is in equilibrium with the applied pressure, (dU/dr) is zero and

$$\frac{dP}{dV} = \left\{ \frac{d^2U}{dr^2} \left(\frac{dr}{dV}\right)^2 \right\}_{r = \delta_o} \tag{6.20}$$

When equation (6.20) is substituted into (6.16), the bulk modulus is given by

$$K = -V\left\{ \frac{d^2U}{dr^2} \left(\frac{dr}{dV}\right)^2 \right\}_{r = \delta_o} \tag{6.21}$$

The volume V of a mole is Nr^3 and so

$$\left(\frac{dr}{dV}\right)^2_{r=\delta_o} = \frac{1}{9N^2\delta_o{}^4} \tag{6.22}$$

Since the total energy per mole is

$$U = \frac{-\alpha^2 e^2 N A_{\delta_o}}{r}\delta_o + \frac{\alpha^2 e^2 N A_{\delta_o}}{nr^n} \delta_o{}^{n-1} \tag{6.23}$$

Then $$\left(\frac{d^2U}{dr^2}\right)_{r = \delta_o} = -\left\{ \alpha^2 e^2 A_{\delta_o} (n-1) \right\} / \delta_o{}^3 \tag{6.24}$$

Finally by substituting (6.24) and (6.22) into (6.20) and rearranging, the expression for the repulsive exponent is found to be

$$n = 1 + \frac{9\,\delta_o{}^4 K}{\alpha^2 e^2 A_{\delta_o}} \tag{6.25}$$

The bulk modulus value required by this equation is in fact, as shown in the derivation (6.17) and (6.18), the isothermal bulk modulus at $0^{o}K$. The value available here is the adiabatic bulk modulus extrapolated to $0^{o}K$ from $77^{o}K$. The conversion of adiabatic to isothermal elastic moduli requires knowledge of the thermal expansion and constant pressure specific heat (See Chapter 2, Section 3.1), neither of which are available for zirconia-yttria solid solutions. But the difference between the isothermal and adiabatic moduli is generally less than one per cent; the temperature dependence of the measured bulk modulus is slight. The value of n, calculated using the extrapolated value of K, is not expected to be significantly in error; for $(ZrO_2)_{0.88}\ (Y_2O_3)_{0.12}$ the repulsive exponent is found to be 9·1 and that for $(ZrO_2)_{0.92}\ (Y_2O_3)_{0.08}$ to be 8·5.

For crystals in which the binding is largely ionic the repulsive exponent, calculated in a similar manner as above, is usually of the order of 9. Presented in Table (6.3) are values of repulsive exponents of many ionic crystals for comparison with the results obtained here. Thus by inference the attractive forces in yttria-stabilised zirconia are consistent with the hypothesis of coulombic attractive forces.

The agreement between experimental values of the cohesive energy and those calculated on the basis of the Born equation for the materials listed in Table (6.3) could accrue from insensitivity

to changes in the repulsive component which accounts for only about 10% of the total. For example, a change of ± 1 in the repulsive exponent leads to a change of only about ± 1% in the total cohesive energy.

In the majority of crystals, the Cauchy relation $C_{12} = C_{44}$, is not obeyed. Ionic crystals are materials in which interatomic forces can be most nearly approximated to central forces, which the Cauchy relation requires. Table (6.3) shows that for none of the ionic crystals listed is the relation exactly obeyed. In fact for the zirconia-yttria solutions the departure is not excessively large. Expressions for the elastic moduli derived on the basis of the Born potential (Kellerman 1940; Krisham and Roy 1952) necessarily predict the Cauchy relation to hold since the model involves only central forces in a centrosymmetric lattice. The origin of the experimental departure from the Cauchy relation was first pointed out by Löwdin (1947), in a quantum mechanical treatment of the lattice energy, who attributed it to the importance of certain integrals which are the origin of multibody forces and which cannot be replaced by equivalent two body central forces. Löwdin's theory predicts the correct sign for the deviation from the Cauchy relation but not quite the actual magnitude.

Thus the interionic central force model is not strictly applicable to the zirconia-yttria solid solutions, as indeed to

any other ionic crystal. But, as mentioned previously, the insensitivity of the cohesive energy to the relatively short range, non-central force components leads to a realistic value of cohesive energy.

CHAPTER 7

Elastic wave propagation in the group VB semimetals

7.1 Introduction

The aim of the work presented in this chapter is to compile and discuss the orientation dependence of elastic wave propagation in the group VB semimetals. By virtue of their unusual rhombohedral A7 crystal structure of space group D^5_{3d} ($R\bar{3}m$), the elements arsenic, antimony and bismuth constitute a unique series. While the crystal symmetries are identical, the antimony and bismuth lattices are much less distorted than that of arsenic, which in fact tends towards a layer-like structure. Thus it is interesting to contrast the elastic behaviour of arsenic with that of antimony and bismuth.

Elastic wave velocities in arsenic were measured and the elastic constants thus obtained were found to show distinctive differences from those of antimony (Epstein and deBretteville 1965) and bismuth (Eckstein, Lawson and Reneker 1960). These differences are discussed in terms of the layer-like nature and thus the highly anisotropic binding forces which are present in arsenic but not in the other two elements.

7.1.1 Crystallography of arsenic

Arsenic crystallises in a rhombohedral structure of space group D^5_{3d} ($R\bar{3}m$). Two interpenetrating face-centred rhombohedral lattices form the crystal lattice. Figure (7.1) shows the unit

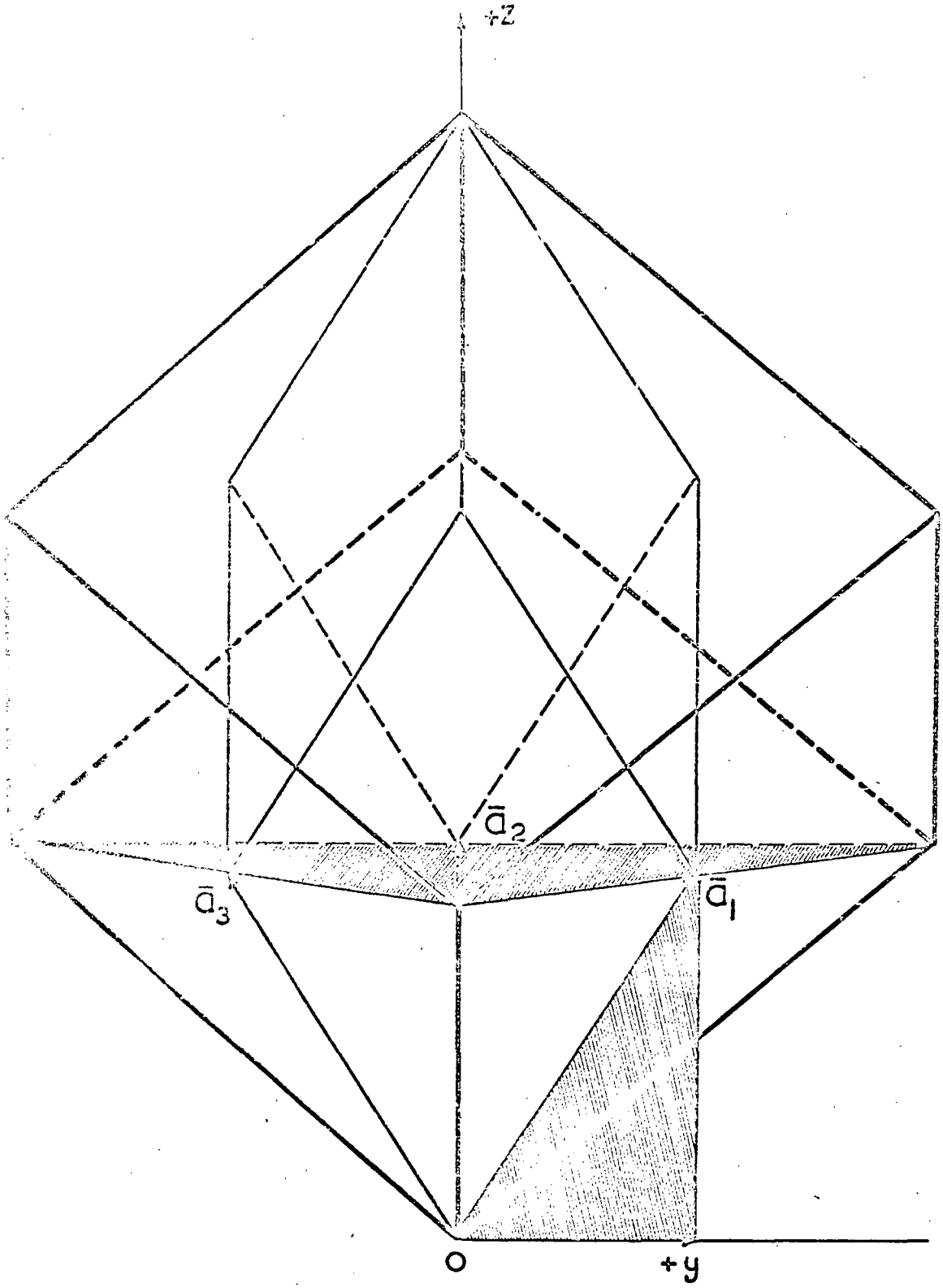

Figure (7.1) The primitive rhombohedral cell sited inside the large face-centred rhombohedron for the A7 structure.

cell and primitive translation vectors. Any unit cell contains two atoms, each pertaining to a different rhombohedral sub-lattice. The two face-centred rhombohedrons are separated along the body diagonal by a fraction 2u of this diagonal (Falicov and Golin 1965). A value of u equal to 0·25 corresponds to that primitive rhombohedron constructed in the closely related structure composed of two interpenetrating face-centred cubes. This displacement parameter u is 0·226 for arsenic, 0·2336 for antimony and 0·23407 for bismuth, emphasising that arsenic is considerably more distorted than bismuth or antimony; while the latter two have almost cubic crystal structures, arsenic is far from being so. Indeed, arsenic tends towards a layer-like crystal structure. Any particular atom is sited on one of the (111) planes and has three nearest neighbours on the adjacent parallel plane: three next nearest neighbours lie on another (111) plane on the other side of the given atom but much further away. The nearest neighbour and next nearest neighbour distances are 2·51Å and 3·15Å respectively. Thus planes normal to the trigonal [111] direction occur in pairs in which the atoms are comparatively close together while the double layers are more widely spaced. Three different arrangements of atoms on the planar networks are extant. A projection onto the (111) plane (Figure 7.2)) shows

Figure (7.2) (a) The arrangement of the three types of atomic network A, B and C for arsenic shown projected onto the xy plane. (b) The sequential nature of the planes normal to the Z-axis in arsenic.

the relationship between these networks, labelled A, B, C, which follow sequentially along the z-axis and are separated by the short and long interplanar spacings in turn. The crystal structure is described by the sequence, shown in Figure (7.2) 123123123 of three types of double layer network.

A right-handed orthogonal set of coordinate axes may be defined following the normally accepted convention for trigonal crystals (Cady 1964). The z-axis (trigonal direction) formed by the intersection of three mirror planes mutually oriented at $\pm 120^{\circ}$ lies along the long body diagonal of the primitive rhombohedral unit cell defined from the lattice translation vectors a_1, a_2 and a_3 (see Figure (7.1)). The y-axis (bisectrix) for which there are three options, is defined by projecting an a_i onto the trigonal plane: the positive y direction is taken outwards from the origin O of the a_i. A positive x-axis (binary) completes the right-handed set.

The symmetry elements for arsenic are shown in Figure (7.3). The z-axis exhibits threefold rotatory inversion symmetry while the three possible x and y axes show twofold and mirror symmetry respectively. Axes of pseudo-symmetry are described later with reference to crystal orientation, (see (7.3.1)).

7.2 The characteristics of elastic wave propagation in trigonal crystals

Although elastic constant determinations of trigonal crystals is similar to the tetragonal class (see chapter 5), there are several points peculiar to the trigonal system which warrant complete elucidation.

The $\bar{3}m$ point group of arsenic places it in the RI Laue group which involves six independent elastic moduli as detailed below,

$$\begin{array}{cccccc} C_{11} & C_{12} & C_{13} & C_{14} & 0 & 0 \\ C_{12} & C_{11} & C_{13} & -C_{14} & 0 & 0 \\ C_{13} & C_{13} & C_{33} & 0 & 0 & 0 \\ C_{14} & -C_{14} & 0 & C_{44} & 0 & 0 \\ 0 & 0 & 0 & 0 & C_{44} & C_{14} \\ 0 & 0 & 0 & 0 & C_{14} & \frac{1}{2}(C_{11}-C_{12}) \end{array} \qquad (7.1)$$

where the C_{ij}'s connect the stress components to the strain components in the right-handed orthogonal Cartesian coordinate system previously defined (7.1.1).

The form of the determinantel equation (2.23) giving conditions for wave equation (2.22) solutions to exist, is determined by the form of the equations (2.24). For arsenic these are

$$
\begin{aligned}
L_{11} &= n_1^2 C_{11} + \tfrac{1}{2} n_2^2 (C_{11}-C_{12}) + n_3^2 C_{44} + 2n_3 n_2 C_{14} \\
L_{12} &= 2n_3 n_1 C_{14} + \tfrac{1}{2} n_1 n_2 (C_{11}+C_{12}) \\
L_{13} &= n_3 n_1 (C_{13}+C_{44}) + 2n_1 n_2 C_{14} \\
L_{22} &= \tfrac{1}{2} n_1^2 (C_{11}-C_{12}) + n_2^2 C_{11} + n_3^2 C_{44} - 2n_2 n_3 C_{14} \\
L_{23} &= (n_1^2 - n_2^2) C_{14} + n_2 n_3 (C_{44}+C_{13}) \\
L_{33} &= (n_1^2 + n_2^2) C_{44} + n_3^2 C_{33}
\end{aligned}
\tag{7.2}
$$

The most straightforward direction for analysis is the [001] threefold symmetry direction. Solution of (2.23) for this direction yields the velocities of a degenerate pure transverse and a pure longitudinal wave as $(C_{44}/\rho)^{\frac{1}{2}}$ and $(C_{33}/\rho)^{\frac{1}{2}}$ respectively.

The only other major crystallographic directions which are pure directions are any one of the three x-axes directions, which are indistinguishable from one another and are perpendicular to mirror planes (see Figure (7.3)). But although the modes in the [100] direction are pure, the particle displacement vectors for the two transverse waves is not known without a priori knowledge of the elastic moduli. This is overcome in practice by a rotation of the Y-cut transducer until two distinguishable transverse wave velocities are recorded. The solutions for the [100] direction wave velocities are for the pure longitudinal

$$\rho V^2 = C_{11} \tag{7.3}$$

and for the two pure transverse waves

$$\rho V^2 = \tfrac{1}{4}(C_{11}-C_{12}+2C_{44}) \pm \tfrac{1}{4}\sqrt{(C_{11}-C_{12}-2C_{44})^2+16C_{14}^2} \qquad (7.4)$$

The angle ϕ which the particle displacement vector makes with the x-y plane is given by

$$\tan\phi = \frac{R_{o3}}{R_{o2}} = \frac{-C_{14}}{C_{44}-\rho V^2} \qquad (7.5)$$

obtained by substitution of (7.4) into (2.22). The angle ϕ has two values corresponding to the two transverse wave velocities and differing by $\pi/2$ demonstrating that the particle displacement vectors for the three solutions are mutually orthogonal as required. (The eigenvectors corresponding to the three eigenvalues of an equation such as (2.22) in which the coefficients of the eigenvector components form a symmetric matrix, are mutually orthogonal. For the particular case of elastic wave propagation, this orthogonality of wave polarisations was first pointed out by Lord Kelvin (1904)).

Thus by measurement of the five wave velocities obtainable along the [001] and [100] directions of propagation, all the elastic constants except C_{13} are calculable. But it must be emphasised that in the case of C_{14} only its magnitude is obtained;

the sign of C_{14} is found from propagation in a mirror plane as discussed below. It should be noted that the sign of C_{14} is dependent upon the definition of axes (7.3).

Inspection of equation (7.2) shows that C_{13} is available from velocity measurements in directions for which both n_1 and n_2 are not zero and n_3 is not zero. The most straightforward directions which embrace these direction cosine requirements are those which lie in the yz plane at any angle to the y-axis except 0° and 90°. Solutions of equation (2.23) show that a pure transverse wave can propagate at all angles in the yz plane with a velocity given by

$$\rho V^2 = n_2^2(C_{66}-C_{44}) + C_{44} + 2n_2n_3C_{14} \tag{7.6}$$

The velocities of the remaining two modes are

$$\rho V^2 = n_2^2(C_{11}-C_{33})+C_{44}+C_{33}-2n_2n_3C_{14}\pm[(n_2^2(C_{11}-C_{33})+C_{33}-2n_2n_3C_{14})^2 +4\,(n_2n_3(C_{44}+C_{13})-n_2^2C_{14})^2-(n_2^2C_{11}+n_3^2C_{44}-2n_2n_3C_{14})(n_2^2(C_{44}-C_{33})+C_{33})\,]^{\frac{1}{2}} \tag{7.7}$$

For all directions in the yz plane except the z-axis and one other direction, these velocities correspond to that of a quasi-longitudinal mode (positive sign) and that of a quasi-transverse mode (negative sign). The one direction in the yz plane in

addition to the z-axis which can support three pure modes occurs when

$$\tan^{-1}\left(\frac{n_3}{n_2}\right) = \frac{n_2^2 C_{11} + n_3^2 C_{44} - 2n_2 n_3 C_{14} - \rho V^2}{n_2^2 C_{14} - n_2 n_3 (C_{44} + C_{13})} \qquad (7.8)$$

where V is the velocity of the pure longitudinal mode along this direction.

Propagation in the yz plane has two advantages over use of directions in the xz plane (which also satisfy the direction cosine requirements for inclusion of C_{13} into the velocity expressions). Firstly the yz plane directions are, except for the z-axis and one other direction, all quasi-pure directions; all directions in the xz plane except for the x-axis which is pure, are impure directions. Secondly the sign of C_{14} is not available from velocity measurements in the xz plane.

7.3 Experimental details and results

The crystals used here were those grown by Jeavons and Saunders (1968) by the vapour phase method from 99.9995 per cent purity arsenic for low temperature galvanomagnetic measurements (Jeavons and Saunders, 1969). The perfection of the crystals was high as evidenced by the low dislocation etch pit density (10^4 cm^{-2})

on the cleaved trigonal plane.

As mentioned previously (7.2.1) for the $R\bar{3}m$ structure, the tensor component signs can depend upon the definition of a right-handed (+x, +y, +z) axial set in the particular crystal under investigation. In the present instance this is so for C_{14}. The method for assignment of axes to samples used here is now described.

7.3.1 Orientation of samples: etch pit studies

(Work performed in this section was a joint effort by Mr. Z. Sumengen and myself).

The x-axis may be identified from Laue back reflection photographs by reference to the relationship between the large rhombohedron and a distorted cube; the $[100]^*$ directions show pseudo-fourfold symmetry and the body diagonal directions (except [111] show pseudo-threefold symmetry. The quadrant in the mirror plane formed by the +y and +z axes contains a pseudo-threefold axis and that formed by the -y and +z axes a pseudo-fourfold axis. One practical approach to assignment of such a right-handed system in a particular sample is to inspect etch pits on the (111) cleaved surfaces.

---

* In this section, direction indices are referred to the large face-centred rhombohedron shown in Figure (7.1).

Crystals were cleaved to expose the (111) planes and etched with an etch composed of two parts hydrofluoric acid, one part nitric acid and one part glacial acetic acid (Jeavons and Saunders 1968). Straight slip lines, mutually oriented at 120° are observed on the (111) plane along the $[10\bar{1}]$ directions, that is parallel to the three binary directions. Etch pits (see Figure (7.4)) on a given plane all have the same orientation and are almost triangular in shape, the sides of the 'triangle' being somewhat rounded. The tangents to the centre of the pit sides are parallel to the slip lines. With the +z-axis defined as the outward normal to the exposed (111) plane, the orientation of the etch pits with respect to the +x+y+z axial set was determined from back reflection Laue photographs, reference being made to the above mentioned pseudo-symmetry axes. It was found that a vector drawn from a pit centre, normal to a pit side, points along the +y-axis; see Figure (7.4). A cleavage plane may be exposed on opposite sides of a given sample thus allowing two possible definitions of the +z-axis as outward normals to these faces. For this etch pit orientation rule to be consistent, the etch pits must point in opposite directions on these two faces: this was confirmed experimentally.

Figure (7.3) Class $\bar{3}$ m symmetry elements.

Figure (7.4) Etch pits on (111) cleaved plane of arsenic. The +ve *y* axis points from a pit centre normal to a pit side when the +Z axis is defined as the outward normal to the exposed cleavage plane.

Brown et al (1968) suggest for bismuth that a unique assignment of +x+y+z axes can be made using a twinning plane. If the (111) plane is intersected by a twinning plane such that a z-axis intercepts the twinning plane below the (111) surface, then the +y-axis points from the binary line, defined as the intersection of the two planes, to an origin where the z-axis cuts the surface (see Figure 2 of their paper). This rule is correct, if, as described in the literature (Hall 1954) the twinning planes are (110) planes. To test this, a large (approximately 2 cm x 1 cm x 1 cm) twinned crystal of arsenic was examined by use of back reflection Laue photographs. The twin plane was found to be (110), within the accuracy of $\pm 0.5^{\circ}$. The (111) planes on either side of the twin plane were exposed by cleaving and the etch pit orientations examined. The results, illustrated in Figure (7.5), verify experimentally that the rule proposed by Brown et al (1968) for bismuth also holds for arsenic.

7.3.2 Elastic wave velocities and elastic moduli in arsenic

Samples for ultrasonic measurements were oriented by the X-ray back reflection Laue technique and by reference to the etch pit orientation on the (111) cleaved surface (7.3.1). Parallel surfaces normal to the desired propagation direction were obtained by spark cutting and planing as described in (3.5). The

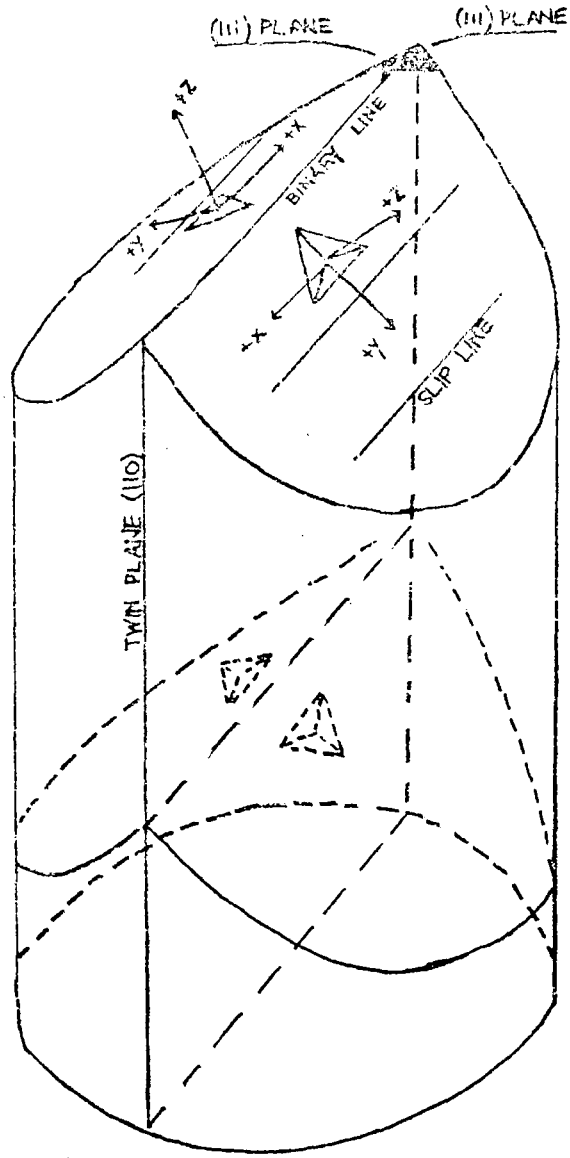

Figure (7.5). Schematic of the orientations found for a twinned arsenic crystal. Etch pit orientation on the (111) cleaved surfaces and one of the three sets of slip lines (each parallel to a possible binary x direction) are illustrated. The intersection of the (111) planes on either side lies parallel to a binary direction; the twin plane which is the (110), contains a binary direction. The relationship between etch pits and the Cartesian ($+x, +y, +z$) coordinate system on either side of the twin plane is shown.

ultrasound was excited using the appropriate cut transducers (3.4) bonded to the sample. Difficulties in bonding the transducer to the samples were encountered. A large number of bonding agents were tried (see (3.6.3)) without success. The ultrasound was finally injected by coupling the transducers to the samples with tensol cement. The measurements of ultrasound wave velocities were limited by the bond behaviour to those obtained at room temperature. In the directions used for wave velocity measurements the ultrasound suffered attenuations in the range 3 to 4 db per μsec. In fact for the direction at 14.5° to the positive y-axis in the yz plane in the +y+z quadrant, no echoes were observed for the quasi-longitudinal or quasi-transverse modes; velocity measurements in this direction were limited to the pure transverse mode.

Initial measurements of the velocities of waves propagating in arsenic were jointly undertaken by Mr. Z. Sumengen and myself. The elastic moduli calculated from these velocities were presented in a paper (Pace, Saunders and Sumengen 1970) a copy of which is bound at the back of this thesis.

To improve the accuracy of a set of elastic constant measurements a valuable procedure is to use a predetermined set to estimate the wave velocity surface and the behaviour of the energy flux associated with the elastic waves. Then this

TABLE (7.1)

Equation number	Equations relating the elastic stiffnesses to the wave velocities	Propagation direction	Polarisation direction	Experimental velocities ($\times 10^5$ cm.sec^{-1})
7.9	$\rho V_1^2 = C_{11}$	100	100	4.79
7.10	$\rho V_2^2 = \frac{1}{2}[(C_{66}+C_{44})+((C_{44}-C_{66})^2+4C_{14}^2)^{\frac{1}{2}}]$	100	001	2.99
7.11	$\rho V_3^2 = \frac{1}{2}[(C_{66}+C_{44})-((C_{44}-C_{66})^2+4C_{14}^2)^{\frac{1}{2}}]$	100	010	1.89
7.12	$\rho V_4^2 = C_{33}$	001	001	3.20
7.13	$\rho V_5^2 = C_{44}$	001	in xy plane	2.05
7.14	$2\rho V_6^2 = \frac{1}{2}(C_{11}+C_{33})+C_{44}-C_{14}$ $+((\frac{1}{2}C_{11}-\frac{1}{2}C_{33}-C_{14})^2+(C_{13}+C_{44}-C_{14})^2)^{\frac{1}{2}}$	$0, 1/\sqrt{2}, 1/\sqrt{2}$	$0, 1/\sqrt{2}, 1/\sqrt{2}$	4.32
7.15	$2\rho V_7^2 = \frac{1}{2}(C_{11}+C_{33})+C_{44}-C_{14}$ $-((\frac{1}{2}C_{11}-\frac{1}{2}C_{33}-C_{14})^2+C_{13}+C_{44}-C_{14})^2)^{\frac{1}{2}}$	$0, 1/\sqrt{2}, 1/\sqrt{2}$	$0, -1/\sqrt{2}, 1/\sqrt{2}$	1.38
7.16	$\rho V_8^2 = \frac{1}{2}(C_{66}+C_{44})+C_{14}$	$0, 1/\sqrt{2}, 1/\sqrt{2}$	100	2.43
7.17	$\rho V_9^2 = \cos^2(14.5)C_{66}+\sin^2(14.5)C_{44}$ $+2\sin(14.5)\cos(14.5)C_{14}$	0, .9681, .2504	100	2.78

Elastic stiffness constant equations and room temperature experimental velocities in arsenic crystals.

information allows determination of a more accurate set. This procedure has been followed here. The previously determined (Pace, Saunders and Sumengen 1970) elastic constant set was used to establish the overall features of the phase velocities, the directions of energy flux and particle displacement vectors. On this basis further velocity measurements were founded. In particular to minimise the effects of the quasi-pure mode propagation in the yz plane, the aim was to get closer to the pure mode direction in the yz plane (which was found to be 14.5° from the +y-axis in the +y+z quadrant from the initial data (Pace, Saunders and Sumengen 1970)).

Table (7.1) presents a summary of the relationship between the measured velocities and the elastic moduli for the various propagation and polarisation directions used.

7.3.3 Least-mean squares determination of the elastic moduli

The computer programme for the least-mean square fit of r variables to q ($q > r$) equations has been described in connection with the elastic moduli determination of the tetragonal indium-thallium alloy (chapter 5).

Table (7.2) presents the room temperature values of the six elastic moduli of arsenic obtained from a least-mean squares computer fit to nine velocities. Data for antimony and bismuth

TABLE (7.2)

	C_{11}	C_{12}	C_{13}	C_{14}	C_{33}	C_{44}	C_{66}
As	130•2±1•0	30•3±2•1	64•3±1•1	-3•71±0•52	58•7±1•0	22•5±0•5	50•0±1•6
Sb	99•4	30•9	26•4	21•6	44•5	39•5	34•2
Bi	63•22	24•4	24•7	7•20	38•11	11•30	19•40
	S_{11}	S_{12}	S_{13}	S_{14}	S_{33}	S_{44}	S_{66}
As	30•3	20•2	-55•2	1•67	137•8	45•0	20•2
Sb	16•2	-6•1	-5•9	-12•2	29•5	38•6	44•6
Bi	25•74	-8•01	-11•35	-21•5	40•77	115•9	67•51

Elastic stiffness and compliance constants of arsenic (this work), antimony (Epstein and deBretteville 1965) and bismuth (Eckstein, Lawson and Reneker 1960).

Units are 10^{10} dynes cm^{-2} for the stiffness and 10^{-13} cm^2 $dyne^{-1}$ for the compliance constants.

is also included for purposes of comparison.

The nature of the equations (7.9[illegible]) to (7.17) is such that the errors in some of the elastic moduli is likely to be larger than that in others. The moduli which are expected to be subject to the least errors are those which are related directly to a velocity measurement.

An extensive survey of the effect of experimental errors in the velocities on the elastic moduli was carried out: the moduli were calculated by the least-mean squares methods using combinations of velocity errors. A maximum error of 1% in measured wave velocities was taken throughout. The moduli obtained in this way are given in Table (7.3). Many more combinations of experimental velocities each changed by 1% could have been used for further least-mean squares determination of the moduli. But, as Table (7.3) shows, a good assessment of the effect of the unavoidable (see (3.7.4)) experimental error in velocity measurement on individual moduli is obtained. The error quoted for each elastic stiffness constant in Table (7.2) was obtained from the scatter in its value in Table (7.3): moduli most affected by velocity errors are C_{12} and C_{14}. In particular the error in C_{14}, much the smallest modulus, is substantial but by no means large enough to change its sign; this is significant because the sign of C_{14} in arsenic is opposite to that in bismuth and antimony.

TABLE (7.3)

Velocities which have been changed by +1% of their experimental value	Resultant moduli					
	C_{11}	C_{12}	C_{13}	C_{14}	C_{33}	C_{44}
	130•2	30•3	64•27	-3•716	58•73	22•52
V_1	132•2	32•48	64•94	-3•539	58•65	22•47
V_2	130•0	28•83	63•94	-4•24	58•62	22•61
V_3	130•2	30•55	64•33	-3•574	58•72	22•77
V_4	130•1	30•19	65•03	-3•623	59•78	22•50
V_5	130•2	30•27	64•13	-3•998	58•66	22•75
V_6	130•3	29•65	64•33	-3•687	58•73	22•50
V_7	130•4	30•45	63•81	-3•735	58•74	22•53
V_8	130•7	31•08	64•86	-2•753	58•84	22•40
V_9	131•2	31•04	64•67	-3•971	58•91	22•61
V_1V_2	132•1	31•27	64•64	-4•051	58•58	22•56
$V_1V_2V_3$	132•0	31•35	64•58	-3•930	58•49	22•80
$V_1V_2V_3V_4$	131•8	31•35	65•40	-3•848	59•60	22•78
$V_1V_2V_3V_4V_5$	131•5	30•89	65•17	-4•127	59•53	23•01
$V_1V_2V_3V_4V_5V_6$	132•0	29•9	65•20	-4•130	59•50	23•00

Estimation of the errors in individual moduli of arsenic resulting from an experimental velocity error of 1%. Each row represents the results of a least-mean squares computer calculation of the C_{ij} using the velocity data as given in Table (7.1) except that those velocities indicated in column one are changed by +1%.

Another important feature is that C_{13} and C_{33} do not have large errors; because of the layer like nature of arsenic these two moduli dominate the components of the Gruneisen tensor (see 7.5).

7.4 Compilation of elastic wave propagation characteristics for arsenic, antimony and bismuth

Knowledge of the elastic moduli allows evaluation of the propagation characteristics of elastic waves in any direction of a crystal. The wave velocity surface is a three dimensional entity. Here, xy, yz and xz cross sections of the wave velocity surfaces are presented for the three elements arsenic, antimony and bismuth. A computer programme (see appendix (2)) was written to calculate the velocities for directions at every degree interval in the three planes. Velocities along directions in the yz plane were obtained from solutions of equations (7.6) and (7.7), while velocities along directions in the xy plane were obtained from solutions of the cubic equation

$$\rho^3 V^6 + A\rho^2 V^4 + B\rho V^2 + C = 0 \qquad (7.17)$$

where

$$A = -(L_{11} + L_{22} + L_{33})$$

$$B = (L_{11}L_{22} + L_{11}L_{33} + L_{22}L_{33} - L_{23}^2 - L_{12}^2 - L_{13}^2)$$

$$C = (L_{11}L_{23}^2 + L_{12}^2 L_{33} + L_{13}^2 L_{22} - L_{11}L_{22}L_{33} - 2L_{12}L_{13}L_{23})$$

The L's are given by equation (7.2) with $n_3 = 0$.
Similarly the velocities for propagation directions in the xz plane were obtained from solutions of equation (7.17) with $n_2 = 0$.

The xy, yz and zx cross sections of each of these three A7 structure crystals are presented in Figures (7.6) and (7.7). Each cross section will now be discussed in turn.

(i) xy cross section

In crystals of the $R\bar{3}m$ point group the xy plane is the plane normal to the threefold inversion symmetry axis. Because sound velocities are independent of the sense of direction, the xy velocity sections (Figure (7.6)) exhibit sixfold rotational symmetry about the z-axis. For the purpose of direct comparison, the sections (Figure (7.6) a, c, d) of all three elements are drawn to the same scale, although the origins differ. On this scale the three velocities in arsenic are apparently independent of direction. However, expansion of the scale (Figure (7.6) b) shows that arsenic also obeys the symmetry requirements.

Plausibly the lack of sensitivity in the xy plane of the velocities in arsenic in contrast to that in antimony and bismuth arises from the relatively small control exercised over the atomic motion in the xy plane by the forces between the double layers.

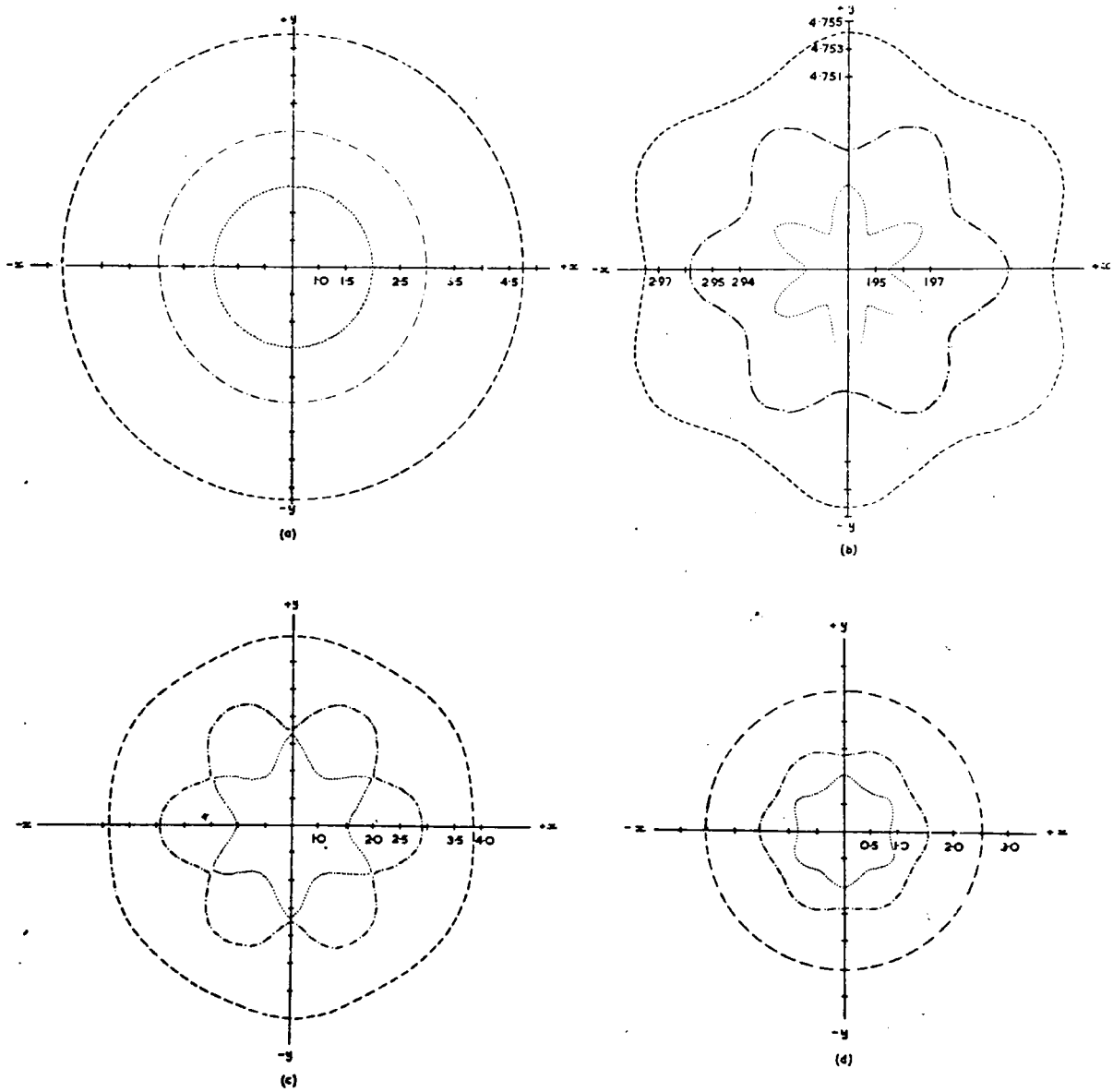

Figure (7.6) x-y velocity sections for : (a) and (b) arsenic ; (c) antimony ; (d) bismuth. Units are $\times 10^{5}$ cm sec^{-1}

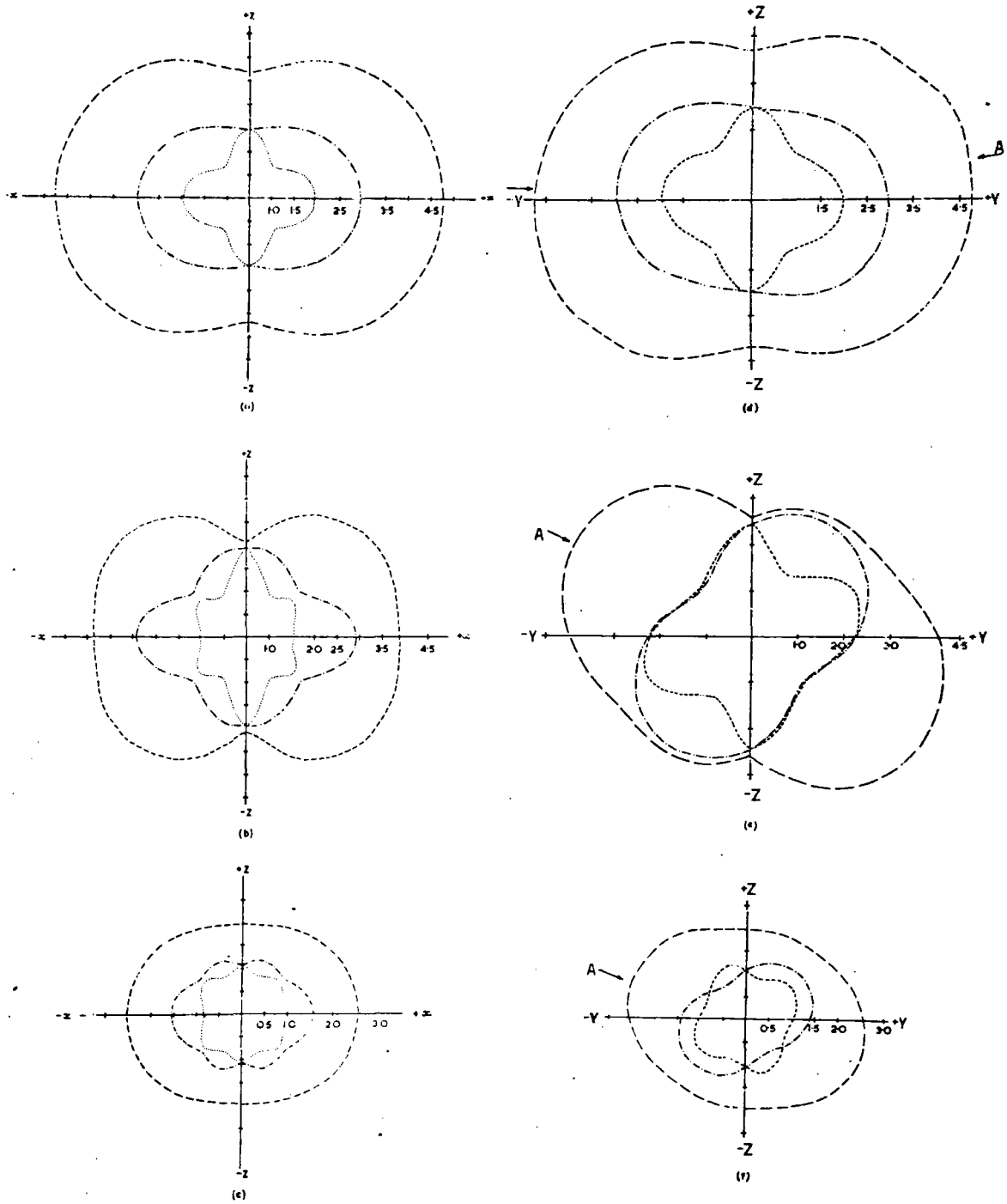

Figure (7.7) x-z and y-z velocity sections for : (a) and (d) arsenic ; (b) and (e) antimony ; (c) and (f) bismuth. Units are $\times 10^{5}$ cm sec^{-1}

(ii) zx cross section

The zx plane is normal to the yz mirror plane and includes both the binary (x) axis and the z-axis. In consequence these velocity cross sections show 2m symmetry (see Figure (7.7) a,b,c). The intersection at the z-axis of the two quasi-transverse wave sections occurs because two degenerate pure shear waves can be propagated down the z-axis. The relative softness of arsenic along the z-axis is manifested in the elongation of the section (Figure (7.7) a) along the x-direction.

(iii) yz cross section

Cross sections in the yz plane reflect the twofold rotational symmetry about the x-axis (Figure (7.7) d,e,f). The importance of an unambiguous assignment of the right-handed, orthogonal (+x, +y, +z) axial set to the particular sample under investigation is well demonstrated by these sections: velocities in the +y+z quadrant differ markedly from those in the -y+z quadrant, especially in antimony and bismuth. The arrow labelled A in each section indicates the pure mode direction in the yz plane in addition to the z-axis itself. For such a direction the particle displacement vectors are either parallel or perpendicular to the propagation direction. In the former case the wave is pure longitudinal and consequently the energy flux vector is also parallel to the

propagation direction.

We now turn to a detailed discussion of wave propagation in the yz plane.

7.4.1 Energy flux vectors for directions in the yz plane of arsenic, antimony and bismuth

Of considerable interest both experimentally and theoretically are the energy flux vectors* associated with elastic wave motion in anisotropic crystals. For example, in the pulse echo ultrasonic experiments deviation of energy flow from the propagation direction can result in the wave impinging on the specimen sidewalls giving rise to mode conversion and echo train deterioration.

The ith Cartesian component P_i of the energy flux vector is given by equation (2.33) as

$$P_i = -\left(\frac{p\omega}{2v}\right)^2 C_{ijkl} R_{o_j} R_{o_k} n_l \qquad (7.18)$$

For propagation in the yz plane of trigonal $\bar{3}m$ crystals it is found that P_1, that is the energy flux component along the x-axis, is zero for all three modes. Thus, the direction of energy flow is always in the yz plane for any mode propagation along any direction in that plane. Because of this, the direction of energy

---

* The energy flux is the rate of maximum flow of energy across a unit cross sectional area normal to the wave vector per unit time.

flow for modes propagating in the yz plane may be described by the angle β the energy flux vector makes with the positive y-axis. (A positive angle is measured from the +y to the +z-axis).

$$\beta = \tan^{-1}(P_3/P_2) \tag{7.19}$$

For the pure transverse mode which can propagate along any direction in the yz plane

$$\beta_{T_1} = \tan^{-1}\left(\frac{n_2C_{14} + n_3C_{44}}{n_2C_{66} + n_3C_{14}}\right) \tag{7.20}$$

In the case of the quasi-modes in the yz plane

$$\begin{aligned} P_2 &= (n_2C_{11}-n_3C_{14})R_{o2}^2+(-2n_2C_{14}+n_3C_{44}+C_{13})R_{o2}R_{o3}+n_2C_{44}R_{o3}^2 \\ P_3 &= (-n_2C_{14}+n_3C_{44})R_{o2}^2+n_2(C_{44}+C_{13})R_{o2}R_{o3}+n_3C_{33}R_{o3}^2 \end{aligned} \tag{7.21}$$

Thus the angle β_L which the energy flux associated with the quasi-longitudinal mode makes with the positive y-axis is

$$\beta_L = \tan^{-1}\frac{-n_2C_{14}+n_3C_{44}+n_2(C_{44}+C_{13})\tan\phi+n_3C_{33}\tan^2\phi}{n_2C_{11}-n_3C_{14}+(n_3(C_{44}+C_{13})-2n_2C_{14})\tan\phi+n_2C_{44}\tan^2\phi}$$

where ϕ (= $\tan^{-1}(R_{o3}/R_{o2})$) is the angle the particle displacement vector makes with the positive y-axis. For clarity, all the angles used here are shown in the coordinate system in Figure (7.8)d.

The angle β_{T_2} which the energy flux associated with the quasi-transverse mode makes with the positive y-axis is obtained from equation (7.21) by replacing ϕ by $\phi+\frac{\pi}{2}$ because of the orthogonality of the particle displacement vectors.

A computer programme (see appendix (2)) was written to calculate the energy flux and particle displacement directions for the three modes which can propagate along any direction in the yz plane. The results are plotted for arsenic, antimony and bismuth in Figure (7.8) a,b,c, as angular deviations from the propagation direction versus propagation direction. The particle displacement vector for the pure and quasi-pure transverse modes are not shown; the former is always perpendicular to the plane of the diagram and the latter always differs by $\pi/2$ from that for the quasi-longitudinal mode.

Examination of Figure (7.8) a,b,c, shows that in all three elements the condition for pure longitudinal mode propagation $\underline{n} \wedge \underline{R_o} = 0$ (that is that the propagation direction $\underline{n}$ and particle displacement vectors $\underline{R_o}$ are parallel) is obeyed twice in the yz plane. One pure mode axis is the z-axis itself. The other direction is given in Table (7.4). It is interesting to note that for antimony and bismuth this pure mode direction is much the same; but that for arsenic is in a different quadrant than the other two. Since one of the transverse waves with propagation

Figure (7.8) Deviation of the energy flux associated with the quasi-longitudinal (·····), quasi-shear (—·—·—) and pure shear(— — —) waves from the propagation direction in the Y Z plane of (a) arsenic, (b) antimony and (c) bismuth. The particle displacement deviation for the quasi-longitudinal wave is also shown (——) in each case.

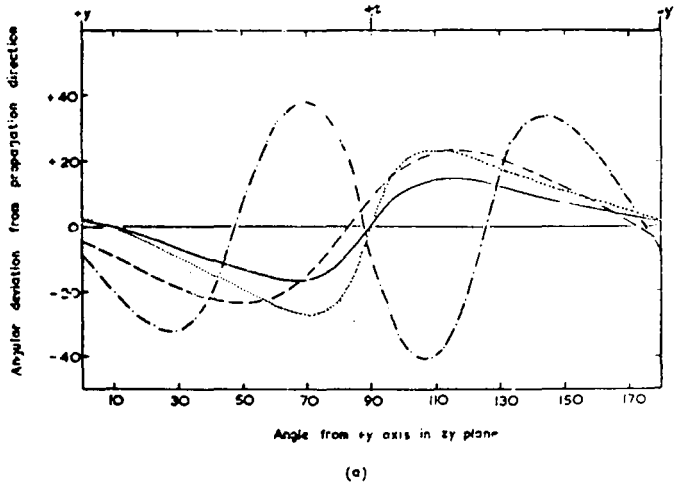

(a)

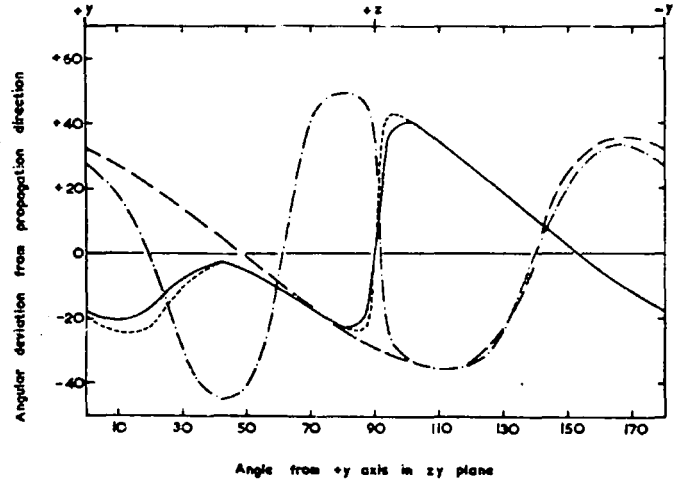

(b)

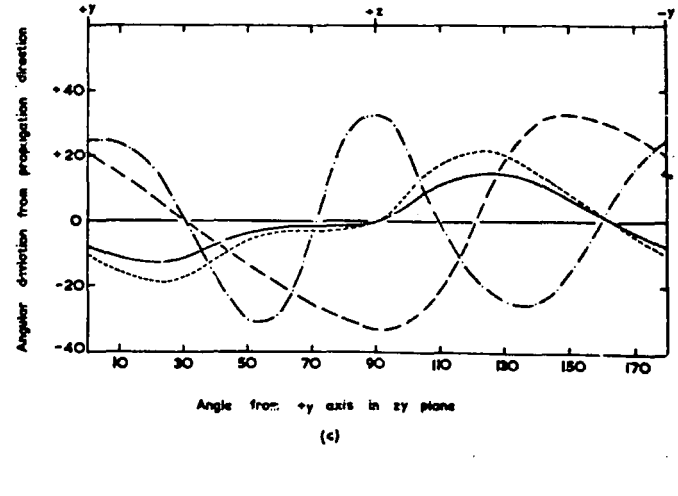

(c)

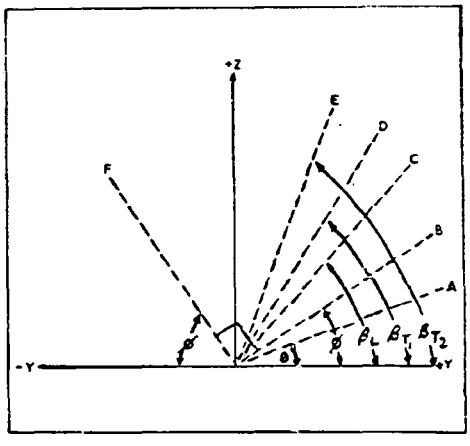

(d)

TABLE (7.4)

		Arsenic	Antimony	Bismuth
Pure mode direction		10°	153°	163°
Energy flux deviation from propagation direction				
Pure mode direction	Fast shear	-9.5°	$+29^{\circ}$	$+30^{\circ}$
	Slow shear	-22°	$+25^{\circ}$	$+6^{\circ}$
45° to +y axis	Fast shear	-23°	$+2^{\circ}$	-10°
	Slow shear	-10°	-44°	-25°
	Longitudinal	-17°	-3°	-8.5°
14.5° to +y axis	Fast shear	-12°		
	Slow shear	-27°		
	Longitudinal	-2°		
Semi-angle of the cone of internal conical refraction		9°	28.5°	32.5°

The pure mode direction in the yz plane, in addition to the z-axis, is given for arsenic, antimony and bismuth. (The angle is defined by an anticlockwise rotation about the +x-axis from the +y-axis). Also, the extent to which the energy flux associated with various elastic waves deviates from propagation directions of special interest is collected.

vector in the yz plane is always a pure mode, the propagation direction which supports the pure longitudinal mode must by orthogonality carry another pure transverse mode. Whereas the energy flux associated with a pure longitudinal wave is always parallel to the propagation direction, this is not true for pure transverse waves unless the mode axis has twofold, fourfold or sixfold rotational symmetry or is perpendicular to a plane of reflection symmetry (Waterman 1959). This is not so here, therefore, the energy flux deviates from this pure mode axis. The angle of deviation for all elements is collected in Table (7.4). All ultrasonic measurements of the elastic wave velocities in these three elements have included either or both of the directions at $\pm 45^{\circ}$ to the z-axis in the yz plane so that a complete set of elastic constants is made available. The deviations of the energy flux from these propagation directions for all three modes for the three materials are also given in Table (7.4); in some cases this deviation is substantial.

An interesting result of the deviation of the energy flux vector from the propagation vector is the phenomenon of internal conical refraction. Waterman (1959) has discussed this in some detail. In the present instance, the degenerate pure transverse wave which can be propagated along the z-axis exhibits internal

conical refraction with a cone semi angle given by $\tan^{-1}(C_{14}/C_{44})$. This angle is much smaller in arsenic than in either antimony or bismuth (see Table (7.4)). The phenomenon is manifested in Figure (7.8) a,b,c, as an equal and opposite deviation at 90° of the energy flux vectors associated with the two transverse waves.

Wave propagation in the xy and zx planes cannot be treated in this straightforward way: examination of equation (7.18) for these planes shows that, x and z axes excepted, there are three non-zero components of the energy flow (P_1, P_2 and $P_3 \neq 0$).

7.5 Discussion of results

The discussion of the crystallography of arsenic (7.1.1) introduced the idea that arsenic tended towards a double layer-like structure. Binding between successive double layers is weak - as evidenced by the ease of cleavage to expose (111) planes - while on the other hand within each double layer atoms are bound tightly. The crystal chemistry of the group VB semimetals has been discussed in some detail in relation to band structure (Cohen and Falicov 1964). Plausibly the deeper lying outer shell s^2 electrons participate less in the interatomic binding than do the three p electrons: a valency of three commonly occurs for these elements. For arsenic in particular, bonding within the double

layer planes would arise essentially from overlap of the p^3 orbitals, resulting in three bonds almost at right angles. The interbond angle in the layer planes is actually $97^{\circ}12'$: some sp hybridisation probably occurs. On this basis the gross features of the band structure become understandable (Cohen, Falicov and Golin 1964): two bands, essentially s-bonding and s-antibonding, are completely occupied while three nearly full predominately p-bonding bands overlap slightly with nearly empty p-antibonding bands to give the characteristic semimetallic behaviour. Antimony and bismuth do not exhibit such pronounced layer-like structure and cannot have bonds localised within the double layers to the same extent as in arsenic.

Mechanical and thermal properties characteristic of layer-like structures are anticipated for arsenic. Thus an attempt is made to correlate the elastic constant data obtained here with the double layer-like structure of arsenic.

7.5.1 The Gruneisen tensor of arsenic

The thermal expansion of solids is a direct consequence of the anharmonicity of the lattice vibrations or rather of the interatomic potential energy function and has been studied using various approximation techniques. In the quasi-harmonic approximation (Collins and White 1964), the atoms in the crystal

lattice are considered to execute harmonic vibrations but the frequencies of the vibrations are volume dependent.

The Gruneisen relation

$$3\alpha = \gamma C_v k/v \tag{7.22}$$

where 3α is the volume expansion coefficient, C_v is the constant volume specific heat and k is the bulk modulus, is a consequence of the quasi-harmonic approximation (Collins and White 1964) if the Gruneisen constant γ is given by

$$\gamma = \sum_{i=1}^{3N} \gamma_i C_i \Big/ \sum_{i=1}^{3N} C_i \tag{7.23}$$

where $\gamma_i = -\left(\frac{\partial \ln \omega_i}{\partial \ln v}\right)_T$ and ω_i is the frequency of the ith lattice mode.

The thermal expansion of a crystal can be specified completely in terms of the linear expansion coefficients α_x, α_y, α_z measured along three mutually perpendicular axes. For uniaxial crystals the thermal expansion is specified by α_{33} the expansion coefficient parallel to and α_{11} that perpendicular to the principal axis, in the case of arsenic the z-axis. Knowledge of α_{33} and α_{11}, the elastic moduli and the specific heat allows evaluation of the Gruneisen tensor, which may be written (Key 1967)

$$\gamma_{ij} = C^T_{ijmn}\alpha_{mn}/\rho C_v \tag{7.24}$$

where C^{T}_{ijmn} are the isothermal elastic constants, α_{mn} are the linear thermal expansion coefficient components and ρC_v is the constant volume heat capacity per unit volume.

The isothermal constants are available from equation (2.14) and the constant volume heat capacity from

$$C_v = C_p - \frac{1}{\rho} TC_{ij}\, s\alpha_{ij}\alpha\, s \qquad (7.25)$$

but it is more convenient to use values obtained directly from experiment i.e. constant pressure heat capacity and adiabatic elastic constants. Equation (7.22) may (Barron and Munn 1967) be written

$$\gamma_{ij} = C_{ijmn}\alpha_{mn}/\rho C_p \qquad (7.26)$$

For crystals with $R\bar{3}m$ symmetry the Gruneisen tensor has the form

$$\begin{matrix} \gamma_{11} & \gamma_{12} & \gamma_{13} \\ \gamma_{21} & \gamma_{22} & \gamma_{23} \\ \gamma_{31} & \gamma_{32} & \gamma_{33} \end{matrix} = \frac{1}{\rho C_p} \begin{pmatrix} A & 0 & 0 \\ 0 & B & 0 \\ 0 & 0 & C \end{pmatrix} \qquad (7.27)$$

where $A=B=(C_{11}+C_{12})\alpha_{11}+C_{13}\alpha_{33}$ and $C = 2C_{13}\alpha_{11}+C_{33}\alpha_{33}$.
Calculated Gruneisen tensor components for arsenic are compared with those of antimony and bismuth in Table (7.5).

TABLE (7.5)

		Arsenic	Antimony	Bismuth
Thermal Expansion $\times 10^{-5}$ $^{o}K^{-1}$	α_{11}	0•3 (1)	0•768 (2)	1•211 (2)
	α_{33}	4•3 (1)	1•619 (2)	1•685 (2)
Gruneisen Tensor	γ_{11}	1•71 (3)	1•20 (2)	1•32 (2)
	γ_{33}	1•53 (3)	0•94 (2)	1•10 (2)
Compressibility $\times 10^{-13}$ $cm^2 dynes^{-1}$	β	17•92 (3)	25•8 (4)	30•83 (5)
	β_1	-4•75 (3)	4•1 (4)	6•38 (5)
	β_{11}	27•42 (3)	17•5 (4)	18•07 (5)

(1) Childs (1953)

(2) Bunton and Weintroub (1968)

(3) This work

(4) Epstein and deBretteville (1965)

(5) Eckstein et al (1960)

The thermal expansion, Gruneisen tensor and compressibilities of arsenic, antimony and bismuth.

Recently Munn (1969) has discussed the Gruniesen tensor of antimony and bismuth and has predicted a greater anisotropy for arsenic at high temperatures than for the other two elements. Because the crystal lattice of arsenic is much more distorted than that of bismuth or antimony, its properties in general are the most anisotropic of the three elements as exemplified by the linear compressibilities and thermal expansion (see Table (7.5)), but this is not so for the Gruneisen tensor at room temperature.

The linear compressibilities, defined as the relative decrease in length of a line when the crystal is subject to unit hydrostatic pressure, has two components for rhombohedral materials

$$\beta_{\underline{1}} = S_{11}+S_{12}+S_{13} \tag{7.28}$$

and

$$\beta_{11} = 2S_{13}+S_{33} \tag{7.29}$$

for length changes perpendicular and parallel to the trigonal axis respectively. The bulk compressibility is

$$\beta = 2(S_{11}+S_{12}+\tfrac{1}{2}S_{13})+S_{33} \tag{7.30}$$

Calculated values of β, $\beta_{\underline{1}}$, β_{11} are collected in Table (7.5) for arsenic, antimony and bismuth. Along the trigonal axis arsenic is much the most compressible of the three elements. Like

certain other highly anisotropic crystals (such as graphite and tellurium), when subjected to hydrostatic pressure, the arsenic lattice actually enlarges along the layer planes, as shown by the negative sign of β_1. This property is discussed later (7.4.2) on the basis of a model of weak interlayer binding and strong binding within each double layer. Lattice vibrations will be excited preferentially in the direction of greater linear compressibility on account of the lower vibrational frequencies, thus the thermal expansion along this direction will be much the greater. Gruneisen and Goens (1924) have provided quantitative relationships for the thermal expansion in anisotropic crystals,

$$\alpha_x = \alpha_{11} = (S_{11}+S_{12})q_x + S_{13}q_z \qquad (7.31)$$

$$\alpha_z = \alpha_{33} = 2S_{13}q_x + S_{33}q_z \qquad (7.32)$$

where q_x and q_z are thermal pressure coefficients derivable from lattice theory. The elastic stiffness within the layers is much greater than that along the z-axis resulting in α_{33} being much larger than α_{11}. In arsenic $S_{11}+S_{12}$ (= 50.4 $cm^2 dynes^{-1} \times 10^{-13}$) is close in magnitude but opposite in sign to S_{13} (= -55.19 cm^2 $dynes^{-1} \times 10^{-13}$) and hence α_{11} is small. But S_{33} (= 137.8 $\times 10^{-13}$ $cm^2 dynes^{-1}$) is substantially larger than $2s_{13}$ (= 110.38 $\times 10^{-13}$

$cm^2 dynes^{-1}$), hence α_{33} turns out to be much larger than α_{11}.

Therefore as a result of the highly anisotropic elasticity of arsenic the Gruneisen tensor components become to a good approximation

$$\gamma_{11} = \frac{\alpha_{33} C_{13}}{\rho C_p} \qquad (7.33)$$

$$\gamma_{33} = \frac{\alpha_{33} C_{33}}{\rho C_p} \qquad (7.34)$$

Thus, since C_{13} (= 64.27 x 10^{10} dynes cm^{-2}) and C_{33} (= 58.74 x 10^{10} dynes cm^{-2}) are almost equal, the anisotropy of the Gruneisen tensor components for arsenic at room temperature is not large. Table (7.5) gives the values obtained for the Gruneisen tensor components of arsenic and in addition the high temperature limiting values of the tensor components for antimony and bismuth. These are substantially smaller than those of arsenic. For antimony and bismuth the γ_{ii} are close to unity and so the normal mode lattice frequencies are effectively inversely proportional to the volume, while for arsenic these frequencies have a more marked volume dependence.

7.5.2 The linear compressibility of arsenic

Arsenic is the least compressible of the three elements arsenic, antimony and bismuth as far as bulk dilation is concerned,

but as mentioned previously, along the trigonal axis it is by far the most compressible. The large change in the spacing between the layer planes and the resultant enhanced repulsive forces direct atoms outwards in the xy plane. As in the case of the thermal expansion components, the negative cross compliance term S_{13} being so much larger for arsenic than for antimony or bismuth controls the anisotropy of the linear compressibilities.

Because the binding forces between the double layer planes is so weak it has often been suggested in text books that the double layer planes are held together largely by Van der Waal's forces. Such a model cannot be used for rigorous computations: the high z-axis electrical conductivity (Jeavons and Saunders 1969) and the known Fermi surface point to some degree of orbital overlap between the double layer planes. However it is particularly suited to calculation because to a first approximation interlayer cohesion only need be considered. The exact nature of the interatomic binding within each double layer is not of paramount importance, provided it is tight and the double layers can be taken as rigid.

A joint effort by Mr. Z. Sumengen, Dr. G.A. Saunders and myself produced an expression for the lattice potential energy function of arsenic on the basis of the above model assuming a

Lennard-Jones 6-n potential along the z-direction. The detailed computations are presented in "The elastic constants and interatomic binding in arsenic" a copy of which is bound at the back of this thesis. The elastic constant data used in that paper are those obtained from the initial measurements performed by Mr. Z. Sumengen and myself.

To assess the validity of the model, linear thermal expansion and compressibility components along the z-axis were calculated and compared with experimental values. Good agreement obtained when the repulsive exponent n was chosen as 8, (see Table 7.6)).

7.6 Conclusion

The distortion of the crystal lattice of arsenic (rhombohedral angle $\alpha = 54^{\circ}10'$) and its resultant layer-like nature in comparison with antimony ($\alpha = 57^{\circ}14'$) and bismuth ($\alpha = 57^{\circ}19'$) leads to marked differences in its lattice dynamics; mechanical and thermal properties characteristic of layer structures obtained for arsenic but not for bismuth and antimony. Along the trigonal axis arsenic is much the most compressible of the three elements; and the linear compressibility associated with the xy plane is negative in sign: application of hydrostatic pressure would result in a large decrease in the separation between double layer planes

TABLE (7.6)

Repulsive Exponent	Linear compressibility $\beta_{11} \times 10^{-13}$ dynes^{-1}cm^{-2}		Linear thermal expansion coefficient $\alpha_{33} \times 10^{5}$ $^{o}K^{-1}$		Interlayer cohesive energy ergs cm^{-2}
	measured	calculated	measured	calculated	
8	27•42	21•74	4•3*	5•87	515
10		10•92		3•90	746
12		7•39		1•27	875

* Childs (1953)

Measured and calculated values of the z-axis linear compressibility, thermal expansion coefficient and interlayer cohesive energy for three values of repulsive exponent in the van der Waals model for arsenic.

while the xy plane would actually enlarge. This has been discussed on the basis of a model of weak interlayer binding forces but tight binding within each double layer.

For all three elements the compliance constant S_{13} is negative but it is much larger for arsenic than for antimony and bismuth; at the same time S_{33} is positive in all cases but is much the largest for arsenic. If a simple compressional stress σ_{33} is applied (that is on the xy plane in the z-direction), the strains are $\epsilon_{11} = +S_{13}\sigma_{33}$, $\epsilon_{22} = +S_{13}\sigma_{33}$ and $\epsilon_{33} = +S_{33}\sigma_{33}$ thus each material will contract along the z-axis and expand in the xy plane. For arsenic the response to this applied stress is greater than for antimony and bismuth.

A more striking difference in the behaviour of arsenic ensues on a simple compression σ_{11} applied along the x-axis (the y-axis behaviour is similar). Now the resultant strains are $\epsilon_{11} = +S_{11}\sigma_{11}$, $\epsilon_{22} = +S_{12}\sigma_{11}$, $\epsilon_{33} = +S_{13}\sigma_{11}$, $\epsilon_{23} = +S_{14}\sigma_{11}$ and $\epsilon_{32} = +S_{14}\sigma_{11}$. As S_{11} is positive, each element will contract along the x-axis but S_{12} is positive only for arsenic so while arsenic contracts also along the y-axis, antimony and bismuth will expand; all three will expand along the z-axis. The large magnitude of S_{13} for arsenic is further manifested in the negative sign of the linear compressibility ($= S_{11}+S_{12}+S_{13}$) along directions in the xy plane

and in the very small thermal expansion α_{11} ($= 0.3 \times 10^{-5}\ ^{\circ}K^{-1}$) in the xy plane as compared with that α_{33} ($= 4.3 \times 10^{-5}\ ^{\circ}K^{-1}$) along the z-axis.

These differences between relative magnitudes and signs of the elastic constants of arsenic also reflect in the elastic wave propagation characteristics which differ from those of antimony and bismuth not only in degree but also in kind.

In general in a layer type crystal lattice, vibrations will be excited preferentially in the direction of greater linear compressibility on account of the lower vibrational frequencies. Velocities of elastic waves transmitted within the tightly bound layers will be much greater than those of waves transmitted along the direction of weak binding. Thus for arsenic wave propagation velocities are higher in the xy plane than in the z-direction (see Figures (7.6) and (7.7)). Strong interatomic binding forces within each double layer control the wave propagation within the xy plane: these waves have velocities which are essentially independent of direction. Hence the close similarity between the xz and yz velocity cross sections (Figure (7.7)) for arsenic.

CHAPTER 8

Summary

Summary

The propagation of ultrasonic waves has been studied in several materials in which weak binding exists or develops as the physical conditions are changed; certain basic similarities in the behaviour have emerged. In particular the resemblance of the ultrasonic attenuation and velocity anomalies in the vicinity of the martensitic transformations in TiNi and an indium-thallium alloy suggest that in both these materials a soft phonon mode plays a dominant role in the transition mechanism. The reduced resistance to shear deformation in the vicinity of a phase change is a phenomenon manifested in both TiNi and the indium-thallium alloys and also in the zirconia-yttria solid solutions. In fact in the latter two, the shear constant which most strongly reflects the decrease in lattice stability is the same, namely $(C_{11}-C_{12})/2$. In all three phase changes which have been studied, the elastic anisotropy has been shown to increase markedly as the transition is approached whether by temperature or compositional variations: free carrier concentration changes may account for this effect in the metal alloys. The difference between the bulk modulus of the high and low temperature phases of TiNi has in fact been shown to accrue largely from changes in the free carrier concentration and thus the alteration in the binding energy from one phase to the other

to come primarily from that in the Fermi energy contribution. Knowledge of the compressibilities of crystals has provided a sensitive indication of the presence of relative weakness in binding forces. In particular the linear compressibilities of indium-10.% thallium evidences that this alloy has a greater inclination to collapse into a cubic structure under hydrostatic pressure than has indium itself. In a somewhat similar way a striking manifestation of the double layer-like structure of arsenic has been found in the differences between its linear compressibilities normal and parallel to the layer planes: while the former is large, evidencing the weak interlayer binding forces, the latter is small and actually negative.

The types of weak binding which have been investigated tend to show a marked dependence upon crystallographic direction. To manifest this, orientation dependence of elastic wave propagation characteristics in tetragonal, rhombohedral and cubic crystals has been presented in detail. Thus the presence of relative weaknesses in binding forces between crystals of the same structure has been graphically displayed by various sections of the wave velocity surfaces. These are particularly striking between indium and the indium-10 at.% thallium alloy in the tetragonal crystals and between arsenic and the elements antimony and bismuth in the rhombohedral crystals.

APPENDICES

The computer programmes which were written in Fortran IV to calculate the elastic wave propagation characteristics in tetragonal (4/mmm) and rhombohedral ($\bar{3}$m) crystals are given; the programmes for the tetragonal crystals may be readily adapted for all classes of cubic crystals. The notation used is explained when necessary by comment cards in the programme print outs. In all cases the only input data are the elastic moduli and the density of the crystal.

Appendix (1) Tetragonal and cubic crystals.

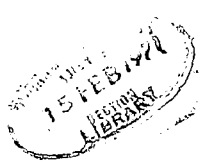

```
G LEVEL  18                    MAIN                    DATE = 70159          21/00/36

C       PROGRAMME FOR CALCULATION OF ELASTIC WAVE VELOCITIES IN
C       THE (110) PLANE OF TETRAGONAL (4/MMM) CRYSTALS
C       (IT MAY BE USED FOR CUBIC CRYSTALS BY MAKING THE APPROPRIATE
C       CHANGES IN THE DATA£  PUT   C13=C12,C33=C11,C66=C44£  )
C       ELASTIC WAVES IN ZRO2-Y2O3       8 PERCENT Y2O3
            REAL N1(360),N2(360),N3(360),L11(360),L12(360),L13(360),L3
     1   3(360),A(360),B(360),C(360),D(360),V1(360),V2(360),V3(360),A1(3
     1  60),E(360),F(360),G(360),H(360),Y1(360),Y2(360),Y3(360)
        REAL C11,C12,C13,C33,C44,C66,R,P,Q,S
        READ(5,7) C11,C12,C13,C33,C44,C66
    7    FORMAT(6E11.4)
C       P IS THE CRYSTAL DENSITY
         P=6.036
C       A1(I) IS THE ANGLE BETWEEN THE (110) DIRECTION AND THE
C       DIRECTION OF PROPAGATION LYING IN THE (110) PLANE
        A1(1)=0.0
        DO 2 I=2,360
    2   A1(I)=A1(I-1)+0.01745
         DO 3 I=2,360
        L11(I)=0.5*((COS(A1(I)))**2)*(C66+C11)+((SIN(A1(I)))**2)*C44
        L12(I)=0.5*((COS(A1(I)))**2)*(C12+C66)
         L13(I)=((COS(A1(I)))*(SIN(A1(I)))*(C13+C44)/(SQRT(2.0)))
         L33(I)=((COS(A1(I)))**2)*(C44)+((SIN(A1(I)))**2)*C33
      A(I)=1.0
       B(I)=-(2.0*L11(I)+L33(I))
        C(I)=(L11(I)**2+2.0*L11(I)*L33(I)-2.0*L13(I)**2-L12(I)**2)
       D(I)=-(L11(I)*(L11(I)*L33(I)-2.0*L13(I)**2)-L12(I)*(L12(I)*L33
     1  (I)-2.0*L13(I)**2))
        E(I)=(C(I)-(3.0*B(I)**2)/(9.0*A(I)))/A(I)
        F(I)=(D(I)-E(I)*B(I)/3.0-((B(I)/3.0)**3)/(A(I)**2))/A(I)
        G(I)=(F(I)**2)/4.0+(E(I)**3)/27.0
        H(I)=(-F(I)/2.0)/(SQRT((-E(I)**3)/27.0))
        H(I)=ATAN((SQRT(1.0-H(I)**2))/H(I))
        Y1(I)=2.0*SQRT(-E(I)/3.0)*COS(H(I)/3.0)
        Y2(I)=-Y1(I)/2.0+SQRT(-E(I))*SIN(H(I)/3.0)
        Y3(I)=-Y1(I)/2.0-SQRT(-E(I))*SIN(H(I)/3.0)
C       THE V£S ARE THE THREE SOLUTIONS OF A CUBIC EQUATION IN PV**2
        V1(I)=Y1(I)-B(I)/(3.0*A(I))
        V2(I)=Y2(I)-B(I)/(3.0*A(I))
         V3(I)=Y3(I)-B(I)/(3.0*A(I))
C       THE FINAL V£S ARE THE THREE WAVE VELOCITIES IN THE (110) PLANE
C       V1 IS THE LONGITUDINAL VELOCITY
C       V2 IS THE SHEAR VELOCITY POLARISED ALONG THE (001) DIRECTION
C       V3 IS THE SHEAR VELOCITY POLARISED ALONG THE (1BAR10) DIRECTION
        V1(I)=SQRT(V1(I)/P)
        V2(I)=SQRT(V2(I)/P)
    3   V3(I)=SQRT(V3(I)/P)
        DO 4 I=2,360
        A1(I)=A1(I)*57.2956
    4  WRITE(6,8) A1(I),V1(I),V2(I),V3(I)
    8    FORMAT(1F10.4,3E14.5)
        STOP
        END
```

```
G LEVEL  18                    MAIN                    DATE = 70159          21/00/56

C       CHARACTERISTICS OF ELASTIC WAVE PROPAGATION IN THE (100) PLANE
C                    OF TETRAGONAL(4/MMM) CRYSTALS
C         ELASTIC WAVES IN ZRO2-Y2O3  8PERCENTY2O3
              REAL A1(360),A2(360),A3(360),A4(360),A5(360),A6(360),A7(36
     1   0),V1(360),V2(360),V3(360),N2(360),N3(360),L11(360),L22(360),L2
     1 3(360),L33(360),A8(360),A9(360)
          REAL C11,C12,C13,C14,C33,C44,C66
          READ(5,7) C11,C12,C13,C33,C44,C66
    7     FORMAT(6F9.4)
C        P IS THE CRYSTAL DENSITY
           P=6.036
C          A1(I) IS THE PROPAGATION DIRECTION  IN THE (100) PLANE
C         MEASURED FROM THE +Y AXIS
C      (AN ANTICLOCKWISE ROTATION FROM +Y AXIS ABOUT THE X-AXIS
C        IS A POSITIVE ROTATION)
          A1(1)=0.0
          DO 2 I=2,360
          A1(I)=A1(I-1)+0.01745
          N2(I)=COS(A1(I))
          N3(I)=SIN(A1(I))
C        THE L'S ARE THE COEFFICIENTS OF THE COMPONENTS OF THE
C         ELASTIC WAVE DISPLACEMENT VECTOR
          L11(I)=((COS(A1(I)))**2)*(C66-C44)+C44
          L22(I)=((COS(A1(I)))**2)*(C11-C44)+C44
           L23(I)=((COS(A1(I)))*((SIN(A1(I)))*(C44+C13)))
          L33(I)=((COS(A1(I)))**2)*(C44-C33)+C33
    9     FORMAT(4F12.5)
C        THE CONDITION FOR SOLUTION OF THE EQUATION OF MOTION
C         IS THAT THE DETERMINANT OF THE COEFFICIENTS OF THE
C          DISPLACEMENT COMPONENTS IS ZERO
C        THIS GIVES A CUBIC EQUATION IN P*V**2
C        V1,V2,V3, ARE THE VELOCITIES OF THE THREE ELASTIC WAVES
C          WHICH CAN PROPAGATE AT AN ANGLE A1(I) TO THE +YAXIS
          V1(I)=SQRT(((N2(I)**2)*(C66-C44)+C44)/P)
         V2(I)=SQRT(((L22(I)+L33(I))+SQRT((L22(I)+L33(I))**2+4.0*(L23(
     1I)**2-L22(I)*L33(I))))/(2.0*P))
          V3(I)=SQRT(((L22(I)+L33(I))-SQRT((L22(I)+L33(I))**2+4.0*(L23(
     1I)**2-L22(I)*L33(I))))/(2.0*P))
C         A3 IS THE ENERGY FLUX VECTOR ASSOCIATED WITH THE PURE SHEAR
          A3(I)=ATAN((TAN(A1(I)))*C44/C66)
C        A2 IS THE POLARISATION VECTOR FOR THE QUASI-LONGITUDINAL
C        WAVE&THAT FOR THE QUASI-SHEAR WAVE IS A2+90
          A2(I)=ATAN(-(L22(I)-P*(V2(I))**2)/L23(I))
C        A4 IS THE ENERGY FLUX VECTOR ASSOCIATED WITH THE QUASI-
C         LONGITUDINAL WAVE AND A8 US THAT FOR THE QUASI-SHEAR WAVE
          A4(I)=ATAN((C44*N3(I)+(C44+C13)*N2(I)*TAN(A2(I))+C33*N3(I)*TAN(
     1    A2(I))**2)/(C11*N2(I)+(C13+C44)*N3(I)*TAN(A2(I))+C44*N2(I)*TAN(
     1    A2(I))**2))
```

```
2 A8(I)=ATAN((C44*N3(I)+(C44+C13)*N2(I)*TAN(A2(I)+1.5708)+C3 *N3(I)*
 1TAN(A2(I)+1.5708)**2)/(C11*N2(I)+(C13+C44)*N3(I)*TAN(A2(I)+1.5708)
 1+C44*N2(I)*TAN(A2(I)+1.5708)**2))
      DO 3 I=2,360
      A1(I)=A1(I)*57.2956
      A2(I)=A2(I)*57.2956
      A3(I)=A3(I)*57.2956
      A4(I)=A4(I)*57.2956
    A8(I)=A8(I)*57.2956
      A5(I)=A2(I)-A1(I)
      A6(I)=A3(I)-A1(I)
      A7(I)=A4(I)-A1(I)
      A9(I)=A8(I)-A1(I)
3     WRITE(6,8) A1(I),V1(I),V2(I),V3(I),A2(I),A5(I),A3(I),A6(I),A4(I
 1 ),A7(I),A8(I),A9(I)
8   FORMAT(12F10.4)
      STOP
       END
```

Appendix (2). Computer programmes for calculating the elastic wave propagation in the Z - Y, X - Y and X - Z planes of R $\bar{3}$m crystals.

```
V G LEVEL  18                    MAIN                    DATE = 70205          22/21/
      C           ELASTIC WAVES PROPOGATION IN THE Z-Y PLANE
      C           OF TRIGONAL (RBAR3M) CRYSTALS
                  DIMENSION A1(400),A2(400),A3(400),V(400),V2(400),A(400)
           1      ,B(400),C(400),D(400),E(400),A5(400),A4(400),R(400),S(400)
           1      ,T(400),P(400),Q(400),G(400),V3(400),V4(400),A6(400),A7(400),
           1      A8(400),A9(400),V5(400),V6(400),T1(400),S1(400),Q1(400),G1(
           1       400),A10(400),A11(400)
                  READ(5,1) C11,C12,C13,C14,C44,C33,C66
      -    1      FORMAT(7F9.4)
      C               W IS THE CRYSTAL DENSITY
                  W=7.8030
      C              A1(I) IS THE PROPAGATION DIRECTION MEASURED IN AN
      C              ANTI-CLOCKWISE SENSE FROM THE +Y AXIS IN THE
      C                    Z-Y PLANE
```

```
          A1(1)=0.0000
        DO 3 I=2,360
          A1(I)=A1(I-1)+0.01745
        A(I)=((COS(A1(I)))**2)*(C11-C33)+C44+C33-(2.0*(COS(A1(I)))*
     1    (SIN(A1(I)))*C14)
        B(I)=((COS(A1(I)))*(SIN(A1(I)))*(C44+C13)-((COS(A1(I)))
     1    **2*C14))
        C(I)=(((COS(A1(I)))**2)*C11+((SIN(A1(I)))**2)*C44-(2*(
     1    COS(A1(I)))*(SIN(A1(I)))*C14))
        D(I)=((COS(A1(I)))**2)*(C44-C33)+C33
        E(I)=(A(I)**2)+4.*((B(I))**2-C(I)*D(I))
        E(I)=SQRT(E(I))
C           V1,V3,V5, ARE THE VELOCITIES OF THE QUASI
C       LONGITUDINAL,QASI-SHEAR AND PURE-SHEAR WAVES
C       V2,V4,V6 ARE THE ELASTIC MODULI DERIVED FROM
C      V1,V3,V5 RESPECTIVELY
        V(I)=SQRT(A(I)+E(I))
        V(I)=V(I)/(SQRT(2.0*W))
        V2(I)=W*V(I)**2
        V3(I)=SQRT(A(I)-E(I))
      V3(I)=V3(I)/SQRT(2.0*W)
        V4(I)=V3(I)**2*W
        V5(I)=(COS(A1(I)))**2*(C66-C44)+C44+2.0*(SIN(A1(I)))*(
     1    COS(A1(I)))*C14
        V5(I)=SQRT(V5(I)/W)
        V6(I)=V5(I)**2*W
C           A8 IS ENERGY FLUX VECTOR----------PURE SHEAR WAVE
        A8(I)=ATAN((COS(A1(I))*C14+SIN(A1(I))*C44)/(COS(A1(I))
     1    *C66+SIN(A1(I))*C14))
        A8(I)=A8(I)*57.2956
C      A2 IS PTLE DISPL VECTOR OF QUASI LONG WAVE
        A2(I)=ATAN((COS(A1(I))**2*C11+SIN(A1(I))**2*C44-2.0*
     7    COS(A1(I))*SIN(A1(I))*C14-V2(I))/(COS(A1(I))**2*C14-
     8    COS(A1(I))*SIN(A1(I))*(C44+C13)))
      A10(I)=ATAN((-COS(A1(I))**2*C14+COS(A1(I))*SIN(A1(I))*(C44+C13
     1  ))/(V4(I)-COS(A1(I))**2*C44-SIN(A1(I))**2*C33))
        G(I)=((COS(A1(I)))*(TAN(A2(I)))**2)*C44
      Q(I)=(-(COS(A1(I)))*2.0*C14+(SIN(A1(I)))*(C44+C13))*(TAN(A2(I)))
        P(I)=(COS(A1(I)))*C11-(SIN(A1(I)))*C14
        T(I)=(SIN(A1(I)))*C33*(TAN(A2(I)))**2
        S(I)=(COS(A1(I)))*(C44+C13)*(TAN(A2(I)))
        R(I)=-(COS(A1(I)))*C14+(SIN(A1(I)))*C44
        S1(I)=(COS(A1(I)))*(C44+C13)*(-1.0/(TAN(A2(I))))
        G1(I)=((COS(A1(I)))*(1.0/(TAN(A2(I))))**2)*C44
```

```
G LEVEL  18                    MAIN                    DATE = 70205          22/21/5(

      Q1(I)=(-(COS(A1(I)))*2.0*C14+(SIN(A1(I)))*(C44+C13))*(-1.0/(
     1  TAN(A2(I))))
      T1(I)=(SIN(A1(I)))*C33*(1.0/(TAN(A2(I))))**2
C       A4 IS ENERGY FLUX VECTOR -----------QUASI-LONG WAVE
      A4(I)=ATAN((R(I)+S(I)+T(I))/(P(I)+Q(I)+G(I)))
C       A6 IS ENERGY FLUX VECTOR-------------QUASI-SHEAR WAVE
      A4(I)=A4(I)*57.2956
      A6(I)=ATAN((R(I)+S1(I)+T1(I))/(P(I)+Q1(I)+G1(I)))
      A6(I)=A6(I)*57.2956
      A3(I)=(A2(I)-A1(I))*57.2956
    3 A2(I)=A2(I)*57.2956
      DO 9 I=2,360
      A1(I)=A1(I)*57.2956
       A5(I)=A4(I)-A1(I)
       A7(I)=A6(I)-A1(I)
      A9(I)=A8(I)-A1(I)
     A10(I)=A10(I)*57.2956
      A11(I)=A10(I)-A2(I)
    9 WRITE(6,4) A1(I),A2(I),A3(I),A4(I),A5(I),V(I),V2(I)
     1  ,V3(I),V4(I),A6(I),A7(I),V5(I),V6(I),A10(I),A9(I)
    4  FORMAT(15F8.2)
       STOP
       END
```

```
C       THIS PROGRAMME CALCULATES THE  VELOCITIES OF THE THREE POSSIBLE
C       SOUND WAVES WHICH CAN PROPAGATE IN THE XY AND XZ PLANES
C       OF RBAR3M CRYSTALS
C       THE ONLY DATA REQUIRED ARE THE ELASTIC STIFFNESS CONSTANTS
C        C11,C12,C13,C14,C33,C44 AND THE MATERIAL DENSITY P
      REAL N1(200),N2(200),L11(200,3),L12(200,3),L13(200,3),L33(200,3)
     1,A(200,3),B(200,3),C(200,3),D(200,3),V1(200,3),V2(200,3),
     1V3(200,3),A1(200),E(200,3),F(200,3),G(200,3),H(200,3),Y1(200,3),
     1Y2(200,3),Y3(200,3),C11(3),C12(3),C13(3),C14(3),C33(3)
      REAL C44(3),C66(3),P(3),L22(200,3),L23(200,3),
     1LA11(200,3),LA12(200,3),LA13(200,3),LA22(200,3),LA23(200,3),
     1LA33(200,3),N3(200),AA(200,3),BA(200,3),CA(200,3),DA(200,3),
     1V1A(200,3),V2A(200,3),V3A(200,3),EA(200,3),FA(200,3),GA(200,3),
     1HA(200,3),Y1A(200,3),Y2A(200,3),Y3A(200,3)
      DO 9 J=1,3
    9 READ(5,10) C11(J),C12(J),C13(J),C14(J),C33(J),C44(J),P(J)
   10 FORMAT(7E10.3)
      A1(1)=0.0
      DO 2 I=2,200
    2 A1(I)=A1(I-1)+0.018
      DO 3 J=1,3
      DO 3 I=2,200
      N1(I)=COS(A1(I))
      N2(I)=SIN(A1(I))
      N3(I)=SIN(A1(I))
      L11(I,J)=(N1(I)**2)*C11(J)+0.5*(N2(I)**2)*(C11(J)-C12(J))
      L12(I,J)=0.5*N1(I)*N2(I)*(C11(J)+C12(J))
      L13(I,J)=2.0*N1(I)*N2(I)*C14(J)
      L22(I,J)=0.5*(N1(I)**2)*(C11(J)-C12(J))+N2(I)**2*C11(J)
      L23(I,J)=(N1(I)**2-N2(I)**2)*C14(J)
      L33(I,J)=(N1(I)**2+N2(I)**2)*C44(J)
      A(I,J)=-1.0
      B(I,J)=L11(I,J)+L22(I,J)-L33(I,J)
      C(I,J)=-L11(I,J)*L22(I,J)-L11(I,J)*L33(I,J)-L22(I,J)*L33(I,J)+L23(
     1I,J)**2+L12(I,J)**2+L13(I,J)**2
      D(I,J)=L11(I,J)*L22(I,J)*L33(I,J)-L11(I,J)*L23(I,J)**2-L33(I,J)*L1
     12(I,J)**2+2.0*L12(I,J)*L23(I,J)*L13(I,J)-L22(I,J)*L13(I,J)**2
      E(I,J)=(C(I,J)-(3.0*B(I,J)**2)/(9.0*A(I,J)))/A(I,J)
      F(I,J)=(D(I,J)-E(I,J)*B(I,J)/3.0-((B(I,J)/3.0)**3)/(A(I,J)**2))/A(
     1I,J)
      G(I,J)=(F(I,J)**2)/4.0+(E(I,J)**3)/27.0
      H(I,J)=(-F(I,J)/2.0)/(SQRT((-E(I,J)**3)/27.0))
      H(I,J)=ATAN((SQRT(1.0-H(I,J)**2))/H(I,J))
      Y1(I,J)=2.0*SQRT(-E(I,J)/3.0)*COS(H(I,J)/3.0)
      Y2(I,J)=-Y1(I,J)/2.0+SQRT(-E(I,J))*SIN(H(I,J)/3.0)
      Y3(I,J)=-Y1(I,J)/2.0-SQRT(-E(I,J))*SIN(H(I,J)/3.0)
      V1(I,J)=Y1(I,J)-B(I,J)/(3.0*A(I,J))
      V2(I,J)=Y2(I,J)-B(I,J)/(3.0*A(I,J))
      V3(I,J)=Y3(I,J)-B(I,J)/(3.0*A(I,J))
```

```
      V1(I,J)=SQRT(V1(I,J)/P(J))
      V2(I,J)=SQRT(V2(I,J)/P(J))
      V3(I,J)=SQRT(V3(I,J)/P(J))
      LA11(I,J)=(N1(I)**2)*C11(J)+N3(I)**2*C44(J)
      LA12(I,J)=2.0*N3(I)*N1(I)*C14(J)
      LA13(I,J)=N3(I)*N1(I)*(C13(J)+C44(J))
      LA22(I,J)=0.5*N1(I)**2*(C11(J)-C12(J))+N3(I)**2*C44(J)
      LA23(I,J)=N1(I)**2*C14(J)
      LA33(I,J)=N1(I)**2*C44(J)+N3(I)**2*C33(J)

   15 FORMAT(6E10.3)
      AA(I,J)=-1.0
      BA(I,J)=LA11(I,J)+LA22(I,J)+LA33(I,J)
      CA(I,J)=-LA11(I,J)*LA22(I,J)-LA11(I,J)*LA33(I,J)-LA22(I,J)*LA33(I,
     1J)+LA23(I,J)**2+LA13(I,J)**2+LA12(I,J)**2
      DA(I,J)=LA11(I,J)*LA22(I,J)*LA33(I,J)-LA11(I,J)*LA23(I,J)**2-LA13(
     1I,J)**2*LA22(I,J)-LA33(I,J)*LA12(I,J)**2+2.0*LA12(I,J)*LA23(I,J)*
     1LA13(I,J)
      EA(I,J)=(CA(I,J)-(3.0*BA(I,J)**2)/(9.0*AA(I,J)))/AA(I,J)
      FA(I,J)=(DA(I,J)-EA(I,J)*BA(I,J)/3.0-((BA(I,J)/3.0)**3)/(AA(I,J)**
     12))/AA(I,J)
      GA(I,J)=(FA(I,J)**2)/4.0+(EA(I,J)**3)/27.0
      HA(I,J)=(-FA(I,J)/2.0)/(SQRT((-EA(I,J)**3)/27.0))
      HA(I,J)=ATAN((SQRT(1.0-HA(I,J)**2))/HA(I,J))
   16 FORMAT(1E20.3)
      Y1A(I,J)=2.0*SQRT(-EA(I,J)/3.0)*COS(HA(I,J)/3.0)
      Y2A(I,J)=-Y1A(I,J)/2.0*SQRT(-EA(I,J))*SIN(HA(I,J)/3.0)
      Y3A(I,J)=-Y1A(I,J)/2.0-SQRT(-EA(I,J))*SIN(HA(I,J)/3.0)
      V1A(I,J)=Y1A(I,J)-BA(I,J)/(3.0*AA(I,J))
      V2A(I,J)=Y2A(I,J)-BA(I,J)/(3.0*AA(I,J))
      V3A(I,J)=Y3A(I,J)-BA(I,J)/(3.0*AA(I,J))
      V1A(I,J)=SQRT(V1A(I,J)/P(J))
      V2A(I,J)=SQRT(V2A(I,J)/P(J))
    3 V3A(I,J)=SQRT(V3A(I,J)/P(J))
      DO 27 I=2,200
   27 A1(I)=A1(I)*57.2956
      DO 4 J=1,3
      DO 4 I=2,200
    4 WRITE(6,8) J,A1(I),V1(I,J),V2(I,J),V3(I,J),V1A(I,J),V2A(I,J),V3A(I
     1,J)
    8 FORMAT(1I6,1F10.4,6E14.5)
C       XY PLANE  R3AR3M CRYSTALS  ELASTIC WAVE VELOCITIES V1 V2 V3
C       XZ PLANE  R3AR3M CRYSTALS  ELASTIC WAVE VELOCITIES V1A V2A V3A
C       IF J=1 ARSENIC
C       IF J=2 ANTIMONY
C       IF J=3 BISMUTH
      STOP
      END
```

REFERENCES

Allgaier, R.S., (1967) Symp. TiNi United States N.O.L Tech. Rep. 68-16.

Alper, T. (1968) Thesis, Durham University.

Barrett, C.S., (1966) "Structure of metals" (McGraw Hill, New York) Chapter XXII.

Barrett, H.H., (1969) Phys. Rev., 178, 743.

Barron, T.H.K. and Munn, R.W., (1967) Phil. Mag., 15, 85.

Berman, H.A., Rozner, A.G. and West, E.D., (1967) J. Appl. Phys., 38, 4473.

Born, M. (1914) Ann. Physik., 44, 605.

Born, M. and von Karman, T., (1912) Physik. Z., 13, 297.

Born, M., (1919) Verhandl. dent. physik. Ges., 21, 13.

Born, M., (1921) Z. Physik., 7, 124.

Born, M., (1923) Atomtheorie des festen Zustandes (Leipzig)

Born, M. and Meyer, J.E., (1932) Z. Physik., 75, 1.

Born, M. and Meyer, J.E., (1933)

Born, M. and Huang, K., (1954) "Dynamical thoery of crystal lattices" (Oxford University Press).

Bowles, J.S., Barrett, C.S. and Guttman, L., (1950) J. Metals, 188, 1478.

Bradley, D., (1965) J. Acoust. Soc. Am., 37, 700.

Brown, R.D., Hartman, R.L. and Koenig, S.H., (1968) Phys. Rev., 172, 598.

Brugger, K., (1965) J. Appl. Phys., 36, 759.

Buehler, W.J. and Wiley, R.C., (1962) Trans. Quart., 55, 269.

Bunton, G.V. and Weibtroub, S., (1969) J. Phys. C. (Solid State Phys.), Ser. 2, 2, 116.

Burkart, M.W. and Read, T.A., (1953) Trans. AIME, 188, 1478.

Cady, W.G., (1964) "Piezoelectricity" (Dover Publications Inc., New York), p.23.

Chandrasekar, B.S. and Rayne, J.A., (1961) Phys. Rev., 124, 1011.

Childs, B.G., (1953) Rev. Mod. Phys., 25, 665.

Cochran, W., (1960) Adv. Phys., 9, 387.

Cochran, W., (1961) Adv. Phys., 10, 401.

Cohen, M.H., Falicov, L.M. and Golin, S., (1964) I.B.M. J. Res. Dev., 8, 215.

Collins, J.G. and White, G.K., (1964) Prog. Low Temp. Phys., 4, 450.

Cowley, R.A., (1965) Phil. Mag., 11, 673.

deLange, R.G. and Zijderveld, J.A., (1968) J. Appl. Phys., 39, 2195.

Duwez, P., Brown, F.H. and Odell, F., (1951) J. Electro. Chem. Soc., 98, 356.

Eckstein, Y., Lawson, A.W. and Reneker, D.H., (1960) J. Appl. Phys., 31, 1535.

Epstein, S. and deBretteville, A.P., (1965) Phys. Rev., 138, A771.

Ewald, P.P., (1921) Ann. Physik., 64, 253.

Falicov, L.M. and Golin, S., (1965) Phys. Rev., 137, A871.

Fuchs, K., (1936) Proc. Roy. Soc., A153, 622.

Goff, J.F., (1964) J. Appl. Phys., 35, 2919.

van Gool, W. and Piken, A.G., (1969) J. Mat. Sci., 4, 95.

Graham, J., (1955) J. Inst. Metals, 84, 86.

Granato, A. and Truell, R., (1956) J. Appl. Phys., 27, 1219.

Gruneisen, E. and Goens, E., (1924) Z. Physik., 29, 141.

Guttman, L., (1950) Trans. AIME, 188, 1472.

Haber, F., (1919), Verhandl. dent. physik. Ges., 21, 750.

Hall, E.O., (1954) "Twinning and diffusionless transformations in metals", (Butterworths, London) p.57.

Harrison, W.A., (1961) Phys. Rev., 118, 1182.

Henry, N.F.M., Lipson, H. and Wooster, W.A., (1951) "The interpretation of X-ray diffraction photographs", (MacMillan, London)

Huntington, H.B., (1958) "Solid State Physics", Ed. Seitz, F and Turnbull, D., Vol. 7 (Academic Press, New York).

Inone, M., (1968) J. Phys. Soc. Japan, 25, 288.

Jeavons, A.P. and Saunders, G.A., (1968) Br. J. Appl. Phys., 1, 869.

Jeavons, A.P. and Saunders, G.A., (1969) Proc. R. Soc., A310, 415.

Jeavons, A.P., (1969) Thesis, Durham University.

Jones, H., (1949) Physica., 15, 13.

Jones, H., (1952) Phil. Mag., 43, 105.

Keating, P.N., (1966) Phys. Rev., 145, 637.

Kellerman, E.W., (1940) Phil. Trans. Roy. Soc., A238, 513.

Kelvin (Lord), (1904) "Baltimore Lectures", (Cambridge University Press).

Key, S.W., (1967) J. Appl. Phys., 38, 2923.

Krisham, K.S. and Roy, S.K., (1952) Proc. Roy. Soc., 210, 481.

Leigh, R.S., (1951) Phil. Mag., 42, 139.

Lipson, H. and Stokes, A.R., (1941) Nature, 148, 437.

Love, A.E.H., (1944) "A treatise on the mathematical theory of elasticity", (Dover Publications Inc., New York).

Lowdin, P.O., (1947) Arkiv. Mat. Ast. Fysik., 35A, 30.

Lucke, K., (1956) J. Appl. Phys., 27, 1433.

Luo, H.L., Hagen, J. and Merrian, M.F., (1965) Acta Met., 13, 1012.

Marcinkowski, M.J., Sastri, A.S. and Koskimmaki, D., (1968) Phil. Mag., 18, 445.

Mason, W.P., (1955) Phys. Rev., 97, 557.

Mason, W.P. (1968) "Microplasticity", Ed. McMahon, C.J., (J. Wiley, New York) p.287.

Mayer, J.E., (1933) J. Chem. Phys., 1, 270.

Meyerhoff, R.W. and Smith, J.F., (1963) Acta Met., 11, 529.

Miller, G.F. and Musgrave, M.J.P., (1956) Proc. Roy. Soc., 236, 352.

Munn, R.W., (1969) Adv. Phys., 18, 515.

Musgrave, M.J.P., (1954) a. Proc. Roy. Soc., 226, 339.

b. Proc. Roy. Soc., 226, 356.

Musgrave, M.J.P., (1957) Proc. Camb. Phil. Soc., 53, 897.

Musgrave, M.J.P., (1959) Rep. Prog. Phys., 28, 74.

Neighbours, J.R. and Schacher, G.E., (1967) J. Appl. Phys., 38, 5366.

Nelson, J.B. and Riley, D.P., (1945) Proc. Phys. Soc., 57, 160.

Novotny, D.B. and Smith, J.F., (1965) Acta Met., 13, 881.

Nye, J.F., (1957) "Physical properties of crystals and their representation by tensors and matrices", (Oxford Clarendon Press).

Pace, N.G., Saunders, G.A. and Sumengen, Z., (1970) J. Phys. Chem. Solids, 31, 1467.

Pahlmann, J.E. and Smith, J.F., (1968) J. Less Common Metals, 16, 397.

Papadakis, E.P., (1968) "Physical Acoustics", vol. IV-B, Ed. Mason, W.P., (London and New York: Academic Press) p.269.

Pollock, J.T.A. and King, H.W., (1968) J. Mat. Sci., 3, 372.

Pretty, E.R., (1970) "Martensite : Fundamentals and technology", Ed. Pretty, E.R., (Longman Group Ltd., London) Chapter 1.

Rayne, J.A. and Chandrasekar, B.S., (1962) Phys. Rev., 125, 1952.

Rehwald, W., (1970) Solid State Comm., 8, 607.

Ruff, O. and Ebert, F.E., (1929) Z. anorg. u. allgem. chem., 180, 19.

Ryshkewitch, E., (1960) "Oxide Ceramics", (Academic Press; New York and London).

Schweitzer, H., (1931) Z. angew. chem., 44, 151.

Sharan, B. and Bajpai, R.P., (1969) J. Phys., Soc. Japan, 26, 1359.

Sherman, J., (1932) Chem. Rev., 11, 93.

Siefert, W.V. and Worrel, F.T. (1951) J. Appl. Phys., 22, 1257.

Sirdeshmukh, D.B., (1967) J. Appl. Phys., 38, 4083.

Spinner, S. and Rozner, A.G., (1966) J. Acoust. Soc. Am., 40, 1009.

Stout, J.W. and Guttman, L., (1952) Phys. Rev., 88, 703.

Truell, R. and Elbaum, C., (1962) "Handbuch der Physik", Ed. Flugge (Springer-Verlag, Berlin) vol. X1/2, p.153.

Truell, R. and Oates, W., (1963) J. Acoust. Soc. Am., 35, 1382.

Valentiner, S., (1940) Ztsch fur Metallkunde, 32, 244.

Wang, F.E., Buehler, W.J. and Pickart, S.J., (1965) J. Appl. Phys., 36, 3232.

Wang, F.E., deSavage, B.F. and Buehler, W.J., (1968) J. Appl. Phys., 39, 2166.

Wasilewski, G.J., (1965) Trans. Metall. Soc. AIME, 233, 1691.

Waterman, P.C., (1959) Phys. Rev., 113, 1240.

Wechsler, M.S., Lieberman, D.S. and Read, T.A., (1953) Trans. AIME, 197, 1503.

White, G.K., (1959) "Low temperature physics", (Oxford University Press), Chapter 6.

Winder, D.R. and Smith, C.S., (1958) J. Phys. Chem. Sol., 4, 128.

Woodruff, T.O. and Ehrenreich, H., (1961) Phys. Rev., 123, 1553.

Zener, C., (1937) Phys. Rev., 52, 230.

Zhdanov, G.S., (1965) "Crystal Physics", (Oliver and Boyd, London) Chapter 6.

PUBLICATIONS

To date, the contents of this thesis are embodied in the following publications.

1. The elastic constants and interatomic binding in yttria-stabilised zirconia.
   N.G. Pace, G.A. Saunders, Z. Sumengen and J.S. Thorp.
   J. Mat. Sci., 4, 1106, (1969).

2. The elastic constants and interatomic binding forces in arsenic.
   N.G. Pace, G.A. Saunders and Z. Sumengen. J. Phys. Chem. Sols., 31, 1467, (1970).

3. Ultrasonic study of the martensitic phase change in TiNi.
   N.G. Pace and G.A. Saunders. Phil. Mag., 22, 73, (1970).

4. The Gruneisen tensor of arsenic.
   N.G. Pace and G.A. Saunders. J. Phys. C. Solid State Physics., 3, L169, (1970).

5. Elastic wave propagation in group VB semimetals.
   N.G. Pace and G.A. Saunders. J. Phys. Chem. Sols., (In press).

JOURNAL OF MATERIALS SCIENCE 4 (1969) 1106–1110

The Elastic Constants and Interatomic Binding in Yttria-Stabilised Zirconia

N. G. PACE, G. A. SAUNDERS, Z. SÜMENGEN, J. S. THORP
Department of Applied Physics and Electronics, University of Durham, UK

Received 1 July 1969

Zirconia (ZrO_2) can be forced into a cubic fluorite structure by the addition of more than 7 mol % yttria (Y_2O_3). The elastic stiffness constants of cubic zirconia single crystals containing 8 and 12 mol % yttria have been determined between 77 and 300° K by an ultrasonic pulse echo technique. Elastic constants are almost temperature-independent and at 77° K are for the 8 and 12 mol % respectively: $C_{11} = 2.04$, $C_{12} = 0.87$, $C_{44} = 1.58$; $C_{11} = 2.23$, $C_{12} = 0.973$, $C_{44} = 1.54$ (units: 10^{12} dynes cm^{-2}). Compressibilities and elastic compliances are also presented. The data provide a basis for discussion of crystalline stability and the nature of the interatomic forces. The decreasing cubic lattice stability as the yttria content is reduced is demonstrated quantitatively. An ionic model closely characterises the binding forces. The repulsive energy is about 12% of the Madelung attractive energy. Debye temperatures calculated from the elastic constant data extrapolated to 0° K are 595 and 604° K for the 8 and 12 mol % respectively.

1. Introduction

Zirconium oxide, ZrO_2, is of great importance as a refractory. However, it is polymorphic [1]. The normal monoclinic modification (space group $P2_1/C$) [2] transforms at about 1000° C into a tetragonal form; a considerable volume contraction of about 9% ensues: zirconia itself cannot be fired into a strong, stable, sintered ceramic. But when certain cubic oxides, including yttria (Y_2O_3), form solid solutions with zirconia, a stabilised cubic structure with a fluorite type of lattice is assumed. Such materials can be fired; no transformations at elevated temperatures take place in the stabilised alloys. Valency requirements indicate that oxygen vacancies are now present, due to the replacement of tetravalent Zr^{4+} ions by trivalent Y^{3+} ions; in consequence, electrical conductivity is enhanced. Zirconia-yttria solid solutions are of technical importance as refractory conductors, especially in connection with high temperature electrodes in magneto-hydrodynamic generators and for fuel cell applications. One unfortunate result of high temperature current passage through the stabilised zirconia is a marked tendency for fragmentation of both sintered, polycrystalline electrodes and single crystal specimens. Studies of the way in which electrical currents alter the bulk properties of single crystals are in progress in an attempt to solve this problem. To back up this work, detailed knowledge of the mechanical properties and the nature of the bonding is required.

The elastic constants of single crystals furnish basic mechanical and lattice thermodynamic information. The present concern is to report elastic constant measurements, made using the ultrasonic pulse-echo technique, for yttria-stabilised zirconia. Data are used as a basis for discussion of the stability of the crystals and the nature of the interatomic forces in them.

2. Experimental Details

Two compositions of the solid solutions of yttria with zirconia have been studied, one of 8 mol % Y_2O_3 and the other 12 mol % Y_2O_3, the former because it is close to the stability edge (~ 7 mol % Y_2O_3) [3] of the cubic phase. Single crystals were grown by electrofusion from pure powdered zirconia and yttria. Samples were cut from the crystallised melts and oriented from back-reflection Laue photographs. X-ray examina-

tions showed high crystal perfection, there being no evidence for mosaic imperfections, and that the material was in the cubic phase. The chemical purity was high. Optical spectrographic analysis showed that the only impurities, present at trace level, were silicon, hafnium, magnesium and tin. This result was substantiated by the absence of observable electron spin resonance spectra (sought at 9 GHz and 4.2° K), which also indicated freedom from other paramagnetic impurities.

Crystals were aligned to within 1° of the prerequisite [1 1 0] crystallographic axis, then two (1 1 0) faces were cut by a diamond wheel and lapped flat and parallel to each other to better than 0.001 cm to avoid ultrasonic diffraction and phase sensitivity effects. Ultrasonic wave transit times along the crystal were measured to an accuracy of $\pm$ 1% by the single-ended, pulse-echo technique at carrier frequencies between 10 MHz and 50 MHz. Velocities were independent of frequency over this range. Identical results, within experimental error, were obtained from different crystals of the same composition. Resonant, gold-plated quartz transducers, X-cut for longitudinal and Y-cut for shear waves, were used to excite the ultrasound. For Y-cut transducers, the bonding material used (10^6 cs silicone fluid) was unsatisfactory above 200° K, limiting the range of experiment. However, the velocities were not very temperature-dependent. Further experimental details may be found elsewhere [4].

As the strains induced by ultrasonic waves are only of the order of 10^{-7}, Hooke's law is valid and each stress component T_{ij} can be considered as a linear homogeneous function of the strain components ϵ_{kl}:

$$T_{ij} = C_{ijkl}\,\epsilon_{kl}\,(i, j, k, l = 1, 2, 3)\,, \qquad (1)$$

where the connecting components are the elastic stiffnesses or moduli C_{ijkl}. The usual matrix notation giving these constants as C_{ij} is achieved by replacing 11 by 1, 22 by 2, 33 by 3, 23 by 4, 13 by 5 and 12 by 6. Symmetry in cubic crystals reduces the 6×6 array for C_{ijkl} in equation 1 so that only three independent elastic constants remain.

In the present work, velocities v, of longitudinal and slow and fast shear waves propagated along the [1 1 0] direction were measured. In this case

$$\rho v_1^2 = \rho v^2_{\text{long}} = (C_{11} + C_{12} + 2C_{44})/2 = C_n\,;\ q \text{ along } [1\,1\,0];$$
$$\rho v_2^2 = \rho v^2_{\text{shear (1)}} = C_{44};\ q \text{ along } [0\,0\,1];$$
$$\rho v_3^2 = \rho v^2_{\text{shear (2)}} = (C_{11} - C_{12})/2 = C';\ q \text{ along } [1\,\bar{1}\,0]\,, \qquad (2)$$

where q is the polarisation vector and ρ is the sample density. All three elastic constants C_{11}, C_{12} and C_{44} are obtainable from this set of measurements. However, the three elastic constants C_n, C_{44} and C' can also be used to define the three independent stiffnesses and have direct physical significance. For the [1 1 0] direction a normal stress T_n, as applied through the longitudinal sound wave inserted onto the (1 1 0) face, produces a strain S_n parallel to [1 1 0] and T_n/S_n is C_n. For shear waves propagating down and with atomic motion perpendicular to the [1 1 0] direction, two physical situations occur, as shown by equation 2; first, for atoms vibrating in the [0 0 1] direction, the ratio of the shear stress to shear strain is C_{44}, second, for tractions parallel to [1 $\bar{1}$ 0] the ratio is $(C_{11} - C_{12})/2$.

Ultrasonic wave velocities at 77 and 196° K are given in table I, together with sample densities (measured by Archimedes' principle) and lattice spacings (obtained from Debye-Scherrer powder photographs taken with Cu Kα radiation applying the Nelson-Riley extrapolation formula).

3. Results and Discussion

The linear combinations of the elastic constants C_n, C_{44} and C' derived from the velocity data, using equation 2, are given as a function of temperature in fig. 1. Calculated values of C_{11}, C_{12} and C_{44} at 77 and 196° K are presented in table II. Another simple deformation is a pure volume dilation without shear, expressed as the bulk modulus K, the measure of stiffness to volume dilation.

$$K = -V\frac{\mathrm{d}P}{\mathrm{d}V} = \frac{C_{11} + 2C_{12}}{3}\,. \qquad (3)$$

The bulk modulus data are also given in table II. In addition to the stiffnesses C_{ijkl}, tabulations usually include the elastic compliances defined by

$$\epsilon_{ij} = S_{ijkl}\,T_{ij}\,. \qquad (4)$$

S_{ijkl} is the reciprocal tensor of C_{ijkl}. The compliances of cubic crystals are given by

TABLE I Velocities of ultrasonic waves propagating down the [110] axis in zirconia-yttria solid solutions, the measured density and the lattice spacing

	Ultrasonic wave velocity cm/sec × 10^5			Density at room temperature gm cm^{-3}	Lattice spacing at room temperature Å
	Longitudinal	Shear			
		Fast	Slow		
$(ZrO_2)_{0.92}(Y_2O_3)_{0.08}$				6.036 ± 0.001	5.1276 ± 0.0001
77° K	7.09	5.12	3.11		
196° K	7.09	5.12	3.11		
$(ZrO_2)_{0.88}(Y_2O_3)_{0.12}$				5.894 ± 0.001	5.1401 ± 0.0001
77° K	7.30	5.78	3.26		
196° K	7.30	5.78	3.24		

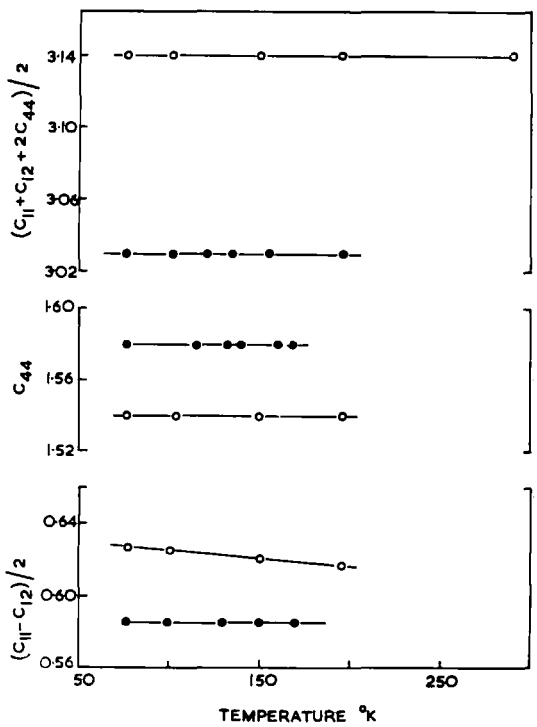

Figure 1 The temperature-dependence of the measured linear combinations of the elastic constants of $(ZrO_2)_{0.88}(Y_2O_3)_{0.12}$ (open circles) and $(ZrO_2)_{0.92}(Y_2O_3)_{0.08}$ (closed circles). The units are 10^{12} dynes cm^{-2}.

$$S_{11} = \frac{-(C_{11}+C_{12})}{(C_{11}+2C_{12})(C_{12}-C_{11})};$$

$$S_{12} = \frac{C_{12}}{(C_{11}+2C_{12})(C_{12}-C_{11})};$$

$$S_{44} = \frac{1}{C_{44}}. \quad (5)$$

Calculated values of S_{ij} are collected in table II.

The three independent compliances for cubic crystals can also be defined as the two reciprocal shear moduli S_{44} and $2(S_{11}-S_{12})$ and the compressibility $3(S_{11}+2S_{12})$.

The elastic stiffnesses and compliances for the two compositions of crystals are close: the mechanical properties are similar. Some insight can be gained into the degree of crystal stability: for a crystal lattice to be stable, certain relationships must hold between the elastic constants so that the energy density is positive [5]. Both $\frac{1}{2}(C_{11}-C_{12})$ and $(C_{11}+2C_{12})/3$ must be positive in cubic crystals. The greatest difference (~8%) between the elastic constants of $(ZrO_2)_{0.88}(Y_2O_3)_{0.12}$ and $(ZrO_2)_{0.92}(Y_2O_3)_{0.08}$, lies in $(C_{11}-C_{12})/2$. And this is significant. A negative value for $(C_{11}-C_{12})/2$ would lead to a spontaneous collapse of the lattice; the composition at which $(C_{11}-C_{12})/2$ becomes zero, represents the absolute stability limit of the fluorite phase. The decrease of 8% in $(C_{11}-C_{12})/2$ found between $(ZrO_2)_{0.88}(Y_2O_3)_{0.12}$ and $(ZrO_2)_{0.92}(Y_2O_3)_{0.08}$ indicates a reduction in lattice stability.

The absence of a substantial temperature-dependence of $(C_{11}-C_{12})/2$ for these crystals is consistent with the vertical phase boundary line at about 7 mol % Y_2O_3 in ZrO_2 in the phase diagram [3]: if the composition at which the phase change occurs did vary with temperature then $(C_{11}-C_{12})/2$ in compositions near the limit would be temperature-sensitive. A further criterion for stability is that $C_{11}^2 - C_{12}^2 > 0$. The parameter $(C_{11}^2 - C_{12}^2)$ decreases by 18% from the 12 mol % to the 8 mol % solution, again confirming the decreasing lattice stability as the yttria content is reduced.

For an isotropic substance $(C_{11}-C_{12})$ equals $2C_{44}$. The extent to which this relation holds good is an indication of the isotropy of a cubic

TABLE II The elastic stiffness and compliance constants of zirconia-yttria solid solutions

Elastic constants 10^{12} dynes cm^{-2}	$(ZrO_2)_{0.92}(Y_2O_3)_{0.08}$ 77° K	196° K	$(ZrO_2)_{0.88}(Y_2O_3)_{0.12}$ 77° K	196° K
$(C_{11} + C_{12} + 2C_{44})/2$	3.03	3.03	3.14	3.14
$(C_{11} - C_{12})/2$	0.585	0.585	0.627	0.617
C_{44}	1.58	1.58	1.54	1.54
C_{11}	2.04	2.04	2.23	2.22
C_{12}	0.870	0.870	0.973	0.983
$\frac{(C_{11} + 2C_{12})}{3}$ bulk modulus	1.26	1.26	1.39	1.40
$\frac{2C_{44}}{(C_{11} - C_{12})}$ anisotropy ratio	2.70	2.70	2.46	2.50
$\frac{C_{12}}{C_{44}}$ Cauchy relation	0.55	0.55	0.63	0.64
$C_{11}^2 - C_{12}^2$	3.305	3.305	4.032	4.052
Elastic compliances 10^{-12} cm^2 dyne^{-1}				
S_{11}	0.658	0.658	0.610	0.619
S_{12}	− 0.197	− 0.197	− 0.185	− 0.190
S_{44}	0.633	0.633	0.649	0.649

crystal. Values of $2C_{44}/(C_{11} - C_{12})$, quoted in table II, for the alloys, are not close to unity: a shear on a {100} cube face is resisted rather more than one on a diagonal {110} face. If the interatomic lattice forces are central, so that every atom is sited at an inversion point, the Cauchy relation ($C_{12} = C_{44}$) should hold. In the present case the experimental value of C_{12}/C_{44} is ~ 0.6. This is close to that found in MgO but different from the ratios found in the alkali halides in which the Cauchy relations hold quite well. In an alloy consisting of three atomic species and containing vacancies, the central forces model will not hold rigidly.

Knowledge of the bulk modulus can be used to develop an understanding of the type of binding between the atoms in the crystals. One approach is to assume ionic binding in spite of the non-central forces. Then we can write for the potential energy per unit cell

$$\Phi_0 = \frac{-\alpha^2 e^2 \mu A}{r} + \frac{B}{r^n}, \qquad (6)$$

where α is the largest common factor in the valencies of the ions (2 in the present case), μ is the number of molecules per unit cell, A is the Madelung constant and n is the repulsive exponent, which can be determined from the bulk modulus. The constant B in the repulsive term can be found in the usual way from the condition that $d\Phi/dr = 0$, when r takes the equilibrium distance R_0. Then

$$\Phi_0 = \frac{-\alpha^2 e^2 \mu A}{R_0}\left(1 - \frac{1}{n}\right) = \Phi_0^{(1)} + \Phi_0^{(n)} \cdot \qquad (7)$$

Now writing the lattice energy per mole U_0 as $(-N\Phi_0/\mu)$ we have

$$U_0 = \frac{\alpha^2 e^2 N A}{R_0}\left(1 - \frac{1}{n}\right) \cdot \qquad (8)$$

The effect of the presence of oxygen vacancies in the crystals can be taken into account to a first approximation by choosing for R_0 the cube root δ_0 of the molecular volume. The corresponding Madelung constant is then given by

$$\frac{A}{R_0} = \frac{A_{\delta 0}}{\delta_0} \cdot \qquad (9)$$

Then substituting 9 into 8 and introducing numerical values for Avogadro's number N and the electronic charge e, we have

$$U_0 = 280.6\ \alpha^2 (\rho/M)^{1/3} A_{\delta 0}\left(1 - \frac{1}{n}\right), \qquad (10)$$

where M is the gram molecular weight. $A_{\delta 0}$ for the fluorite lattice is 7.33058 [6, 7]. Calculated values for the Madelung energy, $280.6\ \alpha^2 (\rho/M)^{1/3} A_{\delta 0}$, are collected in table III. The attractive energy in the solid solutions is rather greater than that of pure zirconia.

TABLE III Thermodynamic parameters of the zirconia-yttria solid solutions

	$\frac{\rho}{M}$	Madelung attractive energy U_M	Repulsive energy U_n	Total binding energy $U_0 = U_M + U_n$	Debye temperature θ_0
ZrO_2	0.0430	− 2889	—	—	—
$(ZrO_2)_{0.88}(Y_2O_3)_{0.12}$	0.0435	− 2892	+ 321	− 2571	604° K
$(ZrO_2)_{0.92}(Y_2O_3)_{0.08}$	0.0459	− 2945	+ 348	− 2597	595° K

Energy units: kcal/mol

The relationship between the bulk modulus

$$K = -\frac{1}{V}\frac{dP}{dV} = -V\frac{\partial^2 U}{\partial V^2} = -V\left(\frac{\partial^2 U}{\partial x^2}\right)\left(\frac{dx}{dV}\right)^2 \quad (11)$$

and the repulsive exponent can be obtained by differentiating the potential energy expression twice with respect to internuclear distance and substituting into 11. For the fluorite lattice the nearest neighbour distance r_0 is $\sqrt{(3\,a_0/4)}$ and the volume V of a gram molecule is $16/(3\sqrt{3})\,Nr_0^3$. The exponent n can be shown to be

$$n = 1 + \frac{9\,\delta_0^4\,K}{\alpha^2 e^2 A_{\delta 0}} = 1 + \frac{9\,a_0^4\,K}{\alpha^2 e^2 A_{a_0}}. \quad (12)$$

Taking the measured lattice spacing (see table I), the appropriate Madelung constant ($A_{a_0} = 11.63$ for the fluorite lattice) [6, 7], and the measured bulk modulus, n is calculated as 9.1 for $(ZrO_2)_{0.88}(Y_2O_3)_{0.12}$ and 8.5 for $(ZrO_2)_{0.92}(Y_2O_3)_{0.08}$. For many ionic crystals, n is approximately equal to 9: the binding in these solid solutions appears to be largely ionic. By putting the values of n into equation 10, the total lattice energy per mole can be calculated (see table III). Repulsive energies are about 12% of the attractive energies. From the values of U_0, many thermochemical parameters become available.

One useful parameter, the Debye temperature θ_0, may be calculated readily from elastic constant data. Here the method of de Launay, based on the Born-von Karman model, has been used [8].

Then

$$\theta_0 = \frac{h}{k}\left(\frac{9N}{4\pi V}\right)^{1/3}\left(\frac{C_{44}}{\rho}\right)^{1/2}\left[\frac{9}{18+\sqrt{3}f}\right]^{1/3},$$

where values of f are tabulated in [6] in terms of the parameters

$$s = \frac{C_{11} - C_{44}}{C_{12} + C_{44}} \text{ and } t = \frac{C_{12} - C_{44}}{C_{44}}.$$

Elastic constant data have been extrapolated to 0° K. The values of θ_0 derived in this way are 604° K for $(ZrO_2)_{0.88}(Y_2O_3)_{0.12}$ and 595° K for $(ZrO_2)_{0.92}(Y_2O_3)_{0.08}$. Knowledge of the Debye temperature is important in the interpretation of spin-lattice relaxation behaviour [9] particularly in assessing whether direct or Raman processes should dominate the relaxation at a given temperature and in determining the influence of defect sites. In the studies of the effects of current passage in yttria-stabilised zirconia single crystals, it has been shown that, in electrically reduced samples, electron spin resonance spectra are observable at 77 and 4.2° K (9 GHz); these results will be discussed more fully elsewhere.

References

1. A review of the properties of zirconia can be found in E. RYSHKEWITCH, "Oxide Ceramics" (Academic Press, New York and London, 1960) p. 350.
2. D. K. SMITH and H. W. NEWKIRK, *Acta. Cryst.* **18** (1965) 983.
3. P. DUWEZ, F. H. BROWN, and F. ODELL, *J. Electrochem. Soc.* **98** (1951) 360.
4. T. ALPER and G. A. SAUNDERS, *J. Phys. Chem. Solids* **28** (1967) 1637.
5. M. BORN and K. HUANG, "Dynamical Theory of Crystal Lattices" (Clarendon Press, Oxford, 1954) p. 141.
6. J. SHERMAN, *Chem. Rev.* **11** (1932) 93.
7. W. VAN GOOL and A. G. PIKEN, *J. Materials Sci.* **4** (1969) 95.
8. G. A. ALERS, "Physical Acoustics" Vol. IIIB, edited by W. P. Mason (Academic Press, New York and London, 1965) p. 1.
9. D. R. MASON and J. S. THORP, *Phys. Rev.* **157** (1967) 191.

J. Phys. Chem. Solids Pergamon Press 1970. Vol. 31, pp. 1467–1476. Printed in Great Britain.

THE ELASTIC CONSTANTS AND INTERATOMIC BINDING FORCES IN ARSENIC

N. G. PACE, G. A. SAUNDERS and Z. SÜMENGEN
Department of Applied Physics and Electronics, the University of Durham, England

(*Received* 28 *October* 1969)

Abstract—The elastic constants of arsenic single crystals measured by the ultrasonic pulse echo technique at room temperature are presented ($C_{11} = 123{\cdot}6$, $C_{12} = 19{\cdot}70$, $C_{13} = 62{\cdot}30$, $C_{14} = -4{\cdot}16$, $C_{33} = 59{\cdot}11$, $C_{44} = 22{\cdot}57$, units are 10^{10} dyn cm^{-2}). To fix the sign of C_{14}, a right handed axial $(+x, +y, +z)$ set must be unambiguously determined in the sample. To assist this assignment, the relationships have been found between the etch pit orientation on the (111) cleavage plane, the twin plane and the accepted $(+x, +y, +z)$ axial set. In the literature it has often been stated that arsenic crystals consist of double layer planes bound by van der Waals forces. The potential energy function for this model is calculated and the model tested by comparison between theoretical and experimental values of the linear compressibility and thermal expansion. Good agreement obtains. This simple model provides useful physical insight into the lattice properties of arsenic which can be interpreted on the basis of a large component of van der Waals bonding between the double layers.

1. INTRODUCTION

THE ELASTIC constants of solids relate directly to the total crystal energy. The binding forces and thus the characteristic properties of the group *VB* semimetallic elements arsenic, antimony and bismuth are inextricably linked[1] to their unique rhombohedral, A7 crystal structure of space group $D^5_{3d}(R\bar{3}m)$. Two interpenetrating face-centred rhombohedral lattices with an angle of 54°10′ for arsenic, 57°14′ for antimony and 57°19′ for bismuth form the crystal lattice. Figure 1 shows the unit cell and primitive translation vectors. Any unit cell contains two atoms, each pertaining to a different rhombohedral sublattice. The two face-centred rhombohedrons are separated along the body diagonal by a fraction $2u$ of this diagonal[2]. A value of u equal to 0·25 corresponds to that primitive rhombohedron constructed in the closely related structure composed of two interpenetrating face-centred cubes. This displacement parameter u is 0·226 for arsenic, 0·2336 for antimony and 0·23407 for bismuth, emphasising that arsenic is considerably more distorted than bismuth or antimony: while the latter two have almost cubic crystal structures, that of

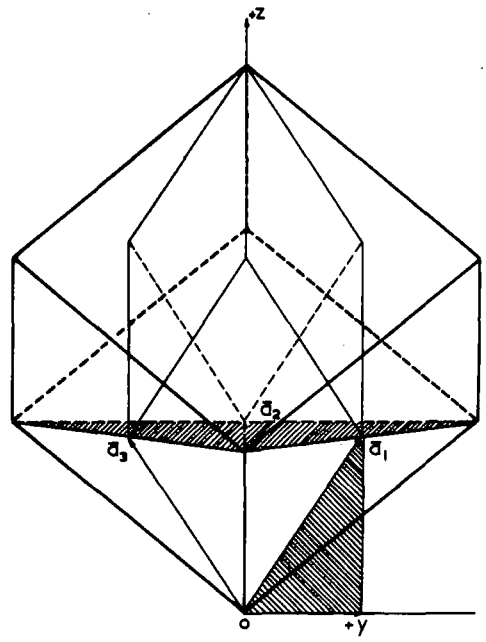

Fig. 1. The primitive rhombohedral cell sited inside the large face-centred rhombohedron for the A7 structure. The primitive translation vectors are denoted by $\mathbf{a}_i$ $(i = 1, 2, 3)$. The standard co-ordinate system is used, in which the y axis is chosen by projecting one of the $\mathbf{a}_i$ onto the (111) plane and taking the positive direction outwards from the origin O of the $\mathbf{a}_i$.

arsenic is far from being so. Indeed arsenic tends towards a layer-like crystal structure. Any particular atom is sited on one of the (111) planes and has three nearest neighbours on the adjacent parallel plane; three next nearest neighbours lie on another (111) plane on the other side of the given atom but much further away. The nearest neighbour (A_1) and next nearest neighbour (A_2) distances are 2·51 Å and 3·15 Å respectively. Thus planes normal to the trigonal [111] direction occur in pairs in which the atoms are comparatively close together, while these double layers are more widely spaced. Three different arrangements of the atoms on the planar networks are extant. A projection on to the *xy* plane (Fig. 2(a)) shows the relationship between these networks, labelled A, B, C, which follow sequentially along the *z*-axis and are separated by the short and long interplanar spacings in turn. The crystal structure is described by the sequence, shown in Fig. 2(b), 123123123 of three types of double layer network.

Binding between successive double layers is weak—as evidenced by the ease of cleavage to expose (111) planes—while on the other hand within the double layers atoms are bound tightly. The crystal chemistry of the group *VB* semimetals has been discussed in some detail in relation to the band structure[1]. Plausibly the deeper lying, outer shell s^2 electrons participate less in the interatomic binding than do the three *p* electrons; a valency of three commonly occurs for these elements. For arsenic in particular, bonding within the double layer planes would arise essentially from overlap of the p^3 orbitals, resulting in three bonds almost at right angles. The inter-bond angle in the layer planes is actually 97°12′, some *sp* hybridisation probably occurs. On this basis the gross features of the band structure become understandable[1]: two bands, essentially *s*-bonding and *s*-antibonding, are completely occupied, while three nearly full, predominantly *p*-bonding bands overlap slightly with nearly empty, *p*-antibonding bands to give the characteristic semimetallic behaviour. Antimony and bismuth do not exhibit such pronounced layer

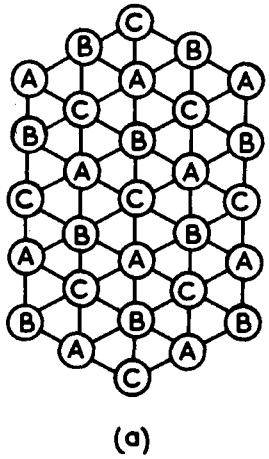

Fig. 2(a). The arrangement of the three types of atomic networks A, B and C for arsenic shown projected onto the *xy* plane.

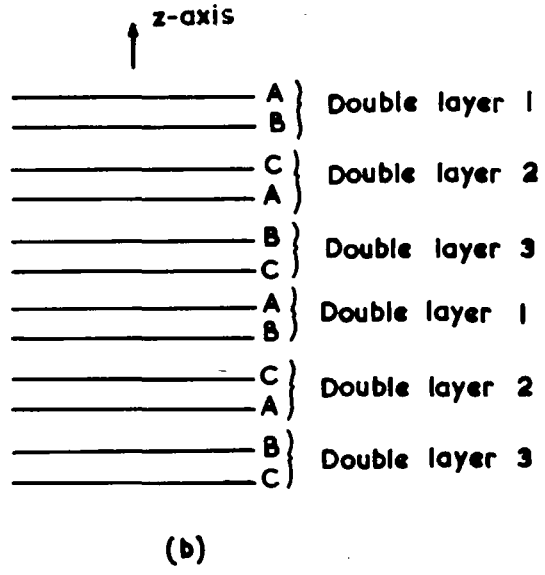

Fig. 2(b). The sequential nature of the planes normal to the *z*-axis in arsenic. Single planes are separated alternatively by $v_0(=2{\cdot}2531$ Å) and $w_0(=1{\cdot}2529$ Å) and are arranged in sequence *ABCABC*. The double layer planes follow the order 123123123.

structure and cannot have bonds localized within the double layers to the same extent as in arsenic.

The present concern is to report and interpret the elastic constants of arsenic. Comparison between the data and that for bismuth [3] and antimony [4] point to a marked difference between the interatomic binding in arsenic on the one hand and in bismuth and antimony on the other. Mechanical and thermal properties characteristic of layer-like structures would be anticipated for arsenic and the elastic constants attest to this. In particular the linear compressibility is much greater across the cleavage planes than along them, where in fact it is negative. Direct evidence is put forward that the atomic planes are loosely connected along the trigonal direction; this is suggestive of the model for arsenic, much quoted in textbooks, that the double layer planes are held together largely by van der Waals forces. This model is tested here. No previous quantitative assessments are available. Such a model cannot be used for rigorous computations: the high z-axis electrical conductivity [5] and the known Fermi surface point to some degree of orbital overlap between the double layer planes. However it is particularly suited to calculation because to a first approximation interlayer cohesion only need be considered. The exact nature of the interatomic binding within each double layer is not of paramount importance, provided that it is tight and the double layers can be taken as being rigid. The lattice sums of the potential energy are computed assuming a Lennard–Jones 6-n potential along the trigonal direction. Hence the energy of cohesion between the double layer planes is calculated. To assess the validity of the model, calculated linear thermal expansion and compressibility are compared with experimental data.

2. EXPERIMENTAL DETAILS AND RESULTS

The elastic constants were obtained from ultrasound velocity measurements on single crystals grown by the vapour phase method [6] from 99·9995 per cent purity arsenic. Crystal perfection was good; back reflection Laue X-ray photographs showed the pinpoint spots which evidence unstrained material. Dislocation etch pit density was of the order of $10^4\,cm^{-2}$ on the (111) cleaved surfaces. Further indications of the state of perfection of these crystals can be gleaned from carrier mobilities and densities obtained from the low field magnetoresistivity tensor [5]. For the A7 structure, the tensor component signs can depend upon the definition of a right-handed $(+x, +y, +z)$ axial set in the particular crystal under investigation [3, 7]. In the present instance, this is so for unambiguous determination of the sign of C_{14}. The co-ordinate system used here is illustrated in Fig. 1. The trigonal (z) axis, formed by the intersection of three mirror planes mutually orientated at $\pm 120°$, lies along the long body diagonal of the primitive rhombohedral unit cell defined from the lattice translation vectors $\mathbf{a}_1$, $\mathbf{a}_2$, $\mathbf{a}_3$. The bisectrix (y) axis, for which there are three options, is defined by projecting an $\mathbf{a}_i$ on to the trigonal plane; the positive y direction is taken outwards from the origin 0 of the $\mathbf{a}_i$. A positive binary (x) axis completes the right-handed set. The axis can be identified from Laue back-reflection photographs by reference to the relationship between the A7 crystal structure and a distorted cubic structure; the [100] directions show pseudo-fourfold symmetry and the body diagonal directions (except [111]) show pseudo-threefold symmetry. The quadrant in the mirror plane formed by the $+y$ and $+z$ axes contains a pseudo-threefold axis and that formed by the $-y$ and $+z$ axes a pseudo-fourfold axis. One practical approach to assignment of such a right-handed system in a particular crystal is to inspect etch pits on the (111) cleaved surfaces. We have found the unique orientation of these etch pits in arsenic crystals. This has proved useful for crystal orientation for the elastic constant measurements among others. For the sake of completion the etch pit orientation on antimony

crystals grown from the melt[8] has been looked at.

Crystals were cleaved to expose the (111) planes and etched. Pits on antimony, produced by Dash 1[9], are almost triangular, while those for arsenic, produced by an etch composed of two parts hydrofluoric acid, 1 part nitric acid and 1 part glacial acetic acid[6], have somewhat rounded sides. Straight slip lines, mutually oriented at 120°, are observed on the (111) plane for both antimony and arsenic along the $[10\bar{1}]$ directions, that is parallel to the three binary axes. Etch pits on a given plane all have the same orientation and each side of any pit, or rather in arsenic the tangent to the side centre, is parallel to the slip lines. The task remaining is to determine how the etch pits are orientated with respect to the $+x$ and $+y$ axes, when the $+z$ axis is defined as the outward normal from the cleaved surface. Etch pits in arsenic and antimony show the same orientation: a vector drawn from the centre normal to a pit side points along $+y$ axis. A cleavage plane can be exposed on opposite sides of a crystal; there are thus two possible definitions of the $+z$ axis as outward normals to these faces. For consistency of the orientation rule, the etch pits must point in opposite directions on these two faces. This has been confirmed.

Brown *et al.*[7] suggest for bismuth that a unique assignment of $+x$, $+y$ and $+z$ axes can be made using a twinning plane. If the (111) plane is intersected by a twinning plane such that a $-z$ axis intercepts the twinning plane below the (111) surface, then the $+y$ axis points from the binary line, defined as the intersection of the two planes, to an origin where the z-axis cuts the surface (see Fig. 2 of their paper). This rule is correct, if, as described in the literature[10], the twinning planes are (110) in Miller indices referred to the large face centred rhombohedron or (211) referred to the primitive rhombohedral cell. We have examined, by use of Laue back-reflection X-ray photographs, the crystallography of a large (2 cm × 1 cm × 1 cm) twinned crystal of arsenic. The twin plane, which is somewhat broadened, has been shown to be the (110). The (111) planes on either side of the twin plane have been exposed by cleaving and the etch pit orientation examined. The results, illustrated in Fig. 3, verify experimentally that the rule proposed[7] holds for arsenic. Further, the relationship between this (110) plane and the right-handed $+x$, $+y$, $+z$ set has been proved geometrically.

Crystals, aligned to within ±1° of the prerequisite directions, were planed to have faces flat and parallel to within 0·0002 cm and about 1 cm apart. Ultrasonic wave transit times were measured by the single-ended pulse-echo technique at a carrier frequency of 10 MHz. Further details of the technique and experimental apparatus may be found elsewhere [3, 11, 12]. Resonant, gold plated, quartz transducers, X-cut for longitudinal and Y-cut for transverse, were used to excite the ultrasound. The transducers were bonded to the crystal surfaces most satisfactorily with tensol cement. Room temperature ultrasonic wave velocities, determined as the statistical mean from the results of many experiments on several different crystals, are presented in Table 1. There are six Voigt elastic stiffness constants for $R\bar{3}m$ crystals; these are best represented by the matrix[3]

$$C_{ij}=\begin{vmatrix} C_{11} & C_{12} & C_{13} & C_{14} & 0 & 0 \\ C_{12} & C_{11} & C_{13} & -C_{14} & 0 & 0 \\ C_{13} & C_{13} & C_{33} & 0 & 0 & 0 \\ C_{14} & -C_{14} & 0 & C_{44} & 0 & 0 \\ 0 & 0 & 0 & 0 & C_{44} & C_{14} \\ 0 & 0 & 0 & 0 & C_{14} & C_{66} \end{vmatrix}. \quad (9)$$

Ultrasonic wave velocities are related[3] to the elastic stiffness constants C_{ij} by the set of equations (1–8) in Table 1. Eight velocities have been measured experimentally to allow two redundant checks for the six stiffness constants. To obtain the C_{ij}, a computer programme has been devised, producing a least-mean-squares fit to all eight velocities. The method is described in detail elsewhere[5].

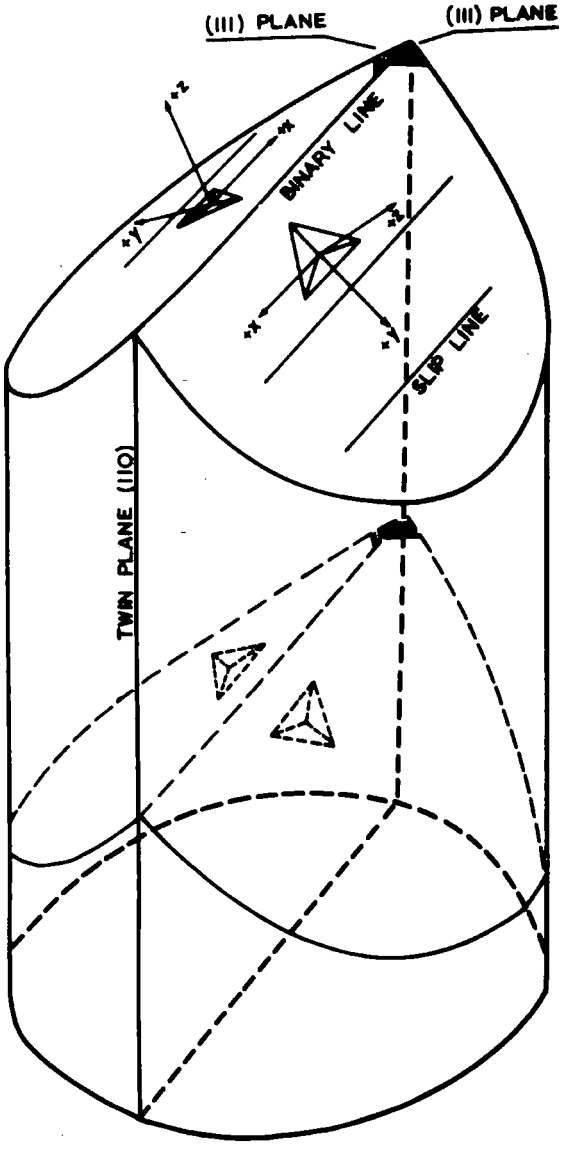

Fig. 3. Schematic of the orientation found for a twinned arsenic crystal. Etch pit orientation on the (111) cleaved surfaces and one of the three sets of slip lines (each parallel to a possible binary x direction) are illustrated. The intersection of the (111) planes on either side lies parallel to a binary direction; the twin plane, which is the (110), contains a binary direction. The relationship between etch pits and the Cartesian $(+x,+y,+z)$ coordinate system on either side of the twin plane is shown.

Each of the velocities is calculated, by inserting an arbitrary set of parameters into the equations (1–8), then divided by the corresponding experimental value and then compared to unity to compute a parameter $SUMSQ$ which is minimized.

$$SUMSQ = \sum_{i=1}^{8} \left| \frac{\text{calculated } \rho v_i^2}{\text{measured } \rho v_i^2} - 1{\cdot}0 \right|^2. \qquad (10)$$

The density of arsenic is taken as 5·766 g cm^{-3}. Calculated values for the C_{ij} for arsenic, together with those of bismuth and antimony are presented in Table 2(a). In addition, Table 2(b) includes the elastic compliances S_{ij}, where S_{ijkl} is the reciprocal tensor of C_{ijkl} (the usual matrix notation giving constants C_{ij} and S_{ij} is used, replacing 11 by 1, 22 by 2, 33 by 3, 23 by 4, 13 by 5, and 12 by 6). The transformation is affected by

$$S_{ij} = (-1)^{i+j}\Delta_{ij}^c/\Delta^c \qquad (11)$$

where Δ^c is the determinant of the C_{ij} terms and Δ_{ij}^c is the minor of the element C_{ij}.

For lattice stability, the crystal strain energy $\frac{1}{2}C_{ij}\epsilon_i\epsilon_j$ must be positive. To ensure this, the principal minor determinants of successive orders of the matrix C_{ij} (equation (9)) must all be greater than zero[13]. For $R\bar{3}m$ crystals, the principal minors are

$$C_{66},\ C_{44}C_{66}-C_{14}^2,\ C_{33}C_{44}(C_{44}C_{66}-C_{14}^2),$$

$$(C_{44}C_{66}-C_{14}^2)[(C_{11}C_{33}-C_{13}^2)C_{44}-C_{14}^2C_{33}],$$

$$(C_{44}C_{66}-C_{14}^2)[C_{44}(C_{11}-C_{12})(-2C_{13}^2+C_{33}$$

$$\times\{C_{11}+C_{12}\})+2C_{14}^2(2C_{13}^2-C_{12}C_{33})].$$

For all three elements, these requirements are satisfied, serving as an additional check on the experimental data.

The Debye temperature has been calculated from the elastic constant data using the harmonic series expansion method[14]. Accurate assessment requires low temperature elastic constants, but the value obtained ($\theta_D = 250$°K) from the room temperature data compares favourably with that (282°K) derived from

Table 1. Elastic stiffness constant equations and room temperature experimental velocities in arsenic crystals

Equation No.	Elastic stiffness constant equations	Propagation direction	Polarisation direction	Experimental velocity ($\times 10^{-5}$ cm/sec)
1	$\rho v_1^2 = C_{11}$	100	100	4·79
2	$\rho v_2^2 = \frac{1}{2}[(C_{66}+C_{44}) + \{(C_{44}-C_{66})^2+4C_{14}^2\}^{1/2}]$	100	001	2·99
3	$\rho v_3^2 = \frac{1}{2}[(C_{66}+C_{44}) - \{(C_{44}-C_{66})^2+4C_{14}^2\}^{1/2}]$	100	010	1·89
4	$\rho v_4^2 = C_{33}$	001	001	3·20
5	$\rho v_5^2 = C_{44}$	001	100 or 010	2·05
6	$2\rho v_6^2 = \frac{1}{2}(C_{11}+C_{33}) + C_{44} - C_{14} + \{(\frac{1}{2}C_{11}-\frac{1}{2}C_{33}-C_{14})^2 + (C_{13}+C_{44}-C_{14})^2\}^{1/2}$	$0, 1/\sqrt{2}, 1/\sqrt{2}$	$0, 1/\sqrt{2}, 1/\sqrt{2}$	4·32
7	$2\rho v_7^2 = \frac{1}{2}(C_{11}+C_{33}) + C_{44} - C_{14} - \{(\frac{1}{2}C_{11}-\frac{1}{2}C_{33}-C_{14})^2 + (C_{13}+C_{44}-C_{14})^2\}^{1/2}$	$0, 1/\sqrt{2}, 1/\sqrt{2}$	$0, -1/\sqrt{2}, 1/\sqrt{2}$	1·38
8	$\rho v_8^2 = \frac{1}{2}(C_{66}+C_{44}) + C_{14}$	$0, 1/\sqrt{2}, 1/\sqrt{2}$	100	2·43

Table 2(a). Elastic stiffness constants in units of 10^{10} cm^{-2} dyn *at room temperature*

	C_{11}	C_{12}	C_{13}	C_{14}	C_{33}	C_{44}	C_{66}	*SUMSQ*	Source
As	123·6	19·7	62·3	−4·16	59·1	22·6	51·9	0·010	This work
Sb	99·4	30·9	26·4	21·6	44·5	39·5	34·2	0·019	[4]
Bi	63·22	24·42	24·4	7·20	38·11	11·30	19·40	0·000	[3]

Table 2(b). Elastic compliance constants in units of 10^{-13} cm^2 dyn^{-1} *at room temperature*

	S_{11}	S_{12}	S_{13}	S_{14}	S_{33}	S_{44}	S_{66}	Source
As	46·6	36·8	−88·0	1·8	202·4	44·9	19·6	This work
Sb	16·2	−6·1	−5·9	−12·2	29·5	38·6	44·6	[4]
Bi	25·74	−8·01	−11·35	−21·50	40·77	115·9	67·51	[3]

specific heat measurements[15]. The energy change most easily computed from theoretical models is that associated with the compressibility, the measure of dilatation without shear under hydrostatic pressure. The volume compressibility in terms of the compliance constants is

$$\beta_v = S_{11} + S_{22} + S_{33} + 2(S_{12} + S_{23} + S_{31}). \quad (12)$$

The linear compressibility, defined as the relative decrease in length of a line when the crystal is subjected to unit hydrostatic pressure, has two components for rhombohedral materials, these are

$$\beta_t = S_{11} + S_{12} + S_{13} \quad (13)$$

$$\beta_z = (S_{11} + S_{12} + S_{13}) - (S_{11} + S_{12} - S_{13} - S_{33}) \quad (14)$$

for length changes perpendicular and parallel to the trigonal axis respectively. Calculated compressibilities for arsenic, antimony and

bismuth are collected in Table 3. Arsenic is the least compressible, so far as bulk dilatation is concerned. But along the trigonal axis, it is the most compressible: of the three elements, arsenic is the most weakly bound along this direction. Most striking and significant is the difference in sign of the two linear compressibilities β_t and β_z for arsenic. When the crystal is subjected to a hydrostatic pressure, it enlarges on the xy plane. A similar effect is shown by graphite[16] and by tellurium[17], crystals also having highly anisotropic structures. In arsenic, in particular, this property is understandable on the basis of weak interlayer binding. The resultant large compressibility produces a big change in the spacing between the double layers and the enhanced repulsive forces direct atoms outwards in the xy plane.

Table 3. Linear and volume compressibilities in units of 10^{-13} cm^2/dyn

	β_t	β_z	β_v	Source
As	−4·6	26·4	17·2	This work
Sb	4·1	17·5	25·8	[4]
Bi	6·38	18·07	30·83	[3]

3. LATTICE SUMMATIONS IN THE VAN DER WAALS MODEL FOR ARSENIC

Lattice properties can be computed from appropriate summations of the potential energy interactions of the atoms in the crystal. The layer-like structure of arsenic, the ready cleavage and the great anisotropy of the linear compressibilities β_t and β_z suggest that certain properties will be dominated by the interlayer cohesion. Certainly this is so[18] for the related semimetal graphite, which also has a layer structure. The purpose now is to calculate the lattice summations of the potential energy along the trigonal direction only in a model of rigid double layer planes interacting with each other by van der Waals forces. To probe this model for arsenic the results will be used to calculate z-axis compressibility and thermal expansion and the energy of cohesion. Then the theoretical assessments will be compared with experiment. The potential energy Φ between two interacting arsenic atoms located on unpaired trigonal planes is written as the sum of a van der Waals attractive term and a repulsive overlap term.

$$\Phi = A\left(\frac{b}{r^n} - \frac{1}{r^6}\right),\ n > 6. \tag{15}$$

Here r is the atomic separation and A and b are positive constants. Physically the London dispersion effect arises from interaction between momentarily induced atomic dipoles: to obtain the van der Waals attractive potential between the atoms, the atomic polarizability α is required[19–22]. Taking the first atomic ionization potential of arsenic as 10·05 eV, we estimate $4{\cdot}9 \times 10^{-24}$ cm^3 for α. Buckingham [23] using self consistent field, wave functions and including electron exchange, has given general relationships between the van der Waals constant A and the polarizability α. For two identical atoms with N electrons in the outer shell, his expressions take the form

$$A = \frac{3}{4}\frac{a^{1/2}e^2}{\sqrt{(\alpha/N)}} \tag{16}$$

which gives A as 230×10^{-60} ergs cm^6 for arsenic. Once A is known, a quantitative expression for the lattice potential energy ψ can be obtained from appropriate summations of Φ. The approach follows that used for graphite[18], although the detailed summation procedures for the A7 structure are more complex.

The potential energy function $\psi(Z_p)$ for interaction between an atom at the origin O with all the atoms on the p^{th} plane at a distance Z_p along the normal to the (111) planes is

$$\psi(Z_p) = A \sum_m [b(Z_p^2 + d_m^2)^{-n/2} - (Z_p^2 + d_m^2)^{-6/2}]. \tag{17}$$

Figure 4 shows the definition of d_m; it is at this point that the three different types of atomic arrangement (Fig. 2(a)) are taken into account. The values of d_m for one type of plane are different from those of the other two. All three types of planes have an identical number σ of atoms per unit area. To simplify, it is convenient to replace direct sums

$$s^n(Z_p) = \sum_m (Z_p{}^2 + d_m{}^2)^{-n/2} \qquad (18)$$

by integrals of the form

$$S^n(Z_p) = 2\pi\sigma \int_0^\infty (Z_p{}^2 + \gamma^2)^{-n/2}\gamma \,.\, d\gamma$$

$$= \frac{2\pi\sigma}{n-2} \cdot Z_p{}^{2-n}. \qquad (19)$$

Extensive machine computations have shown that the difference between $s^n(Z_p)$ and $S^n(Z_p)$ is negligible and this replacement is permissable. We can now write

$$\psi(Z_p) = A[bS^n(Z_p) - S^6(Z_p)]. \qquad (20)$$

Next the potential energy per unit area for interaction between two semi-infinite arsenic crystals can be obtained by summing $\psi(Z_p)$ over all values of Z_p and multiplying by the number of atoms per cm^2 on each plane

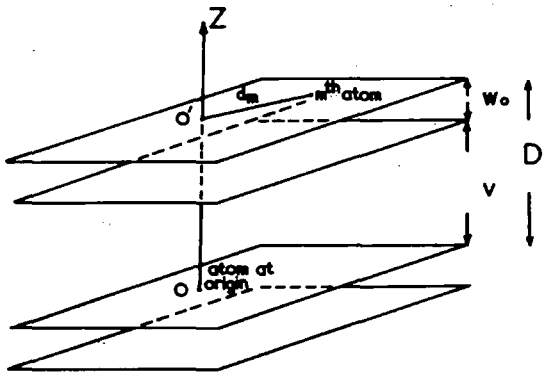

Fig. 4. A schematic diagram of the double layer planes. d_m is the distance of the mth atom on the pth plane from O', the point at which the normal from the origin O intersects that pth plane sited Z_p and O.

$$\sum_p \psi(Z_p) = \sigma A\left[b \sum_p S^n(Z_p) - \sum_p S^6(Z_p)\right]. \qquad (21)$$

To describe the full range of Z_p it is convenient to use three series expressions e_p, f_p and g_p, where

$$e_p = D\left(\frac{v}{D} + p\right), \; f_p = D\left(1 + \frac{w_0}{D} + p\right),$$

$$g_p = D(1+p), \quad p = 0, 1, 2\ldots$$

v and w_0 are respectively the distances between and within the double layers (see Fig. 4) and D is equal to $v + w_0$. Hence

$$\sum_{p=0}^{\infty} S^n(e_p) = \frac{2\pi\sigma D^{2-n}}{n-2} \sum_{p=0}^{\infty} \left(\frac{v}{D} + p\right)^{2-n}. \qquad (22)$$

This summation may be written in terms of the polygamma function $\phi^{(k)}$

$$\sum_{p=0}^{\infty} S^n(e_p) = (-1)^n \frac{2\pi\sigma D^{2-n}}{(n-2)!} \frac{(n-3)}{\phi(u/D)} \qquad (23)$$

where

$$\overset{(k)}{\phi}(r) = (-1)^{k+1} k! \sum_{m=0}^{\infty} (r+m)^{-(k+1)}.$$

When the same substitution is made for the other terms, the potential energy function is obtained as

$$\psi(v) = 2\pi\sigma^2 A\left[\frac{(-1)^n b D^{2-n}}{(n-2)!} \times \left(\overset{(n-3)}{\phi}(v/D) + \overset{(n-3)}{\phi}(1 + w_0/D) + 2\overset{(n-3)}{\phi}(1)\right) - \frac{D^{-4}}{4!}\left(\overset{(3)}{\phi}(v/D) + \overset{(3)}{\phi}(1 + w_0/D) + 2\overset{(3)}{\phi}(1)\right)\right]. \qquad (24)$$

The constant b is determined from the equilibrium condition $(d\psi/dv)_{v=v_0} = 0$. Expressions for the derivatives of $\psi(v)$ with respect to v are obtained by noting that

$$\frac{d\phi^{(n)}}{dv\phi}(v/D) = \frac{w_0}{D^2}\phi^{(n+1)}(v/D) \quad (25)$$

and

$$\frac{d\phi^{(n)}}{dv\phi}(1+w_0/D) = -\frac{w_0}{D^2}\phi^{(n+1)}(1+w_0/D). \quad (26)$$

These derivatives are required for calculation of the compressibility and thermal expansion. Numerical values of the poly-gamma functions were obtained for the first thousand terms by use of a computer. The potential energy functions $\psi(v)$ are plotted for three values $(n = 8, 10, 12)$ of the repulsive exponent in Fig. 5.

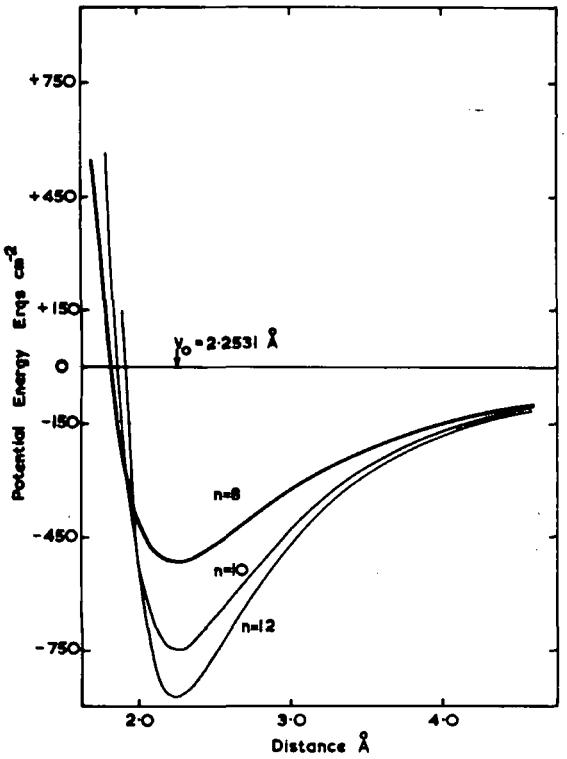

Fig. 5. The potential energy function $\psi(v)$ for interaction between two semi-infinite arsenic crystals. The results for the repulsive exponent $n = 8$, 10, 12 are shown, with the curve for $n = 8$ drawn in the thicker line.

4. DISCUSSION

Now that the experimental data for compressibility is available, it becomes possible to see how well the van der Waals model accounts for the measured lattice properties. A reasonable approximation is to replace the total volume change under hydrostatic compression with that due to the interplanar contraction, when the total energy change is equal to that in the lattice potential energy $\psi(v)$ alone. Then the z-axis linear compressibility may be expressed by

$$\frac{1}{\beta_z} = v\left(\frac{d^2\psi(v)}{dv^2}\right)_{v=v_0}. \quad (27)$$

Calculated values of β_z, taking the repulsive exponent n as 8, 10 and 12 in equation (24), are compared in Table 4 with the experimental result. Best agreement obtains when n is 8.

An independent assessment of the model can be obtained by recourse to thermal expansion data. The thermal expansion is a symmetric tensor of second rank with two independent components for rhombohedral crystals, one (δ_{33}) describing expansion along the z-axis and the other (δ_{11}) in the xy plane. In layer-type crystals anisotropy is enhanced and the thermal expansion coefficient δ_{33} of arsenic is much the greater, again relating to the weak interlayer binding. The linear expansion coefficient δ_{33} can be estimated from the potential energy function $\psi(v)$ following Zhdanov [24] whence

$$\delta_{33} = \frac{Gk}{(v+w_0)B} \quad (28)$$

where k is Boltzmann's constant and B and G are respectively the harmonic and anharmonic restoring force constants for a linear chain of coupled oscillators in a potential $\psi(v)$ and are given by

$$B = (v+w_0)/\beta_z,$$

$$G = -\frac{1}{2}\left(\frac{d\beta_z}{dv}\right)_{v=v_0}. \quad (29)$$

The values of δ_{33} calculated in this way are

Table 4. Measured and calculated values of linear compressibility, thermal expansion and interlayer cohesive energy for three values of repulsive exponent

Repulsive exponent (n)	Linear compressibility ($\beta_z \times 10^{13}$ cm^2 dyn^{-1})		Linear thermal expansion $\delta_{33} \times 10^5$ deg^{-1}		Interlayer cohesive energy (erg cm^{-2})
	Measured*	Calculated*	Measured†	Calculated*	
8	26·4	21·74	5·0	5·87	515
10		10·92		3·90	746
12		7·39		1·27	875

*This work.
†Ref. [25].

given in Table 4. Agreement with the experimental value[25] is good, again when the repulsive exponent is 8. In this case the interlayer cohesive energy is 515 ergs cm^{-2} (0·391 eV/atom) a ratio of 1 : 7·7 of the total cohesive energy (3·0 eV/atom). For graphite where the van der Waals model is certainly a better approximation than it is for arsenic, the same ratio is 1 : 39. So the magnitude of the calculated interlayer cohesive energy is reasonable. No experimental estimates exist for this parameter or the closely related heat of wetting.

The results in Table 4 demonstrate that the simple model of arsenic as a double layer structure held by van der Waals forces can give the correct order of magnitude for the linear compressibility and the thermal expansion along the z-axis. Indeed when the repulsive exponent is taken as 8, agreement is good. Plausibly there is a high proportion of this type of bonding along the z-axis. The model has the virtue of simplicity and allows a clear insight into the nature of lattice and mechanical properties of arsenic.

REFERENCES

1. COHEN M. H., FALICOV L. M. and GOLIN S., *I.B.M.J. Res. Dev.* **8**, 215 (1964).
2. FALICOV L. M. and GOLIN S., *Phys. Rev.* **137**, A871 (1965).
3. ECKSTEIN Y., LAWSON A. W. and RENEKER D. H., *J. appl. Phys.* **31**, 1534 (1960).
4. EPSTEIN S. and DeBRETTEVILLE A. P., *Phys. Rev.* **138**, A771 (1965).
5. JEAVONS A. P. and SAUNDERS G. A., *Proc. R. Soc.* **A310**, 415 (1969).
6. JEAVONS A. P. and SAUNDERS G. A., *Br. J. appl. Phys.* **1**, 869 (1968).
7. BROWN R. D., HARTMAN R. L. and KOENIG S. H., *Phys. Rev.* **172**, 598 (1968).
8. ÖKTÜ Ö. and SAUNDERS G. A., *Proc. phys. Soc.* **91**, 156 (1967).
9. WERNICK J. H., HOBSTETTER J. N., LOVELL L. C. and DORSI D., *J. appl. Phys.* **29**, 1013 (1958).
10. HALL E. O., *Twinning and Diffusionless Transformations in Metals* p. 57. Butterworths, London (1954).
11. ALPER T. and SAUNDERS G. A., *J. Phys. Chem. Solids* **28**, 1637 (1967).
12. PACE N. G., SAUNDERS G. A., SÜMENGEN Z. and THORP J. S., *J. mat. Sci.* **4**, 1106 (1969).
13. BORN M. and HUANG K., *Dynamical Theory of Crystal Lattices*, Chap. 3. Clarendon Press, Oxford (1963).
14. BETTS D. D., BHATIA A. B. and HORTON G. K., *Phys. Rev.* **104**, 43 (1956).
15. TAYLOR W. A., McCOLLUM D. C., PASSENHEIM B. C. and WHITE H. W., *Phys. Rev.* **161**, 652 (1967).
16. RILEY D. P., *Proc. phys. Soc.* **57**, 486 (1945).
17. BRIDGMAN P. W., *Proc. Am. Acad. Arts Sci.* **60**, 305 (1925).
18. GIRIFALCO L. A. and LAD R. A., *J. chem. Phys.* **25**, 693 (1956).
19. SLATER J. C. and KIRKWOOD J. G., *Phys. Rev.* **37**, 682 (1931).
20. LONDON F., *Trans. Faraday Soc.* **33**, 8 (1937).
21. MARGENAU H., *Rev. mod. Phys.* **11**, 1 (1939).
22. MOTT N. F. and SNEDDON I. N., *Wave Mechanics and its Applications*, Chap. 7. Clarendon Press, Oxford (1948).
23. BUCKINGHAM R. A., *Proc. R. Soc.* **A160**, 94 (1937).
24. ZHDANOV G. S., *Crystal Physics*, Chap. 14. Oliver & Boyd, London (1965).
25. KLEMM W., SPITZER H., NIERMANN H., *Angew. Chem.* **72**, 985 (1960).

Reprinted from
PHILOSOPHICAL MAGAZINE, Vol. 22, No. 175, p. 73, July 1970

Ultrasonic Study of the Martensitic Phase Change in TiNi

By N. G. PACE and G. A. SAUNDERS
Department of Applied Physics and Electronics,
The University of Durham, England

[Received 5 December 1969 and in revised form 27 February 1970]

ABSTRACT

Pulse-echo measurements have been made of the effect of the martensitic transformation, which occurs athermally in TiNi, on the propagation of ultrasound waves both in the vicinity of and away from the transition region. Considerable differences found between the elastic moduli of the two phases are shown to arise mainly from a variation in the free carrier density: the alteration in the binding energy from one phase to the other comes primarily from that in the Fermi energy contribution. The attenuation of the ultrasound, measured in the frequency range 10 MHz to 25 MHz, shows, in addition to the damping losses attributable to the specimen polycrystallinity, a rapid increase as the temperature approaches that of the transition. This is discussed in terms of a temperature dependent relaxation time associated with large amplitude, low frequency phonon modes.

§ 1. INTRODUCTION

NITINOL (TiNi) undergoes a martensitic transition now recognized as the archetype of the shape memory effect (de Lange and Zijderveld 1968). The present concern is to report measurements of the ultrasonic wave propagation in the vicinity of this phase change. The elastic and anelastic properties obtained furnish basic mechanical and thermodynamic information and provide physical insight into the nature of the transition.

At elevated temperatures the structure of the intermetallic compound TiNi is B2 (CsCl) with a lattice spacing of 3·00 Å. On cooling, the material undergoes the diffusionless transition to two slightly different but distinct base centred monoclinic martensites ($a_0^m = 5{\cdot}19$ Å, $b_0^m = 4{\cdot}96$ Å, $c_0^m = 4{\cdot}25$ Å, $\gamma^m = 99°$; $a_0^{m'} = 5{\cdot}19$ Å, $b_0^{m'} = 5{\cdot}52$ Å, $c_0^{m'} = 4{\cdot}25$ Å, $\gamma^{m'} = 116°$; where m and m' refer to the two martensites) (Marcinkowski, Sastri and Koskimaki 1968). If atom types are not considered, the martensite lattices have distorted hexagonal structures. The transition is accomplished by a simple shear on the $(1\bar{1}2)$ planes of the original B2 structure, in either the $[1\bar{1}1]$ or the $[\bar{1}1\bar{1}]$ direction, thus creating the two martensites. When equal amounts of the two martensites are present, there is no net shear strain. This martensitic transformation is unique in that, although it involves distortion, there is no associated volume change (Wang, Buehler and Pickart 1965). It is athermal. The transformation takes place over a temperature range which is extremely composition sensitive, and is not usually complete at room temperature. Further transformation can be induced by plastic deformation. If, after such plastic deformation, the

sample temperature is raised above the transition point, the original shape is regained because the reverse transformation annihilates the deformation (de Lange and Zijderveld 1968). This phenomenon has been termed the shape memory effect and has engineering potential in stored energy devices. Associated with the transition are many anomalous property changes. An extensive investigation of such changes in the electrical resistance, Hall effect, magnetic susceptibility and differential thermal analysis has been made (Wang, de Savage and Buehler 1968). The elastic and anelastic properties of TiNi have been looked at in the kilocycle frequency range (Wasilewski 1965, Spinner and Rozner 1966) and demonstrate a large damping capacity below the transition, another property which could find important engineering applications.

Previously, the only data available on ultrasonic wave propagation in TiNi was the longitudinal sound velocity measured at 5 MHz (Bradley 1965). In this paper we report anomalies in both longitudinal and shear ultrasonic wave velocities and also in the ultrasound attenuation in the vicinity of the transition. The elastic data are discussed in terms of changes in the interatomic binding energy which result from differences in the free carrier concentrations above and below the transition. Previous studies (Wang *et al.* 1968) have suggested that the transition is electronic in origin and that the instabilities exhibited by the lattice result from rather than being the cause of the changing number of free carriers. The elastic constant data presented here provide direct evidence for this interpretation.

§ 2. Experimental Procedures and Results

Samples of arc cast TiNi alloy with a composition close to 50 at. % Ni were kindly supplied by Dr. B. F. deSavage (U.S. Naval Ordnance Laboratory). The transition temperature was 59°C which indicates a nickel content of $50{\cdot}8 \pm 0{\cdot}1$ at. % (Wang *et al.* 1965). A twenty hour, 650°C anneal was used to remove effects of prior working (deSavage, private communication). Ultrasonic samples, cut from the rod by spark erosion, were about 0·4 cm in length and had opposite faces spark planed flat and parallel to within 0·0001 in. Ultrasonic wave velocities and attenuation were measured at carrier frequencies between 10 MHz and 25 MHz by the single-ended pulse-echo method of which details may be found elsewhere (Alper and Saunders 1967, 1969). The ultrasound was excited using gold-plates, quartz transducers, X-cut for longitudinal and Y-cut for shear waves. X-cut transducers bonded successfully to the sample at all temperatures in the range 100°C to −196°C with mannitol (melting point 179°C; measured velocity of longitudinal sound $2{\cdot}1 \times 10^5$ cm sec^{-1}). Bond quality for Y-cut transducers deteriorated in the vicinity of the transition temperature, due to the shears associated with the phase change. This difficulty was compounded by the high shear wave attenuation, thus subjecting measurements of shear wave velocities near the transition temperature to considerably larger errors

than those for the longitudinal wave. Improved bond quality for shear wave injection was achieved by using benzophenone (melting point 47°C) below the transition. The importance of the thermal history on the physical properties of TiNi has been stressed (Wang *et al.* 1968). Experiments carried out as a preliminary to the present work showed that incomplete thermal cycling greatly affects the ultrasonic propagation characteristics of the sample. To ensure an identical thermal history for each set of measurements, samples were always cycled completely between 200°C and −196°C. Once heating or cooling commenced, the sense of the temperature change was not altered. This procedure gave reproducible results. Because the transition is athermal, the measurements were always made during either continuous slow heating or cooling in an oil bath. Most of the measurements were done during slow cooling (0·05°C per minute) and the temperature, measured with a copper/constantan thermocouple, was effectively constant ($\pm 0{\cdot}02$°C) for the time taken over a reading. Results for the heating half of the cycle showed qualitatively the same temperature dependence except that the transition was displaced by about 20°C upwards in temperature. All data quoted here are on the cooling cycle, the correct way to drive the martensitic transition. Throughout the temperature range studied, the velocity showed no dispersion between 10 MHz and 25 MHz to within the experimental accuracy of $\pm 1\%$. Under a stress of 10^8 dynes cm^{-2} applied perpendicularly to the velocity propagation direction at room temperature there was no measurable change in the longitudinal sound velocity.

The elastic moduli characteristic of an isotropic solid are related to the sound velocities (v_L and v_S) by the equations:

$$K = (3\rho v_L^2 - 4\rho v_S^2)/3, \quad . \quad . \quad . \quad . \quad . \quad . \quad . \quad . \quad . \quad . \quad (1)$$

$$\mu = \rho v_S^2, \quad . \quad . \quad . \quad . \quad . \quad . \quad . \quad . \quad . \quad . \quad . \quad . \quad . \quad (2)$$

$$E = \rho v_S^2(3\rho v_L^2 - 4\rho v_S^2)/(\rho v_L^2 - \rho v_S^2), \quad . \quad . \quad . \quad . \quad . \quad (3)$$

$$\sigma = 0{\cdot}5(\rho v_L^2 - 2\rho v_S^2)/(\rho v_L^2 - \rho v_S^2), \quad . \quad . \quad . \quad . \quad . \quad . \quad (4)$$

where K is the bulk modulus, μ is the shear modulus, E is Young's modulus, σ is Poisson's ratio and ρ is the density (6·39 g cm^{-3}). The measured velocities in TiNi, converted to the elastic moduli, are shown in figs. 1 and 2 as a function of temperature. At −196°C the longitudinal and shear elastic moduli are $1{\cdot}90 \times 10^{12}$ and $0{\cdot}39 \times 10^{12}$ dyne cm^{-2} respectively. Errors in the velocities due to thermal expansion ($\Delta l/l = 9{\cdot}1 \times 10^{-6}$ °C^{-1}; Spinner and Rozner 1966) were small enough to be neglected.

The ultrasonic attenuation is shown in fig. 3 as a function of temperature in the frequency range 10 MHz to 25 MHz. In the vicinity of the transition the attenuation increases markedly. The main errors in these attenuation measurements arise from diffraction effects and transducer coupling losses and constitute a temperature independent, apparent background damping upon which the intrinsic material effects are superimposed. The diffraction loss has been shown to be 1·0 dB per a^2/λ (where a is the transducer radius)

and is readily subtracted (Granato and Truell 1956). Coupling losses were found to be 4·2 dB.

The major component of the intrinsic background loss is that associated with ultrasound wave scattering due to the polycrystalline nature of the samples. Each grain is elastically anisotropic and has its crystallographic axes misoriented with respect to those of its neighbours, thus giving rise to elastic gradients which cause an ultrasonic energy loss. In general

Fig. 1

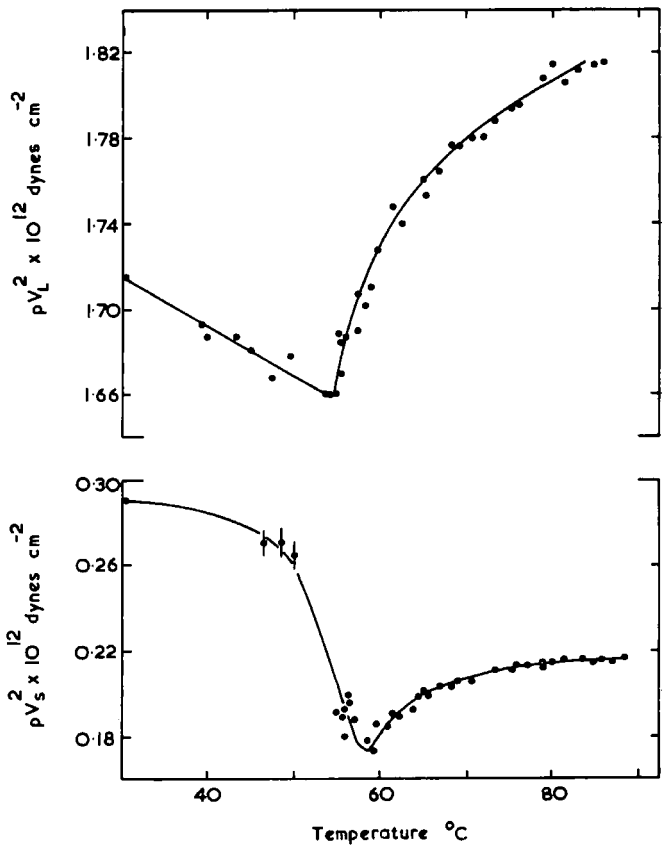

Temperature dependence of the longitudinal ρv_L^2 $(=K+\frac{4}{3}\mu)$ and shear ρv_S^2 $(=\mu)$ elastic moduli in TiNi.

the frequency dependence of the attenuation due to this scattering varies between the fourth and second power, depending upon whether the wavelength of the ultrasound is greater or less than $2\pi D$, where D is an average grain diameter (Papadakis 1968). In the samples used here the grains were equiaxed and had an average diameter of 26 ± 4 microns. Thus Rayleigh ($\lambda > 2\pi D$) scattering is expected. The attenuation separates at 90°C into a constant term and one varying as the fourth power of the

frequency. For longitudinal waves propagating in an elastically isotropic, polycrystalline material with single phase, equiaxed grains, the attenuation α due to Rayleigh scattering is given by (Papadakis 1968):

$$\alpha = TSf^4 \, d\text{B per cm}. \quad . \quad . \quad . \quad . \quad . \quad . \quad . \quad . \quad (5)$$

Here f is the frequency. The scattering coefficient is:

$$S = \gamma^2(8{\cdot}686 \, . \, 8\pi^3/375\rho^2 v_L{}^3)(2/v_L{}^5 + 3/v_S{}^5). \quad . \quad . \quad . \quad . \quad (6)$$

γ is the anisotropy factor $(C_{11} - C_{12} - 2C_{44})$ and is estimated for TiNi as $(-2{\cdot}3 \pm 0{\cdot}5) \times 10^{11}$ dynes cm^{-2} and S as 830 ± 350 dB cm^{-4} MHz^{-4}. These may be compared with those for nickel ($\gamma = -14{\cdot}7 \times 10^{11}$ dynes cm^{-2} and $S = 896$ dB cm^{-4} MHz^{-4}; Papadakis 1968).

Fig. 2

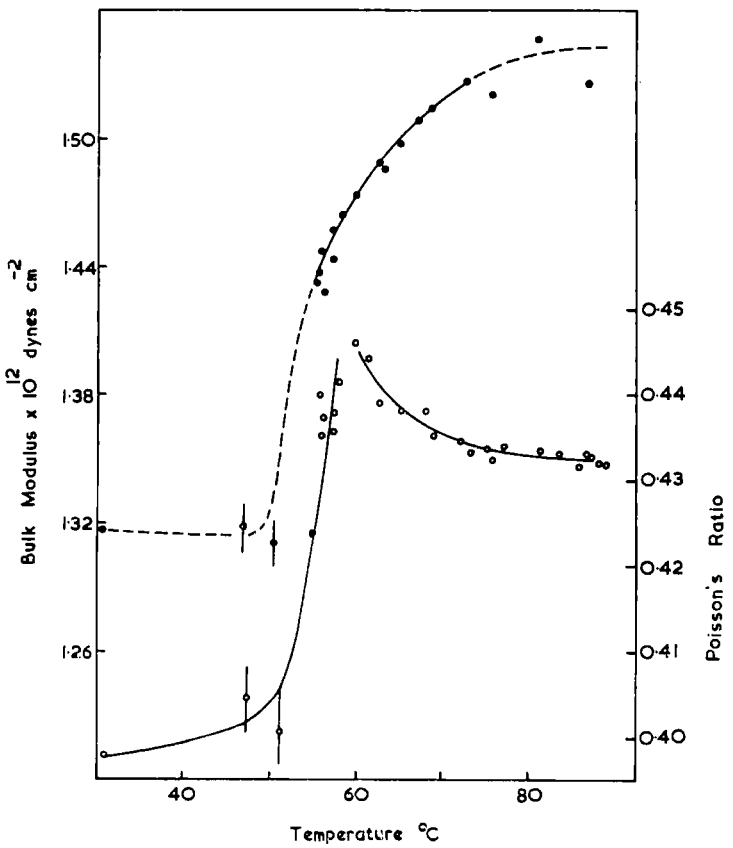

Temperature dependence of the bulk modulus K and Poisson's ratio.

Losses due to heat flow between adjacent grains (Zener loss) and viscous grain boundary losses will be present but do not contribute substantially in TiNi; these losses are estimated to be of the order of 10^{-3} dB/cm. When the losses due to transducer coupling, diffraction and that due to scattering

Fig. 3

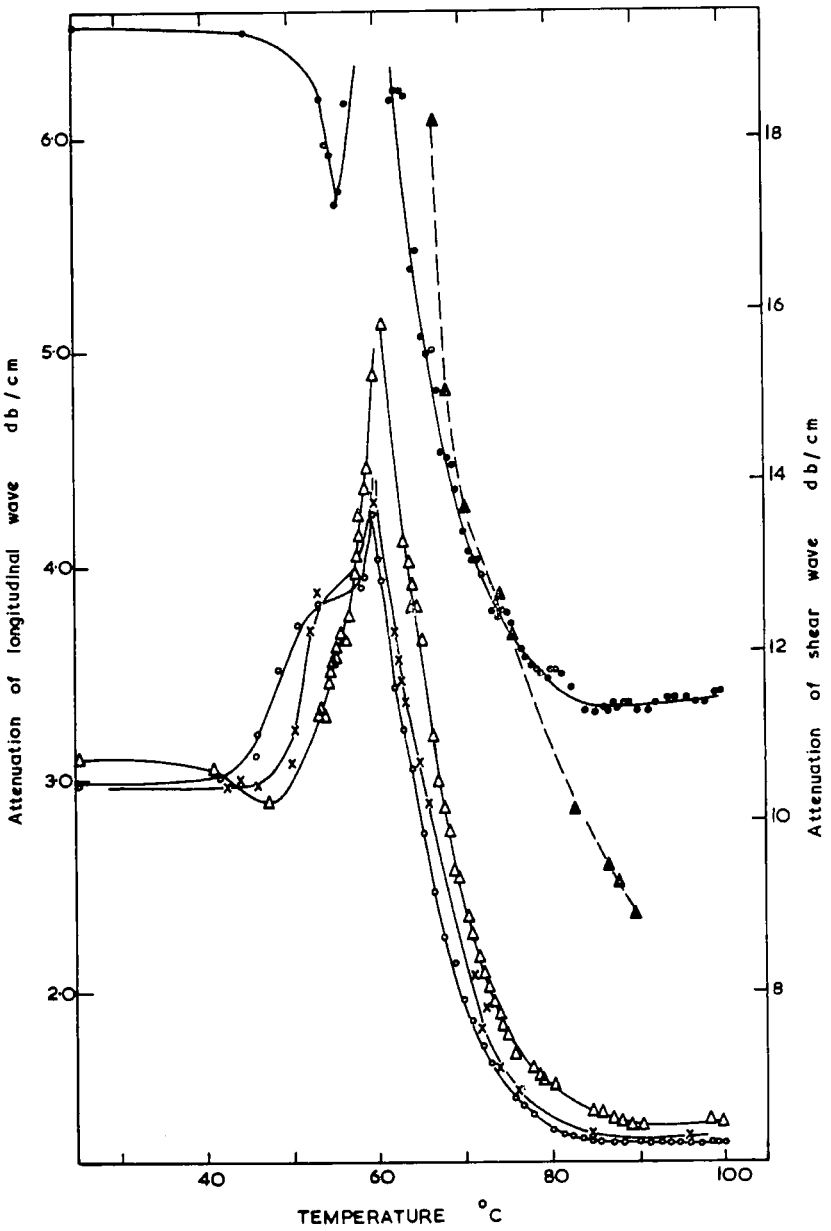

The measured attenuation of both longitudinal and shear ultrasonic waves as a function of temperature in the vicinity of the transition is shown. The results for the longitudinal waves are presented at 10 Mhz (○), 12 Mhz (×), 15 Mhz (△) and 25 Mhz (●). The shear wave attenuation is given at 12 Mhz (▲).

are subtracted from the measured longitudinal attenuation, the remaining attenuation, characteristic of the phase change, is shown in fig. 4 as a function of frequency at various temperatures: the decrement

$$\Delta(=8{\cdot}686\alpha(\text{dB/cm})\,.\,v_{\text{L}}(\text{cm/sec})/f(\text{sec}^{-1}))$$

is also plotted. The physical significance of the attenuation results will be discussed after the elastic constants to which we now turn.

Fig. 4

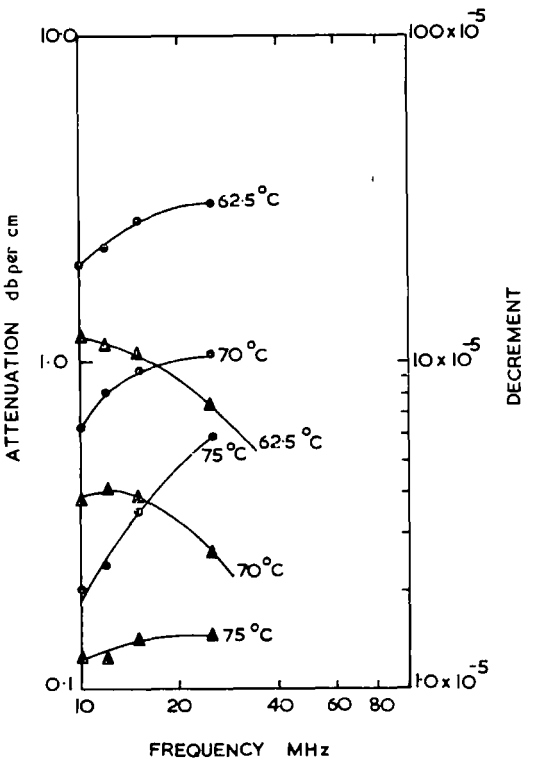

Attenuation (●) and decrement (▲) of longitudinal waves as a function of frequency at several temperatures near the transition.

§ 3. Discussion

The transition in TiNi has no apparent associated volume change and has been shown to be second order from measurements of the specific heat anomaly (Berman and West 1967). It has been suggested (Wang *et al.* 1968) that the instabilities associated with the transition are largely electronic in origin and that the anomalous specific heat can be accounted for by carrier density changes. A two-band model has been put forward for the high temperature, CsCl phase (Allgaier 1967); in a reduced zone scheme the Fermi surface is essentially a hole octahedron (the s band) located near the zone corners and an electron jack at the zone centre. In

the high temperature phase both the number of holes and the electrical resistance are larger than in the low temperature phase, results considered by Wang, deSavage and Buehler on the basis of a 'conduction' to 'covalent' electronic transformation. However, the electrical behaviour on either side of the transition can be interpreted as follows by recourse to the usual features exhibited by transition metals and their alloys. Above the transition the Fermi level location is such that the octahedral pockets of the Fermi surface contain a large number of holes and the overlapping d band a smaller number of heavy holes. Holes in the broad s band carry the current and vacant sites in the narrow, low mobility d band result in a high s–d scattering probability, which reduces the relaxation time for carriers in the s band: the carrier Hall mobility is only $0{\cdot}6\,\mathrm{cm^2\,volt^{-1}\,sec^{-1}}$, so the resistance in this phase is high. Below the transition the Fermi level is above the d band edge, so that the d band is full, and the reduced number of carriers in the s band are more mobile ($\mu_H = 3{\cdot}7\,\mathrm{cm^2\,volt^{-1}\,sec^{-1}}$) with longer lifetimes thus enhancing the conductivity, although the free carrier density ($0{\cdot}35 \times 10^{23}\,\mathrm{cm^{-3}}$) is lower in this phase than in the other ($1{\cdot}56 \times 10^{23}\,\mathrm{cm^{-3}}$).

The large change in the number of free carriers will be reflected in the binding forces and thus in the elastic properties. The temperature variations of the elastic moduli (figs. 1 and 2) exhibit both pronouneed changes at the transition point and the considerable difference between the elastic properties of the two phases of TiNi. The total energy of a system, the second derivative of which with respect to strains gives the elastic constants, may be expressed in the Wigner–Seitz cellular method as the sum of terms which can be calculated separately. These include the Fermi energy, the energy of the lowest electron state and the exchange and correlation terms. A reasonable hypothesis is that the difference between the total energy of the two phases in TiNi can be attributed largely to the change in the Fermi energy. The elastic constant data attest to this. The contributions to the bulk modulus due to the Fermi energy alone is given by (Jones 1949):

$$K_F = \frac{1}{9}\frac{r^2}{\Omega}\frac{d^2E_F}{dr^2}, \quad \ldots\ldots\ldots \quad (7)$$

where r is the radius of the atomic sphere defined so that $(4/3)\pi r^3$ equals Ω. Assuming a free-electron model, that is that the s-band hole octahedra are spheres, the Fermi energy E_F is given by:

$$E_F = \frac{3}{5}\left(\frac{3}{\pi}\right)^{2/3}\left(\frac{\pi^2\hbar^2}{2m}\right)\left(\frac{n}{\Omega}\right)^{2/3}, \quad \ldots\ldots\ldots \quad (8)$$

where n is the number of free carriers per atom. The radius of the atomic sphere is found from the unit cell dimensions to be the same above (1·4772 Å) and below (1·4774 Å) the transition, as expected for a second-order phase change. Differentiation of the Fermi energy twice with respect to r gives the bulk modulus from (7). Therefore, the change in the bulk modulus

between the two phases due to the change in the volume of the Fermi sphere is:

$$\Delta K_F = \frac{3\pi\hbar^2}{20m}\left(\frac{9}{4\pi^2}\right)^{2/3}\left(\frac{n_1^{2/3}-n_2^{2/3}}{r^5}\right), \quad . \quad . \quad . \quad . \quad . \quad (9)$$

where 1 and 2 refer to the high and low temperature phases respectively. From Hall effect measurements (Wang *et al.* 1968) the number of free carriers per atom in the high and low temperature phases is found to be $n_1 = 2{\cdot}11$ and $n_2 = 0{\cdot}47$ respectively. These give a value of ΔK_F equal to $3{\cdot}16 \times 10^{11}$ dynes cm^{-2} which compares with the experimental value of $2{\cdot}3 \times 10^{11}$ dynes cm^{-2} (fig. 2). Thus a most important contribution to the change in those binding forces responsible for resistance to bulk deformation comes directly from the change in the free carrier concentration. Further, this suggests that the magnitudes of the binding energy contributions arising from the energy of the lowest electron state and the exchange and correlation energies are not very different on either side of the transition. The calculated contributions K_F from the Fermi energy to the total bulk modulus K are about 30% of the experimental value above the transition and only 14% below the transition (for $T > T_c$, measured compressibility $= 15{\cdot}6$, $K_F = 4{\cdot}99$; for $T < T_c$, measured compressibility $= 13{\cdot}4$, $K_F = 1{\cdot}83$; units are 10^{11} dynes cm^{-2}). Thus while the total bulk modulus accrues from the large contributions other than that due to the Fermi energy, the difference in the bulk modulus between the two phases can be largely accounted for by the free carrier component.

The main feature exhibited by the shear modulus shown in fig. 1 is that the low temperature phase is the more resilient against shears. This is demonstrated strikingly by the difference between the Poisson ratios of the two phases away from the transition region (see fig. 2). The larger the Poisson ratio is (the maximum possible vealu is 0·5), the less stable the material is to shears. No contribution is made by the Fermi energy to the shear modulus unless the Fermi surface is in contact with, or intersects as it does in TiNi, the Brillouin zone boundaries. For example, the stability of β-brass with respect to shears across the (110) plane in the $[1\bar{1}0]$ direction arises minly from the change in the Fermi energy as a result of shearing the Brillouin zone (Jones 1952). Similarly in TiNi, since the number of holes is less in the low temperature phase, the area of the Brillouin zone boundary which the hole octahedron cuts is smaller than that in the high temperature phase, thus giving an increase in the shear stability below the transition, as demonstrated by the shear modulus and the Poisson ratio.

The difference in elastic properties of TiNi between the two phases away from the transition point thus arises mainly from changes in the free carrier concentration.

Another feature to consider is the appearance of pronounced changes in the moduli and an anomalous increase in the ultrasound attenuation near the phase transition (fig. 3). In particular the instability of the phases to a shear is clearly demonstrated by the Poisson ratio (fig. 2),

which rises sharply towards its maximum possible value of 0·5 at the transition.

A system undergoing a second-order phase change passes through a critical region in which the parent phase exhibits incipient instability (Callen 1961). This implies that some branch of the phonon dispersion curve in the parent phase approaches zero frequency. It is known (Cochran 1960) that the temperature dependences of dispersion relationships of particular normal modes are closely associated with displacive phase transitions. In particular it has been shown that a transverse optic mode of long wavelength in strontium titanate (Barker and Tinkham 1962) and potassium tantalate (Perry and McNelly 1967) has an anomalous temperature dependence: the square of its frequency is proportional to the temperature measured from the transition temperature. At this temperature the crystal is unstable and consequently the displacive ferroelectric transition occurs due to an instability against this mode of vibration.

In a similar way the transition in TiNi seems to be linked with an unstable phonon mode. The decrement, shown in fig. 4, exhibits a maximum at progressively lower frequencies as the temperature approaches that of the transition, indicative of a relaxation process whose relaxation time is strongly temperature dependent. The origin of this relaxation process may be found in the anomalously large temperature dependent amplitudes of the unstable modes. The ultrasound will be influenced by these large amplitude modes through phonon–phonon interactions: a large ultrasonic attenuation results with a consequent rapid change in the elastic moduli in the vicinity of the transition.

References

Allgaier, R. S., 1967, Symp. TiNi, United States N.O.L. Tech. Rep. 68–16.

Alper, T., and Saunders, G. A., 1967, *J. Phys. Chem. Solids*, **28,** 1637; 1969, *Phil. Mag.*, **20,** 225.

Barker, A. S., and Tinkham, M., 1962, *Phys. Rev.*, **125,** 1527.

Berman, H. A., and West, E. D., 1967, *J. appl. Phys.*, **38,** 4473.

Bradley, D., 1965, *J. acoust. Soc. Am.*, **37,** 700.

Callen, H. B., 1961, *Thermodynamics* (New York: Wiley), p. 173.

Cochran, W., 1960, *Adv. Phys.*, **9,** 387.

Granato, A., and Truell, R., 1956, *J. appl. Phys.*, **27,** 1219.

Jones, H., 1949, *Physica*, **15,** 13; 1952, *Phil. Mag.*, **43,** 105.

de Lange, R. G., and Zijderveld, J. A., 1968, *J. appl. Phys.*, **39,** 2195.

Marcinkowski, M. J., Sastri, A. S., and Koskimaki, D., 1968, *Phil. Mag.*, **18,** 945.

Papadakis, E. P., 1968, *Physical Acoustics*, Vol. IV–B, edited by W. P. Mason (London and New York: Academic Press), pp. 269–328.

Perry, C. H., and McNelly, T. F., 1967, *Phys. Rev.*, **154,** 456.

Spinner, S., and Rozner, A. G., 1966, *J. acoust. Soc. Am.*, **40,** 1009.

Wang, F. E., Buehler, W. J., and Pickart, S. J., 1965, *J. appl. Phys.*, **36,** 3232.

Wang, F. E., de Savage, B. F., and Buehler, W. J., 1968, *J. appl. Phys.*, **39,** 2166.

Wasilewski, G. J., 1965, *Trans. metall. Soc. A.I.M.E.*, **233,** 1691.

probably not beyond current technique in suitable materials. Particularly interesting is the production of good quality ultrathin crystals of materials with 'layer structure', such as GaSe (Kurtin 1969) and $Bi_8Te_7S_5$ (Ugaz and Soonpaa 1968). Ugaz and Soonpaa believe that QSE conditions prevailed in their films.

School of Mathematics and Physics,
University of East Anglia,
Norwich, NOR 88C

A. A. Cottey
20th July 1970

Filatov, O. N., and Karpovich, I. A., 1969, *Sov. Phys.–Solid St.*, **11**, 1328–30.
Friedman, A. N., 1967, *Phys. Rev.*, **159**, 553–63.
Kurtin, S., 1969, *Solid St. Commun.*, **7**, 1.
Nedorezov, S. S., 1967, *Sov. Phys. JETP*, **24**, 578–83.
Price, P. J., 1960, *IBM J. Res. Dev.*, **4**, 152–7.
Tavger, B. A., and Demikhovskii, V. Ya., 1969, *Sov. Phys.–Uspekhi*, **11**, 644–58.
Ugaz, E., and Soonpaa, H. H., 1968, *Solid St. Commun.*, **6**, 417–20.

The Grüneisen tensor of arsenic

Abstract. The components of the Grüneisen tensor of arsenic are presented and discussed in terms of the layer-like nature of the crystal structure. Strong elastic crosslinkage results in a lower anisotropy of the tensor components than might be anticipated.

The Grüneisen constant is an important parameter in the study of the equation of state and in the theory of anharmonic effects in solids. The present concern is to report and interpret values of the components of the Grüneisen tensor for arsenic. The characteristic properties of the group VB semimetallic elements arsenic, antimony and bismuth are closely linked to their unique rhombohedral A7 crystal structure of space group D^5_{3d} ($R\bar{3}m$). The crystal lattice of arsenic is considerably more distorted than that of bismuth and antimony; indeed arsenic tends towards a layer-like structure; planes normal to the trigonal (z) direction occur in pairs. Binding between these successive double layers is weak. Mechanical and thermal properties characteristic of layer-like structures obtain for arsenic (Pace *et al.* 1970) but not for antimony and bismuth.

The Grüneisen tensor can be evaluated from (Keys 1967)

$$\gamma_{ij} = C_{ijkl}\,\alpha_{kl}/\rho C_p \tag{1}$$

where ρC_p is the specific heat per unit volume at constant pressure and the C_{ijkl} are the adiabatic elastic stiffness constants. For uniaxial crystals the thermal expansion tensor α_{kl} has two independent components α_{11} and α_{33}. Thus for trigonal ($\bar{3}m$) crystals the Grüneisen tensor is

$$\begin{vmatrix} \gamma_{11} & \gamma_{12} & \gamma_{13} \\ \gamma_{21} & \gamma_{22} & \gamma_{23} \\ \gamma_{31} & \gamma_{32} & \gamma_{33} \end{vmatrix} = \frac{1}{\rho C_p} \begin{vmatrix} A & 0 & 0 \\ 0 & A & 0 \\ 0 & 0 & B \end{vmatrix} \tag{2}$$

where

$$\begin{aligned} A &= C_{11}\alpha_{11} + C_{12}\alpha_{11} + C_{13}\alpha_{33} \\ B &= 2C_{13}\alpha_{11} + C_{33}\alpha_{33} \end{aligned} \tag{3}$$

and the elastic stiffnesses are expressed in matrix notation. Calculated Grüneisen tensor components for arsenic are compared with those for antimony and bismuth in the table. The elastic constant data used was obtained by the ultrasonic pulse echo technique (Pace *et al.* 1970, Pace and Saunders to be published) on vapour grown single crystals (Jeavons and Saunders 1968). The constant pressure specific heat ($C_p = 1{\cdot}898 \times 10^7$ erg deg^{-1} cm^{-3}) was taken from Nogteva *et al.* (1966).

Recently Munn (1969) has discussed the Grüneisen tensor of antimony and bismuth and has predicted a greater anisotropy of its components at higher temperatures for arsenic than for the other two elements. However, while the layer-like nature of arsenic is attested to by the linear compressibility and the thermal expansion components (see the table), the anisotropy of the Grüneisen tensor is not so pronounced as might have been anticipated. This result is understandable on the basis of a strong elastic crosslinkage between the thermal expansions along the z axis and in the xy plane. The linear compressibilities parallel ($\beta_\parallel$) and perpendicular ($\beta_\perp$) to the trigonal axis are given by

$$\beta_\parallel = 2S_{13} + S_{33} \qquad \beta_\perp = S_{11} + S_{12} + S_{13} \tag{4}$$

where the S_{ij} are the compliance constants. When subjected to hydrostatic pressure, the arsenic lattice actually enlarges in the xy plane. Along the trigonal axis arsenic is much the most compressible of the three elements. This has been discussed elsewhere (Pace *et al.* 1970) on the basis of a model of weak interlayer binding forces but strong bonds within each double layer. For all three elements the compliance constant S_{13} is negative but its magnitude is much larger for arsenic ($-55{\cdot}19 \times 10^{-13}$ cm^2 dyn^{-1}) than for bismuth ($-11{\cdot}35 \times 10^{-13}$ cm^2 dyn^{-1}) or antimony ($-5{\cdot}9 \times 10^{-13}$ cm^2 dyn^{-1}); in the case of arsenic this results in a negative sign for $\beta_\parallel$.

Lattice vibrations will be excited preferentially in the direction of greater linear compressibility on account of the lower vibrational frequencies; thus the thermal expansion along this direction will be much the greater. Grüneisen and Goens (1924) have provided qualitative relationships for the thermal expansion in anisotropic crystals.

$$\alpha_x = \alpha_{11} = (S_{11} + S_{12})q_x + S_{13}q_z$$

$$\alpha_z = \alpha_{33} = 2S_{13}q_x + S_{33}q_z$$

where q_x and q_z are thermal pressure coefficients derivable from lattice theory. In arsenic $S_{11} + S_{12}$ ($=50{\cdot}4 \times 10^{-13}$ cm^2 dyn^{-1}) is close in magnitude but opposite in sign to S_{13} ($= -55{\cdot}19 \times 10^{-13}$ cm^2 dyn^{-1}): α_{11} is small. But the magnitude of S_{33} ($=137{\cdot}8 \times 10^{-13}$ cm^2 dyn^{-1}) is substantially larger than that of $2S_{13}$ ($=110{\cdot}4 \times 10^{-13}$ cm^2 dyn^{-1})

		Arsenic	Antimony	Bismuth
Thermal expansion (10^5 K^{-1})	α_{11}	0·3[a]	0·768[b]	1·211[b]
	α_{33}	4·3[a]	1·619[b]	1·685[b]
Grüneisen parameter	γ_{11}	1·71[c]	1·20[b]	1·32[b]
	γ_{33}	1·53[c]	0·94[b]	1·10[b]
Compressibility (10^{13} cm^2 dyn^{-1})	β	17·92[d]	25·8[e]	30·83[f]
	$\beta_\perp$	−4·75[d]	4·1[e]	6·38[f]
	$\beta_\parallel$	27·42[d]	17·5[e]	18·07[f]

a, Childs 1953; b, Bunton and Weintroub 1968; c, this work; d, Pace *et al.* 1970, Pace and Saunders, to be published; e, Epstein and de Bretteville 1965; f, Eckstein *et al.* 1960.

hence α_{33} turns out to be larger than α_{11}. This is reflected in the Grüneisen tensor components because, for arsenic alone, to a good approximation

$$A = \alpha_{33}C_{13} \qquad B = \alpha_{33}C_{33}. \tag{5}$$

And, since C_{13} ($=64{\cdot}27 \times 10^{10}$ dyn cm^{-2}) and C_{33} ($=58{\cdot}74 \times 10^{10}$ dyn cm^{-2}) are close, the anisotropy of the Grüneisen tensor components for arsenic at room temperature is not large. The table gives the high temperature limiting values of the Grüneisen tensor coefficients for antimony and bismuth. These are substantially smaller than those of arsenic. For antimony and bismuth the γ_{ii} are close to unity and so the normal mode lattice frequencies are effectively inversely proportional to the volume; while for arsenic these frequencies have a more marked volume dependence.

Department of Applied Physics and Electronics
University of Durham.

N. G. Pace
G. A. Saunders
28*th July* 1970

Bunton, G. V., and Weintroub, S., 1969, *J. Phys.* C.: *Solid St. Phys.*, **2**, 116–123.
Childs, B. G., 1953, *Rev. Mod. Phys.*, **25**, 665–670.
Eckstein, Y., Lawson, A. W., and Reneker, D. H., 1960, *J. appl. Phys.*, **31**, 1534–1538.
Epstein, S., and de Bretteville, A. P. Jnr., 1965, *Phys. Rev.*, **138**, A771–A779.
Grüneisen, E., and Goens, E., 1924, *Z. Phys.*, **29**, 141–156.
Jeavons, A. P., and Saunders, G. A., 1968, *J. Phys.* D.: *Appl. Phys.*, **1**, 869–872.
Keys, S. W., 1967, *J. appl. Phys.*, **38**, 2923–2928.
Munn, R. W., 1969, *Adv. Phys.*, **18**, 515–543.
Nogteva, V. V., Paukov, I. E., and Strelkov, P. G., 1966, *Sov. Phys.–Solid St.*, **7**, 1884–1886.
Pace, N. G., Saunders, G. A., and Sümengen, Z., 1970, *J. Phys. Chem. Sol.*, **31**, 1467–1476.

Orientation kinetics of Gd^{3+}–F^- interstitial pairs in CaF_2

Abstract. The esr spectrum from substitutional Gd^{3+} ions with adjacent trapped F^- interstitials broadens significantly above about 100°C. The temperature-dependent part of the relaxation time associated with this broadening is compatible with the relaxation time derived by dielectric relaxation measurements on identically treated crystals. These results are interpreted in terms of the orientational diffusion of the trapped F^- interstitial ion around the immobile Gd^{3+} ion in a cation site. The relaxation time is given by $\tau = \tau_0 \exp(Q/kT)$, with $\tau_0 = 8{\cdot}2 \times 10^{-14}$ s and $Q = 0{\cdot}38$ eV.

Several authors (principally Chen and McDonough 1964, 1966, 1969 and Caffyn *et al.* 1967) have reported observation of dielectric relaxation in CaF_2 containing trivalent impurities. They have attributed this relaxation to dipoles, each composed of a trivalent ion on a cation site associated with a fluorine ion on the nearest interstitial sites. These relaxations occur, at temperatures from 100 to 300°C, in the frequency range from 10^2 to 10^5 Hz.

On the other hand, Rewaj (1968) has observed that the esr spectrum from the same complex (tetragonal centre) in GdF_3-doped CaF_2 disappears at about 150°C. Rewaj has attributed this disappearance to thermal dissociation of the complex into isolated Gd^{3+} ions and free F^- interstitials. Franklin and Marzullo (1970), repeating the Rewaj experiment, found that the dissociated state could not be captured even by as drastic a quench as a direct plunge of the hot crystal into a dry-ice–acetone mixture. Since the disappearance of the esr spectrum from the tetragonal centres is accompanied by marked line broadening,

they adopted the explanation put forth by Watkins (1959) to account for a similar phenomenon occurring in NaCl containing $MnCl_2$, namely that at the temperature of disappearance the lifetime of the F^- interstitial in any given site is comparable to the period of the microwave signal used to observe the esr spectrum.

The dielectric and esr results quoted above should give information about essentially the same process, but, in fact, they are quite incompatible. The esr relaxation time at 150°C is of the order of 10^{-9} s, while that from the dielectric experiments of Chen and McDonough is greater than 10^{-5} s at the same temperature.

We have now found a Debye-type relaxation in the dielectric spectrum of CaF_2 containing 0·08 mol.% GdF_3, annealed in He–HF at 800°C. This relaxation is compatible with the esr linebroadening data from similar crystals containing either 0·08 mol.% or 0·01 mol.% GdF_3. Figure 1 shows a plot of the logarithm of the relaxation times against inverse temperature from both measurements.

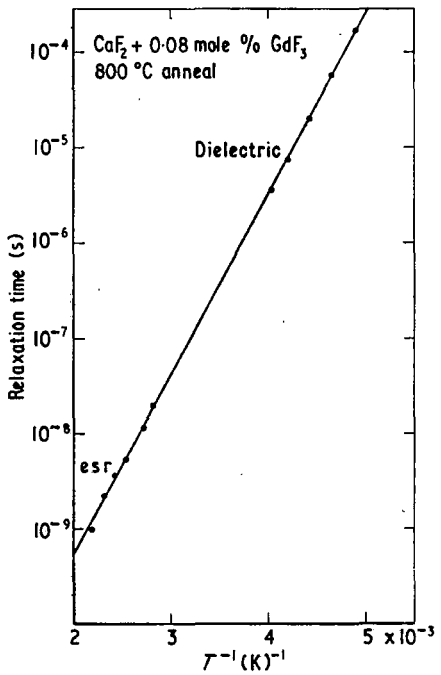

Figure 1. Temperature dependence of the esr and dielectric relaxation times arising from reorientation of Gd^{3+}–F^- interstitial pairs in CaF_2.

The dielectric relaxation time is ω_m^{-1}, where ω_m is the circular frequency at which the imaginary part of the dielectric constant rises to a maximum. The esr time was calculated from the line-breadth

$$\frac{1}{\tau_{esr}} = \frac{1}{\tau_T} - \frac{1}{\tau_I} \tag{1}$$

where

$$\tau_T = \frac{H_0}{\sqrt{3}\pi\nu_0\Delta H} \tag{2}$$

with ν_0 the microwave frequency (9·1 GHz), H_0 the magnetic field at the centre of the (derivative absorption) line, ΔH the peak to peak breadth of the line on the magnetic field axis, and τ_I the temperature independent relaxation time obtained by minimizing the error